DYNAMICS OF A DISCHARGE-EXCITED XeCl LASER

By

© WING YEE LEE, B.Eng., M.S.

A Thesis

Submitted to the School of Graduate Studies

in Partial Fulfilment of the Requirements

for the Degree

Doctor of Philosophy

McMaster University

DYNAMICS OF A DISCHARGE-EXCITED XeCl LASER

DOCTOR OF PHILOSOPHY (1983) McMASTER UNIVERSITY
(Physics) Hamilton, Ontario

TITLE: Dynamics of a Discharge-Excited XeCl Laser

AUTHOR: Wing Yee Lee, B.Eng. (McMaster University)
M.S. (University of Rochester)

SUPERVISOR: Professor E.A. Ballik

NUMBER OF PAGES: xxi , 316

ABSTRACT

The optical output characteristics of a photo-preionized avalanche discharge XeCl exciplex laser are studied experimentally and analytically. Experimental results are presented for the laser system employing a range of He/Xe/HCl mixtures and discharge conditions. An output energy of ~200 mJ, in an almost flat-topped 60-ns duration (FWHM) optical pulse, has been attained. A viable kinetic scheme has been developed for modelling the laser output pulses, and for investigating the dynamical processes in a pulsed discharge.

The $B\ ^2\Sigma_{\frac{1}{2}}^+ \rightarrow X\ ^2\Sigma_{\frac{1}{2}}^+$ emission is characterized by means of Franck-Condon calculations using wavefunctions derived from a Rittner-type potential for the excimer B-state, and a new potential-energy function for the ground X-state. This new function reproduces accurately (~±1%) published experimentally-derived data, and demonstrates the "super-harmonicity" of the ground-state molecule. The primary exciplex formation channels, deduced from the electronic structure, are the recombination of Xe^+ and Cl^- ions, and the "harpooning" processes via the Rydberg molecules $Xe(^3P_2)\cdot Cl(^2P_{3/2})$ and $Xe(^3P_1)\cdot Cl(^2P_{3/2})$. The latter two processes contribute to high optical gain when ion densities are low.

A comprehensive kinetic model is developed on the basis of achieving good agreement between computed and observed optical pulse-shapes, in terms of total energy, peak power, pulse duration, delay time for onset of emission, and rise- and fall-times. The rate coefficients for electron collision processes are calculated using

electron-energy distribution functions derived from Monte-Carlo electron transport simulations (electron-electron scattering is included). Calculated intrinsic laser parameters (unsaturated gain, absorption coefficient and saturation irradiance) are in good agreement with values determined from output-power measurements (employing different output couplers and in-cavity attenuators) used together with gain-saturation theory.

ACKNOWLEDGEMENTS

I am sincerely grateful to Dr. E.A. Ballik for his supervision and support throughout the course of this work. Also, I would like to thank the members of my Supervisory Committee: Dr. D.R. Eaton, Dr. B.K. Garside and Dr. R.G. Summers-Gill for their interest in this research.

In addition, I would like to express my gratitude to Mr. C. Dang, Ms. S.K. Lee and Mr. T. Tricker for their encourgement in many ways.

Lastly, I cannot adequately express my appreciation and love to my wife, Pat, for her patience, care and encouragement, and for the long hours she spent in typing this umfamiliar material.

TABLE OF CONTENTS

		Page
ABSTRACT		iii
ACKNOWLEDGEMENTS		v
TABLE OF CONTENTS		vi
LIST OF FIGURES		ix
LIST OF TABLES		xx
CHAPTER 1	INTRODUCTION	1
	1.1 Preliminaries of Excimer Lasers	1
	1.2 Rare-Gas Halide Exciplex Systems	2
	1.3 Principles of a Xenon Monochloride Laser	7
	1.4 Organization of the Thesis	11
CHAPTER 2	MOLECULAR STRUCTURE OF XENON MONOCHLORIDE	16
	2.1 Introduction	16
	2.2 The Weakly-Bound Ground State and Its Determination	18
	2.3 The Excimer States	39
	2.4 Radiative B → X Electronic Transition	43
	2.5 Experimental Observation of the B → X Emission Spectra	60
	2.6 The Rydberg States and Their Relation to Exciplex Formation	67
	2.7 Summary	69
CHAPTER 3	AN AVALANCHE DISCHARGE LASER SYSTEM	72
	3.1 Introduction	72
	3.2 Development of a Photoionized, Avalanche Discharge Laser System	74
	3.2.1 Electrical Circuitry	74
	3.2.2 Mechanical Construction	80

		Page
	3.2.3 Gas Handling System	87
	3.3 System Performance	89
	3.3.1 Output Energy	93
	3.3.2 Electrical Characteristics	105
	3.3.3 Optical Characteristics	129
	3.4 Summary	146
CHAPTER 4	ELECTRON TRANSPORT SIMULATION OF INITIAL AVALANCHE DEVELOPMENT IN He/Xe/HCl DISCHARGES	151
	4.1 Introduction	151
	4.2 Monte-Carlo Simulation of Electron Transport	156
	4.2.1 Principle of Calculation	157
	4.2.2 Cross-Sections for Electron Collision Processes	167
	4.3 Application to He/Xe/HCl Discharges: Determination of Electron Energy Distributions and Reaction Rates	177
	4.4 Concluding Remarks	205
CHAPTER 5	REACTION KINETICS AND EXCIPLEX FORMATION	206
	5.1 Introduction	206
	5.2 Production of Photoelectrons	210
	5.3 Particle Dynamics and Exciplex Radiation	214
	5.4 Quasi-Steady-State Determination of Laser Gain	247
	5.5 Determination of Laser Parameters Using Intracavity Attenuators	252
	5.6 Discussion	254
CHAPTER 6	CONCLUSIONS	258
APPENDIX A	A POTENTIAL FUNCTION FOR AN IONIC-COVALENT MIXED STATE	266
APPENDIX B	AN EXACTLY SOLVABLE WAVE EQUATION FOR A REPULSIVE POTENTIAL	268
APPENDIX C	FRANCK-CONDON FACTORS AND DENSITIES FOR THE XeCl B → X SYSTEM	274

	Page
APPENDIX D STRUCTURAL ANALYSIS OF THE LASER SYSTEM	281
APPENDIX E SOLUTION OF THE BOLTZMANN TRANSPORT EQUATION FOR ELECTRONS	291
APPENDIX F CALCULATIONS FOR THREE-BODY COLLISION PROCESSES INVOLVING DOUBLE CROSSINGS OF POTENIAL-ENERGY CURVES	295
REFERENCES	302

LIST OF FIGURES

		Page
Fig. 1-1	Typical potential energy curves distinguishing a rare-gas halide molecule (RX) and a rare-gas dimer (R_2).	4
Fig. 2-1	Potential energy diagram of xenon monochloride.	17
Fig. 2-2	Comparison of theoretical and experimentally-derived potential energy curves for the XeCl ground state ($X\ ^2\Sigma^+$).	21
Fig. 2-3	Theoretical potential energy curves for the XeCl lowest excited state ($A\ ^2\Pi_{3/2,1/2}$).	23
Fig. 2-4	Comparison of calculated and experimentally-derived ground-state potential energy curves and vibrational levels in XeCl.	33
Fig. 2-5	Birge-Spooner diagram for the XeCl ground state.	34
Fig. 2-6	The transformed variable s(r) for the XeCl ground state.	37
Fig. 2-7	Vibrational wavefunctions, $\psi_{v''}(r)$, for the XeCl ground state.	38
Fig. 2-8	Repulsive wavefunctions for the XeCl ground state.	40
Fig. 2-9	Comparison of theoretical and experimentally-derived excimer states of XeCl (B(1/2) or III(1/2), C(3/2) or IV(3/2), and D(1/2) or IV(1/2)).	44
Fig. 2-10	The transformed variable s(r) for the XeCl B $^2\Sigma^+$ state.	51
Fig. 2-11	Vibrational wavefunctions, $\psi_{v'}(r)$, for the XeCl B $^2\Sigma^+$ state.	52
Fig. 2-12	Graphical plots of Franck-Condon factors and densities and normalized "lineshape" function versus wavelength	54

Page

(in air) for the v' = 0 progression in the XeCl B → X system.

Fig. 2-13 Comparison of various "lineshape" functions using the tentative transition dipole-moment functions from Tamagake et al. [81]. 55

Fig. 2-14 Stimulated and spontaneous emission spectrograms of the B → X transition, using a He/2.5% Xe/0.3% HCl mixture at 1665-Torr pressure and an electrode spacing of 2.60 cm. 62

Fig. 2-15 Stimulated emission spectrogram of the B→X transition, using the same operating conditions as employed in Fig.2-14(a), but without an external reflector. 63

Fig. 2-16 Stimulated emission spectrogram of the B → X transition, using a He/2.5% Xe/0.3% HCl mixture at 1794-Torr pressure and an electrode spacing of 2.29 cm. 64

Fig. 2-17 A schematic potential energy diagram of XeCl showing the formation channels of the XeCl(B) exciplex. 70

Fig. 3-1 Discharge circuit. 76

Fig. 3-2 High-voltage trigger system. 78

Fig. 3-3 Circuit diagram of a dual 3-V pulse generator. 79

Fig. 3-4 Overall view of the laser system. 81

Fig. 3-5 Main section of the discharge chamber. 82

Fig. 3-6 Cross-sectional view of the laser. 83

Fig. 3-7 Supporting structure of the laser discharge chamber. 85

Fig. 3-8 Preionizer assembly. 86

Fig. 3-9 Nitrogen-pressurized spark gap. 88

Fig. 3-10 Schematic diagram of the gas handling system. 90

		Page
Fig. 3-11	Output energy as a function of charging voltage and total gas pressure, using an electrode spacing of 1.65 cm, and mixtures of He/0.5% Xe/0.1% HCl, He/0.5% Xe/0.2% HCl, and He/5.0% Xe/0.2% HCl.	95
Fig. 3-12	Output energy as a function of charging voltage and total gas pressure, using an electrode spacing of 1.65 cm, and mixtures of He/1.0% Xe/0.2% HCl, He/2.5% Xe/0.2% HCl, and He/0.5% Xe/0.3% HCl.	97
Fig. 3-13	Output energy as a function of charging voltage and total gas pressure, using an electrode spacing of 1.65 cm, and mixtures of He/1.0% Xe/0.3% HCl, He/2.5% Xe/0.3% HCl, and He/5.0% Xe/0.3% HCl.	98
Fig. 3-14	Output energy as a function of charging voltage and total gas pressure, using a He/1.0%Xe/0.2%HCl mixture, and electrode spacings of 1.97 cm, 2.29 cm and 2.60 cm.	99
Fig. 3-15	Output energy as a function of charging voltage and total gas pressure, using a He/2.5%Xe/0.3%HCl mixture, and electrode spacings of 1.97 cm, 2.29 cm and 2.60 cm.	101
Fig. 3-16	Output energy as a function of charging voltage and total gas pressure, using an electrode spacing of 1.97 cm, and mixtures of He/1.0% Xe/0.1% HCl and of He/2.0% Xe/0.2% HCl.	103
Fig. 3-17	Output energy as a function of total gas pressure and charging voltage, using an electrode separation of 1.65 cm, and a He/0.5% Xe/0.2% HCl mixture.	104
Fig. 3-18	Optical output and laser efficiency as functions of stored energy, in the laser system employing a 1.65-cm electrode separation, and a He/0.5% Xe/0.2% HCl mixture at a total gas pressure of 2957 Torr.	106
Fig. 3-19	Optical energy and laser efficiency as functions of	107

		Page
	stored energy, in a laser system employing a 1.65-cm electrode separation, and the optimum mixture and gas pressure at each discharge energy.	
Fig. 3-20	Construction of a "half-shielded" high-voltage probe.	108
Fig. 3-21	Pulse response of several high-voltage probes.	109
Fig. 3-22	Measured dc attenuation factor for a Tektronix P6015 high-voltage probe.	110
Fig. 3-23	Calibration curve for a "half-shielded" $CuSO_4$ high-voltage probe used together with two ÷10 attenuators.	111
Fig. 3-24	Pulse response of a commercial current transformer (Ion Physics CM-10-M).	112
Fig. 3-25	Discharge characteristics of the laser system employing a He/0.5% Xe/0.2% HCl mixture at 2957-Torr pressure and 35-kV charging voltage.	114
Fig. 3-26	Discharge characteristics of the laser system employing a He/0.5% Xe/0.2% HCl mixture at 2880-Torr pressure and 35-kV charging voltage.	115
Fig. 3-27	Discharge characteristics of the laser system employing a He/0.5% Xe/0.2% HCl mixture at 2570-Torr pressure and 30-kV charging voltage.	116
Fig. 3-28	A current waveform for the preionizer circuit.	118
Fig. 3-29	Basic equivalent-circuit diagram for the laser discharge.	119
Fig. 3-30	Time delays as functions of charging voltage, using an electrode spacing of 1.65 cm, and a He/0.5% Xe/0.2% HCl mixture at 2957-Torr pressure.	121
Fig. 3-31	Time delays as functions of gas pressure for charging voltages of 25 kV, 30 kV and 35 kV, using an electrode	122

Page

spacing of 1.65 cm, and a He/0.5% Xe/0.2% HCl mixture.

Fig. 3-32 Capacitance multiplier factor for a Murata 909A ceramic capacitor as a function of voltage. 124

Fig. 3-33 Electrical characteristics of the main discharge, as functions of time, for the laser system employing an electrode spacing of 1.65 cm, a 35-kV charging voltage, and a He/0.5% Xe/0.2% HCl mixture at 2957-Torr pressure. 126

Fig. 3-34 Electrical characteristics of the main discharge, as functions of time, for the laser system employing an electrode spacing of 1.65 cm, a 35-kV charging voltage, and a He/0.5% Xe/0.2% HCl mixture at 2880-Torr pressure. 127

Fig. 3-35 Electrical characteristics of the main discharge, as functions of time, for the laser system employing an electrode spacing of 1.65 cm, a 30-kV charging voltage, and a He/0.5% Xe/0.2% HCl mixture at 2570-Torr pressure. 128

Fig. 3-36 Oscillograms of discharge-circuit currents and optical output pulses for the laser system employing an electrode spacing of 1.65 cm, charging voltages of 25 kV, 30 kV and 35 kV, and a He/0.5% Xe/0.2% HCl mixture at 2570-Torr, 2828-Torr, 2957-Torr, 3087-Torr and 3345-Torr pressures. 130

Fig. 3-37 Oscillograms of discharge-circuit currents and optical output pulses for the laser system employing an electrode spacing of 1.65 cm, charging voltages of 25 kV, 30 kV and 35 kV, and a He/1.0% Xe/0.2% HCl mixture at 2311-Torr, 2570-Torr and 2828-Torr pressures. 131

Fig. 3-38 Oscillograms of discharge-circuit currents and optical output pulses for the laser system employing an electrode spacing of 1.65 cm, charging voltages of 25 kV, 30 kV and 35 kV, and a He/2.5% Xe/0.2% HCl mixture at 1794-Torr, 2053-Torr and 2311-Torr pressures. 132

Page

Fig. 3-39 Oscillograms of discharge-circuit currents and optical output pulses for the laser system employing an electrode spacing of 1.65 cm, charging voltages of 25 kV, 30 kV and 35 kV, and a He/5.0% Xe/0.2% HCl mixture at 1536-Torr, 1794-Torr and 2053-Torr pressures. 133

Fig. 3-40 Optical pulsewidth as a function of total gas pressure for the laser system employing an electrode spacing of 1.65 cm, charging voltages of 25 kV, 30 kV and 35 kV, and a He/0.5% Xe/0.2% HCl mixture. 135

Fig. 3-41 Comparisons of the optical output energies and the optical pulsewidths, as functions of charging voltage, in the presence and the absence of an external rear (98%) reflector, for the laser system employing a 1.65-cm electrode spacing and a He/0.5% Xe/0.2% HCl mixture at 2957-Torr pressure. 136

Fig. 3-42 Oscillograms of preionizer current, discharge-circuit current, and optical output pulses obtained with and without an external rear (98%) reflector, for the laser system employing a 1.65-cm electrode spacing, charging voltages of 23 kV, 26 kV, 29 kV, 32 kV and 35 kV, and a He/0.5% Xe/0.2% HCl mixture at 2957-Torr pressure. 137

Fig. 3-43 Oscillograms of discharge-circuit currents and optical output pulses, for the laser system employing an electrode spacing of 1.97 cm, charging voltages of 25 kV, 30 kV and 35 kV, and a He/1.0% Xe/0.2% HCl mixture at 2311-Torr, 2828-Torr and 3345-Torr pressures. 138

Fig. 3-44 Oscillograms of optical output pulses, employing a 2.29-cm electrode spacing, 25-kV, 30-kV and 35-kV charging voltages, and a He/2.5% Xe/0.3% HCl mixture at 1277-Torr, 1536-Torr, 1794-Torr, 2053-Torr and 2311-Torr pressures. 139

Page

Fig. 3-45 Comparison of various optical output pulses produced from a laser system employing a 1.65-cm electrode spacing, a 35-kV charging voltage, and a He/0.5% Xe/0.2% HCl mixture at 2880-Torr pressure. 141

Fig. 3-46 Optical output energy and pulsewidth, as functions of cavity loss, for the laser system employing an electrode spacing of 1.65 cm, a charging voltage of 35 kV, and a He/0.5% Xe/0.2% HCl mixture at 2880-Torr pressure. 143

Fig. 3-47 Comparison of various optical output pulses produced from a laser system employing a 1.97-cm electrode spacing, a 35-kV charging voltage, and a He/1.0% Xe/0.2% HCl mixture at 2311-Torr pressure. 144

Fig. 3-48 Optical output energy and pulsewidth, as functions of cavity loss, for the laser system employing a 1.97-cm electrode spacing, a 35-kV charging voltage, and a He/1.0% Xe/0.2% HCl mixture at 2311-Torr pressure. 145

Fig. 3-49 Comparison of various optical output pulses produced from a laser system employing a 2.29-cm electrode separation, a 30-kV charging voltage, and a He/2.5% Xe/0.3% HCl mixture at 1794-Torr pressure. 147

Fig. 3-50 Optical output energy and pulsewidth, as functions of cavity loss, for the laser system employing a 2.29-cm electrode spacing, a 30-kV charging voltage, and a He/2.5% Xe/0.3% HCl mixture at 1794-Torr pressure. 148

Fig. 3-51 Oscillogram of the fluorescence from a discharge employing a He/0.5% Xe/0.2% HCl mixture at 2957-Torr pressure and a 16-kV charging voltage. 149

Fig. 4-1 Coordinate systems employed in a random-walk simulation of electron motion in a gas. 158

Fig. 4-2 Vector diagrams illustrating the scattering of two colliding electrons. 163

Page

Fig. 4-3 Cross-sections for electron collisions with helium. 171

Fig. 4-4 Cross-sections for electron collisions with xenon. 172

Fig. 4-5 Cross-sections for electron collisions with hydrogen chloride. 174

Fig. 4-6 Mean-free-path for electron collisions, as a function of electron energy, in a He/0.5% Xe/0.2% HCl mixture at 3000-Torr pressure. 180

Fig. 4-7 Average electron energy for a He/0.5% Xe/0.2% HCl discharge mixture. 182

Fig. 4-8 Average fractional energy loss for a He/0.5% Xe/0.2% HCl discharge mixture. 183

Fig. 4-9 Electron energy distribution at $E/p_0 = 5.0$ V/cm-Torr for a He/0.5% Xe/0.2% HCl mixture at 3000-Torr pressure. The degree of ionization is assumed to be 10^{-5}. 186

Fig. 4-10 Comparison of various electron energy distribution functions. 188

Fig. 4-11 Electron energy distribution functions for a He/0.5% Xe/0.2% HCl mixture at $E/p_0 = 5.0$ V/cm-Torr, when the Coulomb effect is neglected and when the degree of ionization is 2.5×10^{-5}. 190

Fig. 4-12 Variation of the parameters h and k, as a function of E/p_0, for a He/0.5% Xe/0.2% HCl mixture at an ionization level of 10^{-5}. 191

Fig. 4-13 Variation of the parameters h and k, as a function of E/p_0, for a He/0.5% Xe/0.2% HCl mixture at an ionization level of 2.5×10^{-5}. 192

Fig. 4-14 Electron energy distribution function for a He/0.5% Xe/0.2% HCl mixture at an ionization level of 10^{-5} and E/p_0 equal to 2.5 V/cm-Torr, 5.0 V/cm-Torr and 193

Page

7.5 V/cm-Torr.

Fig. 4-15 Relaxation of electron energy distribution for a He/0.5% Xe/0.2% HCl mixture at E/p_0 = 5.0 V/cm-Torr and an ionization level of 10^{-5}. 194

Fig. 4-16 Energy relaxation of a 0-eV primary electron for a He/0.5% Xe/0.2% HCl mixture, for an ionization level of 10^{-5}, and for E/p_0 equal to 7.5 V/cm-Torr, 5.0 V/cm-Torr and 2.5 V/cm-Torr. 196

FIg. 4-17 Variation of average electron-collision frequency, with time, for a 0-eV primary electron drifting in a He/0.5% Xe/0.2% HCl discharge medium at an ionization level of 10^{-5}, and for E/p_0 = 7.5 V/cm-Torr, 5.0 V/cm-Torr and 2.5 V/cm-Torr. 197

Fig. 4-18 Occurrence frequencies for various electron collision processes in a discharge derived from simulations of a He/0.5% Xe/0.2% HCl mixture at 3000-Torr pressure, and E/p = 5.0 V/cm-Torr. The degree of ionization is assumed to be 10^{-5}. 198

Fig. 4-19 Spatial development of an avalanche from a 0-eV primary electron in a He/0.5% Xe/0.2% HCl medium at an ionization level of 10^{-5}, and for E/p_0 = 7.5 V/cm-Torr, 5.0 V/cm-Torr and 2.5 V/cm-Torr. 199

Fig. 4-20 Multiplication of a 0-eV primary electron in a He/0.5% Xe/0.2% HCl discharge medium at an ionization level of 10^{-5} and at E/p_0 = 7.5 V/cm-Torr, 5.0 V/cm-Torr and 2.5 V/cm-Torr. 201

Fig. 5-1 A schematic diagram for the simplified XeCl laser kinetics in a He/Xe/HCl mixture. 208

Fig. 5-2 Temporal evolution of active species in a XeCl laser discharge. 221

Page

Fig. 5-3 A schematic diagram illustrating the important channels for the production and loss of Xe^+ ions in a XeCl laser discharge. 224

Fig. 5-4 A schematic diagram illustrating the important channels for the production and loss of Cl^- ions in a XeCl laser discharge. 226

Fig. 5-5 A schematic diagram illustrating the important channels for the production and loss of Xe^* atomic species in a XeCl laser discharge. 228

Fig. 5-6 A schematic diagram illustrating the important channels for the production and loss of Xe^{**} atomic species in a XeCl laser discharge. 229

Fig. 5-7 A schematic diagram illustrating the important channels for the production and loss of Cl atoms in a XeCl laser discharge. 232

Fig. 5-8 A schematic diagram illustrating the important channels for the formation and decay of $XeCl^*$ and XeCl in a XeCl laser discharge. 239

Fig. 5-9 A schematic diagram illustrating the important channels for the formation and decay of the triatomic exciplex Xe_2Cl^* in a XeCl laser discharge. 242

Fig. 5-10 Results of kinetic modelling for a He/0.5% Xe/0.2% HCl laser mixture at 2957-Torr operating pressure, 35-kV charging voltage and 1.65-cm electrode separation. 243

Fig. 5-11 Results of kinetic modelling for a He/0.5% Xe/0.2% HCl laser mixture at 2880-Torr operating pressure, 35-kV charging voltage and 1.65-cm electrode separation. 244

Fig. 5-12 Results of kinetic modelling of a He/0.5% Xe/0.2% HCl laser mixture at 2570-Torr operating pressure, 30-kV charging voltage and 1.65-cm electrode separation. 245

		Page
Fig. 5-13	Application of gain-saturation theory to the determination of laser parameters.	255
Fig. D-1	A load diagram showing the forces acting on an end-plate of the laser supporting structure.	282
Fig. D-2	Maximum bending stress acting on the end-plate.	287
Fig. D-3	Representation of the discharge chamber by a thick-walled cylinder.	289
Fig. F-1	A schematic diagram illustrating pseudo-crossings of potential-energy curves.	296

LIST OF TABLES

		Page
Table 2-1	Dunham coefficients for the XeCl ground state: A. Comparison of Dunham coefficients for the XeCl ground state obtained from the approximation (Eq. (2-10)), the least-squares-fit calculations using the potential function given by Eq.(2-6), and the experimental values of Sur et al. [44].	30
	B. Computer results of Dunham coefficients for the XeCl ground state obtained from a least-squares fit of the vibrational energies ($G_{v''}$), which are calculated using the potential function given by Eq.(2-6).	31
Table 2-2	Vibrational energy levels of the XeCl ground state and their classical turning points.	32
Table 2-3	Spectroscopic parameters for the truncated Rittner potential functions of the excimer B and D states in XeCl [44].	45
Table 2-4	Vibrational energy levels of the XeCl B state and their classical turning points.	47
Table 2-5	Dunham coefficients for the XeCl B state: A. Comparison of Dunham coefficients for the XeCl B state obtained from a least-squares-fit calculation using the truncated Rittner potential given by Eq. (2-22), and the experimental values of Sur et al. [44].	48
	B. Computer results of Dunham coefficients for the XeCl B state obtained from a least-squares fit of the vibrational energies ($G_{v'}$), calculated using the truncated Rittner potential function given by Eq.(2-22).	49

		Page
Table 2-6	Calculated values of Einstein A coefficients, oscillator strengths and stimulated-emission cross-sections for B(v' = 0) to X(v" = 0-22) transitions in XeCl.	57
Table 3-1	XeCl laser parameters.	92
Table 4-1	Electron energy losses in elastic and inelastic collisions with He, Xe, HCl and electrons.	162
Table 4-2	Rate coefficients of electron collision processes used in kinetic studies of the XeCl exciplex system.	202
Table 5-1	Intermediate kinetic processes in the XeCl laser discharge.	215
Table 5-2	Kinetic processes for formation and decay of exciplex species.	218
Table 5-3	Photoabsorbers in the XeCl laser discharage.	220
Table 5-4	Threshold energies of discharge species considered in the kinetic calculations for the XeCl laser system.	234
Table 5-5	Comparison of optical output energies determined experimentally and using the kinetic model.	246
Table 5-6	Some rate equations employed in the concise kinetic model for evaluating laser parameters.	248
Table 5-7	Steady-state laser parameters, for various XeCl laser discharges, determined by the concise kinetic model.	251
Table F-1	Rate coefficients for three-body processes relating to pseudo-crossings of potential-energy curves.	301

CHAPTER 1

INTRODUCTION

1.1 Preliminaries of Excimer Lasers

The past decade has seen the discovery and development of a novel class of powerful, short-wavelength lasers, which profited from the concurrent technological advances in gaseous electronics. These lasers, mostly accomplished by high-intensity electron-beam pumping of high-pressure mixtures, are generally (although sometimes mistakenly) known as excimer lasers. Optical emission is via an electronic transition between two molecular levels, the lower of which is usually the ground state and which dissociates very rapidly. Of particular interest in these laser systems are their promising characteristics of high specific energy, high quantum efficiency and high inversion density.

An excimer (excited dimer) is specifically meant to be a homonuclear molecule which is bound only in an excited state, but which has a repulsive, or weakly attractive, ground state. However, the term is often applied to describe a heteronuclear diatomic (properly known as exciplex, or excited complex), a triatomic or even a polyatomic molecule which behaves similarly. Promising candidates for excimers are the closed-shell atomic species (with the ground-state term $^1S_0$) and the closed-shell and open-shell atomic combinations ($^1S_0 + {}^2S$, ^2P, or ^3P), all of whose ground-state configurations are fundamentally unstable, or perhaps bound by a weak van der Waals interaction. Typical excimer

families are the rare-gas halides and their triatomics, the diatomic rare gases, the rare-gas oxides, the Group IIB metallic diatomics, the mercuric halides, and the molecular halogens [1].

Excimer transitions are characteristically broad-band. These were observed relatively long ago [2,3], and attributed to bound-free transitions [4] of excited molecules which are formed by collisions of excited and ground-state atoms [5]. Later, it was suggested that the lower-level molecular dissociation was a possible means of achieving laser operation [6]. Primarily, the "bottle-necking" effect that suppresses population inversion in most laser systems is substantially reduced because the ground state depletes very rapidly, and within a molecular vibrational period ($\sim 10^{-12}$ - 10^{-14} s). The first successful operation of such a laser system was the xenon excimer exploiting the $A\ ^{1,3}\Sigma_u^+ \longrightarrow X\ ^1\Sigma_g^+$ transitions near 172.2 nm [7,8]. However, the most notable successes are the rare-gas halide systems. These deliver a wide range of pulse intensities, durations and wavelengths for diverse applications in such fields as isotope separation, photochemistry, and laser fusion.

1.2 Rare-Gas Halide Exciplex Systems

Of the various families of excimer lasers discovered to date, the rare-gas halide (RGH) systems have been attracting the most active experimental and theoretical investigations. Compared to their predecessors (the rare-gas dimer lasers), they are more efficient lasers and are scalable to high output power in the ultraviolet and the

adjacent visible spectral regions. At present, the largest energy is ∿350 J in a single 600-ns pulse, produced by a transversely e-beam excited KrF laser system operating at 248.4 nm, and at an intrinsic efficiency of ∿10% [9].

Bound-free transitions in rare-gas monohalides were initially characterized by Golde and Thrush [10], and by Velazco and Setser [11, 12], in studies of reactive quenching of metastable rare-gas atoms by halogens. Laser action on the $B\ ^2\Sigma^+_{1/2} \longrightarrow X\ ^2\Sigma^+_{1/2}$ bands of XeBr at 281.8 nm [13], XeF at 353.1 nm [14,15], KrF at 248.4 nm and XeCl at 308.0 nm [16], were first achieved in 1975. Soon after, laser action was demonstrated in ArF at 193.2 nm [17], KrCl at 222.1 nm [18], and ArCl at 175.0 nm [19]. These systems were initially excited by direct e-beam pumping, with the exception of ArCl which was first demonstrated using a Blumlein discharge technique. In contrast to the rare-gas excimers that require vigorous e-beam pumping and operation at high pressure, the RGH exciplexes can be formed efficiently by avalanche discharges in gaseous mixtures at moderate (several atmospheric) pressure. This is mainly because of the larger stimulated-emission cross-section due to relatively long wavelengths and narrow linewidths associated with transition between states in an exciplex structure.

The exciplexes and dimers are compared in Fig.1-1. The emitting state of a RGH molecule, RX^*, is characteristically ionic, and bound by an energy in excess of 3 eV. By contrast, an excited rare-gas dimer, R_2^*, is a Rydberg-state molecule which is covalently bound with energy ∿1 eV. This suggests that RX^* should radiate at a longer wavelength

Fig. 1-1

Typical potential energy curves distinguishing a rare-gas halide molecule (RX) and a rare-gas dimer (R_2).

A. Rare-Gas Halide

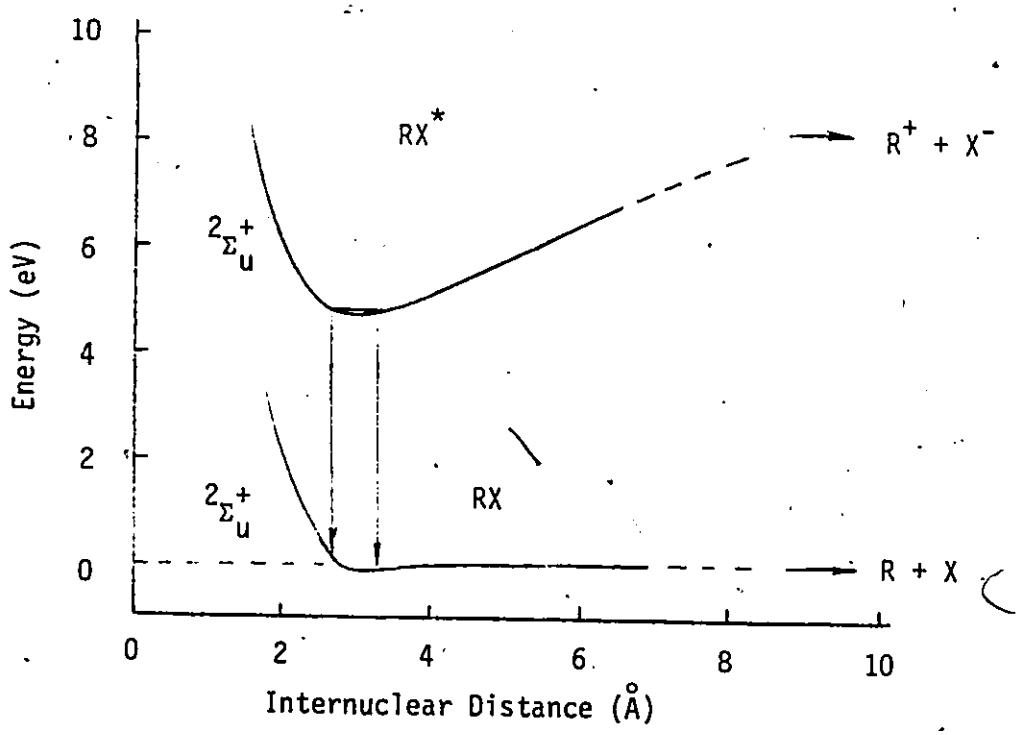

B. Rare-Gas Dimer

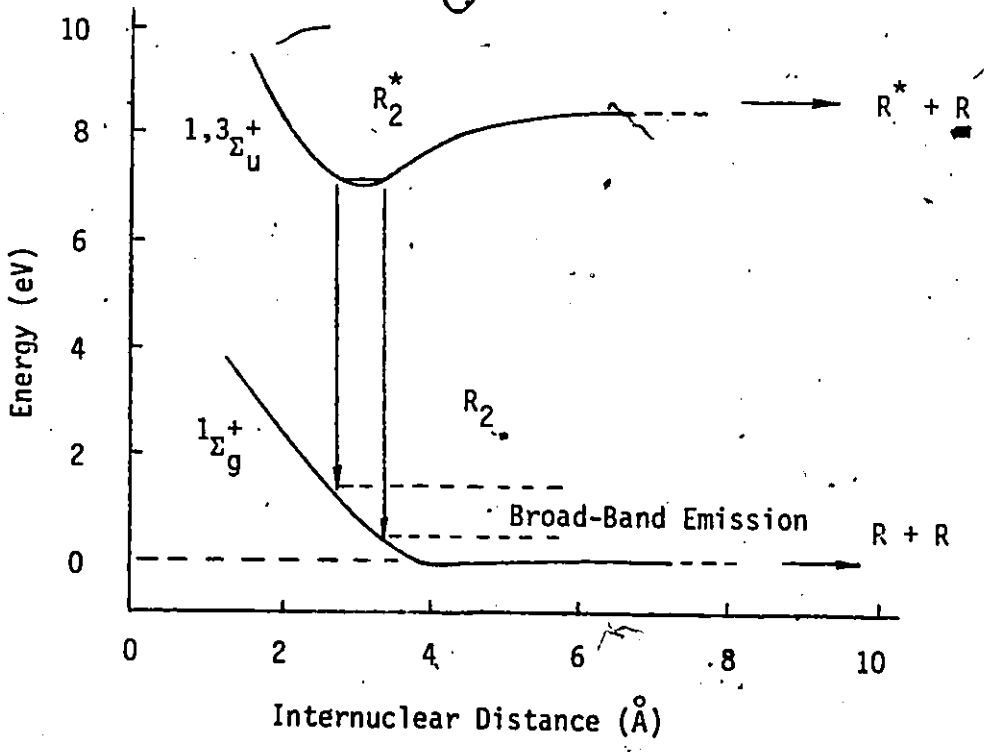

than R_2^*, assuming that the ionic and Rydberg limits at a large nuclear separation do not differ by more than $\sim$1 eV. Indeed, both experimental observations and theoretical predictions have confirmed a wavelength ratio of about 2:1 in the radiation. Moreover, a ground-state RGH molecule is smaller in size than its corresponding rare-gas dimer in the ground configuration. Therefore, the equilibrium nuclear separation of RX is located relatively closer to the minimum of the upper RX^* state than the distance between the minima of R_2 and R_2^*. In effect, a radiative transition from the upper RX^* state usually terminates in the nearly flat region of the ground-state potential, rather than on the steeply repulsive slope. Consequently, emission spectrum of a RGH exciplex is expected to be narrower than in a rare-gas excimer.

The optical gain may be approximately described by

$$g \simeq \frac{\lambda^4}{8\pi c\tau\Delta\lambda} \cdot \Delta N \quad , \tag{1-1}$$

where λ and $\Delta\lambda$ are the wavelength and the bandwidth of emission, c is the velocity of light, τ is the excited-state lifetime, and ΔN is the inversion density. A broad-band transition and a short wavelength both lower the gain. Therefore, the inversion density must be large in order to achieve adequate laser gain. This is possible if the upper laser level is efficiently populated with a large number of molecules before the radiative decay and collisional quenching of the excited species dominates. With rare gases alone, only vigorous excitation of high-pressure mixtures (usually 10-60 atm) can produce enough excimer species to yield a gain of $\sim$0.1 cm^{-1}, which is typical of the RGH lasers.

The RGH laser systems are inherently powerful because they are capable of gain at high irradiance. Since the reciprocal of the product of the stimulated-emission cross-section and the excited-state lifetime ($1/\sigma\tau$) for a RGH exciplex lies within 10^{23} - 10^{24} cm^{-2}-s^{-1}, the saturation irradiance for such a system is in the order of 100 kW/cm^2, which is very high compared to those for CO_2 and ruby lasers ($\sim$250 W/cm^2 and $\sim$500 W/cm^2, respectively). In order to attain a gain of 0.1 cm^{-1}, the inversion density is in excess of 10^{14} cm^{-3}. This requires that the exciplex species must be produced at a rate of $\geq 10^{23}$ cm^{-3}-s^{-1}. This production rate can be easily achieved through a photoionized avalanche discharge of a rare-gas and halogen (or halide) mixture at a pressure of a few atmospheres. Discharge excitation of RGH lasers was first demonstrated by Burnham et al. [20] using a simple Blumlein circuit (without preionization), and by Burnham and Djeu [21] employing UV-preionization. Optical gains in excess of 0.2 cm^{-1} have been observed in recent systems [22,23].

Long-pulse output from RGH exciplex lasers has been an interesting topic of investigation into possible continuous-wave (cw) operation, or at least quasi-cw or high-repetition-rate laser operation. Outputs with pulse lengths greater than $\sim$1 μs have been mostly associated with systems pumped optically [24,25] or by e-beam or e-beam controlled long-duration discharges [26-28]. The longest duration pulse achieved in an e-beam or e-beam stabilized XeCl exciplex system is about 0.5 μs [29,30]. A pulse duration of $\sim$250 ns has been reported recently, using a Ne/Xe/HCl mixture in an avalanche-discharge laser system employing an electrode

consisting of resistively ballasted pins [31]. Since long-pulse operation necessarily reduces the optical peak power, efficient extraction of energy from such a system becomes the principal concern. However, most systems capable of emitting relatively long pulses have demonstrated efficiencies comparable to, and sometimes even better than, those of short-pulse lasers. From the beginning of this thesis research, a primary interest has been to investigate potential long-pulse operation in discharge-excited XeCl exciplex laser systems.

1.3 Principles of a Xenon Monochloride Laser

In contrast to the highly researched KrF and XeF exciplex lasers, the XeCl system was not initially regarded as a promising candidate for scaling to high efficiency. Chlorine was used as the halogen donor and argon as the buffer gas. This resulted in low laser output energy which was attributed to a low fluorescence yield [16]. The latter was due to the Cl_2 and Ar_2^+ absorption bands, which overlap the $XeCl^*$ emission lines near 308 nm, and which greatly reduce the gain. Ewing and Brau [16] suggested the replacement of chlorine by other chlorine-bearing compounds. Subsequently, Kudryavtsev and Kuz'mina [32] obtained an output energy of 1 mJ from an electric-discharge XeCl laser using CF_2Cl_2 as the chlorine donor. CCl_4, BCl_3 and C_2F_3Cl were also used, but provided less output energy. Later, Ishchenko et al.[33] reported 3.4 mJ output using a mixture containing BCl_3, and Bychkov et al.[34] achieved 21-mJ and 6.2-mJ optical pulses with the aid of the halogen-carriers CCl_4 and $CHCl_3$, respectively. In a major advance, Burnham [35] extracted, from a discharge-pumped mixture of He/Xe/HCl, an energy of 110 mJ, at an

electrical efficiency of ~0.8%. The output was highly competitive with those available from the rare-gas fluoride lasers. Moreover, the substitution of argon by helium as the diluent completely eliminated the photoabsorption by the dimer ion Ar_2^+, and hence improved both the discharge conditions and the laser performance. Neon has also been found to be a desirable buffer medium, especially for e-beam or e-beam sustained discharge devices [30].

Kinetic studies of low-pressure xenon and chlorine mixtures [12] revealed an undulating continuum with peak emission at 304.3 nm and with ~10-nm bandwidth. It was suggested that this broad band was due to the photodissociation of an electrically excited molecule, primarily $XeCl^*$, formed by the bimolecular quenching of a metastable xenon atom with a chlorine species. The processes likely to occur were

$$Xe^* + Cl_2 \longrightarrow XeCl^* + Cl \qquad (1\text{-}2)$$

and

$$XeCl^* \longrightarrow Xe + Cl + h\nu \quad . \qquad (1\text{-}3)$$

The emission spectrum also indicated a strong resemblance between $XeCl^*$ and CsCl (the isoelectronic alkaline halide) in their molecular structures. Further spectral studies, at both high and low pressures [36], confirmed that the excited state $XeCl^*$ was predominantly ionic in character, and could appropriately be described by the alkaline halide model [37].

The principal channels for the formation of $XeCl^*$ are via the three-body ionic recombination

$$Xe^+ + Cl^- + He \longrightarrow (Xe^+ \cdot Cl^-)^* + He \quad , \qquad (1\text{-}4)$$

and via the "harpooning" mechanism:

$$Xe^{*}\cdot Cl \longrightarrow (Xe^{+}\cdot Cl^{-})^{*} \quad . \qquad (1\text{-}5)$$

Under the combination of high electrical excitation energy and a dense medium, Process (1-4) likely predominates. For each positive ion produced, a secondary electron is released and becomes easily attached to an electrophilic molecule to produce a negative ion. In the case of hydrogen chloride as the electronegative molecule, a Cl^{-} ion is formed. It recombines very rapidly with the positive ion Xe^{+} in a three-body collision, involving an extra rare-gas atom, to form an exciplex. It may be noted that ions are abundantly present in an e-beam excited system, and also in an avalanche discharge where rapid multiplication of electrons occurs. Since excitation and ionization of xenon atoms require electron energies far below that for exciting a helium atom, Xe^{*} and Xe^{+} can be generated efficiently by an electric discharge in a He/Xe/HCl mixture. Under the above conditions, the "harpooning" mechanism leading to the exciplex formation is equally important as the ionic channel. In Reaction (1-5), the Rydberg molecule $Xe^{*}\cdot Cl$, which is formed from Xe^{*} and Cl in a reactive quenching process, is transformed into a charge-transfer complex by the jump of an electron within the weakly-attached configuration. This transformation stems from the pseudo-crossing of the Rydberg and ionic potential curves at a large nuclear separation. For a "harpooning" process (such as Reaction (1-2)) to proceed, the excited-state energy of a rare-gas atom must be in excess of the total energy required to dissociate a halogen-donor molecule and to then use the separated halogen atom in forming the exciplex. In a system with hydrogen chloride as the halogen donor, the reaction

$$Xe^* + HCl \longrightarrow XeCl^* + H \qquad (1\text{-}6)$$

is endothermic and does not contribute significantly to the exciplex formation. This has a rate coefficient of $<10^{-11}$ cm^3/s, which has been verified experimentally [38].

Collisional quenching of exciplex species and photoabsorption are the dominant loss mechanisms associated with efficient laser operation. Measured values of the rate constants for interaction between $XeCl^*$ and various quenching agents (e.g., Xe, HCl and electrons) are known. However, very few studies have been made of those quenching mechanisms involving three-body reactions by rare-gas atoms, particularly in processes forming triatomic exciplexes. The Xe_2Cl^* exciplex has been found to radiate coherently near 518 nm [39]. Other depopulating mechanisms of the upper active level, such as collisions with excited particles, have not been experimentally analyzed. The reaction kinetics of the exciplex system is therefore far from being correctly understood. Little is known of the many photoabsorption mechanisms in the gain medium. However, the negative ion Cl^-, having a photodetachment cross-section $>10^{-17}$ cm^2 near the laser wavelength, is generally regarded as the important absorber. In addition, the triatomic exciplex Xe_2Cl^* could also be an appreciable photoabsorber. This is based on analogy with the main absorption on the KrF^* emission being due to the exciplex species Kr_2F^*, whose photodissociation cross-section is estimated to be $\sim 1.6 \times 10^{-18}$ cm^2 [40]. Investigations of absorption in exciplex lasers [41-43] have revealed that it is a complex function of mixture composition and plasma dynamics; the latter is a topic of current interest in exciplex laser research.

1.4 Organization of the Thesis

The objective of the thesis research is to develop an understanding of the radiative B → X transitions and of the dynamical processes in an avalanche discharge XeCl laser system. The reaction kinetics involved in the formation and quenching of the exciplex $XeCl^*$ in a helium discharge medium, containing small quantities of xenon and hydrogen chloride, are studied. A model has been developed which takes into account the important kinetic processes, and which describes the dynamical behaviour of the exciplex in the laser gain medium. This model provides a qualitative assessment of the scalability of parameters such as efficiency, energy extraction capability, and size. The research is also directed at determining the range of output pulsewidths achievable with the XeCl laser system.

Before a comprehensive model can be developed, the basic molecular structure of the XeCl exciplex must be investigated. In Chapter 2, the excimer emission due to the B → X transition is characterized in terms of the Franck-Condon factors and densities, which are determined using the calculated wavefunctions of the two states. Adopting the spectroscopic data analyzed by Sur et al. [44], we are able to represent the excited and the ground electronic states by simple potential functions. While a Rittner-type potential is applicable to the upper state, the lower laser level can best be described by a new type of potential function found in the course of this work. The potential functions are used in quantum-mechanical calculations of the wavefunctions. These wavefunctions are also needed

for evaluating the lifetime of the electronic transition, and the cross-section for stimulated emission. In addition, other electronic states in the exciplex structure are briefly examined. Particular emphasis is placed on the intersections of the excimer state by the two Rydberg curves correlating to the separate-atom limits of Xe ($^3P_2$) + Cl ($^2P_{3/2}$), and Xe ($^3P_1$) + Cl ($^2P_{3/2}$). These curve-crossings, which take place at large nuclear separations, suggest possible channels for the formation of $XeCl^*$ by excited rare-gas atoms and neutral halogen atoms via the "harpooning" mechanisms. They help to maintain optical gain at the late stage of the emission when the ion densities begin to drop.

The design and construction of an electric discharge laser system is presented in Chapter 3. This system incorporates a pair of auxilliary "sliding-spark" discharge sources which photoionize the gas medium before the main discharge is launched. A simple discharge scheme is employed, which makes use of discrete "voltage-peaking" capacitors to transfer intermediate energy to the medium. Results of laser experiments performed using mixtures of various compositions (ranging from 0.25% to 5% Xe and 0.1% to 0.3% HCl) and under different discharge conditions (such as applied electric field, deposited energy, and static-filled gas pressure) are described and compared. A laser efficiency† as high as ~0.5% has been achieved with the laser system.

---

†Laser efficiency is defined as the ratio of optical output energy to total energy stored in the main discharge circuit.

Most noteworthy is the attainment of an almost flat-topped optical pulse with a 60-ns duration, which has an output of ~200 mJ at a laser efficiency of ~0.3%. This pulse was observed using a mixture of He/0.5% Xe/0.2% HCl at a filling pressure of 2880 Torr, a charging voltage of 35 kV, and an electrode spacing of 1.65 cm.

Our kinetic model, based on achieving good agreement between the computed pulseshapes and the observed optical pulses, takes into account many electron and particle collisional processes. These processes are discussed separately in two chapters. In Chapter 4, the electron kinetics in an exciplex system using the above mixture are studied by means of Monte-Carlo simulations of a swarm of electrons drifting from the cathode to the anode and colliding with gas particles in their paths. The characteristic behaviours of these electrons sampled in these numerical studies are statistically analyzed to derive energy distribution functions for the electrons under several discharge conditions. These distribution functions are then applied to evaluate the rate coefficients for the various electron processes which are needed for kinetic calculations in Chapter 5. It is inherently difficult to directly incorporate the electron simulations into the gas kinetic studies. Therefore, the gaseous discharge is modelled using only the energy conservation equation for electrons, together with a set of kinetic equations for the discharge species.

An elaborate kinetic model, in which 245 elementary processes involving 34 reactive species are investigated, is presented in Chapter

5. Although the collisional processes governing the exciplex quenching are far from being correctly understood, the model is, in general, adequate for explaining many features of the XeCl laser operation. Besides the electron processes summarized in Chapter 4, other processes fundamentally related to heavy particle interactions are categorized in Chapter 5. These latter processes take into account the supply of primary electrons due to photoionization of ground and excited atoms as well as photodetachment of negative ions during the photoinitiated and the photosustained stages of the discharge. The intermediate processes include charge-exchange between ions and gas particles, ionic recombination, Penning ionization, Hornbeck-Molnar ionization, and reactions relating substitution and association (e.g., Phelps-Molnar association) of molecules. The $XeCl^*$ exciplex is primarly formed from the ionic and the "harpooning" channels. However, other mechanisms such as dissociative ionic recombinations of $XeHe^+$, and $XeCl^+$, with Cl^- are also investigated. The exciplex species and its ground-state molecule are most likely quenched by collisions with rare-gas atoms, and with electrons. In the kinetic model, there are also associated processes involving the triatomic species Xe_2Cl^* which directly and indirectly influence the laser kinetics. In addition, the model includes photoabsorption by various ions and metastable species.

The primary objective in modelling the dynamics of the exciplex system is to derive probable factors affecting efficient laser operation, such as losses due to collisional quenching or photoabsorption. A knowledge of the temporal evolution of various kinetic species, based

on the kinetic modelling, permits us to recognize the important kinetic chains in the formation and quenching of the exciplex. In addition, characteristics such as optical gain and absorption are evaluated in the calculation. A simplified kinetic scheme selecting only those dominant processes from the detailed model is finally developed. Moreover, in Chapter 5 intrinsic laser parameters (viz., unsaturated gain, absorption coefficient and saturation irradiance) are determined by application of Rigrod's gain-saturation theory [45] to laser output measurements obtained using various intracavity attenuators, instead of different output couplers as was done by Rigrod.

This thesis is concluded in Chapter 6 with a summary of the research work in a general context. The various aspects of the XeCl laser operation are discussed. Special emphasis is placed on the prospect of attaining efficient, long-duration, powerful pulses. Future research projects relating to the exciplex system are also suggested.

CHAPTER 2

MOLECULAR STRUCTURE OF XENON MONOCHLORIDE

2.1 Introduction

Xenon monochloride is a large molecule consisting of 54 + 17 electrons. Extensive theoretical calculations on its molecular structure, covering the five lowest electronic states, have been published [46,47]. Also available in the literature are the experimentally-derived turning points for the potential energy curves of the excimer (B $^2\Sigma^+_{1/2}$ and D $^2\Sigma^+_{1/2}$) and ground (X $^2\Sigma^+_{1/2}$) states [44,48]. These turning points are obtained from spectroscopic analyses of the B → X and D → X electronic transitions corresponding to the peak emissions near 308 nm and 236 nm, respectively. The potential energy diagram of the XeCl exciplex molecule, illustrated in Fig.2-1, is based on the above experimentally-derived data for the Σ states. The Π state curves are based on theoretical calculations. In addition, the figure shows approximate curves for the two lowest Rydberg states, which correlate to the dissociation limits to the metastable atoms Xe($^3P_2$) and Xe($^3P_1$) and the ground-state atom Cl($^2P_{3/2}$). These help to demonstrate the pseudo-crossings of the Rydberg curves and the excimer states.

The XeCl laser system radiates on the vibrational bands (v'=0) → (v"=0-3) of the B → X electronic transition. In this chapter, the B → X transition is characterized in terms of the Franck-Condon factors and densities, the radiative lifetime, and the stimulated-emission cross-section. Potential functions are used to characterize

Fig. 2-1

Potential energy diagram of xenon monochloride. Note that a logarithmic scale is used in order to show the long-range crossings between the Rydberg and excimer states.

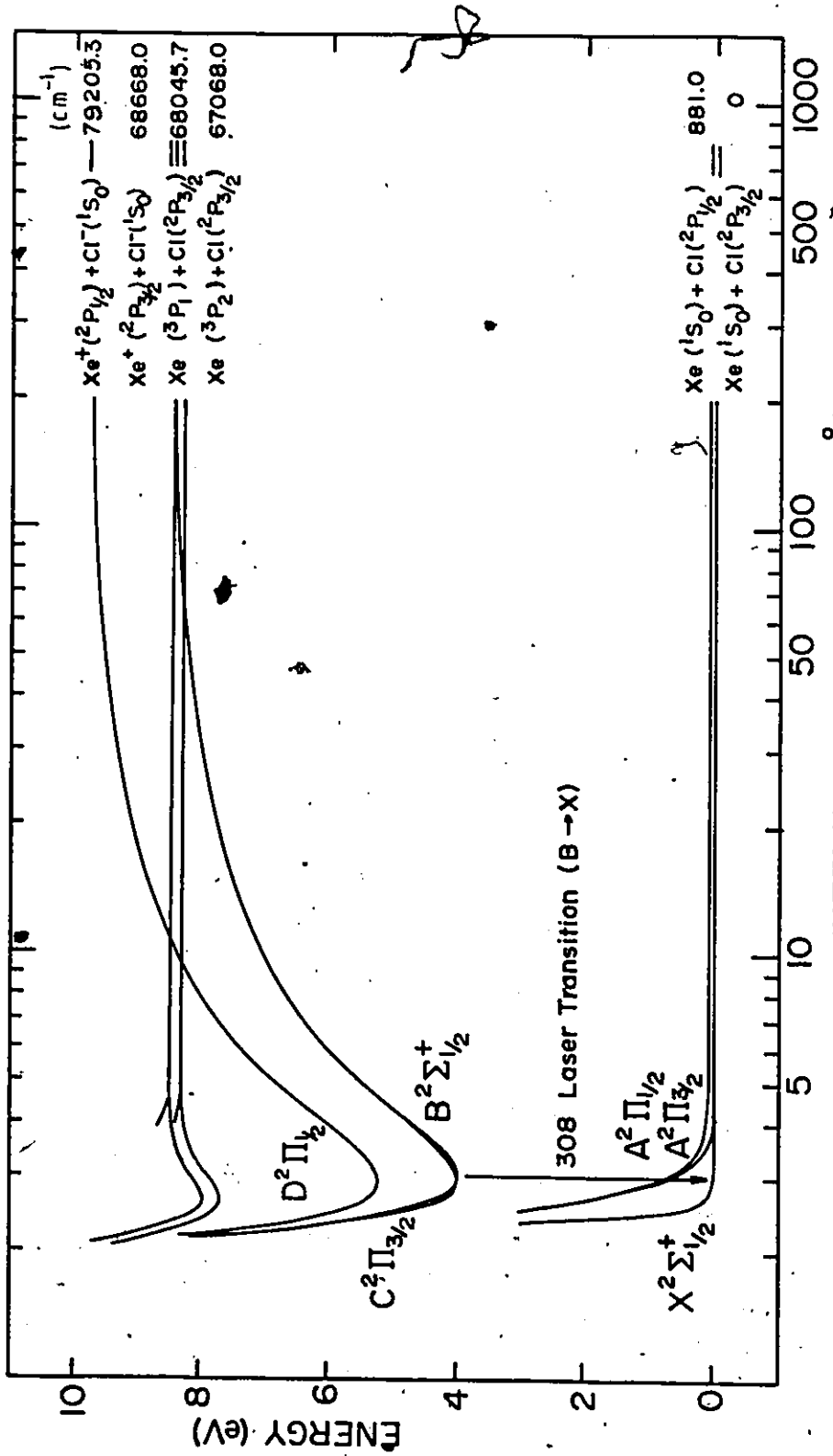
ENERGY (eV)
INTERNUCLEAR DISTANCE (Å)
Xe⁺(²P½)+Cl⁻(¹S₀) — 79205.3 (cm⁻¹)
Xe⁺(²P3/2)+Cl⁻(¹S₀) 68668.0
Xe (³P₁)+Cl(²P3/2) ≡68045.7
Xe (³P₂)+Cl(²P3/2) 67068.0
Xe (¹S₀)+Cl(²P½) = 881.0
Xe (¹S₀)+Cl(²P3/2) = 0
308 Laser Transition (B→X)
D²Π½
C²Π3/2
B²Σ⁺1/2
A²Π1/2
A²Π3/2
X²Σ⁺1/2

the two electronic states, and to evaluate their wavefunctions which are needed for the characterization. These potential functions, which are believed to describe the states fairly accurately, facilitate the quantum-mechanical calculations. These also provide the basis for a simple fundamental understanding of the properties of the exciplex molecule, and of the nature of the binding in different electronic configurations.

The topics discussed in the following sections provide a systematic survey of the XeCl electronic structure. These topics also serve as an introduction to the operation of the XeCl system, both by identifying the channels for the exciplex formation and by characterizing the radiation.

2.2 The Weakly-Bound Ground State and Its Determination

The interaction of closed-shell atoms with each other and with open-shell partners, all in their ground-state electronic configurations, is repulsive except in a short range where weak attraction, perhaps of the van der Waals type, exists. Even for heavy rare-gas atoms, where the outer electrons are remote from the nuclei, the binding strength of neutral dimers is only about 0.024 eV [49]. Therefore, at room temperature, the ground state is essentially dissociative. Although most rare-gas and halogen diatomic combinations behave similarly, xenon combined with fluorine or chlorine has stronger bonding (0.146 eV [50] and 0.035 eV [44], respectively), which is much larger than in a van der Waals molecule of comparable size. In addition, and contrary to usual

diatomic behaviour, the lowest-state potential of XeCl is superharmonic[¶] [44,48] (i.e., the Dunham coefficient Y_{20}, defined in Eq.(2-8), is positive). Furthermore, XeCl (and all other rare-gas halides) has only a small number of vibrational levels contained in the potential energy trough, which allows rapid dissociation of the molecule into neutral atoms. In a later paragraph, the above features (and others) will be described in terms of a new potential function based on empirical data. For XeCl, this calculated function is within ~1% of the best available experimental measurements [44].

From basic theoretical predictions, the covalent states $X\ ^2\Sigma^+_{1/2}$ and $A\ ^2\Pi_{3/2,1/2}$ of a rare-gas ($^1S_0$) - halogen ($^2P_{3/2,1/2}$) diatomic molecule are characteristically repulsive inside the overlapping domain at close internuclear separation. This is due to the unfavourable electron exchange between the doubly-occupied $p\sigma$ orbital of the rare-gas atom and the σ-unfilled $(p\sigma)^1(p\pi)^4$ and the σ-filled $(p\sigma)^2(p\pi)^3$ configurations of the halogen atom. Extensive self-consistent-field molecular-orbital (SCF-MO) calculations on KrF with configuration interaction (CI) [51], and on XeF without CI [52], have revealed that their ground states are definitely chemically unbound in the absence of charge transfer mixing with excited states. All-electron ab initio CI calculations on xenon halides have been carried out by Hay and Dunning [46] using the "double-zeta" quality atomic basis sets (wavefunctions) of

---

[¶]Strictly speaking, the ground-state potential of XeCl is quasi-superharmonic. The superharmonic behaviour is prominent only at the bottom of the potential well, where the molecule oscillates with energy of 26.60 cm^{-1}, compared to $\omega_e'' = 26.22\ cm^{-1}$ (see Tables 2-1 and 2-2). Above the bottom of the well, the energy levels come closer together, and the molecule appears to be a normal harmonic oscillator.

Huzinaga [53] and Dunning [54] for valence orbitals, and the "single-zeta" quality sets for core electrons. Both sets were contracted according to Raffenetti's scheme [55], and augmented by additional Gaussian functions to take into account polarization effects and negative ions. Accuracies of ~0.1 eV in binding energies, and ~10% in transition moments and level lifetimes, are normally achieved in these calculations. The Hay and Dunning (H-D) calculations, as shown in Fig.2-2, do not recover either the ground-state well of XeCl or its proper equilibrium location. Stevens and Krauss [47] point out that this discrepancy is due to the lack of proper basis sets to describe the polarizabilities of ions that are important in the charge-transfer processes involved with the excited states. These processes are in addition to the usual Coulomb and exchange interactions between atoms. Mixing the charge-transfer-state ($Xe^+ \cdots Cl^-$) wavefunction into the ground-state wavefunction distorts the ground-state bonding by reducing the repulsion and by compressing the X $^2\Sigma^+$ potential curve so that the van der Waals contribution predominates, thereby deepening the well. In terms of Mulliken's theory of weakly-binding valence interaction [56], the $^2\Sigma^+$ ground state of XeCl (and that of XeF) represents a kind of electron donor-acceptor complex analogous to a diatomic Lewis acid-Lewis base charge transfer complex [57] (with Xe as the electron-donor base). Indeed, the revised curves of Stevens and Krauss [47], which are determined from first-order configuration interaction (FOCI) calculations employing single configuration SCF techniques for the lowest $^2\Sigma^+$ and $^2\Pi$ states, and from an optimal choice of polarization basis to yield accurate dipole polarizabilities and total energy, provide good agreement with experiment. In particular, the ground-state (X) curve gives a well

Fig. 2-2

Comparison of theoretical and experimentally-derived potential energy curves for the XeCl ground state ($X\ ^2\Sigma^+$). Theoretical results of Hay and Dunning [46], and Stevens and Krauss [47], are denoted by o, and •, respectively. Some of the experimental data points of Sur et al. [44] are denoted by Δ.

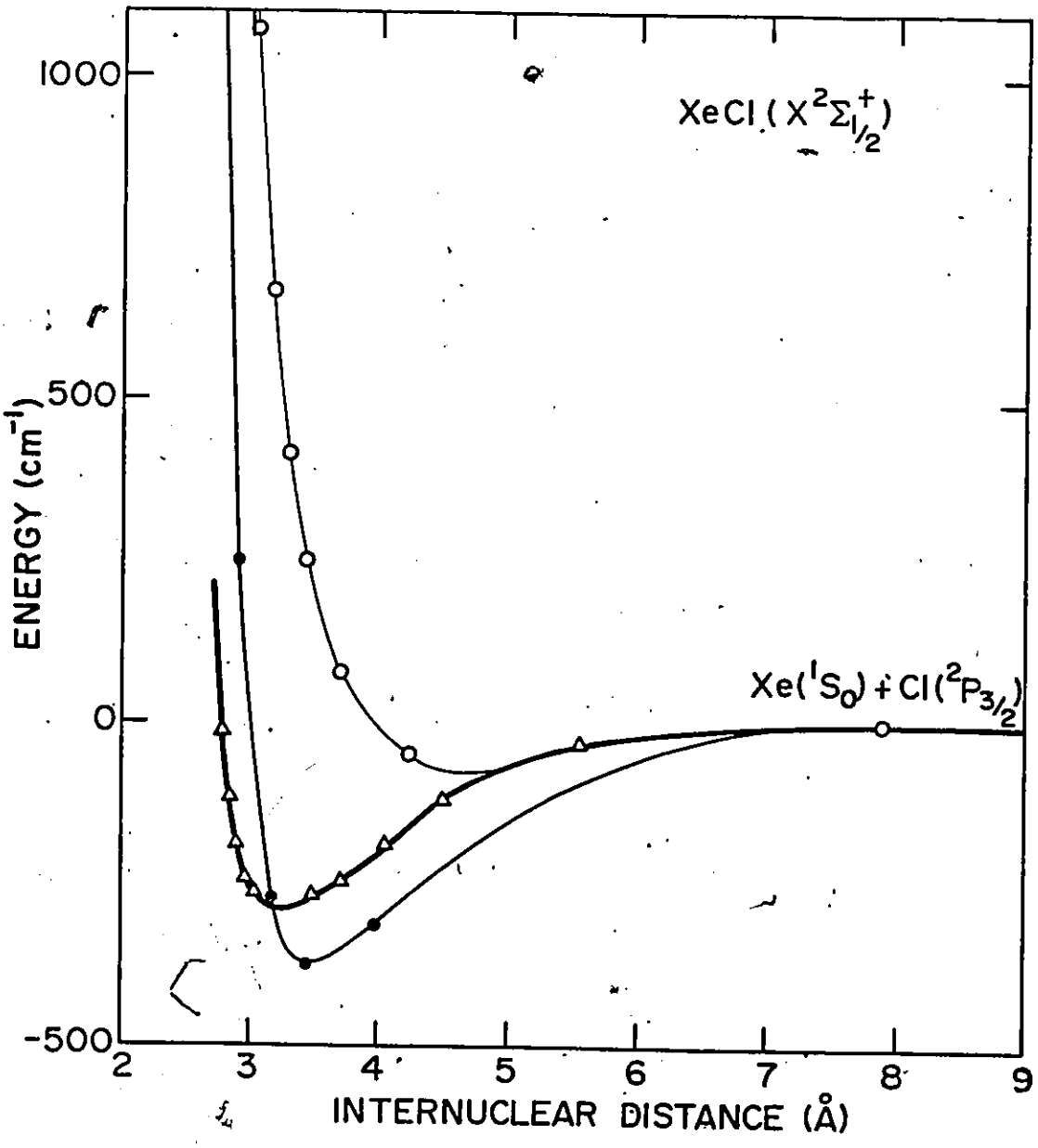
1000
500
0
-500
ENERGY (cm⁻¹)
XeCl (X ²Σ1/2+)
Xe(¹S0) + Cl(²P3/2)
2
3
4
5
6
7
8
9
INTERNUCLEAR DISTANCE (Å)

depth of 0.046 eV for XeCl (0.13 eV for XeF), even though spin-orbit coupling and dispersion effects are neglected. In contrast, the binding between π orbits in A-states (shown in Fig.2-3) is inherently weaker as a result of less configuration mixing (charge transfer). The effect of ionic-covalent mixing merely shifts the $^2\Pi$ curves slightly closer to the origin without substantial deformation to their shapes.

Bound-bound emission in XeCl has been observed for both B → X and D → X transitions [12,36,58]. A comprehensive vibrational analysis has been carried out [44] taking into account 41 bands near 308 nm and 35 bands near 236 nm. The ground state energy curve is characterized by a well depth of 281 cm^{-1} (0.034 eV) at $r_e" = 3.23$ Å, and by the spectroscopic constants $\omega_e" = 26.22\ cm^{-1}$, $\omega_e x_e" = -0.321\ cm^{-1}$, $\omega_e y_e" = -0.0853\ cm^{-1}$ and $\omega_e z_e" = 0.00191\ cm^{-1}$. The dissociation energy D_e, determined from long-range theory [59] for an attractive (van der Waals) potential between atoms, is based on a linear extrapolation of the $g\text{-}G_v$ plot

$$g(G_v) \equiv \left(\frac{dG_v}{dv}\right)^{3/2} = (K_6)^{3/2}(D_e - G_v) \quad . \qquad (2\text{-}1)$$

G_v is the energy of the v^{th} vibrational level, calculated using 4-parameter, least-squares fitted data for 13 measured v" levels. The extrapolation has a theoretical slope of $-K_6^{3/2} = -1.278\ cm^{-1/2}$. It is found that there are 20 possible bound levels in the X-state, and that $\omega_e x_e"$ is <u>negative</u> ($\omega_e x_e"$ for all other diatomics is positive).

Reliable potential curves are based on experimental data. These curves are usually derived from the classical Rydberg-Klein-Rees (RKR) equations [60,61,62] which evaluate the turning points at various vibrational

Fig. 2-3

Theoretical potential energy curves for the XeCl lowest excited state ($A\ ^2\Pi_{3/2,1/2}$). The solid curves are calculated for the $A\ ^2\Pi_{1/2}$ branch and the dashed curve is derived from the calculated results of Hay and Dunning [46] for the $A\ ^2\Pi_{1/2}$ branch. Theoretical values of Hay and Dunning [46] and of Stevens and Krauss [47] are denoted by (o) and (•), respectively.

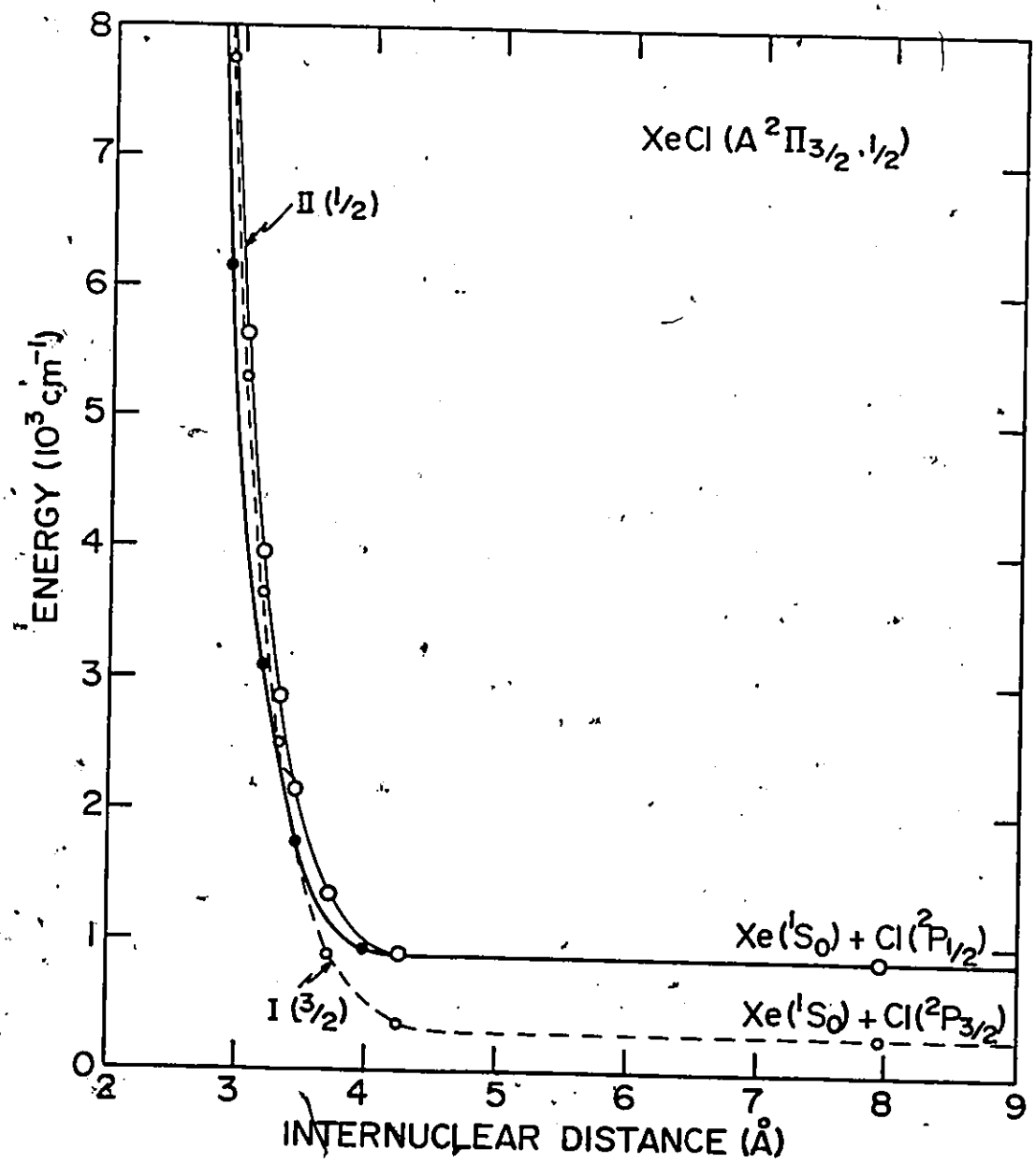
XeCl ($A^2\Pi_{3/2}, 1/2$)
II (1/2)
I (3/2)
Xe($^1S_0$) + Cl($^2P_{1/2}$)
Xe($^1S_0$) + Cl($^2P_{3/2}$)
ENERGY (10^3 cm^{-1})
INTERNUCLEAR DISTANCE (Å)
0
1
2
3
4
5
6
7
8
2
3
4
5
6
7
8
9

levels. However, the long-range interactions are difficult to elucidate, particularly at those high-lying vibrational levels where radiative transitions are weak. Nearly exact reproduction of experimental results by theoretical means is seldom feasible, if not completely impossible. An alterate approach is to introduce empirically-fitted potential functions to describe the molecular states. Few analytic or empirical functions can match molecular parameters satisfactorily†, although it is sometimes erroneously assumed that excellent matching can always be obtained by employing functions with a sufficiently large (but finite) number of parameters. The Dunham curve [63], which is an infinite series representation of a potential function, is not a suitable choice because it is inconvenient to apply. Only appropriate simple functions are known to describe certain molecular structures adequately. Examples are the Morse function [64] for covalent bonding, the Rittner potential [65] for ionic bonding, and the Born-Mayer's exponential [66] for repulsive bonding.

For the XeCl ground-state configuration, the Lennard-Jones (6-12) potential [67] for the van der Waals field is superior to most diatomic potential energy (P.E.) functions, including those of Morse, Rydberg [60] and Varshni [68] (specifically the third function in Ref.[68]). In fact, the generalized forms of the Lennard-Jones potential, the Mecke-Sutherland function [69,70]

---

†It may be noted that the correct functional representation makes it possible to evaluate many important parameters of a molecule. These include the bond strength and length, the force constant (and hence its vibrational and rotational contribution), and the anharmonicity.

$$U(r) = \frac{a}{r^m} - \frac{b}{r^n} \quad , \tag{2-2}$$

and the Sutherland function [71]

$$U(r) = \frac{a}{(r-d)^m} - \frac{b}{(r-d)^n} \quad , \tag{2-3}$$

where a, b, d, m and n are constants and $n \simeq 2m$ for XeCl, are better still. However, all the above functions yield a positive value for $\omega_e x_e$, the anharmonic vibrational constant. Tellinghuisen et al. [48] observed a negative value for $\omega_e x_e$" (superharmonicity). They speculated that this peculiar behaviour of the XeCl ground state might not be significant because only eight v" levels were analyzed and because some bands were not spectroscopically pure due to isotopic blending. The experiment by Sur et al. [44], however, confirmed the early work and the true existence of superharmonicity.

New potential functions of the form

$$U(r) = \frac{A \ln y}{y^n} + \frac{B}{y^p} + \frac{C}{y^q} \tag{2-4}$$

conditionally exhibit superharmonicity. A, B and C are constants related to the dissociation energy D_e, the equilibrium interatomic separation r_e, and the stationary location r_0 where repulsion and attraction are balanced. The independent variable y can be set to either

$$\text{(i)} \ \frac{r-d}{r_e-d} \quad \text{or} \quad \text{(ii)} \ \frac{r-d}{r_0-d} \quad ,$$

where d, a constant, characterizes the extent of the repulsion. Case (i) closely corresponds to the experimentally-derived curve of Sur et al. [44], and in particular, after redefining

$$U(r) \equiv V(r) - D_e \quad ,$$

$$V(r) = D_e \left\{ \frac{a \ln y}{y^n} + \frac{b}{y^p} + \frac{c}{y^q} + 1 \right\} \quad , \qquad (2\text{-}5)$$

where $y = (r-d) / (r_e-d)$,

$a = (q\alpha^p - p\alpha^q) / \mathcal{D}$,

$b = (q\alpha^n \ln \alpha - \alpha^q) / \mathcal{D}$,

$c = (\alpha^p - p\alpha^n \ln \alpha) / \mathcal{D}$,

$\alpha = (r_e-d) / (r_0-d)$,

and $\mathcal{D} = (\alpha^q-\alpha^p) / (q-p)\alpha^n \ln \alpha$.

Using Eq.(2-5), and the data from Ref.[44], the nonlinear least-squares fitted parameters for the XeCl ground state are

$D_e = 299.63 \text{ cm}^{-1}$,

$r_e = 3.2596$ Å ,

$r_0 = 2.7874$ Å ,

$n = 6.922$,

$p = 16.580$,

$q = 16.583$,

and $d = 3.38 \times 10^{-10}$ Å .

The parameters give a residual root-mean-square (RMS) deviation of

3.19 cm^{-1} between measured and calculated energy values. From inspection of the above values, it can be seen that $p \simeq q$ and $d \simeq 0$. Therefore, Eq.(2-5) can be put in the special form

$$V(r) = D_e \{ \frac{a \ln y}{y^n} + \frac{(b \ln y - 1)}{y^p} + 1 \} , \qquad (2\text{-}6)$$

where $y = r / r_e$,

$a = -\alpha^p (p \ln \alpha - 1) / \mathcal{D}$,

$b = -(\alpha^p - p\alpha^n \ln \alpha) / \mathcal{D}$,

$\alpha = r_e / r_0$,

and $\mathcal{D} = (\alpha^p - \alpha^n) \ln \alpha$.

For XeCl, Eq.(2-6) yields the ground-state parameters

$D_e = 298.46\ cm^{-1}$,

$r_e = 3.2616$ Å ,

$r_0 = 2.7879$ Å ,

$n = 6.973$,

and $p = 16.674$.

In addition,

$a = -13.176$,

and $b = -3.498$.

In this case, the residual RMS deviation is 3.08 cm^{-1}. The calculated curve is used for a vibrational analysis to evaluate the coupling constants, the wavefunctions, and the Franck-Condon factors (FCF) for the radiative B → X transition.

Careful inspection of the potential function shows that it is a van der Waals (r^{-6}) potential distorted by a logarithmic-type ($-\ln r/r$) field, which is believed to originate in charge transfer mixing. The effects due to the distorting potential are described in Appendix A.

The vibrational energy levels for a stable molecule are usually written in standard notation as

$$G_v = \omega_e(v + 1/2) - \omega_e x_e(v + 1/2)^2 + \omega_e y_e(v + 1/2)^3 + \omega_e z_e(v + 1/2)^4 + \cdots \quad (2\text{-}7)$$

These may also be derived from Dunham's general expansion

$$F_{vK} = \sum_{\ell,j} Y_{\ell j} (v + 1/2)^{\ell} [K(K+1)]^j . \quad (2\text{-}8)$$

For vibrations only,

$$G_v = \sum_{\ell} Y_{\ell 0} (v + 1/2)^{\ell} . \quad (2\text{-}9)$$

A low order approximation yields the following Dunham coefficients [63]:

$$Y_{00} = \frac{B_e}{8} (3a_2 - 7/4\ a_1^2)$$

$$Y_{10} = \omega_e \left[1 + \frac{B_e^2}{4\omega_e^2} (25a_4 - 95/2\ a_1a_3 - 67/4\ a_2^2 + 459/8\ a_1^2a_2 - 1155/64\ a_1^4)\right]$$

$$Y_{20} = \frac{B_e}{2} \left[3(a_2 - 5/4\ a_1^2) + \frac{B_e^2}{2\omega_e^2} (245a_6 - 1365/2\ a_1a_5 - 885/2\ a_2a_4 - 1085/4\ a_3^2 + 8535/8\ a_1^2a_4 + 1707/8\ a_2^3 + 7335/4\ a_1a_2a_3 - 23865/16\ a_1^3a_3 - 62013/32\ a_1^2a_2^2 + 239985/128\ a_1^4a_2 - 209055/512\ a_1^6)\right]$$

$$Y_{30} = \frac{B_e^2}{2\omega_e} [10a_4 - 35a_1a_3 - 17/2\ a_2^2 + 225/4\ a_1^2a_2 - 705/32\ a_1^4]$$

$$Y_{40} = \frac{5B_e^3}{\omega_e^2} [7/2\ a_6 - 63/4\ a_1a_5 - 33/4\ a_2a_4 - 63/8\ a_3^2 + 543/16\ a_1^2a_4 + 75/16\ a_2^3 + 483/8\ a_1a_2a_3 - 1953/2\ a_1^3a_3 - 4989/64\ a_1^2a_2^2 + 23265/256\ a_1^4a_2 - 23151/1024\ a_1^6]$$

etc., (2-10)

where $B_e = h/8\pi^2\mu r_e^2 c$, and $\omega_e = (4B_e a_0 hc)^{1/2}$.

μ is the reduced mass of the molecule, and h and c have the usual meaning. The "a" coefficients can be derived from the expansion

$$V(r) = hca_0\xi^2 (1 + a_1\xi + a_2\xi^2 + a_3\xi^3 + \cdots) , \qquad (2\text{-}11)$$

where $\xi = (r-r_e)/r_e$. Table 2-1A shows a comparison of the computed Dunham coefficients (and other parameters) for the XeCl ground state using Eq.(2-10), and using a least-squares fit to the energy levels calculated by Eq.(2-23) and given in Table 2-1B. Also shown are the corresponding coefficients derived by Sur et al. [44] from their experimental data, which are also used in our calculations. In all cases, the important parameters (Y_{10} and Y_{20}) are in very good agreement. It should be noted that Sur et al. use a set of 4 parameters to determine the vibrational energies. They estimate 20 vibrational levels in the potential well shown in Fig.2-4. We have used all of the 16 parameters available in the library subroutine package of ORLSQ (for the CDC Cyber 170/730 computer) in order to achieve the best agreement between the least-squares fitted energy levels and those calculated using the potential function given by Eq.(2-6). As a result, a Birge-Spooner plot of the vibrational energy spacings (Fig.2-5) reveals that a total of 23 (v''_{max}=22.53) levels are contained in the potential well. The finite number of levels results in molecular dissociation into neutral atoms, i.e., XeCl → Xe + Cl. Moreover, the continuum limit is approached more slowly, and is higher than that estimated by Sur et al.

Wavefunctions were found by solving the Schrödinger equation with the aid of the zero approximation of the generalized Wentzel-Kramers-Brillouin (WKB) method [72,73]. Note that the usual WKB solution

Table 2-1

Dunham coefficients for the XeCl ground state:

A. Comparison of Dunham coefficients for the XeCl ground state obtained from the approximation (Eq.(2-10)), the least-squares-fit calculations using the potential function given by Eq.(2-6), and the experimental values of Sur et al. [44]. All units are in cm^{-1} unless stated otherwise.

B. Computer results of Dunham coefficients for the XeCl ground state obtained from a least-squares fit of the vibrational energies ($G_{v''}$), which are calculated using the potential function given by Eq.(2-6). The computed values of $G_{v''}$, using these coefficients in Eq.(2-9), are also shown, along with their departure from the original data.

A

	Present Analysis		Experimental Values	
	Approximation [Eq.(2-10)]	Least-Squares Fit	[44]	
B_e	5.6928			
ω_e	27.5687			
Y_{00}	0.3460	0.0010		
Y_{10}	-27.6007	27.5625	ω_e	26.22
Y_{20}	0.3194	0.4749	$(-\omega_e x_e)$	0.321
Y_{30}	-0.2514	-0.2756	$\omega_e y_e$	-0.0853
Y_{40}	0.0233	0.0484	$\omega_e z_e$	0.00191
D_e	298.46			281.00
r_e(Å)	3.2616			3.23
r_0(Å)	2.7879			

B

LEAST SQUARES FITTING
COEFFICIENTS OF 15TH DEGREE POLYNOMIAL EQUATION

DUNHAM PARAMETERS ----- ENERGY UNIT IS CM**(-1)

Y(0)	=	1.0242595E-03
Y(1)	=	2.7562508E+01
Y(2)	=	4.7488578E-01
Y(3)	=	-2.7562808E-01
Y(4)	=	4.8442858E-02
Y(5)	=	-7.7379518E-03
Y(6)	=	1.0645348E-03
Y(7)	=	-1.2034408E-04
Y(8)	=	1.0900378E-05
Y(9)	=	-7.7608598E-07
Y(10)	=	4.2603108E-08
Y(11)	=	-1.7591658E-09
Y(12)	=	5.2686138E-11
Y(13)	=	-1.0780488E-12
Y(14)	=	1.3459598E-14
Y(15)	=	-7.7252708E-17

V	GV	GV (COMPUTED)	DIFF
0	13.8693	13.8693	-7.302E-10
1	41.6798	41.6793	9.287E-09
2	68.9058	68.9058	-5.226E-08
3	95.0521	95.0521	1.693E-07
4	119.8279	119.8279	-3.370E-07
5	143.0555	143.0555	3.890E-07
6	164.6266	164.6266	-1.566E-07
7	184.4787	184.4787	-2.101E-07
8	202.5823	202.5823	2.871E-07
9	218.9325	218.9325	3.199E-08
10	233.5444	233.5444	-2.854E-07
11	246.4493	246.4493	1.021E-07
12	257.6933	257.6933	2.265E-07
13	267.3357	267.3357	-2.278E-07
14	275.4485	275.4485	-7.854E-09
15	282.1163	282.1163	3.065E-07
16	287.4368	287.4368	-2.874E-07
17	291.5212	291.5212	1.480E-07
18	294.4959	294.4959	-4.940E-08
19	296.5034	296.5034	4.065E-09
20	297.7052	297.7052	-6.590E-09

STANDARD DEVIATION = 2.064E-07

Table 2-2

Vibrational energy levels of the XeCl ground state and their classical turning points. The experimental values o[redacted]r et al. [44] are included in parentheses.

v"	$G_{v"}(cm^{-1})$	$r"_{min}(Å)$	$r"_{max}(Å)$
-0.5	0.0	$r"_e$ = 3.2616 (3.2300)	
0	13.87 (13.18)	3.0809 (3.0645)	3.4982 (3.4927)
1	41.68 (39.78)	2.9865 (2.9843)	3.7106 (3.7235)
2	68.91 (66.31)	2.9374 (2.9400)	3.8828 (3.8971)
3	95.05 (92.34)	2.9050 (2.9089)	4.0434 (4.0512)
4	119.83 (117.51)	2.8814 (2.8853)	4.2014 (4.1991)
5	143.06 (141.49)	2.8632 (2.8664)	4.3614 (4.3477)
6	164.63 (163.99)	2.8488 (2.8511)	4.5267 (4.5024)
7	184.48 (184.77)	2.8372 (2.8385)	4.7003 (4.6680)
8	202.58 (203.65)	2.8276 (2.8281)	4.8849 (4.8493)
9	218.93 (220.48)	2.8196 (2.8195)	5.0836 (5.0521)
10	233.54 (235.15)	2.8130 (2.8124)	5.3000 (5.2839)
11	246.45 (247.63)	2.8075 (2.8066)	5.5836 (5.5554)
12	257.69 (257.89)	2.8029 (2.8019)	5.8052 (5.8822)
13	267.34 (265.98)	2.7992 (2.7982)	6.1071 (6.2906)
14	275.45	2.7961	6.4550
15	282.12	2.7937	6.8636
16	287.44	2.7918	7.3555
17	291.52	2.7903	7.9665
18	294.50	2.7893	8.7580
19	296.50	2.7886	9.8482
20	297.71	2.7882	11.5036
22.5	298.46	2.7879	∞

Fig. 2-4

Comparison of calculated and experimentally-derived ground-state potential energy curves and vibrational levels in XeCl. The solid curve is calculated using the potential function given by Eq.(2-6), and the dashed counterpart is based on the experimental results of Sur et al. [44]. These two curves overlap each other on the repulsive slope. Also shown are the vibrational energy levels in corresponding solid and dashed lines. Note that the highest levels are not shown for reasons of clarity.

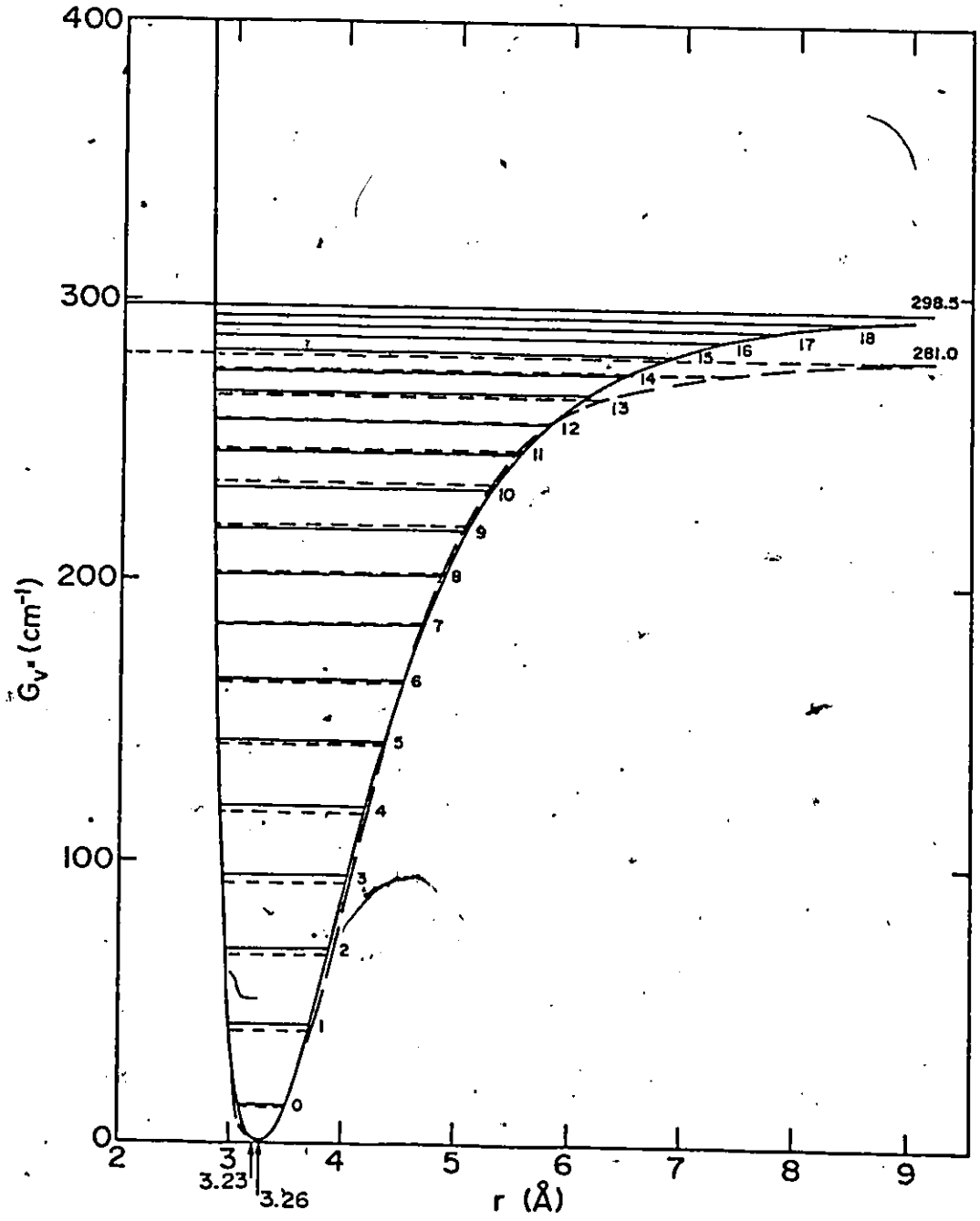
400
300
200
100
0
$G_{v''}$ (cm^{-1})
298.5
281.0
18
17
16
15
14
13
12
11
10
9
8
7
6
5
4
3
2
1
0
2
3
4
5
6
7
8
9
3.23
3.26
r (Å)

Fig. 2-5

Birge-Spooner diagram for the XeCl ground state. $\Delta G_{v"+1/2} \equiv G_{v"+1} - G_{v"}$ is shown as a function of the vibrational quantum number (v").

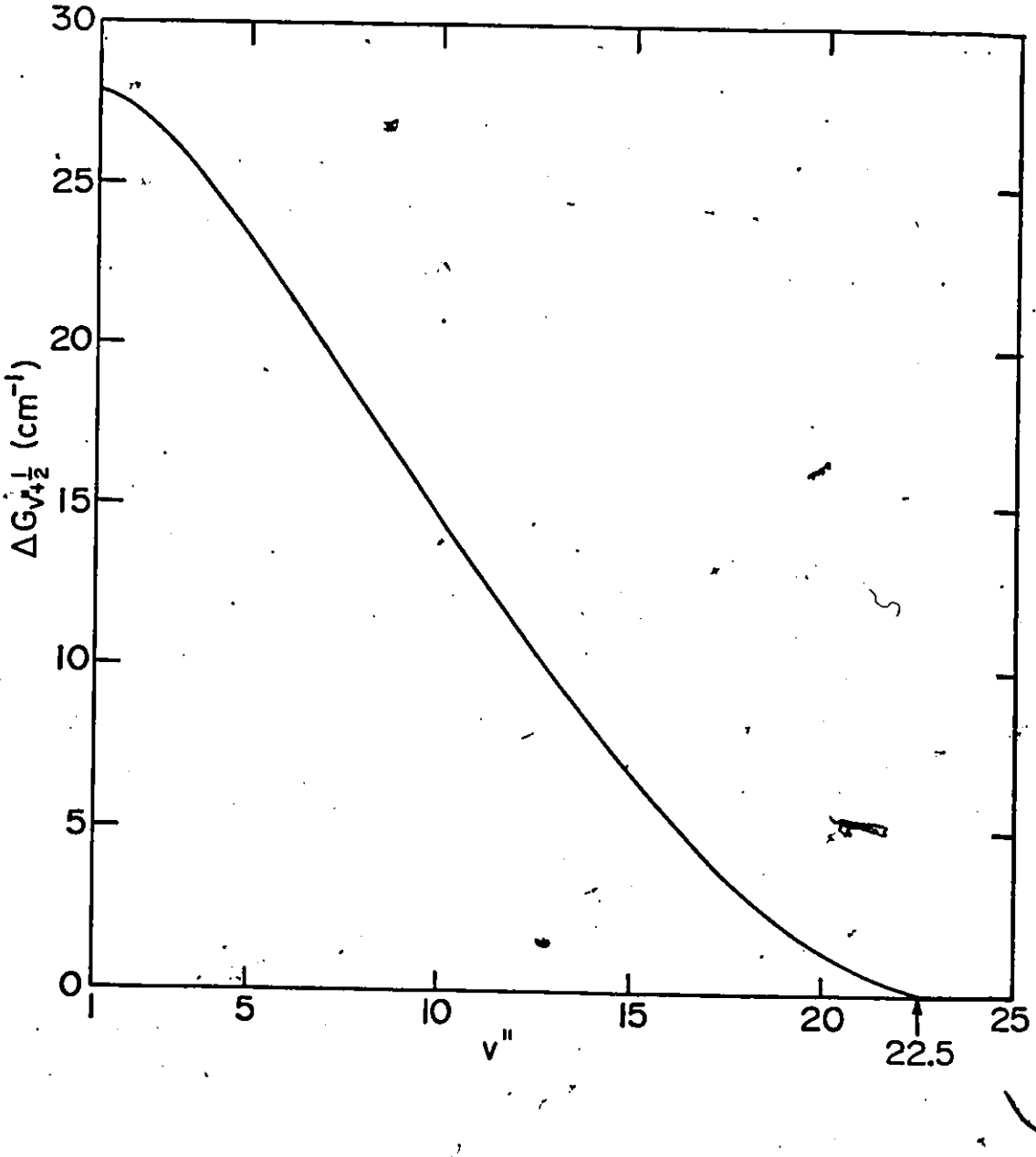
30
25
20
15
10
5
0
$\Delta G_{v+\frac{1}{2}}$ (cm^{-1})
5
10
15
20
25
v''
22.5

of the wave equation, in the Born-Oppenheimer approximation, i.e.,

$$-\frac{\hbar}{2\mu}\frac{d^2\psi_v(r)}{dr^2} + V(r)\psi_v(r) = G_v\psi_v(r) \quad , \tag{2-12}$$

is

$$\psi_v(r) \simeq \{\frac{\hbar^2}{2\mu[G_v - V(r)]}\}^{1/4} \exp\{\int^r \{2\mu[G_v - V(r)]/\hbar^2\}^{1/2} dr\} \quad . \tag{2-13}$$

This may be compared with a similar-type solution of the simple harmonic oscillator

$$\frac{d^2\varphi_v}{ds^2} + (\varepsilon_v - s^2)\varphi_v = 0 \quad , \tag{2-14}$$

namely,

$$\varphi_v(s) \simeq [\varepsilon_v - s^2]^{-1/4} \exp[\int^s (\varepsilon_v - s^2)^{1/2} ds] \quad . \tag{2-15}$$

The exact solution of Eq.(2-14) is well-known, and is

$$\varphi_v(s) = [2^v v!\, \pi^{1/2}]^{-1/2} \exp(-\tfrac{1}{2}s^2) H_v(s) \quad , \tag{2-16}$$

where the eigenvalues are $\varepsilon_v = 2v + 1$ ($v = 0, 1, 2, \cdots$), and where $H_v(s)$ are the Hermite polynomials. Solution of Eq.(2-12) by the generalized WKB method results in the similar equation

$$\psi_v(r) = N_v[\frac{ds(r)}{dr}]^{-1/2} \exp[-\tfrac{1}{2}s^2(r)] H_v[s(r)] \quad . \tag{2-17}$$

The normalization factor

$$N_v = \{2^v\, v!\, \pi^{-1/2} \int_{r_{min}}^{r_{max}} \{2\mu[G_v - V(r)]/\hbar^2\}^{-1/2}\, dr\}^{-1/2} \qquad (2\text{-}18)$$

and

$$\frac{ds(r)}{dr} = \left\{\frac{2\mu[G_v - V(r)]}{\hbar^2[\varepsilon_v - s^2(r)]}\right\}^{1/2} \qquad (2\text{-}19)$$

are determined by inspection of Eqs.(2-13), (2-15) and (2-16). The transformed variable s(r) can be computed directly from Eq.(2-19). At the turning points,

$$s(r_{min}, r_{max}) = \pm(2v + 1)^{1/2} \qquad (2\text{-}20)$$

Figure 2-6 shows the typical behaviour of s(r) for two of the vibrational levels of the XeCl $X\ ^2\Sigma^+$ state. The appropriate values of s(r) are used to calculate the bound-state wavefunctions (shown in Fig.2-7), which will be used with the excimer wavefunctions to determine the emission factors for the B → X transition in a later section.

On the repulsive edge of the ground-state P.E. curve (above the continuum limit), the potential function represented by Eq.(2-6) can also be fitted by the exponential function

$$U(r) = A \exp(-\alpha r) \qquad (2\text{-}21)$$

For 2.0 Å $< r <$ 2.7 Å, the best nonlinear (least-squares) fitted values (using the data given below Eq.(2-6)), $A = 5.711 \times 10^{14}$ cm^{-1} and $\alpha =$ 10.20 Å^{-1}, give a very low standard deviation of 7.5×10^{-5} cm^{-1} between values of U(r) calculated by Eqs.(2-6) and (2-21). In the

Fig. 2-6

The transformed variable s(r) for the XeCl ground state. Only the values of s(r) computed for v" = 0 and v" = 20 are shown. The dashed curve represents the locus of the classical turning points for the ground state.

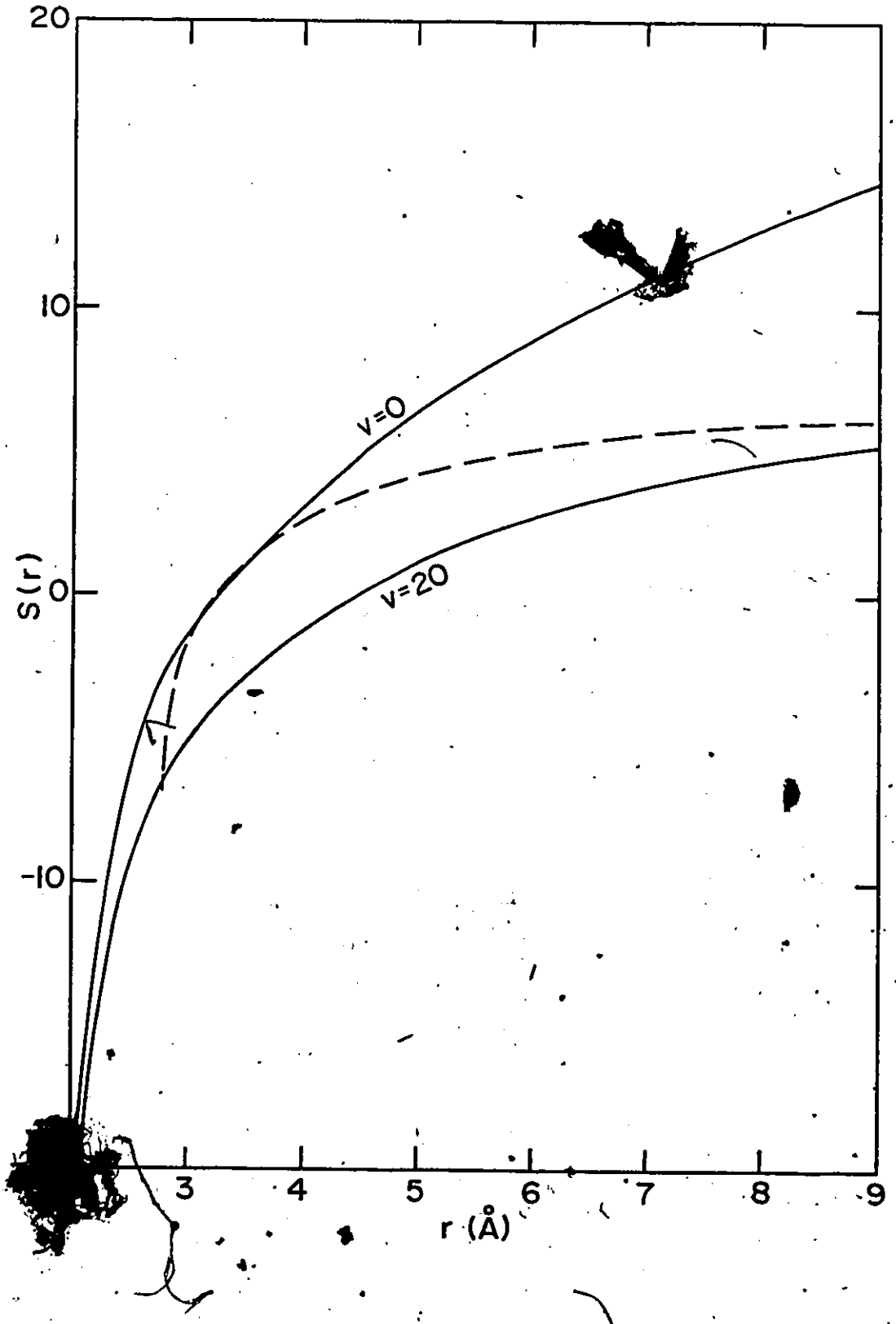
20
10
0
-10
S(r)
v=0
v=20
3
4
5
6
7
8
9
r (Å)

Fig. 2-7

Vibrational wavefunctions, $\psi_{v''}(r)$, for the XeCl ground state. Only those calculated for the four lowest vibrational levels are shown.

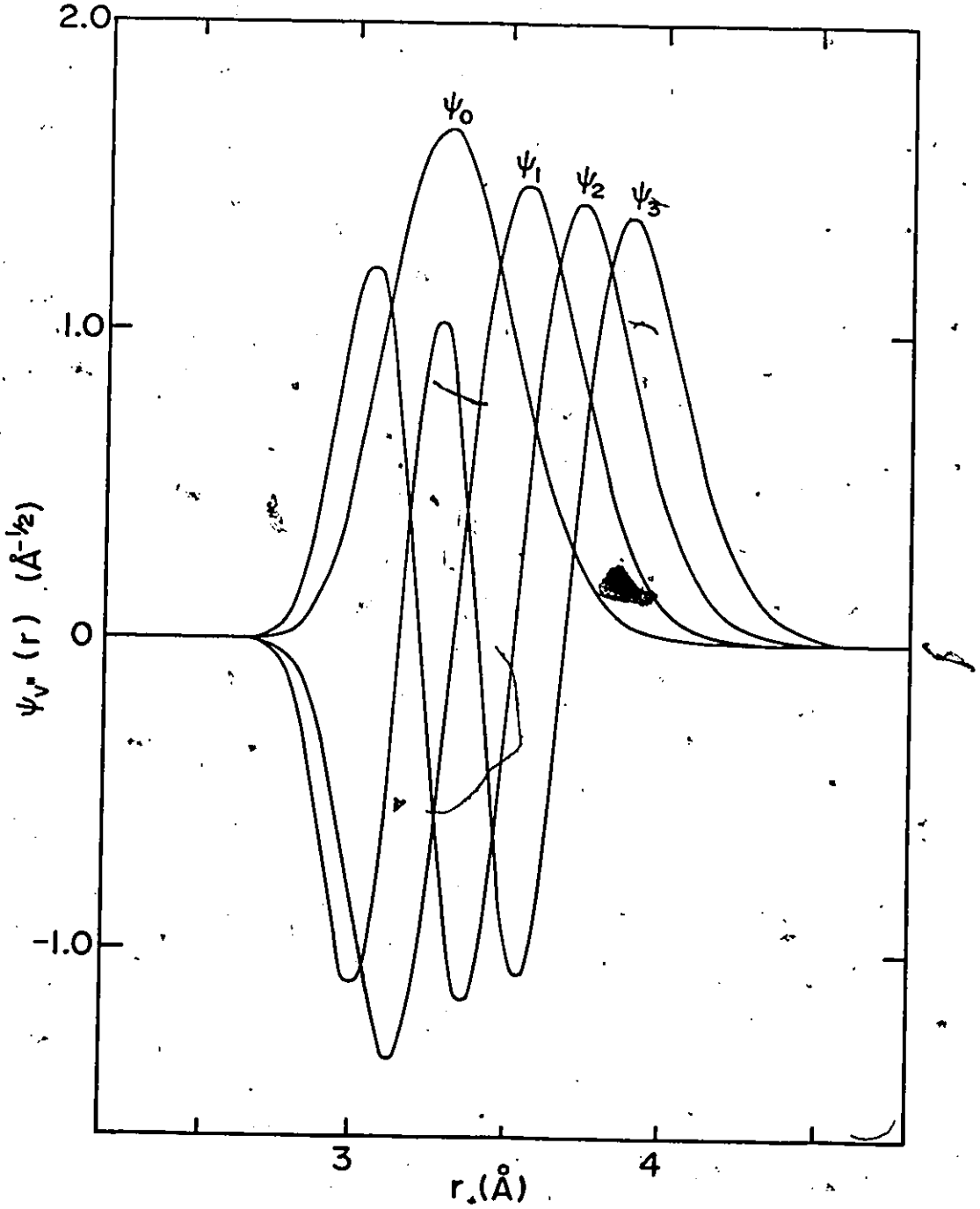
2.0
1.0
0
-1.0
3
4
r (Å)
ψ_v (r) (Å$^{-1/2}$)
ψ_0
ψ_1
ψ_2
ψ_3

more restricted region 2.5 Å < r < 2.7 Å, there is much better agreement using parameters $A = 3.627 \times 10^{14}$ cm^{-1} and $\alpha = 9.99$ Å^{-1}. Wavefunctions solved analytically using the repulsive potential (Eq.(2-21)) are examined in detail in Appendix B. For completeness, Fig.2-8 shows some typical wavefunctions for the repulsive portion of the ground state, which are obtained by using the potential in Eq.(2-6) to solve the Schrödinger equation (Eq.(2-21)).

2.3 The Excimer States

In contrast to the electronic state A $^2\Pi_{3/2,1/2}$, which is repulsive and dissociates to Xe + Cl($^2P_{3/2,1/2}$), the next three higher states, B $^2\Sigma^+_{1/2}$, C $^2\Pi_{3/2}$ and D $^2\Pi_{1/2}$, are strongly-bound excimer states which dissociate diabatically to $Xe^+ + Cl^{-}$††. Of these ionic states, B(1/2)§ and C(3/2) correlate to the ionic fragments $Xe^+(^2P_{3/2})$ and $Cl^-(^1S_0)$, while D(1/2) goes asymptotically to $Xe^+(^2P_{1/2})$ and $Cl^-(^1S_0)$. At their ionic limits, the B (or C) and D states are separated by 1.31 eV [74] due to the spin-orbit splitting in Xe^+. This is similar to the 0.11 eV [74] splitting between the X (or A(3/2)) and A(1/2) states due to spin-orbit splitting in Cl. Temperature-dependent spectral measurements place state C 0.013 eV above B [75], in agreement

---

††Although these excimer states of XeCl tend adiabatically towards the Xe($^3P_2$) + Cl($^2P_{3/2}$) limit, it is still legitimate to regard them as diabatic states since their crossings with the Rydberg curves take place at large distances (see section 2.6).

§For convenience, B(1/2) represents the B $^2\Sigma^+_{1/2}$ state, etc.

Fig. 2-8

Repulsive wavefunctions for the XeCl ground state. ψ_A and ψ_B represent the wavefunctions calculated for ground-state energies of 300 cm^{-1} and 500 cm^{-1} above the potential minimum. Note that the wavefunctions are relative only, and dimensionless.

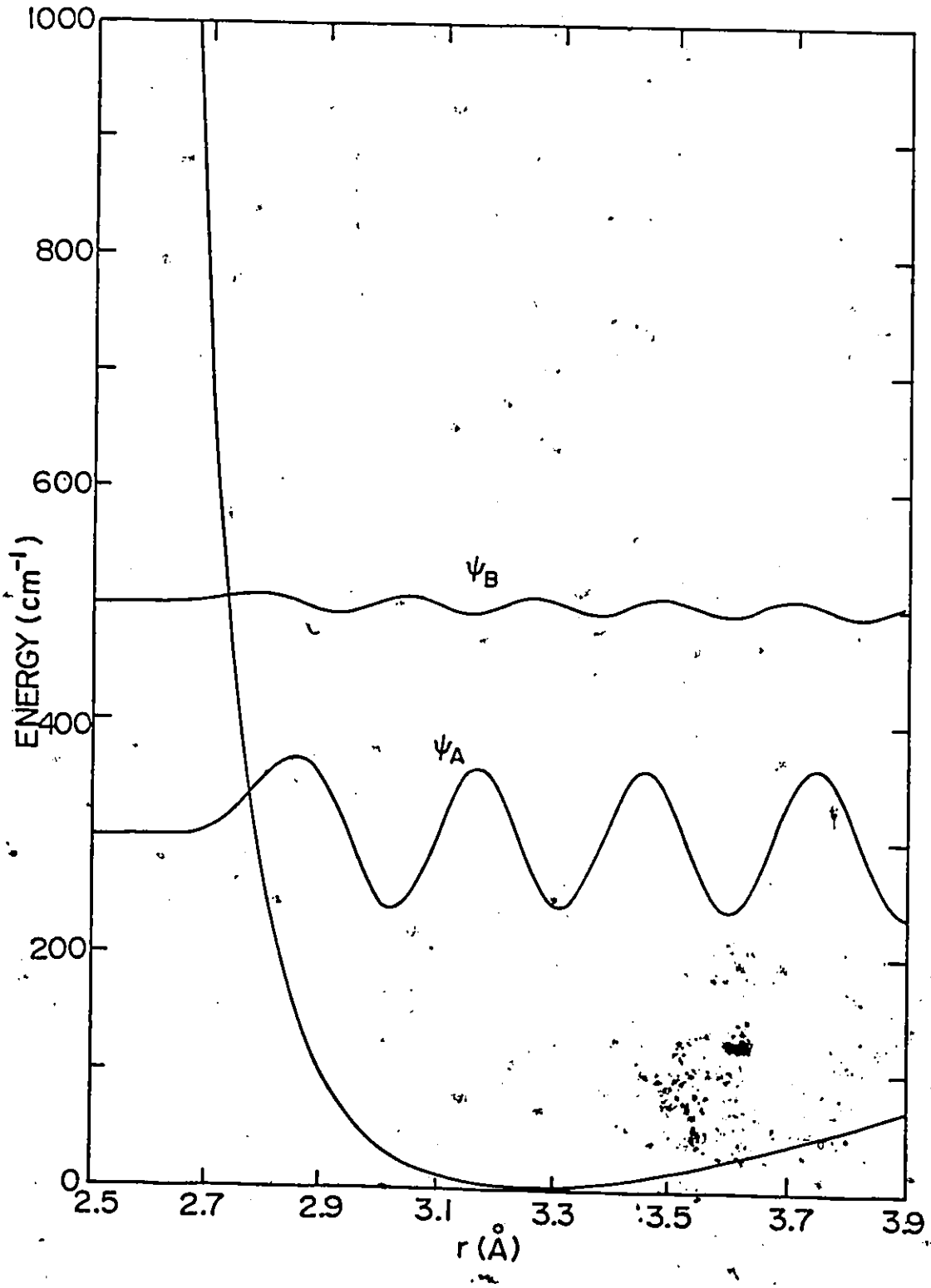
1000
800
600
400
200
0
ENERGY (cm⁻¹)
ψB
ψA
2.5
2.7
2.9
3.1
3.3
3.5
3.7
3.9
r (Å)

with theoretical ordering. However, it was previously suspected that the B state was higher than the C state, in analogy to the 0.074 eV difference in the case of XeF [76], which is anomalous. Despite the difficulty in resolving the overlapping $B \rightarrow A(1/2)$ and $C \rightarrow A(3/2)$ transitions in high-pressure spectra, as well as the lack of accurate data for the branching ratios, the energy ordering of these two closely lying or nearly degenerate states is believed to be normal.

Optical absorption and emission experiments [77] and theoretical calculations [46,47] confirm that the B and D states have large transition moments to the ground state X. As charge transfer excimer states, they are governed by electrostatic interactions at large interionic separations. Because of the relatively high ionization potential of Xe (12.127 eV) [74] and the relatively low electron affinity of Cl (3.615 eV) [78], the lowest ion-pair asymptote of B lies 8.512 eV above the neutral atom limit, which is too high in energy for the Coulomb attraction to make it the molecular ground state. The ionic-covalent mixing and the anisotropy in the dipole polarizability, however, suffice to lower the ionic state so that predissociations, and perturbations of other excited states, are effectively avoided. In addition, the excited ion-pair is kept well above the valence state A, and thermalization to atomic fragments is not likely. Although the bound states are characterized by fairly deep potential wells (D_e' = 4.53 eV for B and 4.61 eV for D [44]), radiative de-excitation from their bottom vibrational levels to a lower repulsive or weakly-bound state still occurs with a good quantum efficiency (48.4% and 56.7% for the

B → X and D → X transitions respectively)[§§].

The XeCl spectral bands $^2\Sigma^+_{1/2} \rightarrow {}^2\Sigma^+_{1/2}$ and $^2\Pi_{1/2} \rightarrow {}^2\Sigma^+_{1/2}$, with peak intensities near 308 nm and 236 nm, respectively, reveal vibrational structures with spacings (194.75 cm^{-1} and 204.34 cm^{-1}, respectively) [44] comparable to that in the alkaline halide CsCl, which is 214 cm^{-1} [79]. It is found that the halide of the alkaline atom adjacent to the rare-gas atom in the Periodic Table can be used as a crude model for the appropriate rare-gas halide [37]. An electrostatic model of the Rittner type is therefore suitable for describing the excimer states. Furthermore, their comparable spectral bandwidths suggest that the two states have similar bond lengths. Detailed analysis shows that the location of the D state minimum is only 0.085 Å less than that of the B state [44].

Sur et al. [44] employ a truncated Rittner potential to represent the B and D curves:

$$U(r) = a + be^{-\beta r} - \frac{c_1}{r} - \frac{c_3}{r^3} - \frac{c_4}{r^4} \quad , \tag{2-22}$$

where a, b and β are constants for the corresponding state, and where a is defined primarily by the asymptotic ionic energy. At large distances, the Coulomb electrostatic interaction (-1/r) is dominant (c_1 = 1.1614 x 10^5 cm^{-1}-Å), while at short range, a Born-Mayer term has to be added to take into account the strong repulsion due to

---

[§§]The quantum efficiency η_Q is defined as the ratio of the emission photon energy hν to the energy E^* of the lowest formation channel. The values quoted in the text are obtained with reference to the lowest Rydberg state limit (corresponding to $Xe(^3P_2)$ + $Cl(^2P_{3/2})$).

ionic-covalent mixing. In addition, an ion-quadrupole term ($-c_3/r^3 = -e^2\langle r^2\rangle/5r^3$) is included to distinguish the splitting of the B and D states that are actually strong admixtures of $^2\Sigma^+$ and $^2\Pi$. With the appropriate electronic average r^2 value for the $Xe^+(^2P_{3/2})$ valence p shell, $\langle r^2\rangle$ = 1.66 Å^2, the estimated c_3 is 3.9 x 10^4 cm^{-1}-Å^3. This term is excluded from the D potential where charge-quadrupole interaction is insignificant for the $Xe^+(^2P_{1/2})$ ion. There is also the ion-induced dipole contribution giving rise to $c_4 = e^2(\alpha_+ + \alpha_-)/2$ = 3.5 x 10^5 cm^{-1}-Å^4 (α_+ and α_- are the ion polarizabilities). Figure 2-9 shows the excimer B and D curves, using the potential function given by Eq.(2-22) and the spectroscopic parameters listed in Table 2-3. For comparison, the theoretical curves of Hay and Dunning, and of Stevens and Krauss, are also included. Both of these calculations predict bond lengths for the B state that are over 0.2 Å longer than the experimentally derived 3.007 Å. In addition, they predict slightly shallower well-depth. With the exception of the repulsive edge, the overall theoretical curves are accurate enough to describe the experimental excimer potentials. At long range, for example, the D curve of Hay and Dunning matches the measured D state to within 1%.

2.4 Radiative B → X Electronic Transition

Radiative transitions, satisfying the selection rule $\Delta\Omega = 0$, have been reported on the B → X, D → X, C → A, D → A and B → A electronic bands. Of particular interest for this thesis is the B → X transition, for which the most intense radiation is at 308 nm. Under excitation at

Fig. 2-9

Comparison of theoretical and experimentally-derived excimer states of XeCl (B(1/2) or III(1/2), C(3/2) or IV(3/2), and D(1/2) or IV(1/2)). Theoretical values of Hay and Dunning [46], and Stevens and Krauss [47], are denoted by (o), and (•), respectively. Experimental data of Sur et al. [44] are not shown but represented by the heavier solid curves.

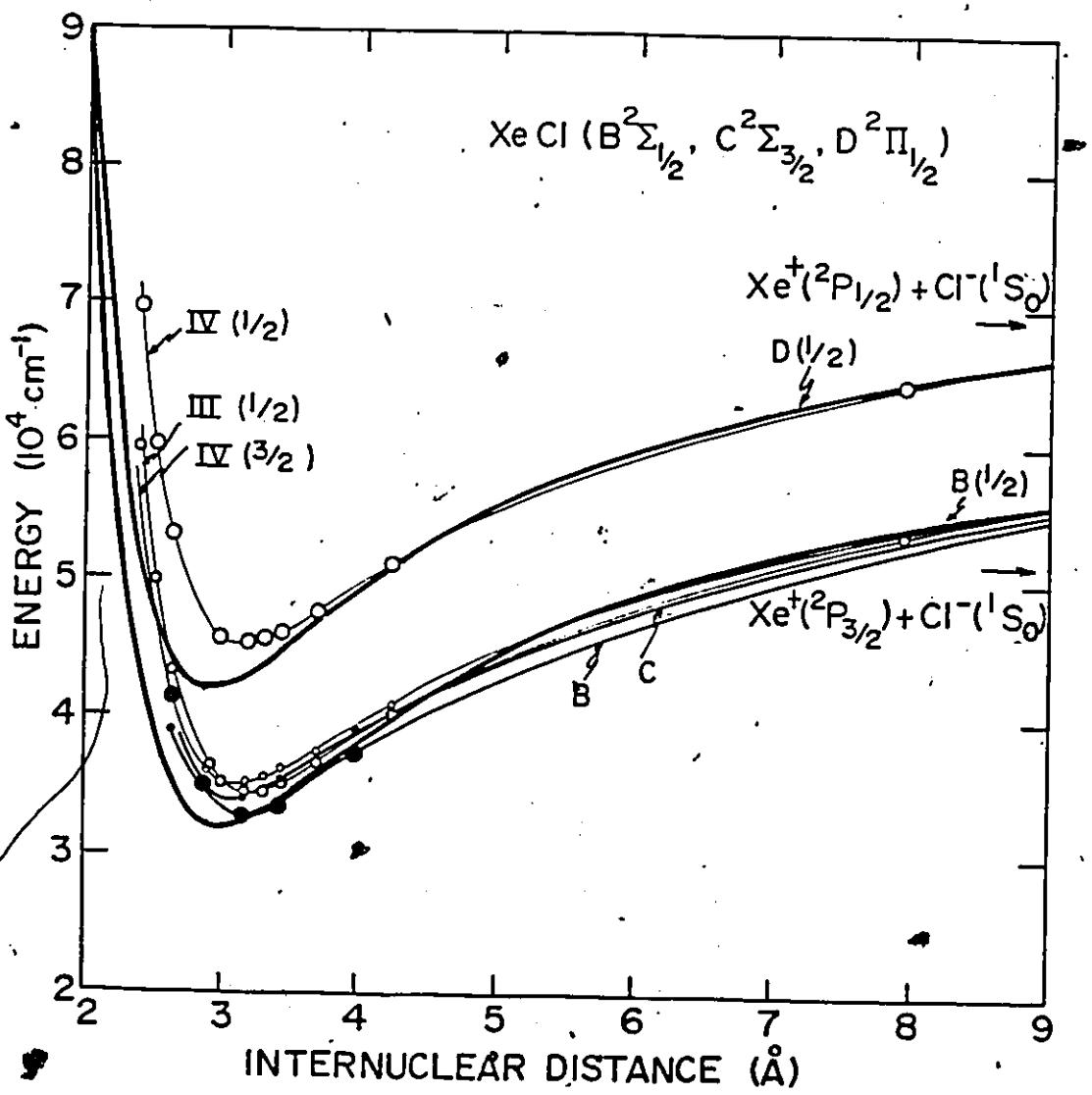
XeCl ($B^2\Sigma_{1/2}$, $C^2\Sigma_{3/2}$, $D^2\Pi_{1/2}$)
$Xe^+(^2P_{1/2}) + Cl^-(^1S_0)$
$Xe^+(^2P_{3/2}) + Cl^-(^1S_0)$
IV (1/2)
III (1/2)
IV (3/2)
D(1/2)
B(1/2)
B
C
ENERGY (10^4 cm^{-1})
INTERNUCLEAR DISTANCE (Å)
2
3
4
5
6
7
8
9

Table 2-3

Spectroscopic parameters for the truncated Rittner potential functions of the excimer B and D states in XeCl [44].

		B	D
T_e'	(cm^{-1})	32405.8*	42347.9**
ω_e'	(cm^{-1})	194.75	204.34
$\omega_e x_e'$	(cm^{-1})	0.627	0.682
D_e'	(cm^{-1})	36553	37148
r_e'	(Å)	3.007	2.922
a	(cm^{-1})	68677.8*	79214.9**
b	(cm^{-1})	1.7348×10^7	2.1316×10^7
β	($Å^{-1}$)	2.5637	2.7261
c_1	(cm^{-1}-Å)	1.1614×10^5	1.1614×10^5
c_3	(cm^{-1}-$Å^3$)	3.9×10^4	0
c_4	(cm^{-1}-$Å^4$)	3.5×10^5	3.5×10^5

*For calculations in this thesis, the parameters T_e' and a for the B state are adjusted to 32412.9 cm^{-1} and 68668.0 cm^{-1}, respectively. These adjusted values are determined from a comparison of our observations of the B → X emission and the calculated results using the ground-state potential given in Eq.(2-6).

**For consistency, the values of T_e' and a for the D state are also adjusted so that the dissociation limits of the B and D states are separated by the energy difference between the $Xe^+(^2P_{3/2})$ and $Xe^+(^2P_{1/2})$ levels, which is 10537.3 cm^{-1} [74]. This gives T_e' = 42355.8 cm^{-1} and a = 79205.3 cm^{-1}.

room temperature, the upper state (B) is virtually all in the v' = 0 vibrational level. Laser operation only occurs on the 0-2, 0-1, 0-3 and 0-0 vibrational bands of the B → X system and only to the left (the repulsive side) of the ground state potential well. This may be contrasted to the XeF transitions, which terminate to the right (positive slope) of the lower shallow potential well.

The upper B state is characterized by a bond strength of 36553 cm^{-1} at 3.007 Å separation, and with vibrational constants $\omega_e' = 194.75\ cm^{-1}$ and $\omega_e x_e' = 0.627\ cm^{-1}$ [44]. With the aid of Rittner's model potential (Eq. (2-22)), the vibrational energy levels $G_{v'}$ (given in Table 2-4) are evaluated using the quantization rule

$$\int_{r_{min}}^{r_{max}} \{2\mu[G_{v'}-V(r)]/\hbar^2\}^{1/2}\, dr = (v'+\tfrac{1}{2})\pi \quad , \qquad (2\text{-}23)$$

where $U(r) = V(r) - D_e$.

$G_{v'}$ can also be expressed in a Dunham's series representation (Tables 2-5A and B). Sur et al. [44] used either 2 or 3 parameters to fit $G_{v'}$. In the present analysis, however, a set of 16 Y coefficients is chosen to least-squares fit the lowest 21 levels, as was done for the ground state. Using v' = 11 as an example, the 2-parameter formula calculates $G_{v'} = 2156.7\ cm^{-1}$, which exceeds the v' = 12 energy of 2154.7 cm^{-1} obtained by "exact" computation (Table 2-5B). Moreover, the anharmonic vibrational constant $\omega_e x_e'$ quoted above (0.627 cm^{-1}) is quite different from the $-Y_{20} = \omega_e x_e' = 3.894\ cm^{-1}$ found here. However, there is a general agreement on the quantity ω_e', which is 192.27 cm^{-1} in the

Table 2-4

Vibrational energy levels of the XeCl B state and their classical turning points.

v'	$G_{v'}(cm^{-1})$	$r'_{min}(\mathring{A})$	$r'_{min}(\mathring{A})$
-0.5	0.0	$r_e' = 3.0066$	
0	95.48	2.9316	3.0882
1	281.96	2.8813	3.1515
2	464.49	2.8486	3.1969
3	643.85	2.8232	3.2350
4	820.46	2.8021	3.2688
5	994.55	2.7838	3.2997
6	1166.32	2.7675	3.3285
7	1335.91	2.7529	3.3557
8	1503.44	2.7395	3.3816
9	1669.00	2.7272	3.4064
10	1832.68	2.7157	3.4303
11	1994.55	2.7051	3.4535
12	2154.67	2.6950	3.4760
13	2313.10	2.6856	3.4979
14	2469.88	2.6766	3.5193
15	2625.07	2.6681	3.5403
16	2778.70	2.6600	3.5608
17	2930.82	2.6523	3.5810
18	3081.46	2.6449	3.6009
19	3230.66	2.6378	3.6204
20	3378.45	2.6309	3.6397
	36553.58		∞

Table 2-5

Dunham coefficients for the XeCl B state:

A. Comparison of Dunham coefficients for the XeCl B state obtained from a least-squares-fit calculation using the truncated Rittner potential given by Eq.(2-22), and the experimental values of Sur et al. [44]. All units are in cm^{-1}.

B. Computer results of Dunham coefficients for the XeCl B state obtained from a least-squares fit of the vibrational energies ($G_{v'}$), calculated using the truncated Rittner potential function given by Eq.(2-22). The computed values of $G_{v'}$, using these coefficients in Eq.(2-9), are also shown, along with their departure from the original data.

A

	Values Obtained From Least-Squares Fit	Experimental Values [44]
Y_{00}	0.2185	
Y_{10}	192.2679	194.75
Y_{20}	-3.8935	-0.627

B

LEAST SQUARES FITTING
COEFFICIENTS OF 15TH DEGREE POLYNOMIAL EQUATION

DUNHAM PARAMETERS ------ENERGY UNIT IS CM**(-1)

Y(0)	=	2.184593E-01
Y(1)	=	1.922679E+02
Y(2)	=	-3.893477E+00
Y(3)	=	9.115173E-01
Y(4)	=	-2.669760E-01
Y(5)	=	6.307349E-02
Y(6)	=	-1.145641E-02
Y(7)	=	1.587869E-03
Y(8)	=	-1.676609E-04
Y(9)	=	1.343567E-05
Y(10)	=	-8.095726E-07
Y(11)	=	3.602610E-08
Y(12)	=	-1.146964E-09
Y(13)	=	2.468907E-11
Y(14)	=	-3.216711E-13
Y(15)	=	1.914565E-15

V	GV	GV (COMPUTED)	DIFF
0	95.4781	95.4781	3.343E-08
1	281.9565	281.9565	-4.268E-07
2	464.4878	464.4878	2.429E-06
3	643.8541	643.8541	-8.001E-06
4	820.4545	820.4545	1.636E-05
5	994.5469	994.5469	-1.999E-05
6	1166.3175	1166.3175	1.037E-05
7	1335.9098	1335.9093	7.108E-06
8	1503.4396	1503.4396	-1.327E-05
9	1669.0034	1669.0034	8.924E-07
10	1832.6834	1832.6834	1.137E-05
11	1994.5511	1994.5511	-5.692E-06
12	2154.6694	2154.6694	-8.116E-06
13	2313.0949	2313.0949	9.626E-06
14	2469.8783	2469.8783	1.904E-06
15	2625.0659	2625.0659	-1.139E-05
16	2778.7002	2778.7003	1.114E-05
17	2930.8206	2930.8206	-5.908E-06
18	3081.4634	3081.4634	1.911E-06
19	3230.6626	3230.6626	-3.185E-07
20	3378.4502	3378.4502	8.171E-08

STANDARD DEVIATION = 9.190E-06

present case, compared to 194.75 cm^{-1} and 188 cm^{-1} calculated by the above authors and by Hay and Dunning [46], respectively.

The excimer vibrational wavefunctions $\psi_{v'}(r)$, shown in Fig.2-11, are determined using the calculated values of the transformed variable s(r) for the B state (Fig.2-10) in the generalized WKB method. These calculations are similar to those employed for the ground state.

The bound-bound B → X emission between vibrational levels v' and v" is appropriately described by the normalized "lineshape" function

$$g_{v'\to v"}(h\nu) = \mathcal{I}_{v'\to v"}(h\nu)/(\frac{dG_{v"}}{dv"}) \quad , \tag{2-24}$$

where

$$\mathcal{I}_{v'\to v"}(h\nu) \equiv \frac{|<v'|\mu_e(r)|v">|^2}{<v'|\mu_e{}^2(r)|v'>} \quad . \tag{2-25}$$

The transition moment, for an ensemble of dipoles $\vec{d} = e\sum_i(-\vec{r}_i)$, given by

$$\mu_e(r)_{B\to X} \equiv <B|\frac{\vec{d}\cdot\vec{r}}{r}|X> \quad , \tag{2-26}$$

is evaluated using the electronic wavefunctions of the two molecular states. As usual, hν and e are the photon energy and the electron charge, respectively. According to the Franck-Condon principle for electronic transitions in diatomic molecules [80], which assumes $\mu_e(r)$ to vary slowly over the region of emission,

$$\mathcal{I}_{v'\to v"}(h\nu) \approx |<v'|v">|^2 \quad . \tag{2-27}$$

The square of the transition matrix element in this equation is the well-known Franck-Condon factor

Fig. 2-10

The transformed variable s(r) for the XeCl B $^2\Sigma^+$ state. Only values of s(r) obtained for v' = 0 and v' = 20 are shown. The dashed curve represents the locus of the classical turning points for the B state.

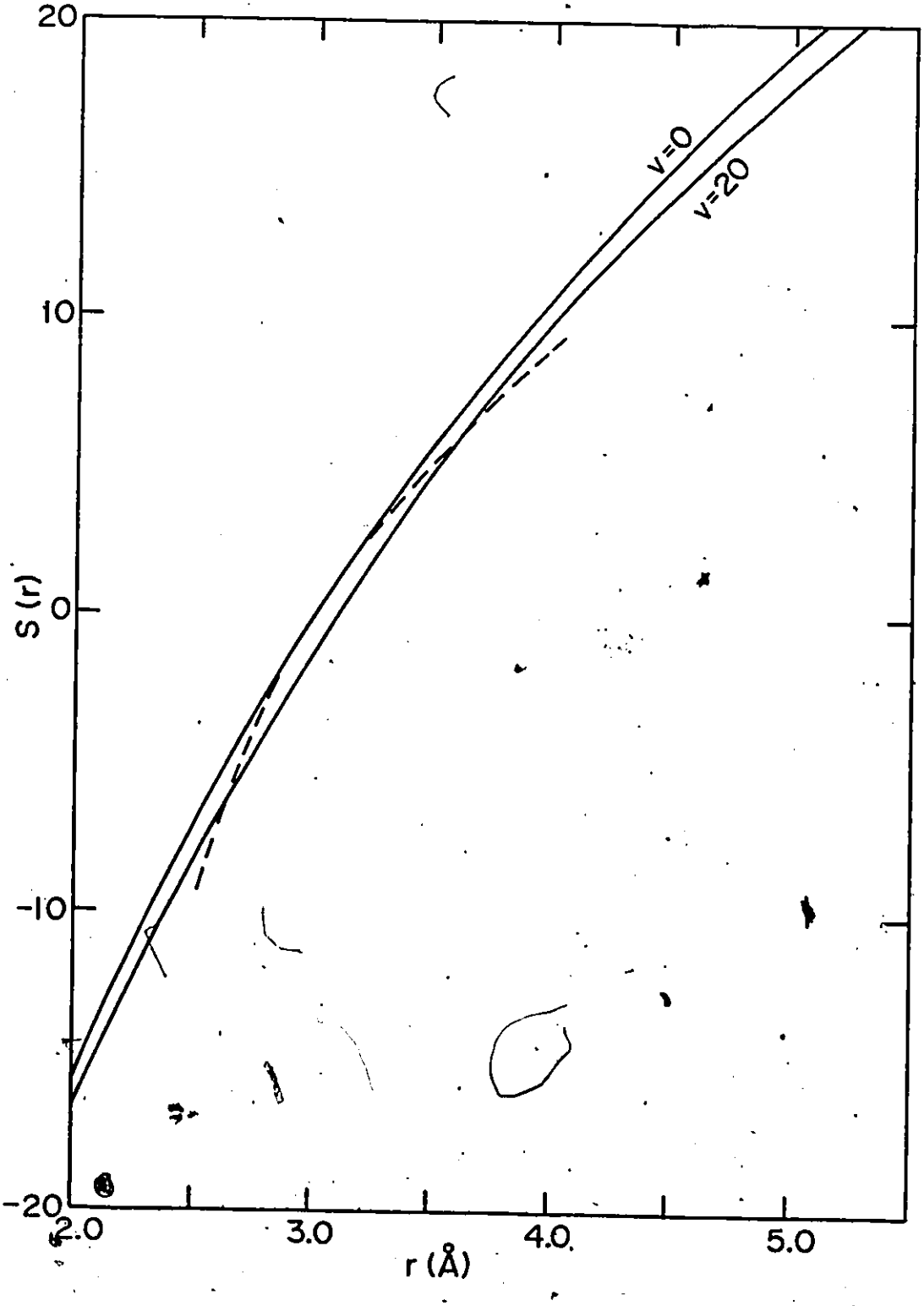
20
10
0
-10
-20
S (r)
2.0
3.0
4.0
5.0
r (Å)
v=0
v=20

Fig. 2-11

Vibrational wavefunctions, $\psi_{v'}(r)$, for the XeCl B $^2\Sigma^+$ state. Only those calculated for v' = 0 and v' = 1 are shown.

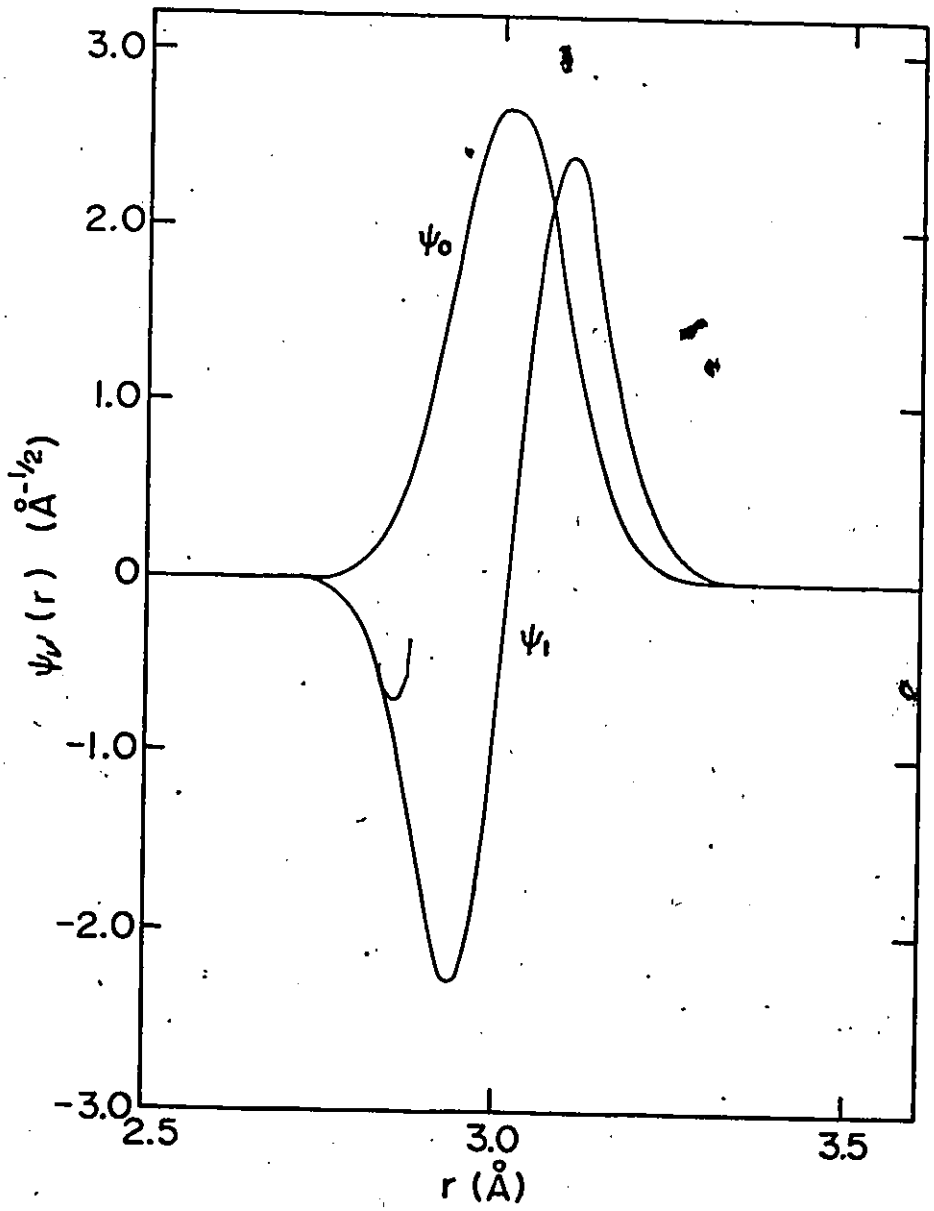
3.0
2.0
1.0
0
-1.0
-2.0
-3.0
2.5
3.0
3.5
r (Å)
ψν (r) (Å-1/2)
ψ0
ψ1

$$FCF(v' \rightarrow v'') \equiv |\langle v'|v''\rangle|^2 = \left[\int_0^\infty \psi_{v'}(r)\psi_{v''}(r)dr\right]^2 \quad . \qquad (2\text{-}28)$$

This factor provides an alternate description of the intensity spectrum via the relationship

$$g_{v' \rightarrow v''}(h\nu) \cong FCF(v' \rightarrow v'')/\left(\frac{dG_{v''}}{dv''}\right) \equiv FCD(v' \rightarrow v'') \quad . \qquad (2\text{-}29)$$

The Franck-Condon density (FCD), defined in Eq.(2-29), is a more realistic representation of the "lineshape" function than the FCF.

Figure 2-12 gives plots of the FCF and FCD, and of the $g_{v' \rightarrow v''}$ functions (using $\mu_e(r)$ and $\mu_e(r+0.213\text{Å})$ values from Hay and Dunning [46]) for the v'=0 progression of the XeCl B → X system. Additional $g_{v' \rightarrow v''}$ functions, using tentative dipole moments from Tamagake et al. [81] (Curves B, C and D in Fig.5 of Ref.[81]), are presented in Fig.2-13. It can be seen from these two figures that the various "lineshape" functions and the FCD curve are very similar. The figures demonstrate that the r-Centroid approximation adopted for calculating the FCD is suitable for describing the emission characteristics of the B → X transition. This is in support of Nicholls' [82] conclusion that the approximation is good for nearly all bands of most spectroscopic systems. Provided that the local peak of the transition moment is wider than 0.2 Å, strongest emission occurs in the 0-2 band, with decreasing radiation in the 0-1, 0-3, 0-4 and 0-0 bands. Substantial coherent emission from the two strongest bands has been observed in our experiments described in the next section.

Fig. 2-12

Graphical plots of Franck-Condon factors and densities, and normalized "lineshape" function versus wavelength (in air) for the v'=0 progression in the XeCl B → X system. The solid curve and bars represent results obtained from Franck-Condon calculations. The dashed and semi-dashed lines correspond to the $g_{0\to v''}(h\nu)$ functions determined using the dipole moments $\mu_e(r)$ and $\mu_e(r+0.213\ \text{Å})$ from Hay and Dunning [46].

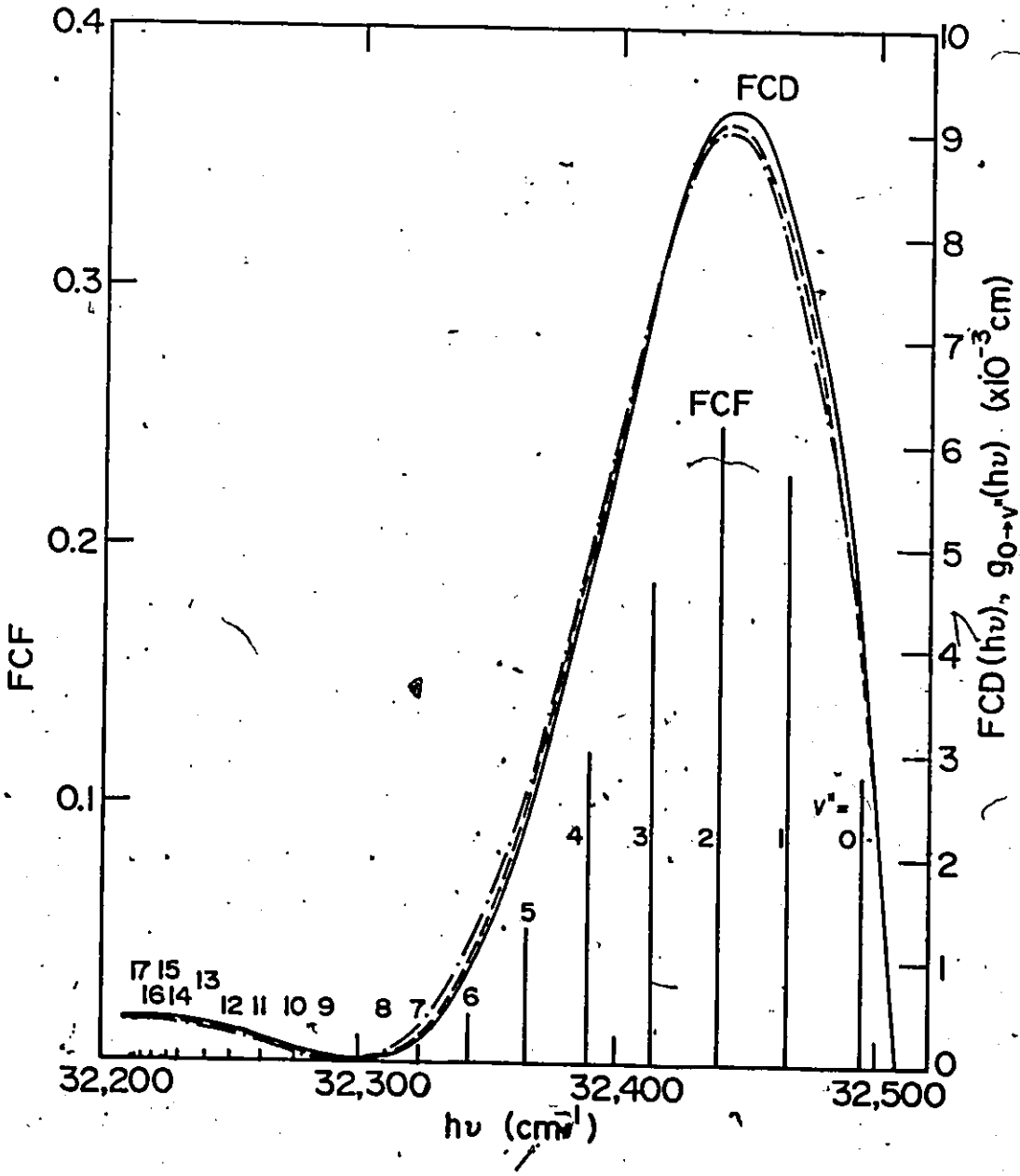
FCD
FCF
FCF
0.4
0.3
0.2
0.1
10
9
8
7
6
5
4
3
2
1
0
FCD(hν), g0→v'(hν) (x10⁻³cm)
v'=
0
1
2
3
4
5
6
7
8
9
10
11
12
13
14
15
16
17
32,200
32,300
32,400
32,500
hν (cm⁻¹)

Fig. 2-13

Comparison of various normalized "lineshape" functions obtained using the tentative transition dipole-moment functions from Tamagake et al. (Curves B, C and D in Ref.[81]).

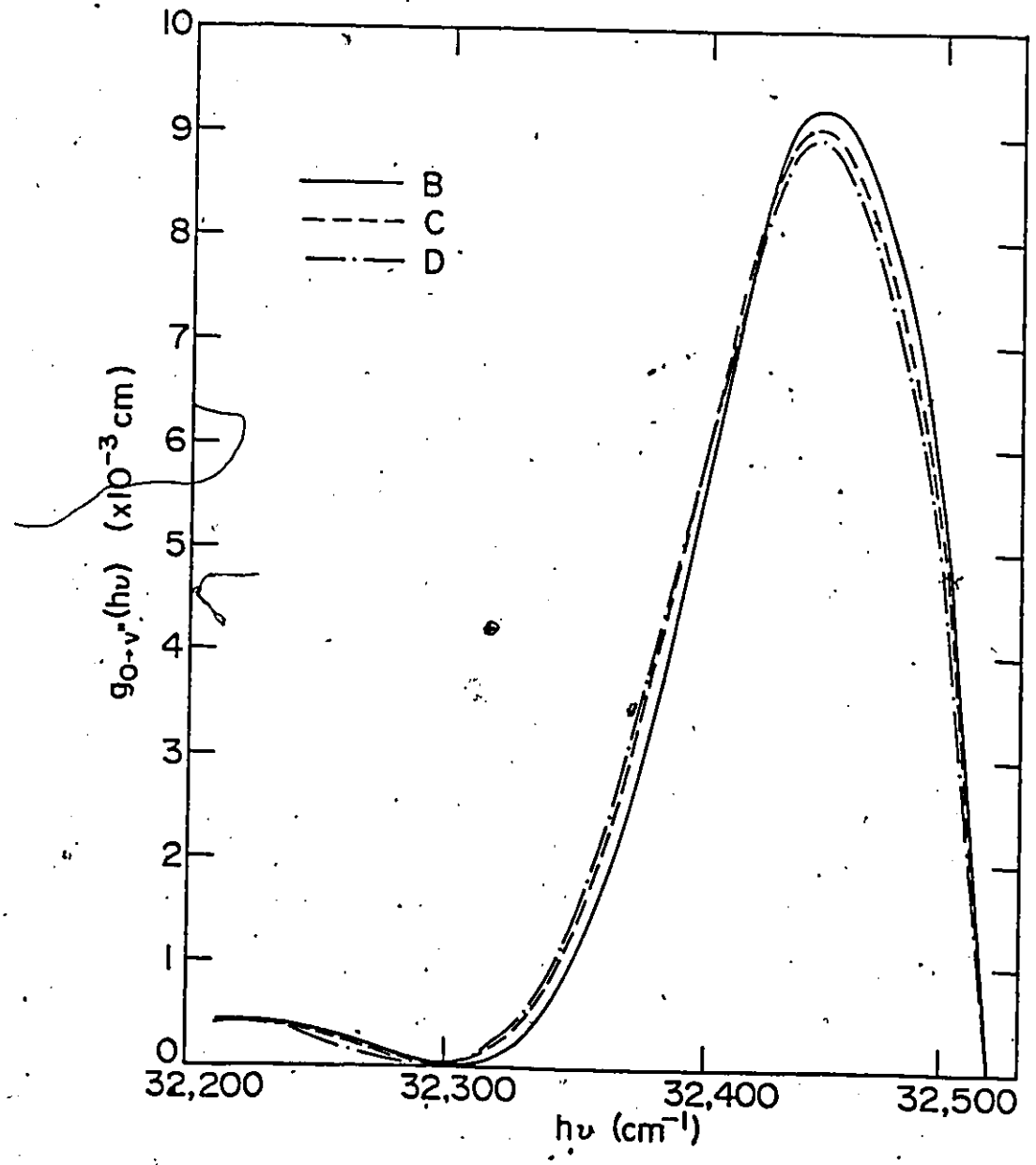
10
9
8
7
6
5
4
3
2
1
0
B
C
D
$g_{o\to v''}(h\upsilon)$ (x10^{-3} cm)
32,200
32,300
32,400
32,500
$h\upsilon$ (cm^{-1})

The FCF and FCD are important in evaluating the fundamental parameters relating to spectral emission, such as the Einstein A coefficient and the stimulated-emission cross-section, given by

$$A_{v'\to v''} = \frac{64\pi^4}{3h}\,\mu_e^{\,2}(r_e')\,\lambda_{v'\to v''}^{-3}\,FCF(v'\to v'') \qquad (2\text{-}30)$$

and

$$\sigma_s\left(\frac{hc}{\lambda_{v'\to v''}}\right) = \frac{8\pi^3}{3hc}|\mu_e(\bar{r})|^2\lambda_{v'\to v''}^{-1}FCD(v'\to v'') \quad , \qquad (2\text{-}31)$$

respectively. $\bar{r}$ is the r-centroid for the transition v'→v". If the $\mu_e(r)$ values are known for the electronic transition, it is proper to calculate

$$A_{v'\to v''} = \frac{64\pi^4}{3h}\lambda_{v'\to v''}^{-3}|\langle v'|\mu_e(r)|v''\rangle|^2 \qquad (2\text{-}32)$$

and

$$\sigma_s\left(\frac{hc}{\lambda_{v'\to v''}}\right) = \frac{\lambda_{v'\to v''}^2}{8\pi}\,A_{v'\to v''}\,g_{v'\to v''}\left(\frac{hc}{\lambda_{v'\to v''}}\right) \quad . \qquad (2\text{-}33)$$

In addition, the radiative lifetime for decay from the upper v' level to the ground state can be determined using

$$\tau_{v'} = \left(\sum_{v''} A_{v'\to v''}\right)^{-1} \quad . \qquad (2\text{-}34)$$

Table 2-6 compares the various values for $A_{0\to v''}$ and $\sigma_s(hc/\lambda_{0\to v''})$ computed using the transition moment functions of Hay and Dunning [46], and of Tamagake et al.[81]. These values are normalized with respect to the theoretical lifetime of the B(v'=0) level ($\tau_{v'=0}$=11 ns [46]). For

Table 2-6

Calculated values of Einstein A coefficients, oscillator strengths and stimulated-emission cross-sections for the B(v'=0) to X(v"=0-22) transitions in XeCl. The values in the first column of each parameter represent, in order, results obtained by employing the Franck-Condon approximation, the transition moment function of Hay and Dunning [46], and the three moment functions B, C and D of Tamagake et al.[81]. The second column gives the corresponding values obtained when the equilibrium locations of the potential curves are increased by 0.213 Å. All calculated values are normalized according to the radiative lifetime of $\tau(v'=0)=11$ ns [46].

V2	EINSTEIN A COEFFICIENT (/S)		OSCILLATOR STRENGTH		STIMULATED-EMISSION CROSS-SECTION (10**(-16) CM**2)	
0	1.004E+07	9.664E+06	1.425E-02	1.372E-02	5.027E-01	4.840E-01
	9.962E+06	9.631E+06	1.414E-02	1.367E-02	4.770E-01	4.457E-01
	1.070E+07		1.519E-02		5.508E-01	
	9.866E+06		1.401E-02		4.675E-01	
	9.506E+06		1.350E-02		4.335E-01	
1	2.085E+07	2.032E+07	2.965E-02	2.890E-02	2.162E+00	2.107E+00
	2.070E+07	2.025E+07	2.944E-02	2.880E-02	2.086E+00	1.995E+00
	2.166E+07		3.080E-02		2.286E+00	
	2.057E+07		2.926E-02		2.058E+00	
	2.009E+07		2.857E-02		1.960E+00	
2	2.288E+07	2.263E+07	3.259E-02	3.223E-02	2.653E+00	2.624E+00
	2.274E+07	2.255E+07	3.239E-02	3.213E-02	2.610E+00	2.566E+00
	2.307E+07		3.286E-02		2.689E+00	
	2.268E+07		3.232E-02		2.595E+00	
	2.249E+07		3.204E-02		2.548E+00	
3	1.765E+07	1.779E+07	2.519E-02	2.538E-02	1.633E+00	1.645E+00
	1.758E+07	1.774E+07	2.509E-02	2.531E-02	1.644E+00	1.672E+00
	1.719E+07		2.452E-02		1.572E+00	
	1.763E+07		2.515E-02		1.650E+00	
	1.779E+07		2.539E-02		1.680E+00	
4	1.057E+07	1.092E+07	1.511E-02	1.561E-02	6.110E-01	6.314E-01
	1.058E+07	1.091E+07	1.512E-02	1.560E-02	6.341E-01	6.743E-01
	9.856E+06		1.409E-02		5.509E-01	
	1.067E+07		1.525E-02		6.442E-01	
	1.101E+07		1.573E-02		6.853E-01	
5	5.038E+06	5.408E+06	7.210E-03	7.740E-03	1.460E-01	1.567E-01
	5.102E+06	5.428E+06	7.301E-03	7.769E-03	1.586E-01	1.795E-01
	4.438E+06		6.351E-03		1.202E-01	
	5.185E+06		7.421E-03		1.637E-01	
	5.514E+06		7.891E-03		1.849E-01	
6	1.822E+06	2.099E+06	2.612E-03	3.009E-03	2.039E-02	2.349E-02
	1.915E+06	2.143E+06	2.744E-03	3.071E-03	2.425E-02	3.036E-02
	1.484E+06		2.127E-03		1.458E-02	
	1.970E+06		2.823E-03		2.565E-02	
	2.195E+06		3.146E-03		3.181E-02	
7	3.816E+05	5.329E+05	5.476E-04	7.647E-04	1.052E-03	1.469E-03
	4.829E+05	6.807E+05	6.930E-04	8.619E-04	1.689E-03	2.612E-03
	2.856E+05		4.098E-04		5.915E-04	
	5.094E+05		7.309E-04		1.877E-03	
	6.234E+05		8.945E-04		2.809E-03	

(CONTINUED)

V2	EINSTEIN A COEFFICIENT (/S)		OSCILLATOR STRENGTH		STIMULATED-EMISSION CROSS-SECTION (10xx(-16) CMxx2)	
8	1.517E+03	3.409E+03	2.180E-06	4.897E-06	2.025E-07	4.549E-07
	3.865E+04	7.334E+04	5.552E-05	1.053E-04	1.195E-05	4.302E-05
	2.719E+03		3.906E-06		5.924E-08	
	4.528E+04		6.504E-05		1.639E-05	
	7.897E+04		1.134E-04		4.981E-05	
9	7.967E+03	6.851E+03	1.146E-05	9.851E-06	2.647E-06	2.276E-06
	1.907E+04	5.307E+03	2.742E-05	7.631E-06	3.248E-06	2.514E-07
	6.833E+04		9.825E-05		4.174E-05	
	1.565E+04		2.251E-05		2.186E-06	
	4.491E+03		6.458E-06		1.798E-07	
10	9.478E+04	7.724E+04	1.364E-04	1.112E-04	1.422E-04	1.159E-04
	1.182E+05	8.338E+04	1.702E-04	1.200E-04	1.408E-04	7.000E-05
	1.978E+05		2.847E-04		3.946E-04	
	1.116E+05		1.607E-04		1.254E-04	
	8.226E+04		1.184E-04		6.802E-05	
11	1.880E+05	1.632E+05	2.708E-04	2.351E-04	5.187E-04	4.504E-04
	2.103E+05	1.706E+05	3.029E-04	2.457E-04	5.086E-04	3.345E-04
	2.908E+05		4.188E-04		9.736E-04	
	2.040E+05		2.939E-04		4.783E-04	
	1.715E+05		2.470E-04		3.377E-04	
12	2.393E+05	2.151E+05	3.450E-04	3.100E-04	8.948E-04	8.041E-04
	2.577E+05	2.217E+05	3.715E-04	3.195E-04	8.850E-04	6.547E-04
	3.254E+05		4.691E-04		1.413E-03	
	2.532E+05		3.649E-04		8.535E-04	
	2.249E+05		3.241E-04		6.726E-04	
13	2.497E+05	2.295E+05	3.602E-04	3.310E-04	1.097E-03	1.008E-03
	2.642E+05	2.349E+05	3.811E-04	3.388E-04	1.097E-03	8.667E-04
	3.160E+05		4.557E-04		1.570E-03	
	2.616E+05		3.773E-04		1.074E-03	
	2.397E+05		3.457E-04		9.005E-04	
14	2.322E+05	2.167E+05	3.350E-04	3.127E-04	1.109E-03	1.035E-03
	2.433E+05	2.210E+05	3.511E-04	3.190E-04	1.119E-03	9.232E-04
	2.805E+05		4.047E-04		1.489E-03	
	2.422E+05		3.494E-04		1.107E-03	
	2.264E+05		3.267E-04		9.671E-04	
15	1.994E+05	1.883E+05	2.878E-04	2.718E-04	9.912E-04	9.361E-04
	2.079E+05	1.916E+05	3.001E-04	2.766E-04	1.009E-03	8.571E-04
	2.333E+05		3.369E-04		1.273E-03	
	2.076E+05		2.997E-04		1.006E-03	
	1.969E+05		2.842E-04		9.033E-04	

(CONTINUED)

V2	EINSTEIN A COEFFICIENT (/S)		OSCILLATOR STRENGTH		STIMULATED-EMISSION CROSS-SECTION (10xx(-16)*CMxx2)	
16	1.607E+05	1.531E+05	2.321E-04	2.211E-04	8.116E-04	7.731E-04
	1.670E+05	1.556E+05	2.411E-04	2.247E-04	8.315E-04	7.216E-04
	1.839E+05		2.656E-04		1.010E-03	
	1.673E+05		2.415E-04		8.338E-04	
	1.602E+05		2.314E-04		7.641E-04	
17	1.218E+05	1.168E+05	1.759E-04	1.687E-04	6.172E-04	5.917E-04
	1.263E+05	1.186E+05	1.824E-04	1.713E-04	6.357E-04	5.601E-04
	1.372E+05		1.982E-04		7.509E-04	
	1.268E+05		1.831E-04		6.401E-04	
	1.223E+05		1.767E-04		5.952E-04	
18	8.596E+04	8.280E+04	1.242E-04	1.196E-04	4.346E-04	4.186E-04
	8.903E+04	8.402E+04	1.286E-04	1.214E-04	4.494E-04	4.002E-04
	9.576E+04		1.383E-04		5.206E-04	
	8.950E+04		1.293E-04		4.539E-04	
	8.679E+04		1.254E-04		4.263E-04	
19	5.496E+04	5.310E+04	7.942E-05	7.672E-05	2.770E-04	2.676E-04
	5.689E+04	5.387E+04	8.219E-05	7.784E-05	2.871E-04	2.575E-04
	6.080E+04		8.784E-05		3.284E-04	
	5.725E+04		8.271E-05		2.906E-04	
	5.569E+04		8.047E-05		2.747E-04	
20	2.991E+04	2.895E+04	4.322E-05	4.183E-05	1.503E-04	1.455E-04
	3.095E+04	2.937E+04	4.471E-05	4.243E-05	1.561E-04	1.405E-04
	3.295E+04		4.761E-05		1.772E-04	
	3.116E+04		4.502E-05		1.581E-04	
	3.037E+04		4.389E-05		1.501E-04	
21	1.172E+04	1.135E+04	1.693E-05	1.640E-05	5.880E-05	5.696E-05
	1.212E+04	1.151E+04	1.751E-05	1.664E-05	6.111E-05	5.512E-05
	1.288E+04		1.861E-05		6.911E-05	
	1.221E+04		1.764E-05		6.195E-05	
	1.191E+04		1.721E-05		5.891E-05	
22	1.497E+03	1.450E+03	2.163E-06	2.096E-06	7.590E-06	7.354E-06
	1.548E+03	1.471E+03	2.237E-06	2.125E-06	7.890E-06	7.121E-06
	1.644E+03		2.376E-06		8.914E-06	
	1.559E+03		2.253E-06		7.999E-06	
	1.522E+03		2.199E-06		7.611E-06	

the two strongest emission bands (0-1 and 0-2), the differences in estimating the stimulated-emission cross-sections are within ±6.4% and ±2.5%, respectively. It may be noted that the cross-sections calculated using the r-centroid approximation are close to the average values.

The oscillator strength associated with a v'→v" spectral line (the Ladenburg f-value), is defined in terms of the Einstein transition probability coefficient $A_{v'\to v"}$ by the expression

$$f_{v'\to v"} = - \frac{mc\lambda^2_{v'\to v"}}{8\pi^2 e^2} A_{v'\to v"} \quad , \qquad (2\text{-}35)$$

where m and c are the electron mass and the velocity of light, respectively. Unlike the ECF, which in strictly theoretical, the dimensionless f-values can be measured using standard spectroscopic techniques for determining transition probabilities. Moreover, these values are particularly useful in evaluating superelastic or excitation rate constants (Chapter 4). The f-values of all v'=0→v" transitions between the electronic B and X states of XeCl, determined using previously computed values of $A_{0\to v"}$, are shown in Table 2-6.

2.5 Experimental Observation of the B → X Emission Spectra

Spontaneous and stimulated emissions of the XeCl B → X system were generated by a pulsed discharge in a multi-atmospheric, UV-preionized gas mixture consisting of helium (high purity), together with substantially smaller quantities of xenon (certified purity) and hydrogen chloride (certified standard). The experimental chamber was constructed primarily of Lucite and equipped with fused-silicia end

windows. Each electrode had an active discharge cross-section of ~0.64 x 50 cm^2 and the electrode spacing was adjustable to a maximum of 2.60 cm. Typically, the device, described in detail in Chapter 3, was capable of discharge current pulses of 100-ns duration (FWHM) at charging voltages to 35 kV and peak currents to 30 kA. Most experiments were performed using a cavity consisting of an external plane 98% reflector and the opposite window as the output coupler. In most cases, however, lasing could easily be achieved without the use of the external mirror (the windows only formed the resonant cavity).

The spectra were obtained by focusing the radiation, with a 5-cm focal-length quartz lens, at the 10-μm wide entrance slit of a 3/4-m Czerny-Turner spectrometer (SPEX model 1500.DP) containing a 1200-lines/mm diffraction grating blazed at 300 nm (Bausch and Lomb model 35-53-15-030). Working at the first order of diffraction, the instrument had a plate factor of 1.016 nm/mm and a resolution of better than 0.01 nm in the region of 308 nm. Spectra were recorded on high contrast, fine grain, orthochromatic film (Kodak 4154) with a thick estar base, and traced by an automatic double-beam recording micro-densitometer (Joyce model MK III c), operating at x50 magnification. A single laser pulse was more than sufficient to expose the film (radiation was usually attenuated). However, for recording spontaneous emission, ten shots were generally needed to provide sufficient exposure.

Wavelengths were calibrated by use of radiation from a standard iron-neon hollow-cathode lamp (Cathodeon Type 30NY/Fe in Ne). A

Fig. 2-14

Stimulated and spontaneous emission spectrograms of the B → X transition, using a He/2.5% Xe/0.3% HCl mixture at 1665-Torr pressure and an electrode spacing of 2.60 cm. The optical cavity consists of an external 98% reflectance mirror and the front window as the output coupler.
(a) Stimulated emission spectrum recorded for operation above threshold (30 kV charging voltage). (b) Spontaneous emission spectrum recorded for operation below threshold (15 kV charging voltage). (c) Emission spectrum from a Fe-Ne hollow cathode lamp.

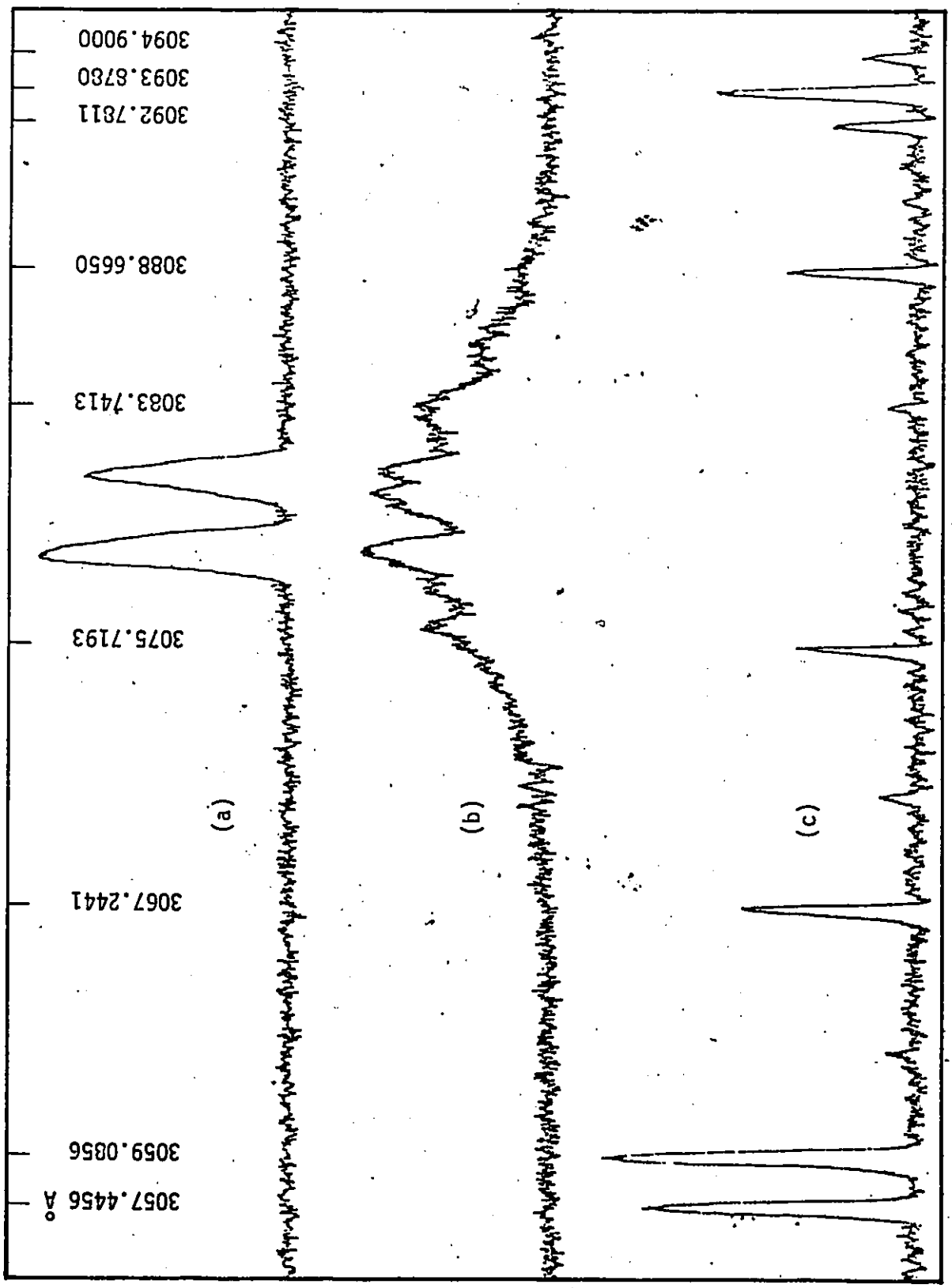
3094.9000
3093.8760
3092.7811
3088.6650
3083.7413
3075.7193
3067.2441
3059.0856
3057.4456 Å
(a)
(b)
(c)

Fig. 2-15

Stimulated emission spectrogram of the B → X transition, using the same operating conditions as employed for Fig.2-14(a), but without an external reflector. The cavity reflectors are the two fused-silica windows.

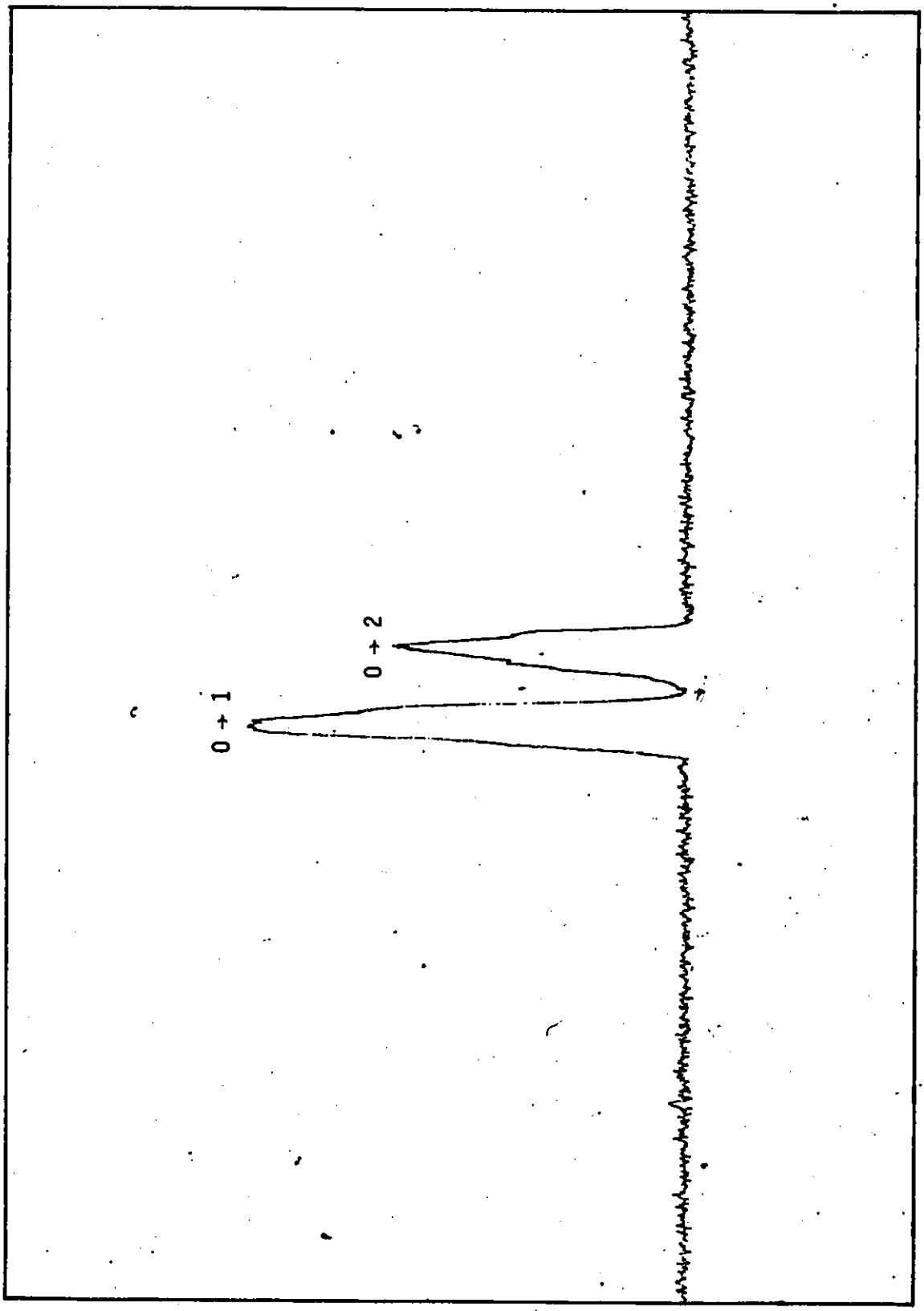
0 + 2
0 + 1

Fig. 2-16

Stimulated emission spectrogram of the B → X transition, using a He/2.5% Xe/0.3% HCl mixture at 1794-Torr pressure and an electrode spacing of 2.29 cm. The optical cavity consists of an external 98% reflectance mirror and the front window as the output coupler.

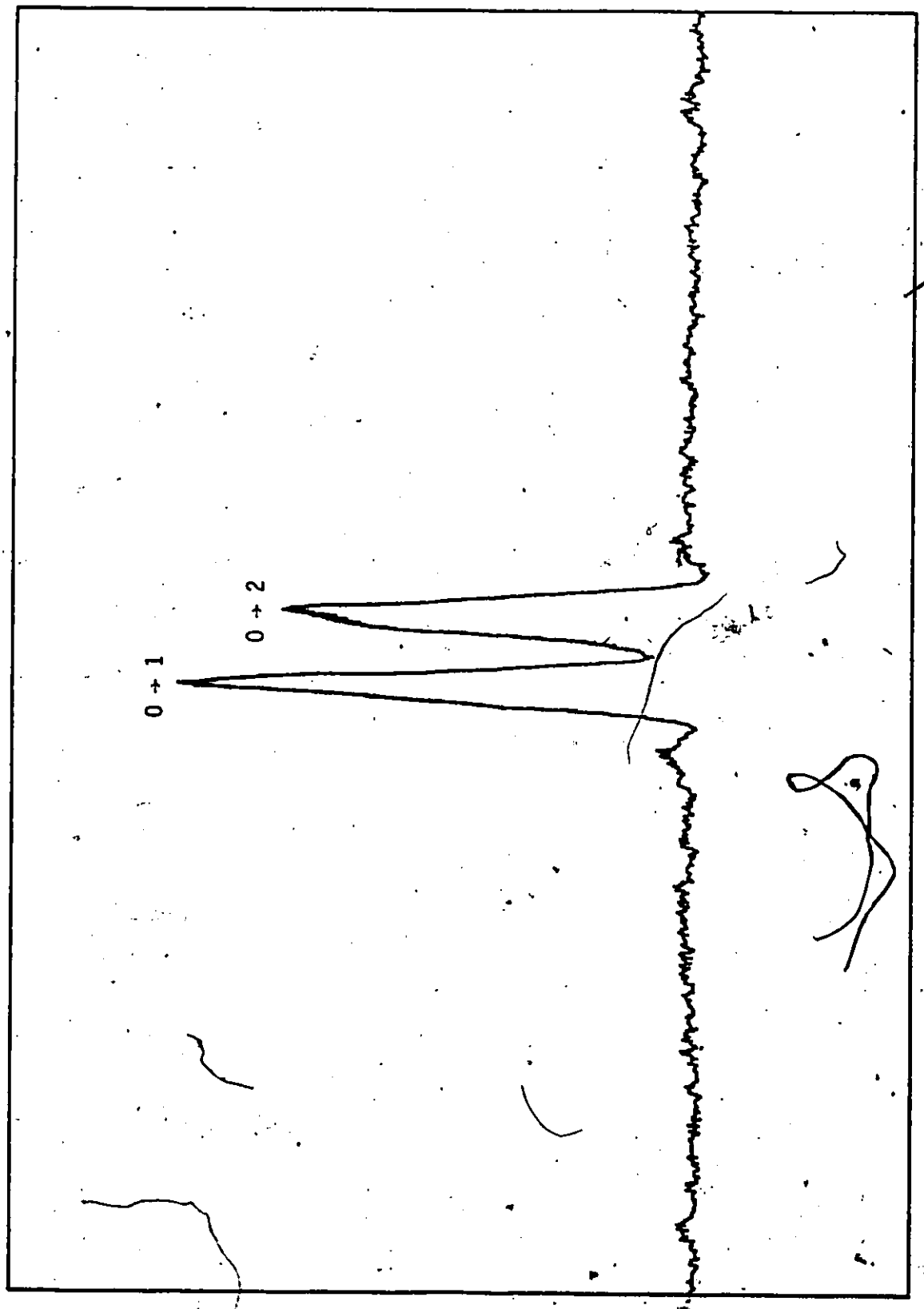
0 + 2
0 + 1

ten-minute exposure was generally adequate. Special care was taken to ensure minimum perturbation of the equipment during measurements, especially the position of the film in the film holder.

Figure 2-14 shows typical stimulated and spontaneous emission spectra recorded for a 1665-Torr mixture of He/2.5% Xe/0.3% HCl using an electrode spacing of 2.60 cm. Operation was above threshold (30 kV charging voltage; threshold at 17 kV) and below threshold (15 kV) in (a) and (b), respectively. By comparison, the lasing (above threshold) spectrum in Fig.2-15 was obtained under the same conditions as Fig.2-14(a), except that the external 98% reflectance mirror was removed. In both cases, the stimulated emission spectra are very similar, with the 0-1 and 0-2 transitions, centred at λ_{air} = 307.937 ± 0.010 nm and 308.175 ± 0.010 nm, clearly present. The spontaneous emission spectrum reveals more structure. In particular, the strong band at λ_{air} = 308.109 ± 0.010 nm, close to the 0-2 transition, has not been identified. The effect of spectral narrowing in going from below threshold to above threshold is evident. In addition, amplification only occurs on the 0-1 and 0-2 transitions. At higher pressures, the much weaker 0-0 and 0-3 bands are suspected to be present. These can just be seen in Fig.2-16, which shows the spectrum observed for the same mixture and charging voltage as above, but at 1794-Torr pressure and a reduced electrode spacing of 2.29 cm. Contrary to theoretical FCF predictions and to some published spectra in the literature [30,32], the 0-1 emission is stronger than the 0-2 emission. Our spectra are very similar to those observed by Fontaine

and Forestier [83], by Maeda et al.[84], and by Ishchenko et al.[33] (the 0-0 and 0-3 transitions are clearly evident in the latter two cases). A satisfactory explanation for these observations has not yet been given[¶¶]. However, consideration of the spontaneous emission spectrum in Fig.2-14(b) and the FCF for the B → X band indicates that the 0-2 transition may be more absorptive than the 0-1 transition.

On the basis of the measured emission wavelengths, the B state is shifted to provide agreement between the observed and calculated values. The ionic limit is found to be 68668.0 cm^{-1} (as shown in Table 2-3). Subtracting from this the ionization potential of Xe (97834.4 cm^{-1} [74]), the electron affinity of Cl is 3.616 eV, in close agreement with the most reliable published value of 3.615 eV [78].

The effective cross-section for the B → X stimulated emission can be determined by weighting the contributions from all coherent emitting lines over their cross-section values. These contributions are appraised using a recorded stimulated-emission spectrum from a laser. Using the transition moment functions of Hay and Dunning [46], and of Tamagake et al.[81], we estimate that the effective cross-section is in

---

[¶¶]It is interesting to note that the stimulated-emission cross-section for the 0-1 transition can only be larger than that for the 0-2 transition if the width of the electronic transition moment is less than 0.2 Å, and if the peak lies at an internuclear separation of ∿3.1 Å. Such a rapidly varying transition moment function has not been reported in the literature, including Refs.[46] and [81], which refer to the XeCl system. The gain on the 0-1 transition is higher than that on the 0-2 transition. Therefore, it is probable that the ground-state molecules in the v"=1 level are depleted faster than those in v"=2 level.

the range 2.23-2.47 $\mathring{A}^2$, with an average value of 2.35 $\mathring{A}^2$. Note that this average value agrees well with our early kinetic model estimates of 2.3 $\mathring{A}^2$ and 2.4 $\mathring{A}^2$, and is in reasonable agreement with the values of 2.5 $\mathring{A}^2$ obtained independently by Levin et al. [85] from kinetic modelling, and 2.6 $\mathring{A}^2$ measured recently by Corkum and Taylor [86] using a saturating picosecond pulse. All these values, however, deviate significantly from the estimate of 4.5 $\mathring{A}^2$ by Brau [87], who employs a saturation parameter of $\overline{\sigma_s \tau}$ = 50 $\mathring{A}^2$-ns and τ = 11 ns.

2.6 The Rydberg States and Their Relation to Exciplex Formation

By analogy with the large rate constant for the $Xe(^3P_2)$ and Cl_2 "harpooning" reaction

$$Xe(^3P_2) + Cl_2 \longrightarrow Xe^+ \cdots Cl^- \cdot Cl \longrightarrow XeCl^* + Cl \ , \qquad (2\text{-}36)$$

the strong B → X lasing, which occurs when using HCl as the halogen donor, has been attributed to the efficient formation of XeCl(B) via the "harpooning" mechanism [87,88]

$$Xe(^3P_2) + HCl \longrightarrow Xe^+ \cdots Cl^- \cdot H \longrightarrow XeCl^* + H \ . \qquad (2\text{-}37)$$

However, in reality, the reaction cross-section is very small because the vertical electron affinity (measured at the crossing location of the ground-state and the dissociative attachment P.E. curves) of HCl is negative (E_a^v (HCl) = -0.78 eV [89]). Consequently, Reaction (2-37) is endothermic and not energetically allowed [90] since the energy possessed by the excited xenon atom (8.315 eV) is insufficient

to dissociate the HCl molecule (D_e = 4.62 eV) and to form the exciplex $XeCl^*$ (the first vibrational level of the excimer state relative to the ground-state separate atom limit is 3.795 eV). Indeed, Kolts et al.[38] have measured the rate coefficient of Reaction (2-37) to be less than 10^{-11} cm^3/s, which is too insignificant to account for the large population of the excimer state.

From basic theoretical considerations, the excitation in Xe of a 5p orbital electron to the 6s orbital gives rise to four atomic states. Three of these states associate with the spectroscopic term ^3P, and one with the ^1P. The 5p-subshell of the excited xenon atom is more than half-filled; therefore, the term with the largest value of total angular momentum (viz., J=2) has the lowest energy. For a Cl atom, however, the two lowest energy levels (in ascending order) are $^2P_{3/2}$ and $^2P_{1/2}$. On the basis of the Wigner-Witmer correlation rules [91], the combination of a ^3P xenon atom and a ^2P chlorine atom gives rise to six doublet (three $^2\Sigma$, two $^2\Pi$ and one $^2\Delta$) and six quadruplet (three $^4\Sigma$, two $^4\Pi$ and one $^4\Delta$) molecular terms. Of these allowed terms, the states $^4\Delta_{7/2,5/2,3/2,1/2}$, $^4\Pi_{5/2,3/2,1/2}$ and $^4\Sigma^+_{3/2,1/2}$ correlate with the separated-atom state $Xe(^3P_2)+Cl(^2P_{3/2})$, and the states $^4\Pi_{-1/2}$, $^4\Sigma^-_{1/2}$, $^2\Delta_{5/2,3/2}$ and $^2\Pi_{3/2,1/2}$ correlate with the state $Xe(^3P_1)+Cl(^2P_{3/2})$. The separated-atom limits of these two lowest Rydberg states are 8.315 eV and 8.437 eV above the $Xe(^1S_0)+Cl(^2P_{3/2})$ ground level, respectively. As both of these limits lie slightly below the ionic limit of $Xe^+(^3P_2)+Cl^-(^1S_0)$ (8.512 eV), pseudo-crossings of the Rydberg states and the excimer curve are expected to occur at large r. Using the excimer potential function for the B state (Section 2.3), the crossing radii of the P.E. curves are ~73 Å and ~187 Å. These contribute large rate constants to

the "harpooning" processes

$$Xe(^3P_2) \cdot Cl(^2P_{3/2}) \longrightarrow Xe^+ \cdot Cl^-(B) , \qquad (2\text{-}38a)$$

and $$Xe(^3P_1) \cdot Cl(^2P_{3/2}) \longrightarrow Xe^+ \cdot Cl^-(B) . \qquad (2\text{-}38b)$$

In the electron jump model, either of these processes corresponds to the transition of a molecular state, in the vicinity of a crossing, from dominantly covalent outside (larger r) to dominantly ionic inside (smaller r), and represents the jump of an electron from $Xe(^3P_2$ or $^3P_1)$ to Cl. This model suggests an efficient mechanism leading to the formation of the XeCl exciplex. However, it also indicates the loss mechanism due to predissociation of the exciplex formed from the ionic channel. As the products of the dissociation are the elementary atoms of the Rydberg molecule themselves, the exciplex can be regenerated. The loss channel, therefore, is effectively a delay for populating the excimer state. The situation for the XeCl exciplex system is illustrated in Fig.2-17, and can be summarized in the following scheme:

$$Xe^+ + Cl^- \left\{ \begin{array}{l} \longrightarrow \\ \longrightarrow Xe(^3P_1) + Cl \left\{ \begin{array}{l} \longrightarrow \\ \longrightarrow Xe(^3P_2) + Cl \longrightarrow \end{array} \right. \\ \longrightarrow Xe(^3P_2) + Cl \longrightarrow \end{array} \right\} XeCl^* . \qquad (2\text{-}39)$$

It may also be mentioned that the ionic recombination of Xe^+ and Cl^-, and the "harpooning" processes involving $Xe(^3P_2$ and $^3P_1)$ and Cl, proceed more favourably in the presence of a third body than in bimolecular reactions. This results from efficient energy transfer via the collision with a light body (e.g., helium).

Fig. 2-17

A schematic potential energy diagram of XeCl showing the formation channels of the XeCl(B) exciplex. These channels include the ionic recombination of $Xe^+(^3P_2) + Cl^-(^1S_0)$, and the "harpooning" processes due to $Xe(^3P_1) + Cl(^2P_{3/2})$ and to $Xe(^3P_2) + Cl(^2P_{3/2})$. The exciplex species formed via the ionic channel also predissociate into excited Xe and ground-state Cl stoms, which later recombine to supplement the exciplex formation. The various transformations are indicated by the arrows shown in the diagram.

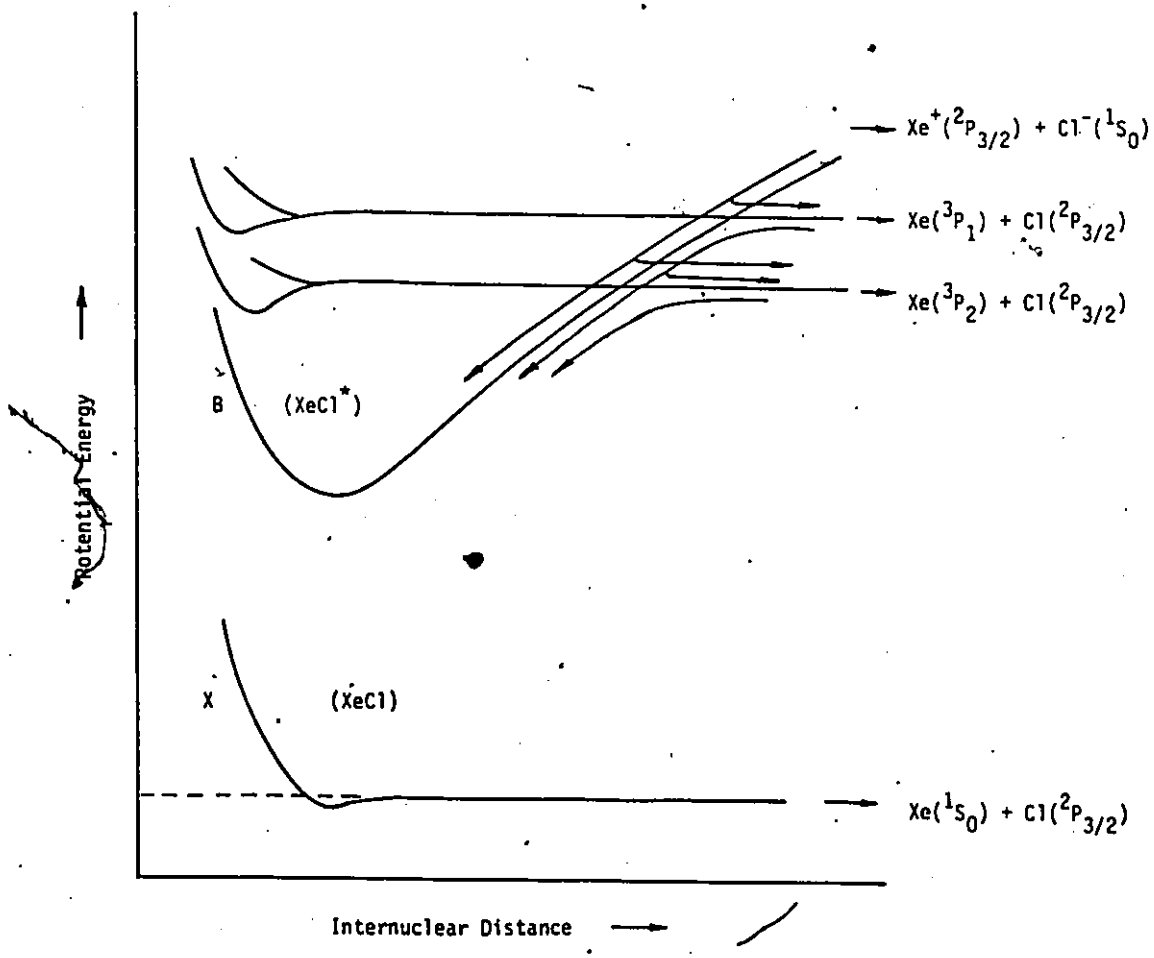
$Xe^+(^2P_{3/2}) + Cl^-(^1S_0)$
$Xe(^3P_1) + Cl(^2P_{3/2})$
$Xe(^3P_2) + Cl(^2P_{3/2})$
B
$(XeCl^*)$
Potential Energy
X
(XeCl)
$Xe(^1S_0) + Cl(^2P_{3/2})$
Internuclear Distance

2.7 Summary

In studying the molecular structure of XeCl, we have made use of potential functions to describe the ground and excimer states. These functions are derived from the empirical data of Sur et al. [44], who have spectroscopically analyzed the B → X and D → X electronic transitions. It should be noted that their complex spectrum has not been completely analyzed. Only a quantitative evaluation on the vibrational levels of the B, D and X states has been carried out, because the locations of the bandheads are difficult to measure. Characteristically the excimer B and D states are ionic and best represented by Rittner-type potential functions. The weakly-bound ground state can be fitted by a logarithmic-type van der Waals potential function which also demonstrates the superharmonicity exhibited by the ground-state molecule.

Results from Franck-Condon calculations are used to characterize the B → X emission spectrum, and to evaluate the associated parameters, namely, the radiative lifetime of the transition and the cross-sections for the stimulated emission and absorption. These calculations predict that the 0 → 2 vibrational band of the B → X transition is strongest. However, we observed the strongest emission from the 0-1 vibrational band. This may be attributed to the self-absorption of the excimer state and the photoabsorption in the discharge medium, predominantly on the 0-2 band.

We have also investigated the "harpooning" processes which arise from the pseudo-crossing of the two lowest Rydberg states and the excimer B curve. They are thought to influence the exciplex formation by acting as supplementary channels, and by delaying the exciplex formed by the ionic recombination from relaxing to the lowest vibrational (emitting) level.

CHAPTER 3

AN AVALANCHE DISCHARGE LASER SYSTEM

3.1 Introduction

Currently, three major discharge systems are employed for exciting rare-gas and halide (or halogen) mixtures. These are the high-intensity electron-beam excitation system, the e-beam sustained discharge system and the avalanche discharge system. For the research reported in this thesis, our preference is for the avalanche discharge system, for reasons outlined below.

An electron-beam system can deliver a large amount of pulsed energy uniformly into a gas medium. However, the system is large and expensive, and is incapable of being driven at high repetition rates. Such systems are necessary for the rare-gas excimers, which, because of their small stimulated-emission cross-sections, must be excited by intense electron-beams operating at dense gas pressures. In contrast, the rare-gas halides require much reduced discharge-input power densities since they have larger stimulated-emission cross-sections resulting from narrower spectral bandwidths and longer emission wavelengths. In addition, the kinetics in a rare-gas and halide (or halogen) mixture favours operation at moderate pressures (few atmospheres). Consequently, the stopping power of the gas medium for energetic electrons is reduced. Any excessive e-beam excitation produces thermal energy together with reduced efficiency.

The photoionized avalanche discharge technique, which has been successfully employed in high-power, multi-atmospheric CO_2 and other gas lasers, is considerably simpler. Although the output energies are usually limited to below a few joules[¶], avalanche discharge systems are efficient, compact, economical and readily adaptable for operation at high pulse-to-pulse rates.. Consequently, these systems are preferred to either the e-beam or the e-beam stabilized discharge systems. Initial RGH exciplex lasers were demonstrated with e-beam pumping techniques [13,16]. However, subsequent experiments were largely carried out on electric avalanche devices using various discharge methods, such as low-inductance capacitor dumping [21], Blumlein (transmission line) excitation [20,93], lumped pulse forming networks [94], and charged coaxial cables [95].

This chapter deals with our investigations into the operation of a multi-atmospheric, photoionized, transversely-excited laser system using a standard discrete-capacitor discharge technique. The chapter is divided into two parts. In Section 3.2, the design and construction of the laser system are detailed, with specific reference to the electrical circuits, the system configuration, the mechanical and optical components, and the gas-handling facilities. Section 3.3 describes the overall performance of the laser system using a range of gas mixtures and pressures, and employing a range of discharge conditions (e.g., charging voltage and electrode spacing).

[¶]Recently, Watanabe and Endoh [92] achieved an output energy of 13.8 J from a wide-aperture UV-preionized XeCl laser.

3.2 Development of a Photoionized, Avalanche Discharge Laser System

A simple, unsustained avalanche discharge is inherently unstable. Under conditions of high energy deposition and high gas pressure ($\geq$ 1 atm), electrons multiply very rapidly as they are accelerated across the electrode gap. The discharge becomes unstable as the plasma impedance collapses. Consequently, electrons useful for inelastic collisions are concentrated in highly conducting filamentary channels (arcs) so that excitation elsewhere is reduced. These arcs are usually localized in regions where the electric field is the highest or where the gas density is nonuniform. Since arcing is detrimental to system efficiency and causes damage to electrodes, it is necessary to precondition the gas medium before most of the electrical power is deposited in the plasma. Volumetric preionization of the discharge region by "hard" ultraviolet radiation provides "seed" electrons which balance spatial electron losses due to localized hot spots. Such preionization is particularly essential in exciting a RGH gas mixture in which the halide (or halogen) is electrophilic, because photoelectrons must also be created to supplement the loss due to electron attachment. A laser system incorporating the photoionization scheme was constructed and used for investigations of the XeCl exciplex system. The laser discharge circuit is presented in the next section, which is followed by a description of the system construction.

3.2.1 Electrical Circuitry

The commom capacitor impulse discharge scheme, as used by Andrews et al. [96] has been adopted in our laser system. The discharge circuit,

shown in Fig.3-1, has the merit of simplicity in both construction and operation. A single high-voltage dc power supply is required for charging simultaneously the main storage capacitor C_s and the preionizer capacitor C_p. The capacitors are charged through the current limiting resistor R and the grounding resistors R_s and R_p. A nitrogen-pressurized spark gap [97] (described in Section 3-3) is used for "switching" both C_s and C_p in order to minimize timing problems. Jitter can be introduced if the preionizer and the main discharge are switched separately, with resulting deterioration of shot-to-shot reproducibility of the output laser pulse.

Energetic ultraviolet photons are emitted from two sets of sliding-spark arrays as a result of discharging capacitor C_p. These arrays are mounted parallel to, and in the mid-plane between, the electrodes, and located symmetrically (distance adjustable from 3-5 cm) about the axis of the main discharge region. The circuit inductance L_p in the preionizer circuit is primarily due to a pair of 0.9-m long braided wires (Beldon 8669) connecting the preionizers to capacitor C_p. From the measured current in the preionizer branch, L_p is estimated to be $\sim$0.57 μH. Because of the low impedance associated with the sliding-spark arrays, photoionization follows the conduction in the circuit with negligible delay (< 10 ns). The energy stored in capacitor C_s (maximum $\sim$60 J) is first transferred to sixteen ceramic "doorknob" capacitors connected in parallel to form the "voltage-peaking" capacitor C. The energy is subsequently deposited into the gas medium, but after a time delay in the range 205-315 ns, which depends on the gas mixture and

Fig. 3-1

Discharge circuit. In our system HV was adjustable (Universal Voltronics BAL-130-14); C_s=0.1 μF, 50 kV (Condenser Products EB 104-50M); C_p=0.05 μF, 50 kV (Condenser Products CP 503-50MXX-3); C=43.2 nF, 40 kV (16 x Murata 909A); R=3 MΩ (20 x 150 kΩ, 50 W), R_s=R_p=27 kΩ (100 x 270 Ω, 1/2 W); L, L_s, L_p represent the circuit inductances, and SG the triggered spark gap.

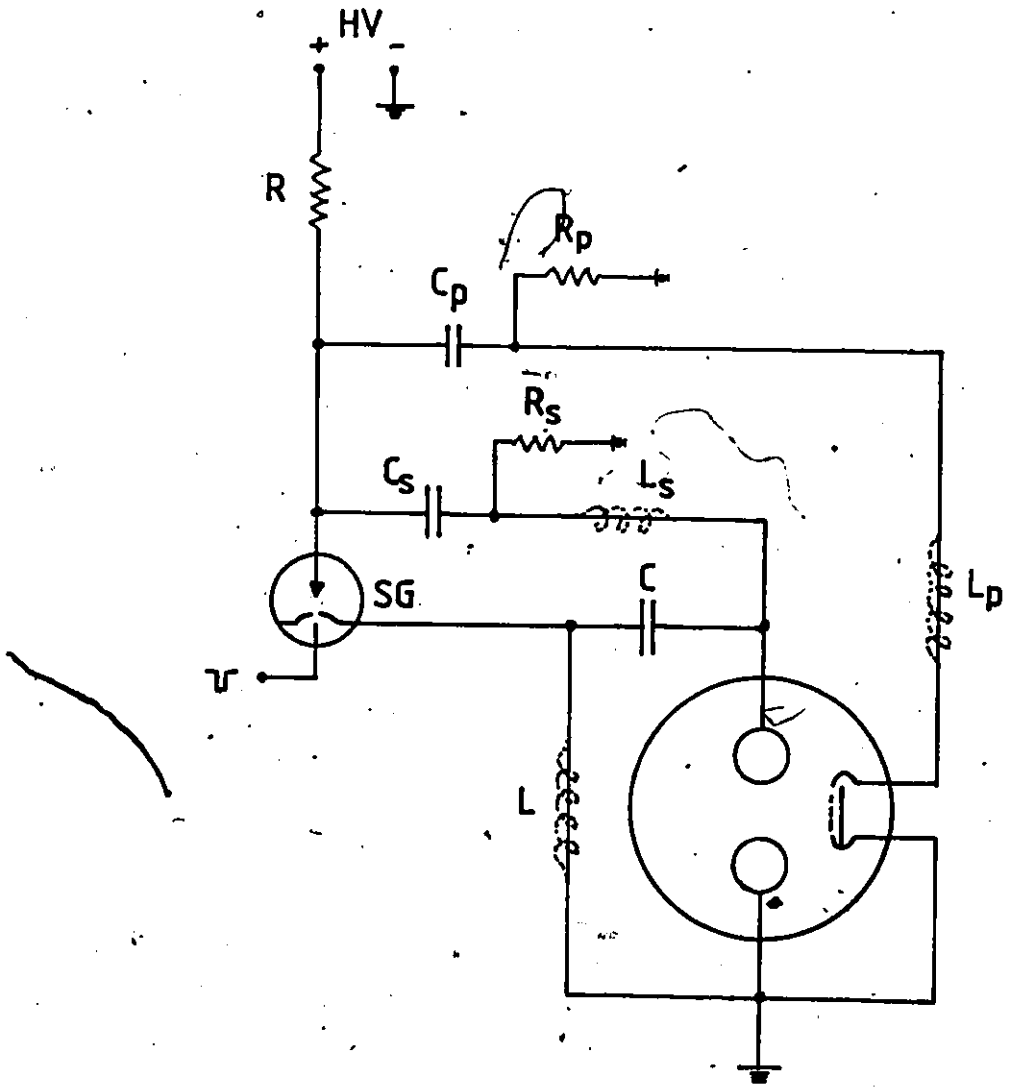
HV
+
−
R
R_p
C_p
R_s
C_s
L_s
SG
C
L_p
L

pressure, the electrode separation and the applied voltage. It should be noted that the ceramic capacitors are not located inside the discharge chamber and close to the electrodes, as done in Ref.[96]. Instead, they are mounted externally, and use the supporting structure to increase the circuital inductance L in order to broaden the discharge current pulse.

The nitrogen-pressurized spark gap is triggered externally by a positive high-voltage pulse. A schematic diagram of the trigger system, including the associated instrumentation, is shown in Fig.3-2(a). The trigger pulse is generated by a simple, inexpensive and very reliable trigger unit employing an automobile ignition coil, as shown in Fig.3-2(b). The circuit is based on the design of Loy and Roland [98], which was originally used to generate negative high-voltage pulses. We produce positive pulses by inverting the polarity of the SCR (2N688). Approximately 2-V amplitude, 50-μs duration pulses are fed via the unity-ratio pulse transformer (Hammond 612G) to turn on the SCR. The ignition coil (Delco D523) is mounted directly on top of an automobile spark plug which provides the trigger electrode for the spark gap. A peak-to-peak voltage (actually a damped oscillation with period 0.2 ms) of ~34 kV is achievable with HV = 100 V.

The pulse generator in Fig.3-3, similar in design to that in Ref.[99], has variable time-delay and repetition rate, and was originally designed for use with two trigger units and spark gaps. The clock section is an astable multivibrator running at any selected frequency between 0.2 Hz and 10 Hz. The +2V output pulses from the generator, or alternatively external +2V pulses, are used to trigger the pulse-processing unit, which produces two sets of output pulses

Fig. 3-2

High-voltage trigger system.

A. Block diagram.

B. Electrical circuit of the trigger unit. A typical output voltage-pulse is shown in the oscillogram.

(a)

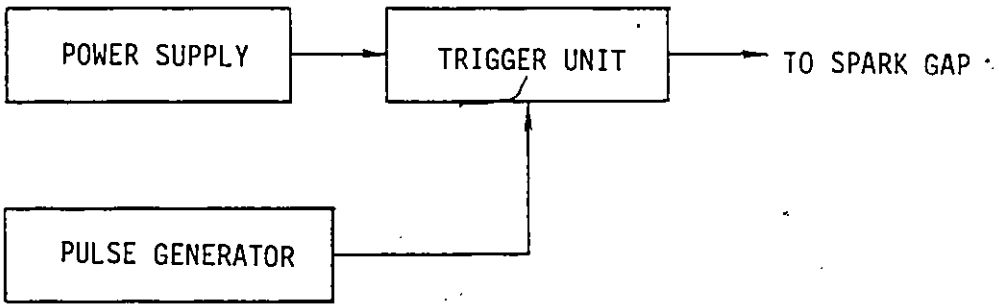
POWER SUPPLY
TRIGGER UNIT
TO SPARK GAP
PULSE GENERATOR

(b)

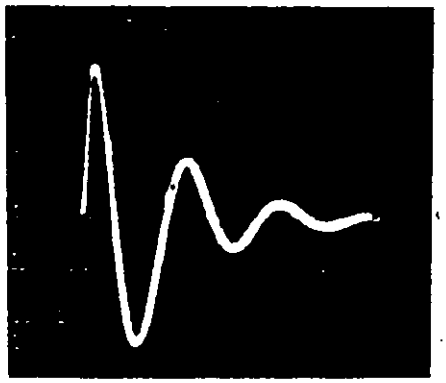

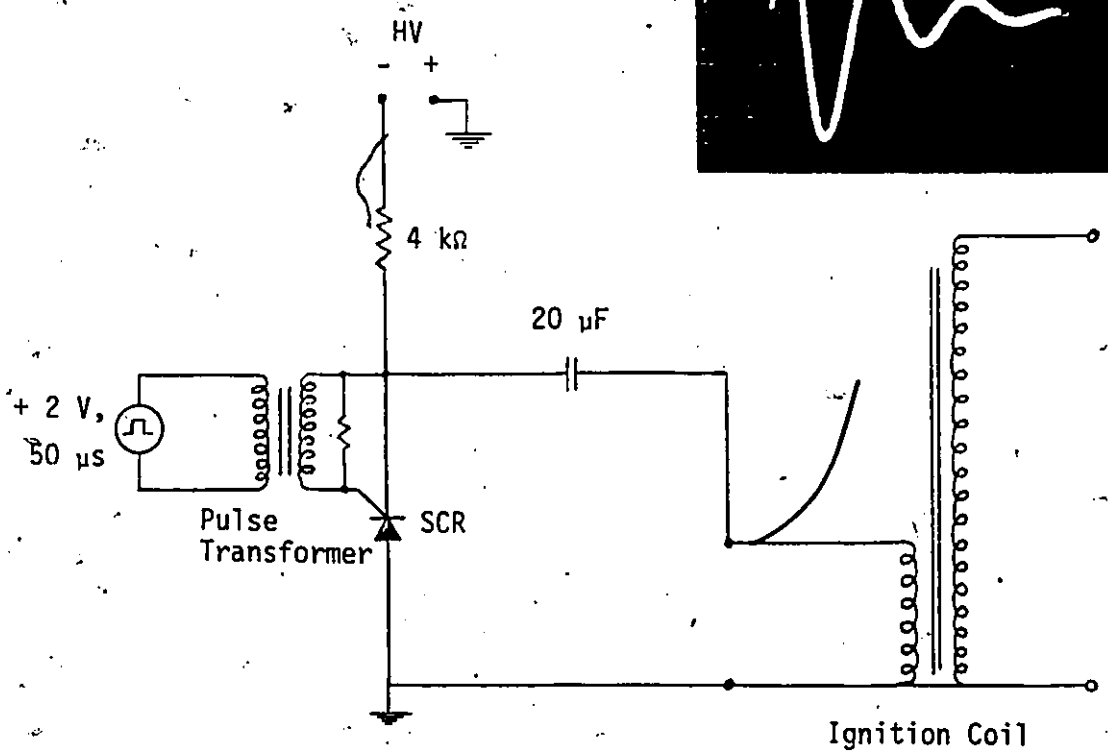
HV
- +
4 kΩ
20 μF
+ 2 V,
50 μs
Pulse
Transformer
SCR
Ignition Coil

Fig 3-3

Circuit diagram of a dual 3-V pulse generator.

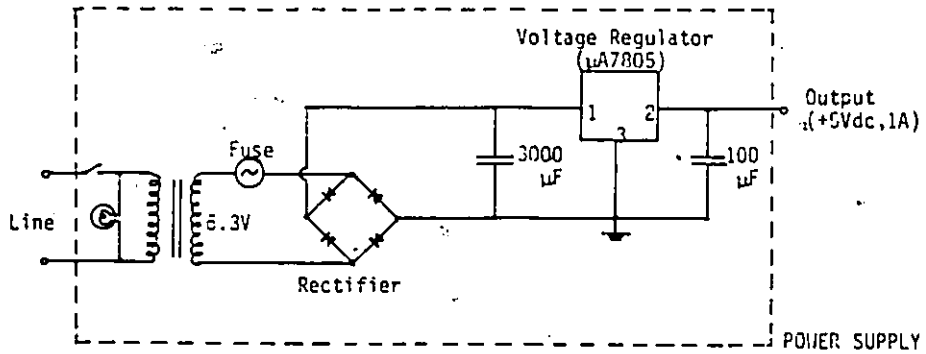

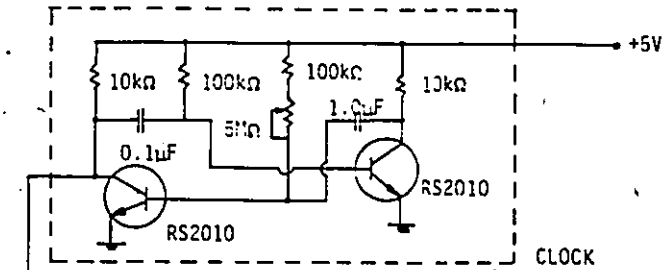

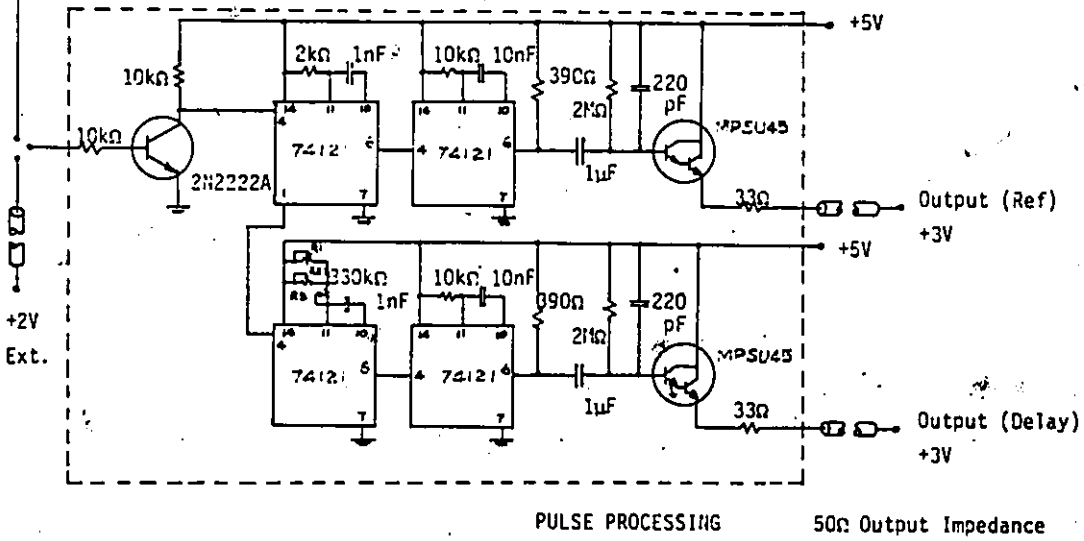

R1 = 1MΩ Trimming resistor
R2 = 2 x 10kΩ single turn variable resistor
R3 = 5kΩ Trimming resistor

With ~70-ns duration, and 3-V amplitude into 50 Ω. These pulses can be separated in time within the range 0-10 ms.

3.2.2 Mechanical Construction

The complete laser system, shown in Fig.3-4, consists of a discharge chamber and its supporting structure, a pair of preionizers and a spark gap unit. The discharge chamber, illustrated in Fig.3-5, employs a 12.7-cm ID acrylic tube, with wall thickness 1.27 cm and length 71.12 cm. This is closed at both ends by Bakelite discs, each of which is equipped with a 2.54-cm diameter fused-silica window (0.32-cm thick). The discharge volume, which can be varied from 22 cm^3 to 83 cm^3, is bounded by a pair of nickel-plated brass electrodes. Each electrode has a plane surface area of 50 x 0.64 cm^2. Electrode separation is adjustable from 1.3 cm to 2.6 cm in steps of 0.32 cm. The electrodes, of overall length 52 cm, were machined from 3.2-cm diameter rods, and both ends were rounded off. A plane surface was also machined parallel to the "discharge" surface, so that gap-adjustment spacers could be inserted between the electrode and a mounting bar (52 x 1.9 x 1.27 cm^3). Each electrode assembly is then supported by eight brass connectors (1.27 cm - diameter), which also provide electrical connections. These connectors are aligned (within 0.1 mm) and then fastened with epoxy resin within holes in the acrylic tube (see Fig.3-6). The "ground" electrode connections are fastened to an aluminum base plate resting on the lower bars of the supporting structure. The "high-voltage" connections are attached to an aluminum bar (50 x 2.54 x 1.27 cm^3) which supports two rows of discrete ceramic capacitors by means of 1.6-mm thick copper sheet. A

Fig. 3-4

Overall view of the laser system.

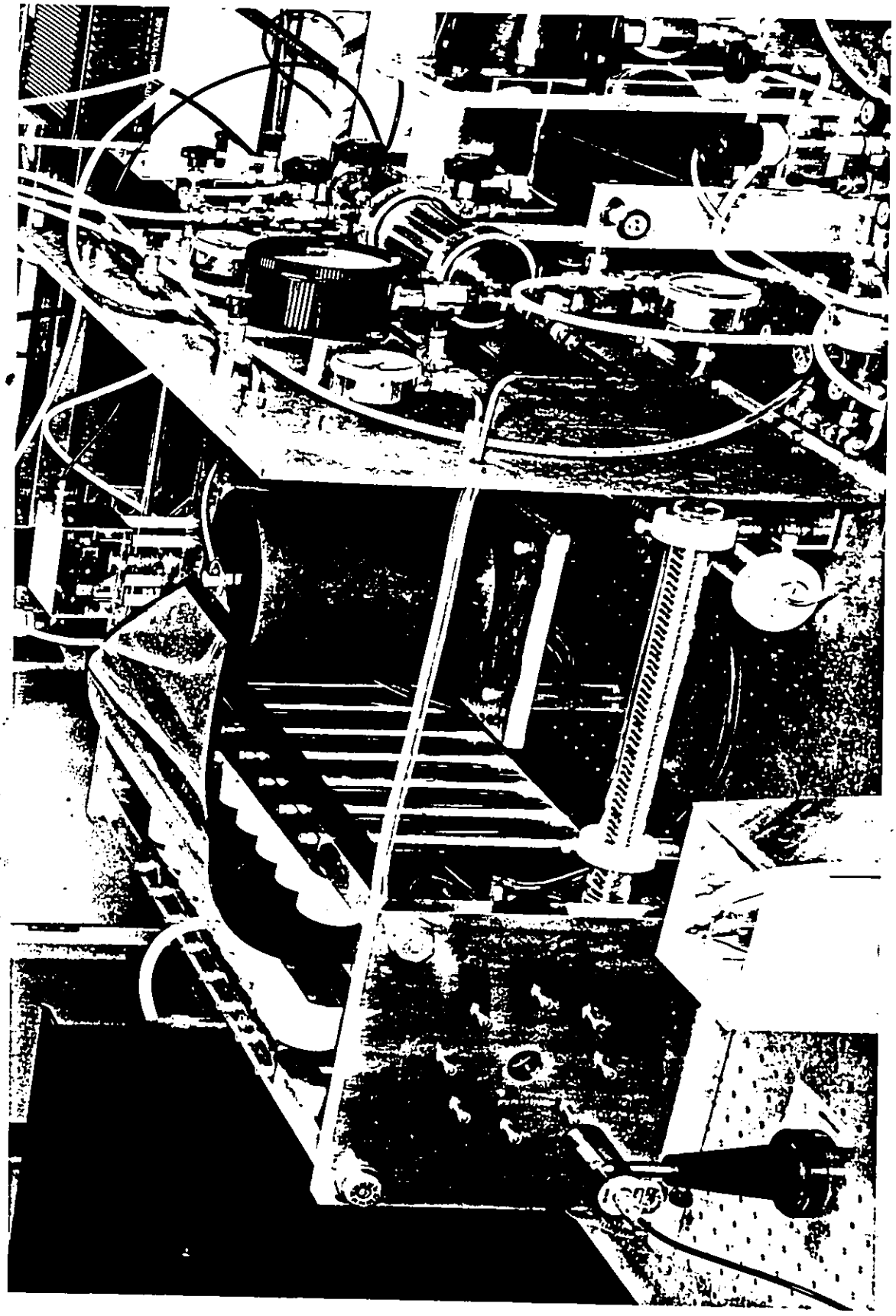

Fig. 3-5

Main section of the discharge chamber. Viton O-rings, represented by ■, are used for seals.

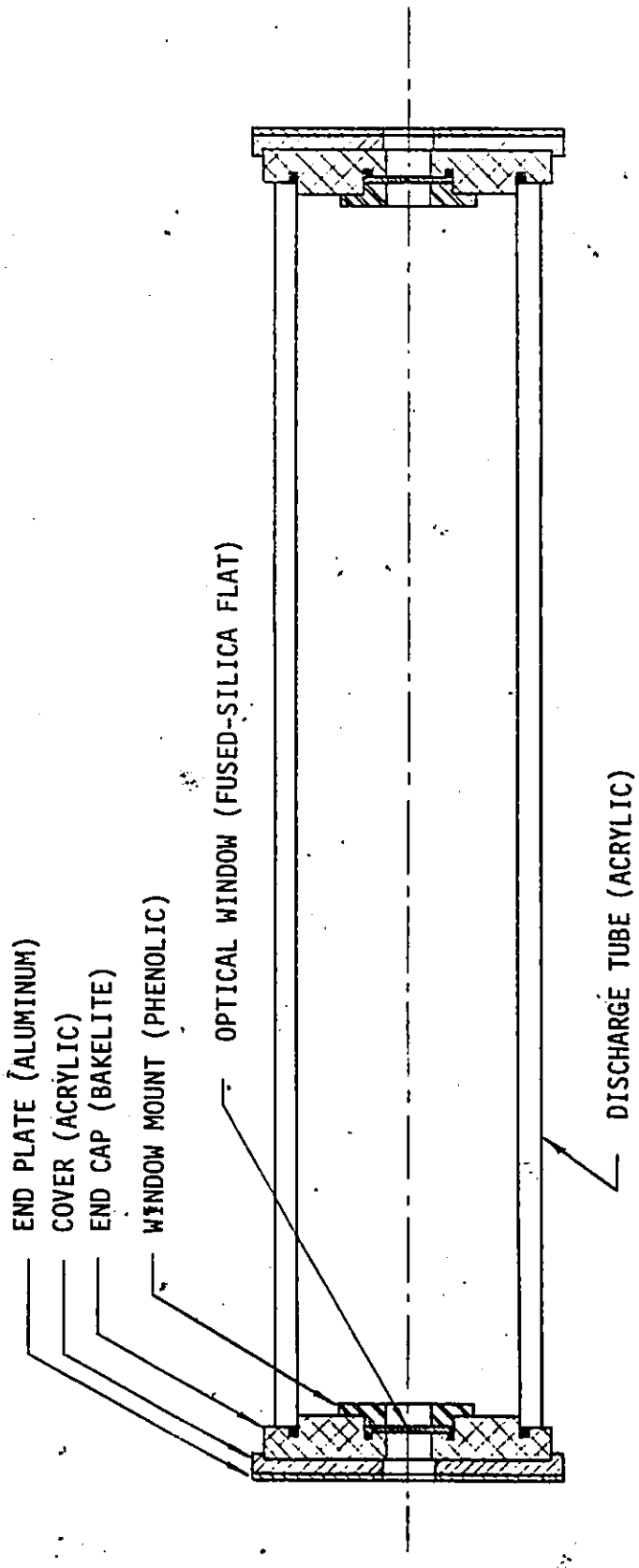
END PLATE (ALUMINUM)
COVER (ACRYLIC)
END CAP (BAKELITE)
WINDOW MOUNT (PHENOLIC)
OPTICAL WINDOW (FUSED-SILICA FLAT)
DISCHARGE TUBE (ACRYLIC)
Scale:
0 5 10 cm

Fig. 3-6

Cross-sectional view of the laser.

A. Discharge tube (acrylic).

B. Electrode (nickel-plated brass).

C. Spacer (nickel-plated brass).

D. Electrode mounting plate (nickel-plated brass).

E. Electrical feedthrough (brass).

F. Supporting plate (aluminum).

G. External mounting plate (aluminum).

H. "Doorknob" capacitors.

I. Conducting strip (copper).

J. Ground sheet (copper).

K. Preionizer.

L. Supporting structure, shown in Fig.3-7.

M. Connecting rods (aluminum).

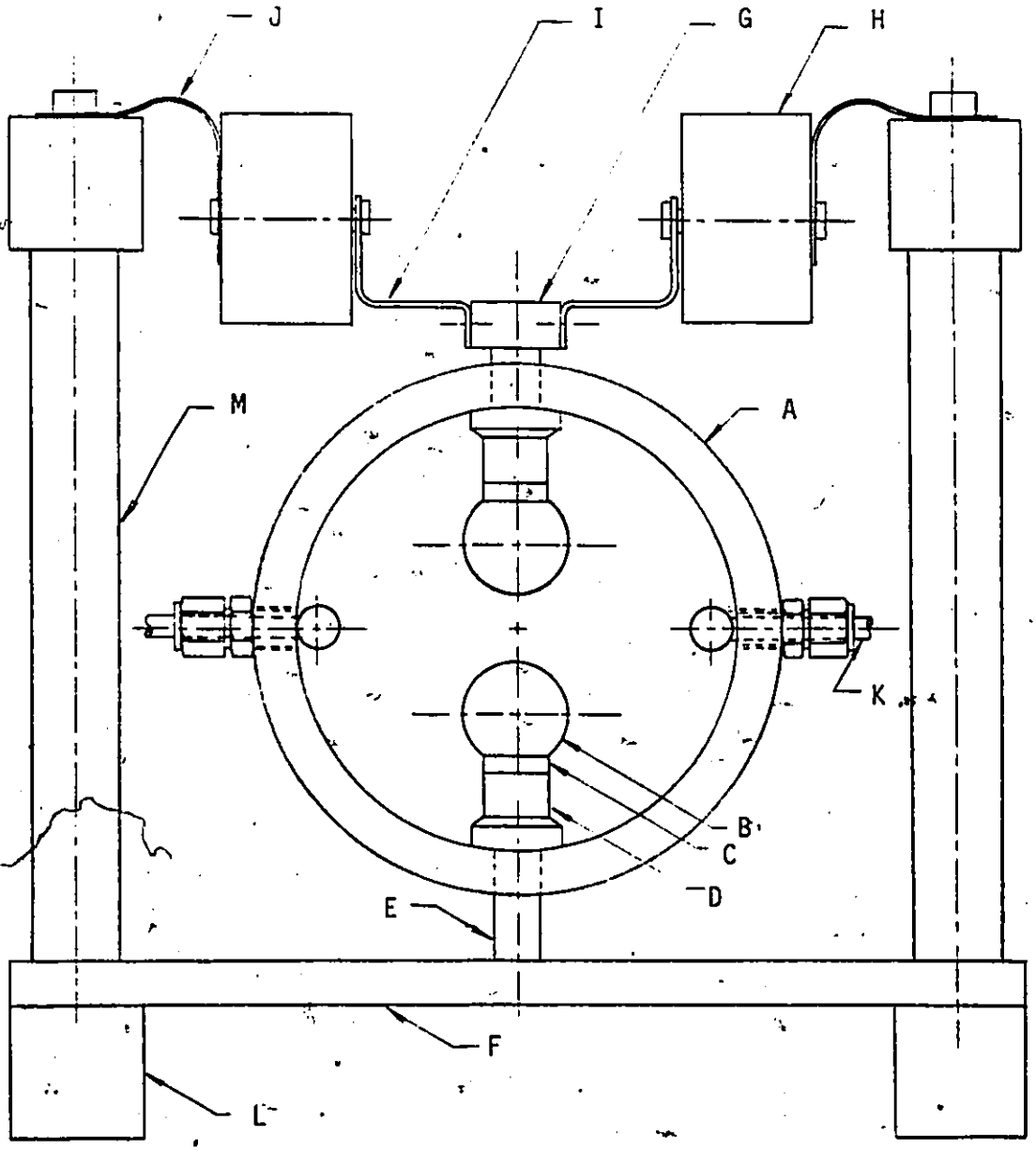
J
I
G
H
M
A
K
B
C
D
E
F
L

pair of 0.1-mm thick copper sheets connect the other end of the capacitors to the upper bars of the supporting structure to complete the discharge circuit. In order to improve current flow in the circuit and to increase the structural stability, 2.54-cm diameter aluminum rods (8 each side) are used between the upper bars and the base plate. For corrosion protection, the inside surfaces of the discharge chamber were coated with a layer of Type E-7 epoxy (Techkits), as recommended by Sarjeant et al. [100]. Viton O-rings are used for sealing detachable components.

The rigid supporting structure, which houses the discharge chamber, consists of two 2.54-cm thick aluminum end plates (31.8 x 30.5 cm^2) joined by four aluminum bars (3.81 x 3.81 cm^2) of length 78.7 cm (see Fig.3-7). High-strength-alloy screws (3/4" - 16 UNF) are used for the assembly. Each end plate contains a 3.2-cm diameter hole, surrounded by eight tapped holes (1/4" - 20 UNC) on a pitch diameter of 14.0 cm. These holes are for screws which push against the Bakelite disc closing the chamber [101]. Detailed structural calculations (Appendix D) show that the supporting structure safely supports chamber pressures of at least 45 atm, which is well in excess of the maximum allowable pressure of the laser chamber (30 atm). The latter is limited by the mechanical strength of the present discharge chamber.

The pair of preionizers (Fig.3-8) are each structured by forming 19 stainless-steel discs (2.54-cm diameter and 0.076-mm thick), equally spaced (3 mm), over the surface of a 10-mm OD Pyrex tube, of wall thickness 1.5 mm, and length 56 cm. A brass rod (6.4-mm OD and 53-cm length), which is assembled to a shaped brass-connector, is inserted into the tube and serves as the "ground" electrode. A similar brass

Fig. 3-7

Supporting structure of the laser discharge chamber.

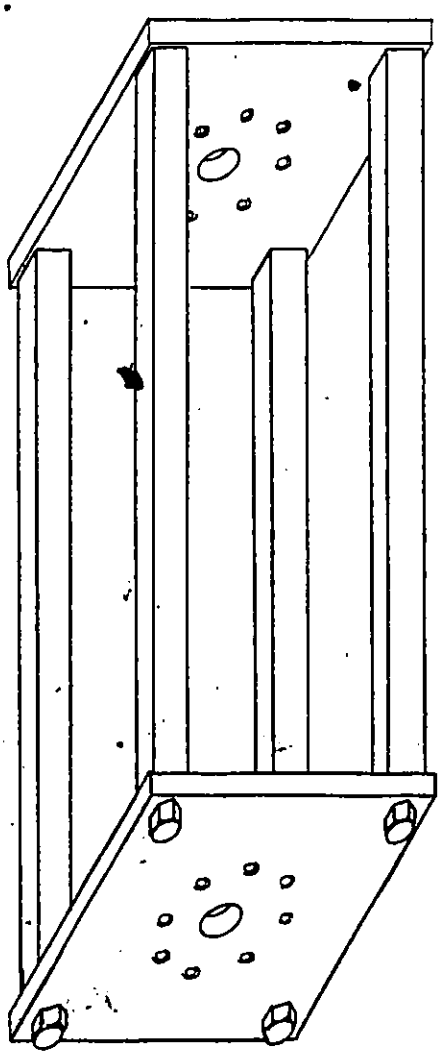

Scale: 0 5 10 cm

Fig. 3-8

Preionizer assembly.

A. High-voltage terminal (brass).

B. Ground terminal (brass).

C. Pyrex tube.

D. Brass rod.

E. Stainless-steel pad.

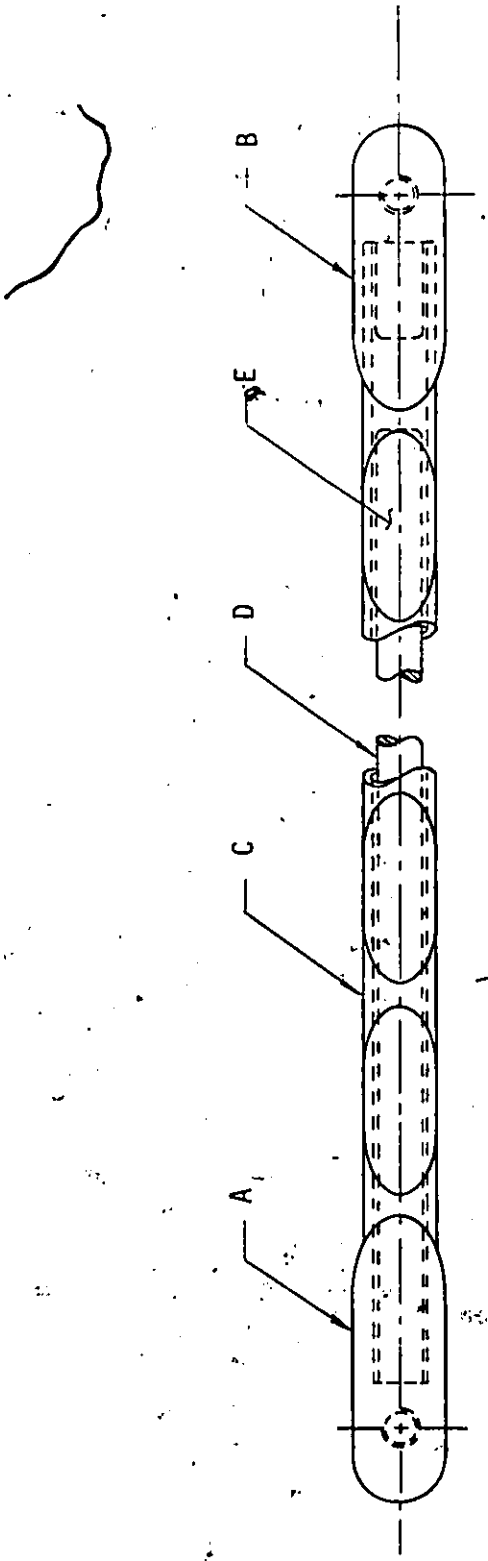

Scale:

0 1 2 3 cm

connector is placed at the other end of the tube and serves as the "high-voltage" electrode. The components are held together with epoxy resin. The tapped holes in the electrodes, 58.4 cm apart, are for mounting. The associated mounting rods are clamped in position by means of Swagelok connectors installed in the discharge-chamber wall. This makes it possible to adjust the location of the preionizer unit over a range of ∿1 cm.

The spark gap unit, shown in Fig.3-9, employs a standard spark plug (14 mm) for the trigger electrode [97]. Nitrogen gas flows into and out of the unit via a pair of Swagelok tube connectors (Nylon). The main electrodes have thin machineable-tungsten discs attached with silver solder (not shown in the figure). The main gap is 8 mm. The spark gap is installed directly to one of the upper aluminum bars of the supporting structure in order to minimize inductance.

Most components of the laser system, excluding the power supplies, the pulse generator, and the gas-handling system (described in the next section), are mounted on a metallic optical table (NRC) and enclosed by four side panels and a top cover which are made of galvanized sheet steel. This minimizes the electromagnetic noise in instrumentation caused by electrical discharges in the laser. Overall dimensions of the enclosure are 93-cm long by 77-cm wide by 50-cm high. Appropriate holes are provided for optical radiation, and for gas and electrical connections.

3.2.3 Gas Handling System

The XeCl laser media employed in our experiments consist of

Fig. 3-9

Nitrogen-pressurized spark gap.

A. Acrylic housing.

B. Spark plug (champion BN-9Y).

C. High-voltage connection.

D. Ground connection.

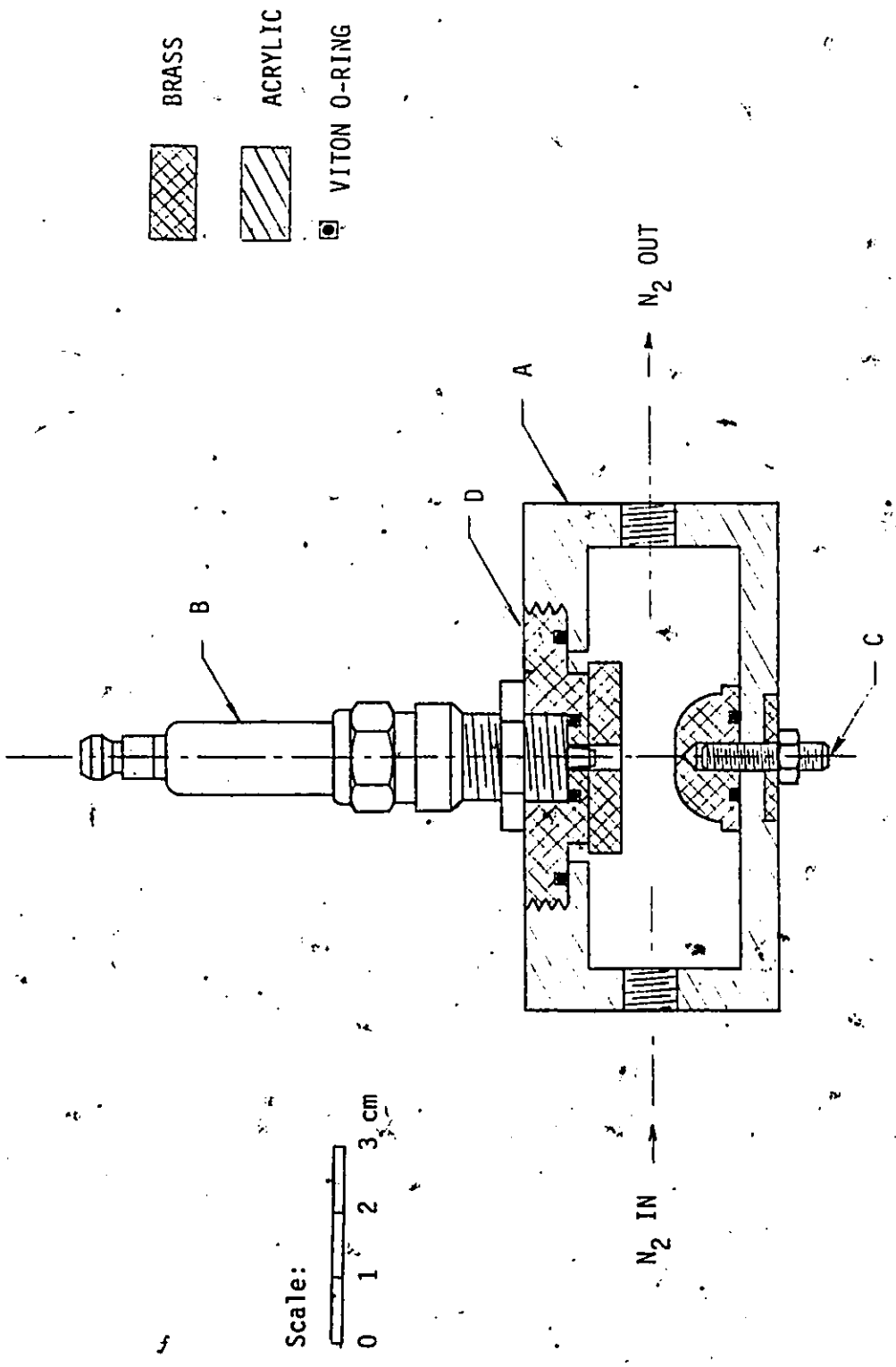
BRASS
ACRYLIC
VITON O-RING
N_2 OUT
N_2 IN
A
B
C
D
Scale:
0 1 2 3 cm

mixtures of helium (high purity), xenon (certified purity), and 5% hydrogen chloride in helium (certified standard), all supplied by Matheson. As indicated in Fig.3-10(a), these mixtures are prepared in a stainless-steel mixing chamber (0.6 ℓ capacity) before being released to the pre-evacuated (and passivated)discharge chamber. Pressures are measured using a 0.5%-accuracy compound gauge (Solfrunt 1981), which is calibrated from vacuum to 100 psig. Because of the large volume differences between the laser and mixing chambers, the Xe, He/0.5% HCl and some He (at appropriate pressures) are first placed in the mixing chamber, allowed to stand for ∿15 min, and then released into the laser. Next additional He is flowed via the mixing chamber into the laser until final pressure is reached. For adequate mixing, the system is allowed to stand for ∿15 min, followed by reduced voltage operation (just below threshold) for ∿10 pulses (∿5 min).

One of the gas components, hydrogen chloride, is highly corrosive when exposed to moist air, and must be carefully disposed of before venting the used mixture (or purging the system) to the atmosphere. In our disposed system, shown in Fig.3-10(b), aqueous caustic soda is used as the gas absorber. When the chamber pressure is high (above an atmosphere), the mixture can bypass the vacuum pump and be directly injected into the solution. Hydrogen chloride "frozen" in the trap is later released in a fume hood.

3.3 System Performance

Experiments have been performed with the laser system using various He/Xe/HCl mixtures and various discharge conditions. Typical

Fig. 3-10

Schematic diagram of the gas handling system.

(a) Gas supply lines and mixing system.

(b) Waste disposal system.

(a)

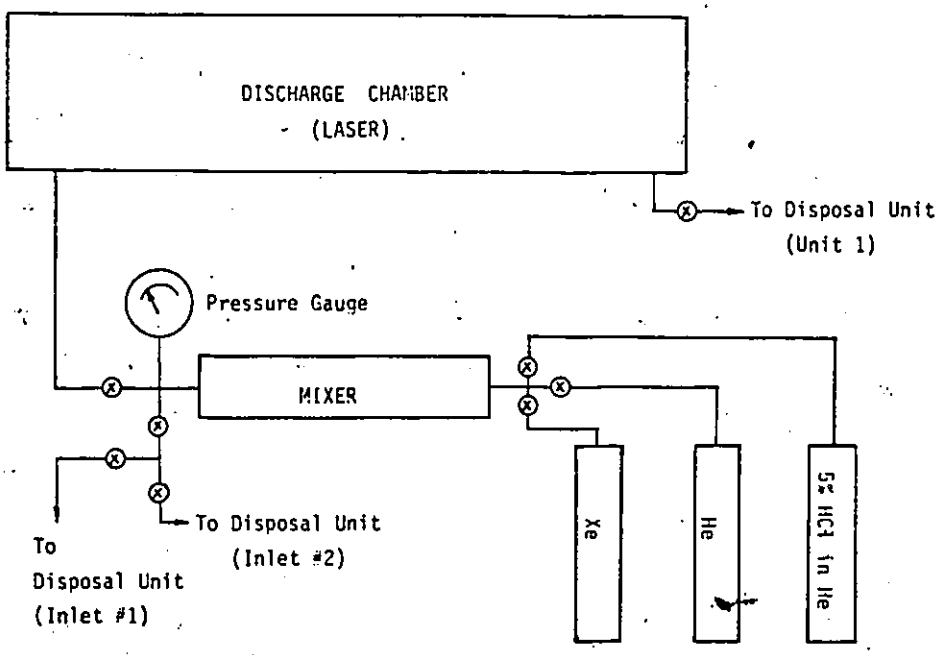
DISCHARGE CHAMBER
(LASER)
To Disposal Unit
(Unit 1)
Pressure Gauge
MIXER
To Disposal Unit
(Inlet #2)
To
Disposal Unit
(Inlet #1)
Xe
He
5% HCl in He

(b)

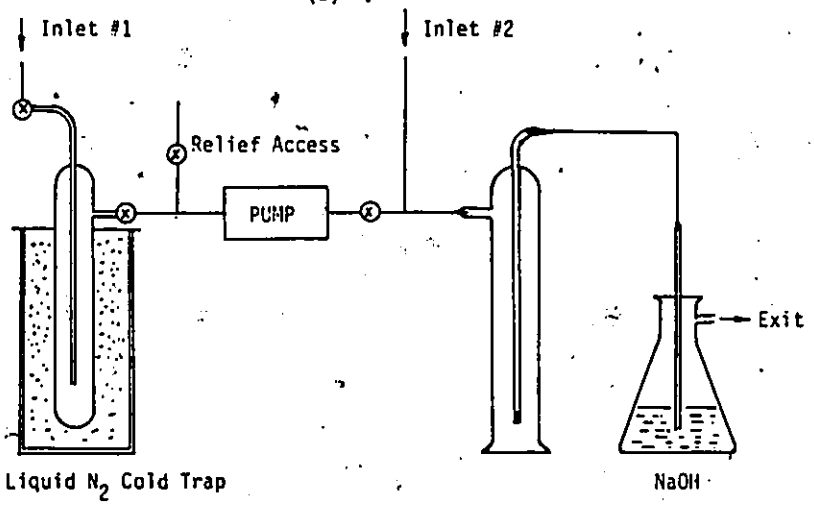
Inlet #1
Inlet #2
Relief Access
PUMP
Exit
Liquid N_2 Cold Trap
NaOH

experimental results describing the characteristics of the laser and the gaseous discharge are presented in the following sections. The important laser parameters are summarized in Table 3-1. Note that the maximum charging voltage of the system has been limited to ∿35 kV in order to avoid damage caused by over-voltage in components.

All experimental results were obtained after the system had been evacuated and then well-passivated using HCl. Adequate passivation was necessary in order to achieve good operating lifetimes and reproducible data (apart from inherent shot-to-shot variations of ∿ ±5%). Moreover, the electrode surfaces were preconditioned by discharging the system using a He/5% HCl mixture at a low pressure, and at the minimum charging voltage, just before the introduction of a test mixture into the discharge chamber. This preconditioning improved both the system stability and the optical output energy. In addition, the static-fill life of a mixture was greatly extended, probably due to the presence of HCl adsorbed by the electrodes and internal surfaces of the discharge chamber. Extensive measurements on the operating lifetime of our laser system have not been made. However, mixtures left in the system for a period of three days were found to be active, although with reduced laser efficiency.

The rear cavity reflector is the only element that can be adjusted in order to optimize laser output. Optimum laser performance is achieved when the laser cavity (usually a 98% rear reflector and the fused-silica front window) is properly aligned. However, bending stresses alter the alignment when the pressure is changed. It was

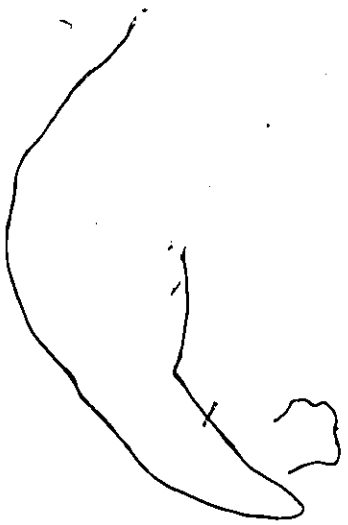

Table 3-1

XeCl Laser Parameters

Mechanical System

Discharge Volume	42-83 cm^3
Discharge Length	50 cm
Discharge Width	0.64 cm
Electrode Separation	1.33-2.60 cm
Operating Pressure	<10 atm

Electrical System

Charging Voltage	≤35 kV
A. Main Discharge:	
Storage Capacitance	0.1 μF (nominal)
"Voltage-Peaking" Capacitance	16 x 2700 pF (nominal)
Peak Current	≲28 kA
Current Pulse Duration	∿100 ns (FWHM)
E/p, at maximum output	∿5.6 V/cm-Torr
E/N, at maximum output	∿18 Td
B. Preionizer Discharge:	
Storage Capacitance	0.05 μF (nominal)
Peak Current (each unit)	≲3.2 kA
Current Pulse Duration (each unit)	∿500 ns (FWHM)

Output Characteristics

Gas Composition	99.3% He/0.5% Xe/0.2% HCl
Gas Pressure	2880 Torr
Electrical Input Energy	∿60 J
Optical Output Energy	200 mJ ± 20%
Optical Output Peak Power	3.4 MW (maximum ∿4 MW)
Optical Pulse Duration	60 ns (FWHM)
Laser Efficiency	0.3% (maximum ∿0.5%)
Optical Emission (B → X):	
Wavelength v'=0 → v"=1	307.937 ± 0.010 nm
v'=0 → v"=2	308.175 ± 0.010 nm
Linewidth	∿0.13 nm

observed that the alteration affected the laser output by <5%. This small change was a consequence of the high gain inherent in the laser.

The effect of mirror reflectance on laser performance was studied. Experiments were carried out by using an additional reflector (either a 92% reflector or a fused-silica flat) in front of the discharge chamber, or by inserting an intracavity attenuator between the rear of the chamber and reflector. Experimental observations are reported in Section 3-7. These are compared with theory in Section 5-5.

3.3.1 Output Energy

The energy of the XeCl B → X transition (308 nm) was measured at charging voltages of 23-35 kV, electrode separations of 1.33 cm, 1.65 cm, 1.97 cm, 2.29 cm and 2.60 cm, and mixtures containing 0.25-5.0% Xe, 0.1-0.3% HCl and the remainder He. The total gas pressure ranged from 1277 Torr (1.7 atm) to 4379 Torr (5.8 atm) (usually at 258.5-Torr intervals). Only part of the experimental data is presented here. However, these are typical results which are sufficient to characterize the laser and to compare different operating conditions. Special emphasis is placed on operation with a 1.65-cm electrode gap. This provided the highest output energy using a charging voltage $\leq$ 35 kV, and also the most consistent data for evaluating laser efficiency and production of long-duration output pulses.

Laser output energy was measured with a pyroelectric joulemeter (Gen-Tec ED-200 #8747) used together with a storage oscilloscope (Tektronix 466). The calibration was not as reliable as the stated accuracy of ± 10%. A similar joulemeter (Gen-Tec ED-200 #8688) gave

readings which were 30% higher. Since most of the data are relative only detector output voltages are presented. However, in cases where absolute energies are given, the detector output readings have been multiplied by 1.15, which corresponds to the mean reading for the two detectors. In this way, the measured energies are estimated to be accurate within ± 20%. The resultant conversion factor is 185 mJ/V.

Experimental results for a 1.65-cm electrode separation appear in Figs.3-11 to 3-13. Figure 3-11 compares output energy data from mixtures containing Xe (0.5%) and HCl (0.1%, 0.2% and 0.3%) in He. The He/0.5% Xe/0.2% HCl mixture gave the highest output energy (∿200 mJ) for charging voltages below 35 kV. The outputs using He/0.5% Xe/0.1% HCl and He/0.5% Xe/0.3% HCl mixtures were lower, with the latter only slightly lower than the former. The optimum HCl content is thus close to, but slightly less than 0.2%. The optimum Xe content is ∿0.5%. As the ratio HCl : He increases, the optimum gas pressure decreases. The concentration of hydrogen chloride in the optimized system, however, does not remain the same, and in fact, decreases much faster than the decreasing concentration of helium. If we consider a comparable output from mixtures containing 0.1% and 0.3% HCl, and assume exciplex quenching by gas particles to be the important loss mechanisms, the quenching rate constant due to HCl should be higher than those due to the rare gases (Xe and He). This is consistent with the results obtained from kinetic measurements [102].

The optical output energies, as functions of Xe content (1.0%, 2.5% or 5.0%) in mixtures containing 0.2% and 0.3% HCl, are shown in

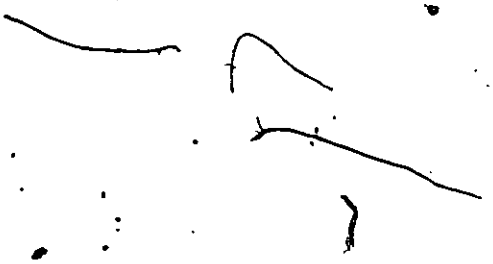

Fig. 3-11

Output energy as a function of charging voltage and total gas pressure, using an electrode spacing of 1.65 cm. The mixtures are: (a) He/0.5%Xe/0.1%HCl, (b) He/0.5%Xe/0.2%HCl, and (c) He/0.5%Xe/0.3%HCl. The optiuum output energies and efficiencies for these mixtures, as functions of charging voltage, are shown in (d), (e), and (f), respectively. The conversion factor is 185 mJ/V.

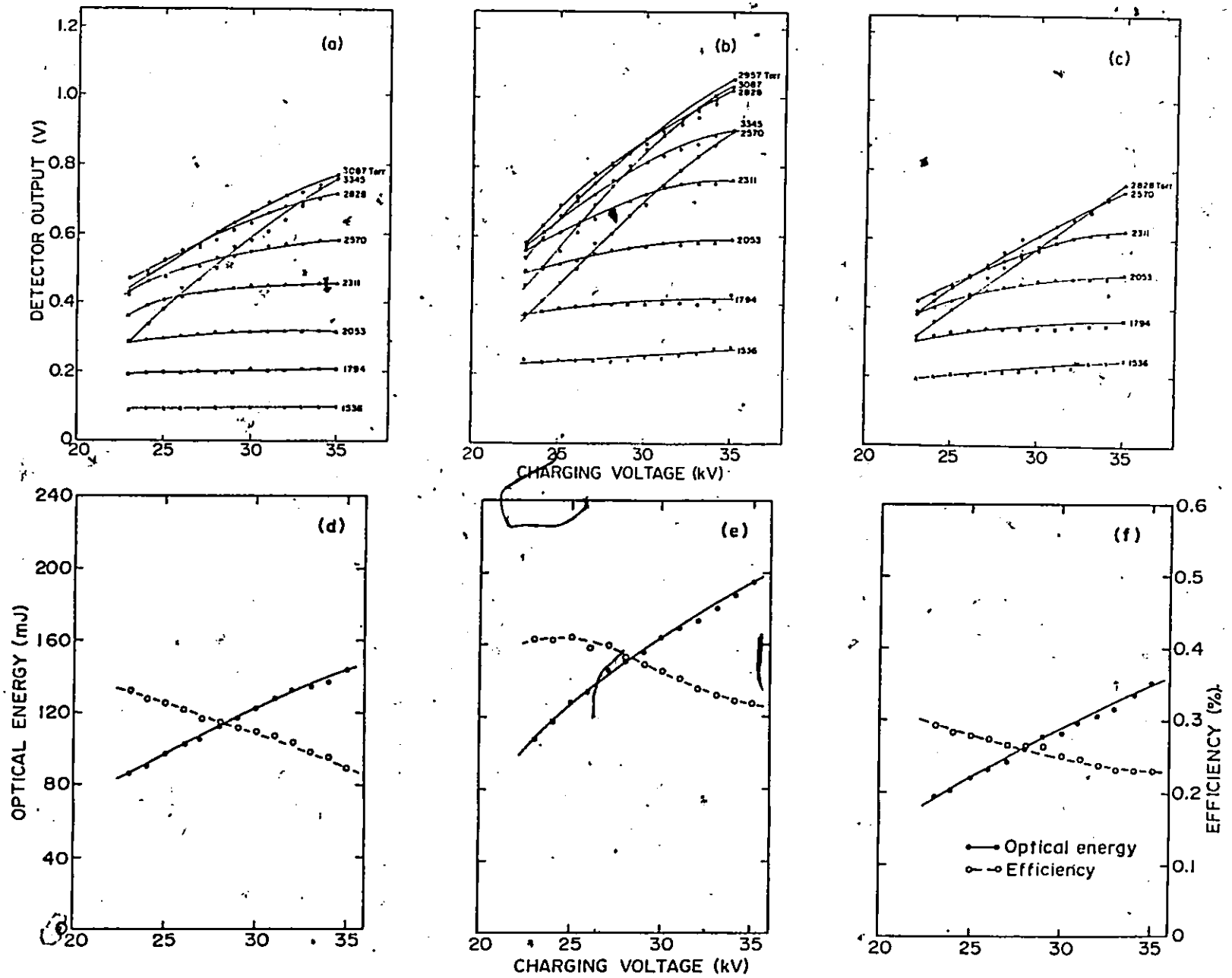
(a)
(b)
(c)
(d)
(e)
(f)
DETECTOR OUTPUT (V)
CHARGING VOLTAGE (kV)
OPTICAL ENERGY (mJ)
EFFICIENCY (%)
Optical energy
Efficiency

Figs.3-12 and 3-13, respectively. In both cases, maximum energy is extracted employing mixtures having a high Xe content (typically 5.0%). As the Xe concentration increases, the optimum gas pressure and He concentration decrease. These results are expected because the number of exciplex species increases with Xe concentration. However, it is interesting to note that for the system employing 0.2% HCl, and a charging voltage >31 kV, the He/0.5% Xe/0.2% HCl mixture at 2957-Torr pressure outperforms the He/5.0% Xe/0.2% HCl mixture at 1794 Torr. This behaviour may be due to the reduction, at lower Xe concentration, in the quenching of exciplex species by electrons which are produced primarily in conjunction with Xe ions. In addition, the ratio of the electron quenching coefficients for the upper (excimer, B) state and the ground (X) state decreases as input energy to the system decreases. The system is still efficient, even though the exciplex concentration is reduced. It should be noted that mixtures containing 0.2% HCl provide better efficiency than those containing 0.3% HCl.

Two typical gas mixtures, He/1.0% Xe/0.2% HCl and He/2.5% Xe/0.3% HCl, are selected for the purpose of comparing the output performance of systems employing electrode separations of 1.97 cm, 2.29 cm and 2.60 cm, and also 1.65 cm, which was studied previously. The output energy data obtained for the first mixture appear in Figs.3-14 (a)-(f) for the three widest separations, and in Figs.3-12(a), (d) for the 1.65-cm separation. The highest output, for charging voltages >32 kV, is obtained using the 1.97-cm separation. For voltages <26 kV, the optimum separation is 1.65 cm. In the intermediate range, these, and the 2.6-cm separation,

Fig. 3-12

Output energy as a function of charging voltage and total gas pressure, using an electrode spacing of 1.65 cm. The mixtures are: (a) He/1.0%Xe/0.2%HCl, (b) He/2.5%Xe/0.2%HCl, and (c) He/5.0%Xe/0.2%HCl. The optimum output energies and efficiencies, as functions of charging voltage, are shown in (d), (e), and (f), respectively. The conversion factor is 185 mJ/V.

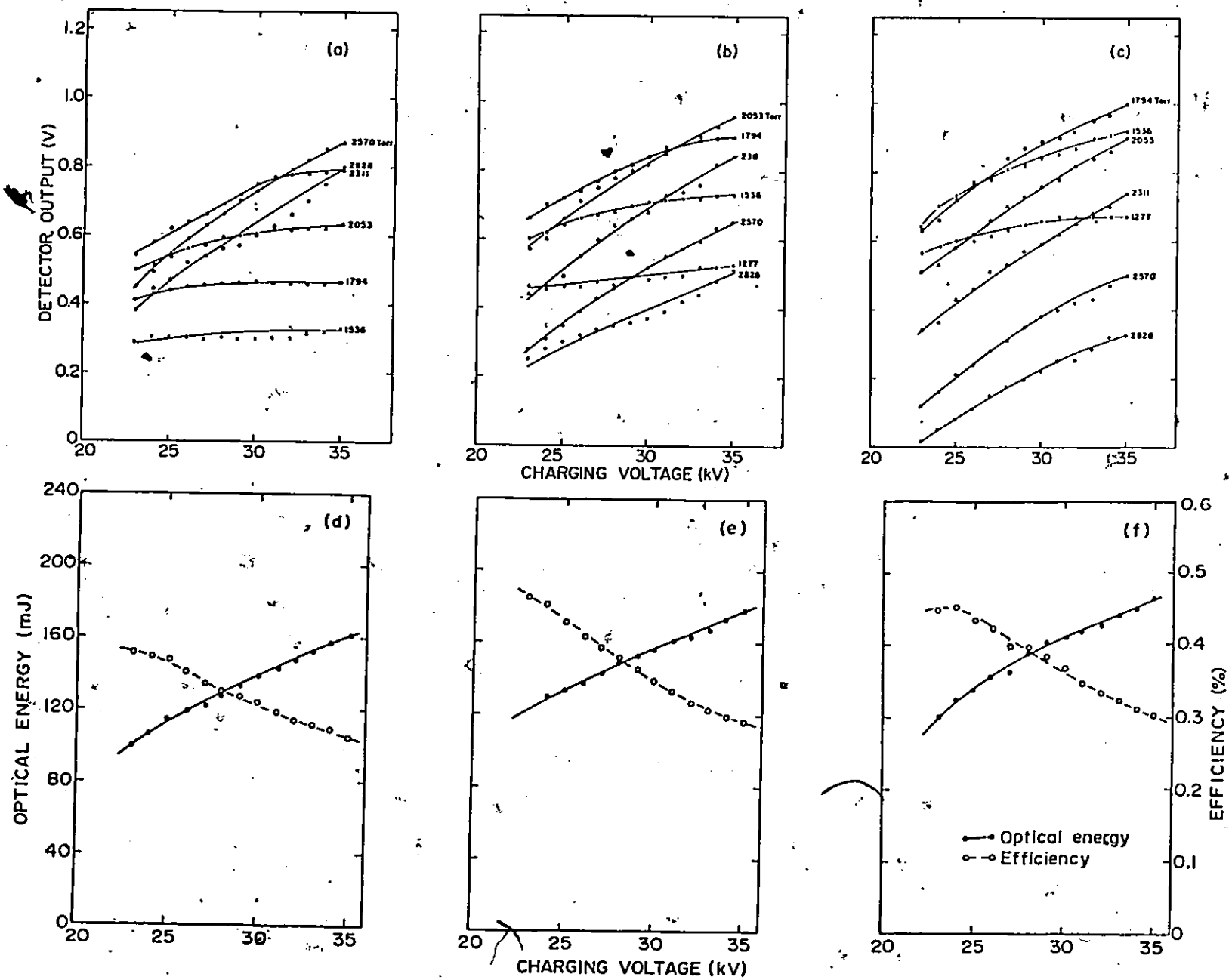
(a)
(b)
(c)
(d)
(e)
(f)
DETECTOR OUTPUT (V)
CHARGING VOLTAGE (kV)
OPTICAL ENERGY (mJ)
EFFICIENCY (%)
Optical energy
Efficiency

Fig. 3-13

Output energy as a function of charging voltage and total gas pressure, using an electrode spacing of 1.65 cm. The mixtures are: (a) He/1.0%Xe/0.3%HCl, (b) He/2.5%Xe/0.3%HCl, and (c) He/5.0%Xe/0.3%HCl. The optimum output overgies and efficiencies for these mixtures, as functions of charging voltage, are shown in (d), (e), and (f), respectively. The conversion factor is 185 mJ/V.

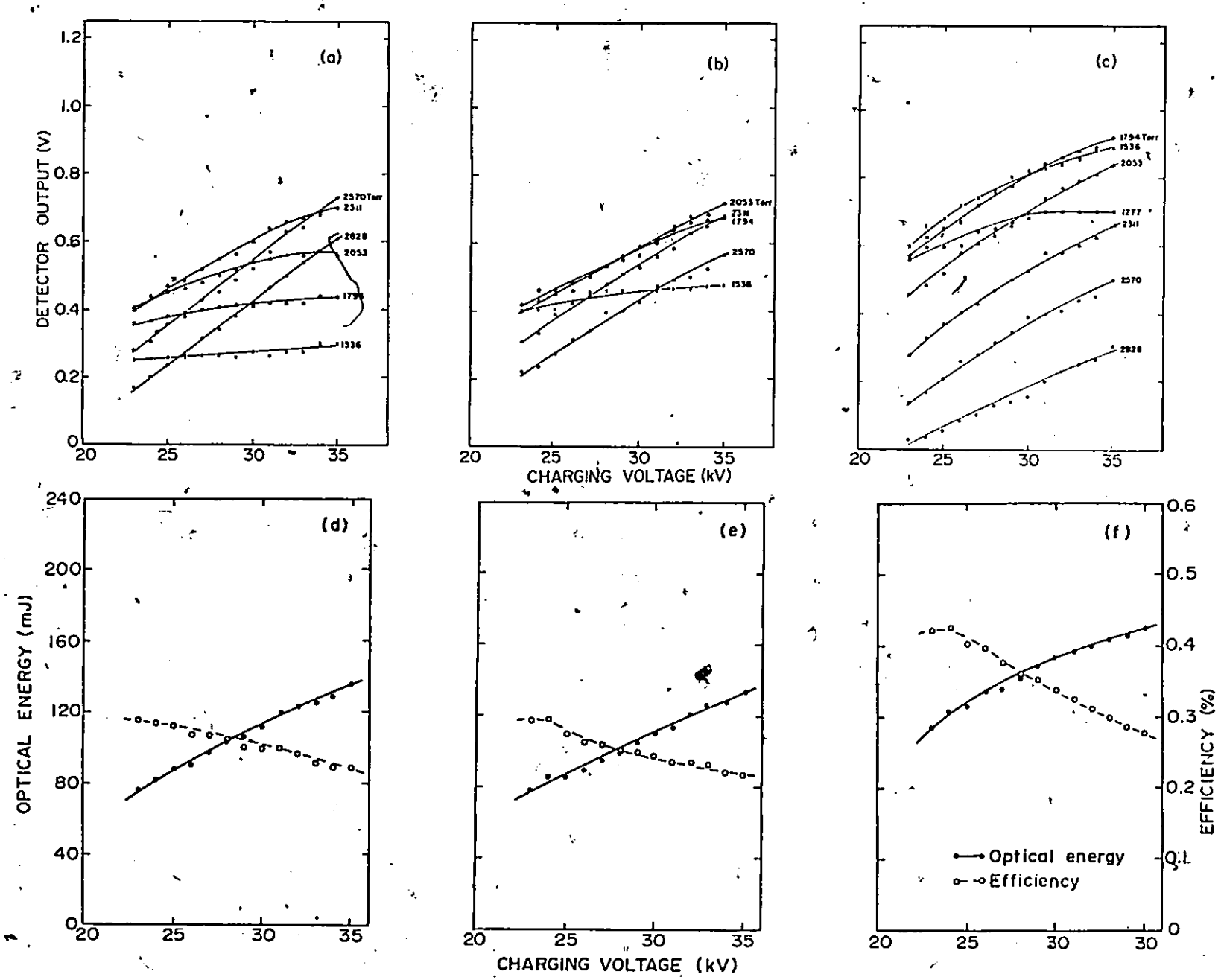
(a)
(b)
(c)
(d)
(e)
(f)
DETECTOR OUTPUT (V)
CHARGING VOLTAGE (kV)
OPTICAL ENERGY (mJ)
EFFICIENCY (%)
Optical energy
Efficiency

Fig. 3-14

Output energy as a function of charging voltage and total gas pressure, using a He/1.0%Xe/0.2%HCl mixture. The electrode spacings are: (a) 1.97 cm, (b) 2.29 cm, and (c) 2.60 cm. These electrode spacings, as functions of charging voltage, are shown in (d), (e), and (f), respectively. The conversion factor is 185 mJ/V.

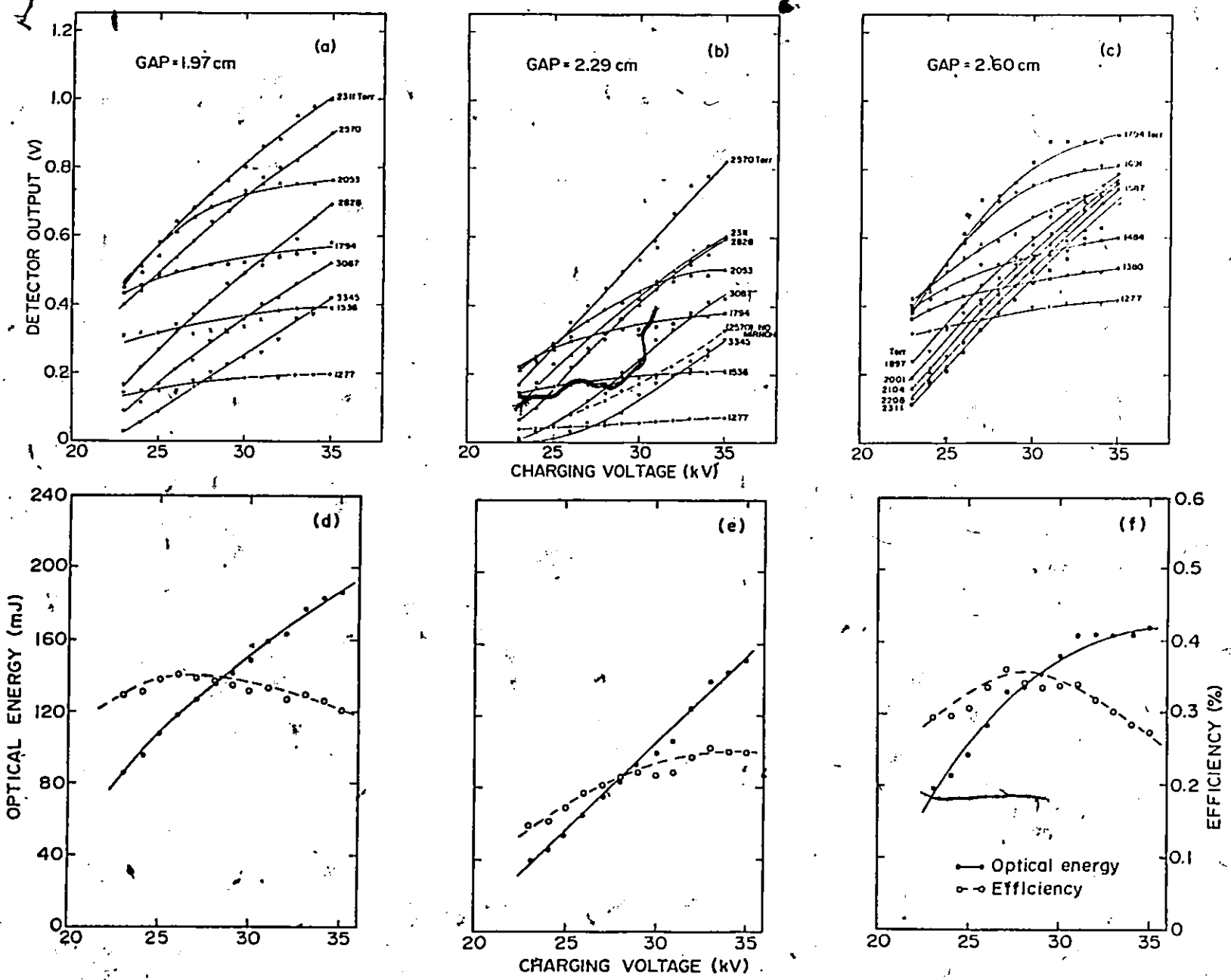
(a)
GAP = 1.97 cm
(b)
GAP = 2.29 cm
(c)
GAP = 2.60 cm
DETECTOR OUTPUT (V)
CHARGING VOLTAGE (kV)
(d)
(e)
(f)
OPTICAL ENERGY (mJ)
EFFICIENCY (%)
Optical energy
Efficiency

yield comparable energy outputs. The output behaviour of the system employing a 2.29-cm electrode separation is anomalous, and not fully understood. As the separation is increased, the optimum operating pressure is reduced. However, the E/p_0 (electric field to optimum gas pressure) ratios at gas breakdown are similar for all of the above electrode separations, and extend from ~4.0 V/cm-Torr at low charging voltages to ~5.6 V/cm-Torr at high voltages (except for the 2.29-cm gap, where the E/p_0 ratios are ~20% lower).

Similar results (shown in Figs.3-15(a)-(f) and Figs.3-13 (b), (e)) are also obtained using the He/2.5% Xe/0.3% HCl mixture. In this case, the best performance at both high and low charging voltages is achieved by adopting the largest electrode separation (2.60 cm). The output energies for all three other separations are lower, but similar to each other. Considering the latter three separations only, the best efficiency is achieved by using the large separation at high charging voltages and the small separation at low voltages, in accordance with the ability to deposit energy into the system. At gas breakdown, E/p_0 ~4.5 V/cm-Torr is favoured for low energy deposition, and ~6.0 V/cm-Torr for high energy deposition. By contrast, E/p_0 values for the 2.60-cm gap are ~25% lower in the low input energy range, yet similar at high input energy. The high E/p_0 values for this mixture, compared to those for the He/1.0% Xe/0.2% HCl mixture, are attributed to the lower optimum operating pressures. In general, the optimum pressures for a particular mixture is lowered if the gap separation is increased. In addition, operation at high E/p_0 and high energy deposition prefers high-pressure

Fig. 3-15

Output energy as a function of charging voltage and total gas pressure using a He/2.5% Xe/0.3% HCl mixture. The electrode spacings are: (a) 1.97 cm, (b) 2.29 cm, and (c) 2.60 cm. The optimum output energies and efficiencies using these electrode spacings, as functions of charging voltage, are shown in (d), (e), and (f), respectively. The conversion factor is 185 mJ/V.

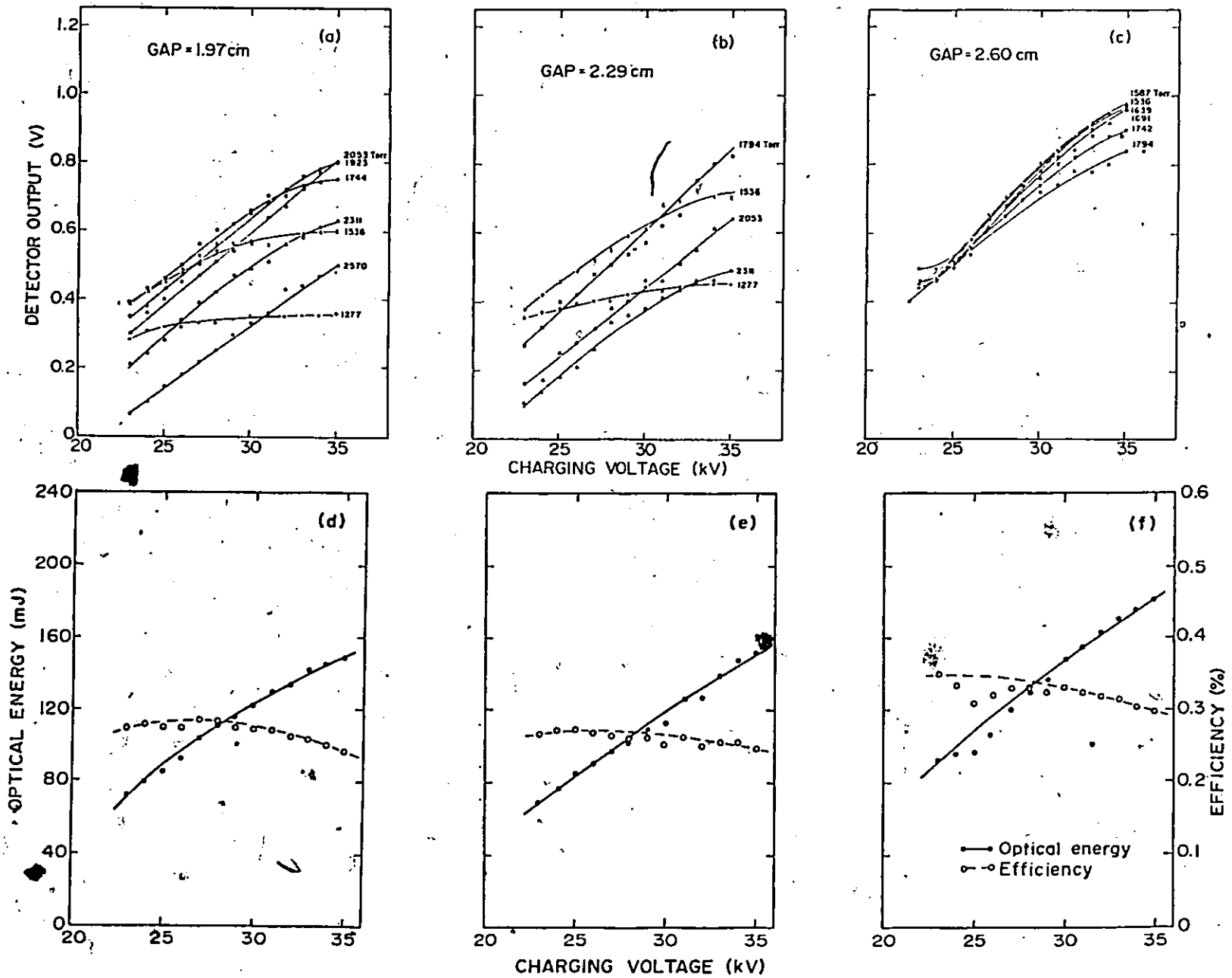
(a)
GAP = 1.97 cm
(b)
GAP = 2.29 cm
(c)
GAP = 2.60 cm
DETECTOR OUTPUT (V)
CHARGING VOLTAGE (kV)
(d)
(e)
(f)
OPTICAL ENERGY (mJ)
EFFICIENCY (%)
Optical energy
Efficiency

operation.

Mixtures having a constant concentration ratio of xenon and hydrogen chloride have also been investigated. In Fig.3-16, two typical mixtures, He/1.0% Xe/0.1% HCl and He/2.0% Xe/0.2% HCl (Xe:HCl = 10:1), are compared for energy output and efficiency in the system employing an electrode separation of 1.97 cm. As the results indicate, both mixtures have similar behaviour. However, the mixture with higher concentrations of Xe and HCl yields slightly better output. Doubling the Xe and HCl concentrations, and hence the exciplex concentrations, should double the output energy. The lower (∿20%) optimum operating pressure for the second mixture has a relatively small effect on output. The small differences in optical energy are probably the result of system losses due to exciplex quenching by gas particles (He, Xe and HCl), and photoabsorption by Xe- and HCl- related species, which are dominant in the XeCl laser.

The above results suggest that, for a particular mixture and electrode separation, there is an optimum operating pressure which increases with energy deposition. Typical energy data obtained for the He/0.5% Xe/0.2% HCl mixture and a 1.65-cm separation gap, shown in Fig.3-11(b), are presented in a different format in Fig.3-17. The operating pressure for optimum output varies from ∿2718 Torr at 23-kV charging voltage to ∿2983 Torr at 35 kV. At high input energy, the change in optimum pressure with charging voltage is gradually reduced. In addition, operation is in the saturation regime, resulting in an optical output energy which increases nearly linearly with energy deposition,

Fig. 3-16

Output energy, as a function of charging voltage and total gas pressure, using an electrode spacing of 1.97 cm. Two mixtures are compared: (a) He/1.0%Xe/0.1%HCl and (b) He/2.0%Xe/0.2%HCl. The optimum output energies and efficiencies using these mixtures, as functions of charging voltage, are shown in (c) and (d), respectively. The conversion factor is 185 mJ/V.

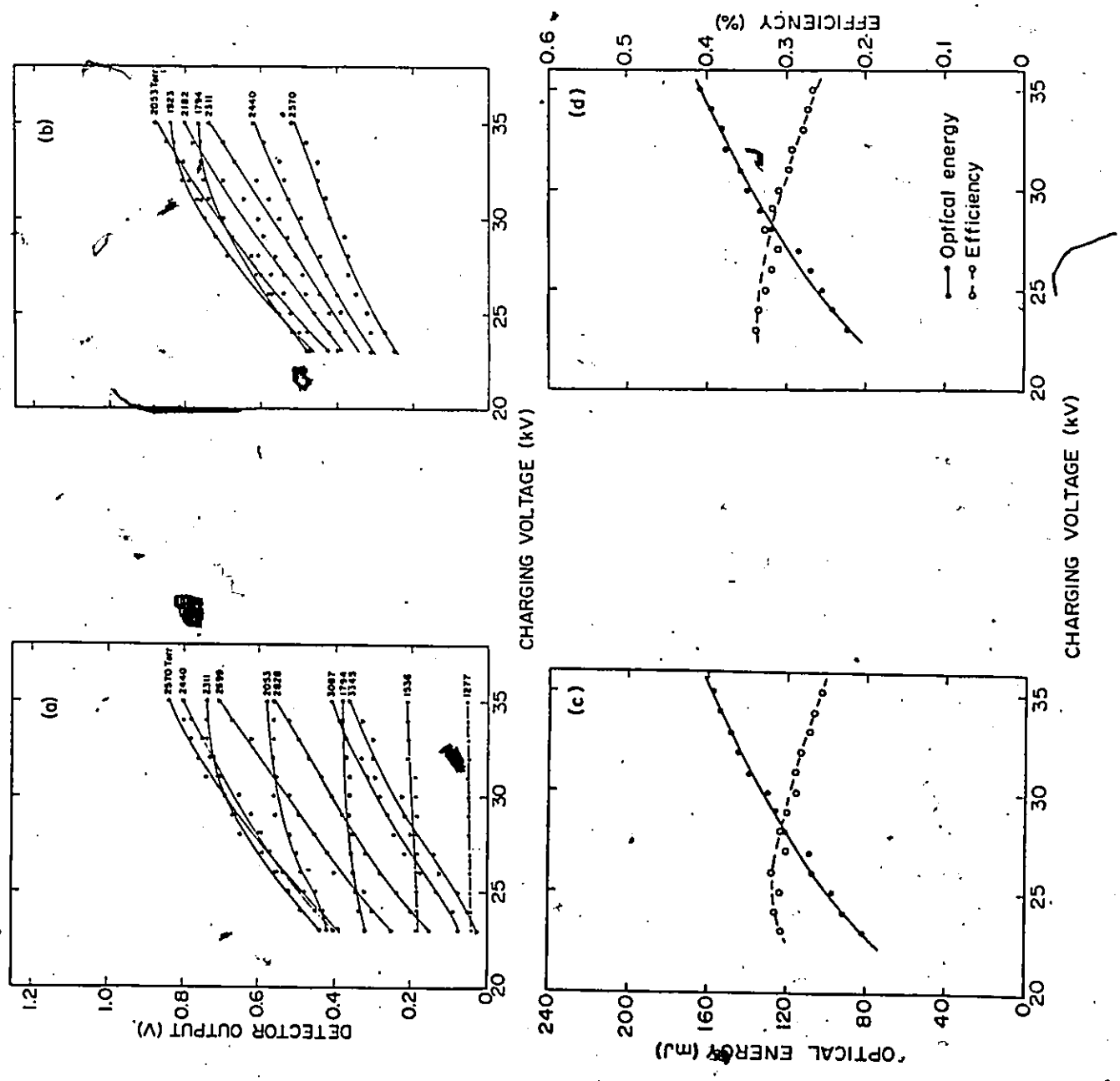
(a)
(b)
(c)
(d)
DETECTOR OUTPUT (V)
OPTICAL ENERGY (mJ)
EFFICIENCY (%)
CHARGING VOLTAGE (kV)
CHARGING VOLTAGE (kV)
Optical energy
Efficiency

Fig. 3-17

Output energy as a function of total gas pressure and charging voltage, using an electrode separation of 1.65 cm, and a He/0.5%Xe/0.2%HCl mixture. The dashed curve represents the optical energy extractable under the optimum discharge conditions. The conversion factor is 185 mJ/V.

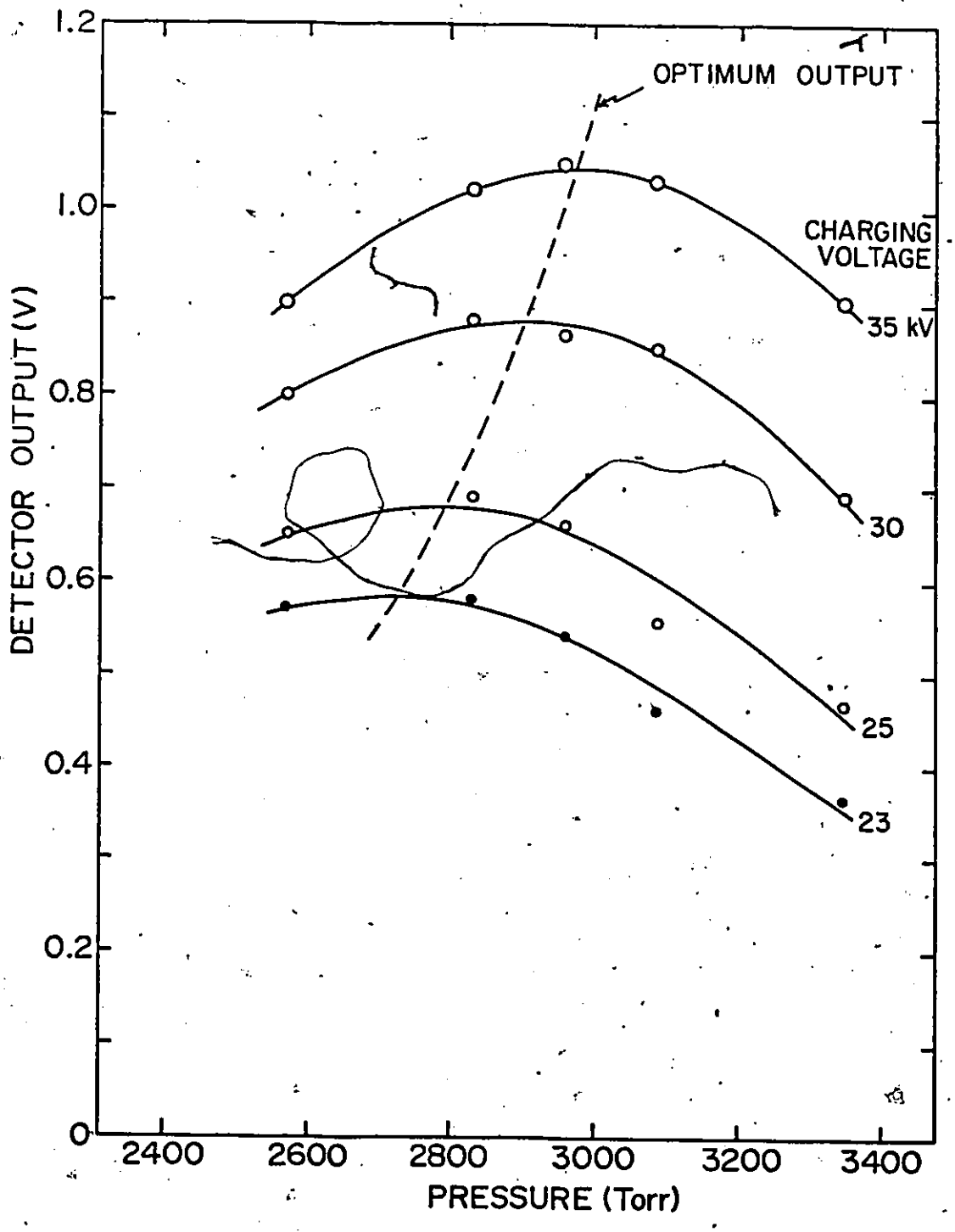
OPTIMUM OUTPUT
CHARGING VOLTAGE
35 kV
30
25
23
DETECTOR OUTPUT (V)
PRESSURE (Torr)
0
0.2
0.4
0.6
0.8
1.0
1.2
2400
2600
2800
3000
3200
3400

and a relatively constant laser efficiency. Figure 3-18(a) shows a typical saturation curve, using the parameters in Fig.3-17, and operating at a pressure of 2957 Torr. At higher output energies, the system efficiency, according to Fig.3-18(b), has a limit of ∿0.3%, compared to the maximum efficiency of ∿0.4% occurring at a charging voltage of ∿25 kV. The highest output and highest efficiency obtainable, using the 1.65-cm electrode separation and the optimum mixture and operating pressure at a given charging voltage, is summarized in Fig.3-19. The best efficiency achieved is ∿0.46% at the low charging voltage of 23 kV and a He/2.5% Xe/0.2% HCl mixture.

3.3.2 Electrical Characteristics

Voltages across the electrodes were probed outside the discharge chamber using a "half-shielded" voltage divider employing a 25-cm column of copper sulphate solution (0.08 M concentration). This probe, illustrated in Fig.3-20, was designed to match into 50 Ω, and was usually operated in conjunction with two standard 50-Ω ÷10 attenuators. Voltages were measured using a 400-MHz bandwidth storage oscilloscope (Tektronix 7834). Measurements on the output of a fast risetime (∿2 ns) pulse generator (E-H 127), for which some results are shown in Figs.3-21 (a) and (b), indicated that the risetime of the voltage probe was probably <1 ns. In addition, the probe was calibrated *in situ* against a commercial high-voltage probe (Tektronix P6015), for which the dc calibration factor is shown in Fig.3-22. The calibration curve for our probe appears in Fig.3-23. The probe scaling factor is not constant for all applied voltages, but increases quite linearly from 40000 at

Fig. 3-18

(a) Optical output and (b) laser efficiency are shown as functions of stored energy, in the laser system employing a 1.65-cm electrode separation, and a He/0.5%Xe/0.2%HCl mixture at a total gas pressure of 2957 Torr.

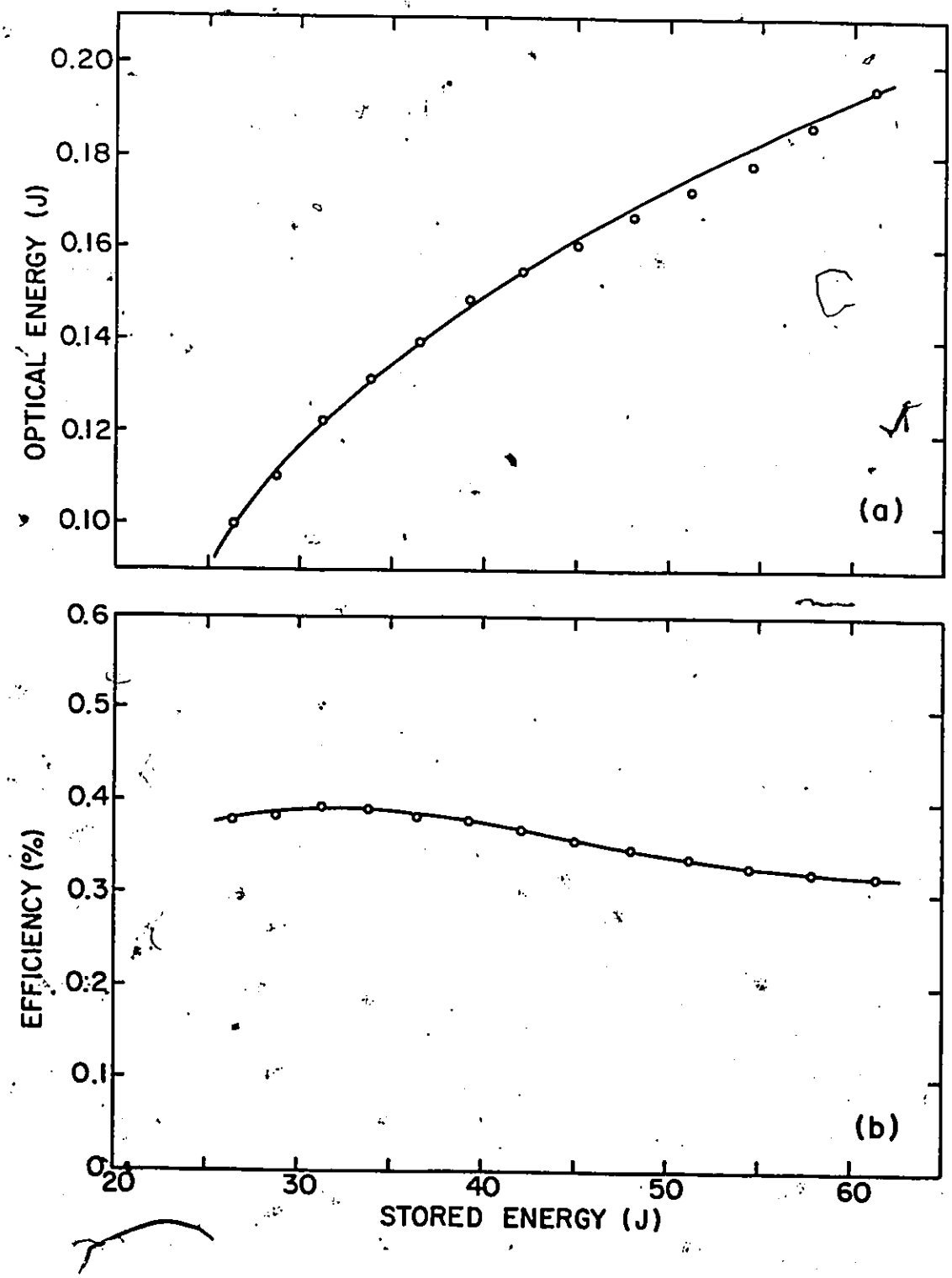
0.20
0.18
0.16
0.14
0.12
0.10
OPTICAL ENERGY (J)
(a)
0.6
0.5
0.4
0.3
0.2
0.1
0
EFFICIENCY (%)
(b)
20
30
40
50
60
STORED ENERGY (J)

Fig. 3-19

(a) Optical energy and (b) laser efficiency are shown as functions of stored energy, in a laser system employing 1.65-cm electrode separation, and the optimum mixture and gas pressure at each discharge energy.

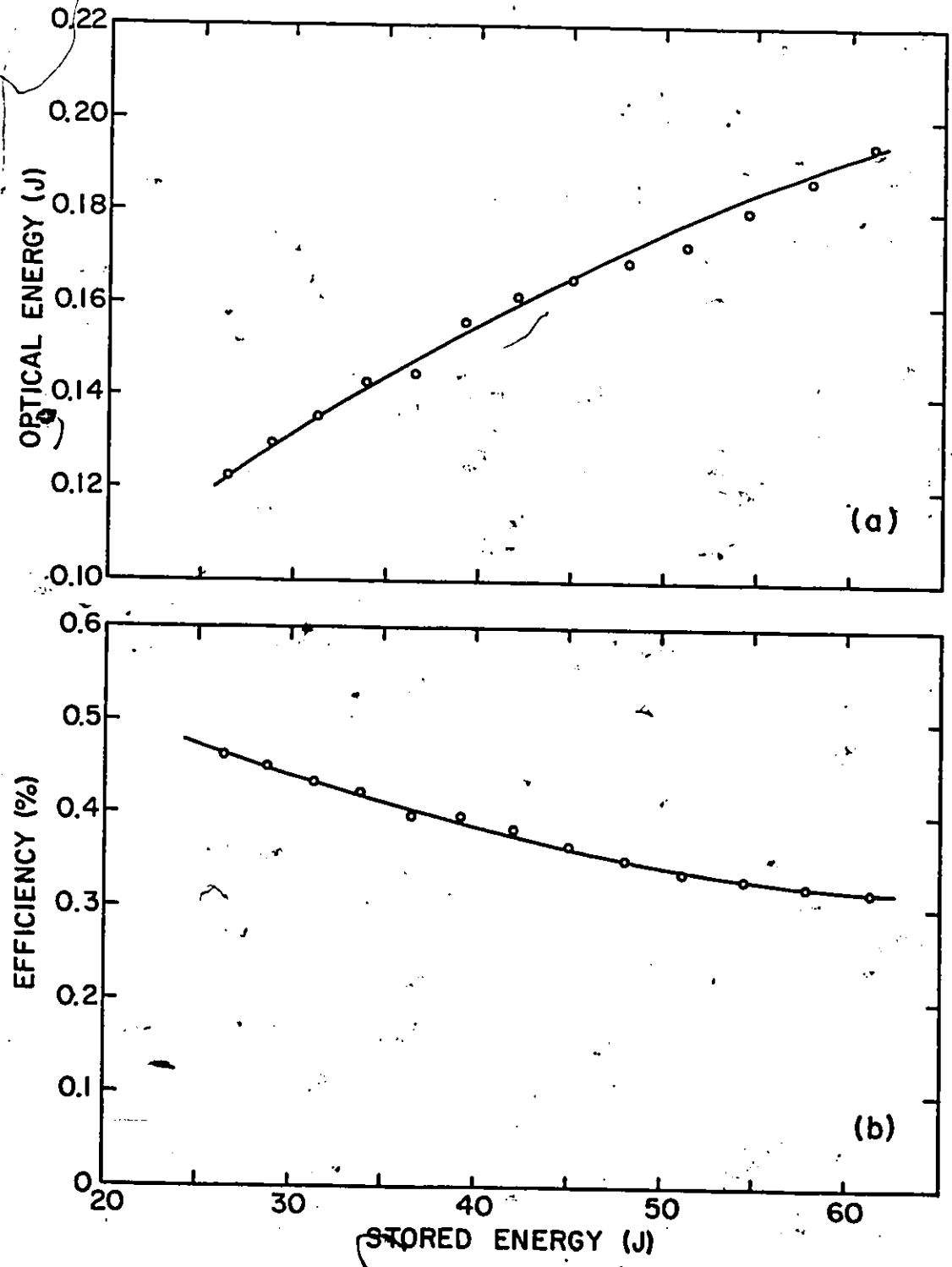
OPTICAL ENERGY (J)
0.22
0.20
0.18
0.16
0.14
0.12
0.10
(a)
EFFICIENCY (%)
0.6
0.5
0.4
0.3
0.2
0.1
0
(b)
20
30
40
50
60
STORED ENERGY (J)

Fig.3-20

Construction of a "half-shielded" $CuSO_4$ high-voltage probe.

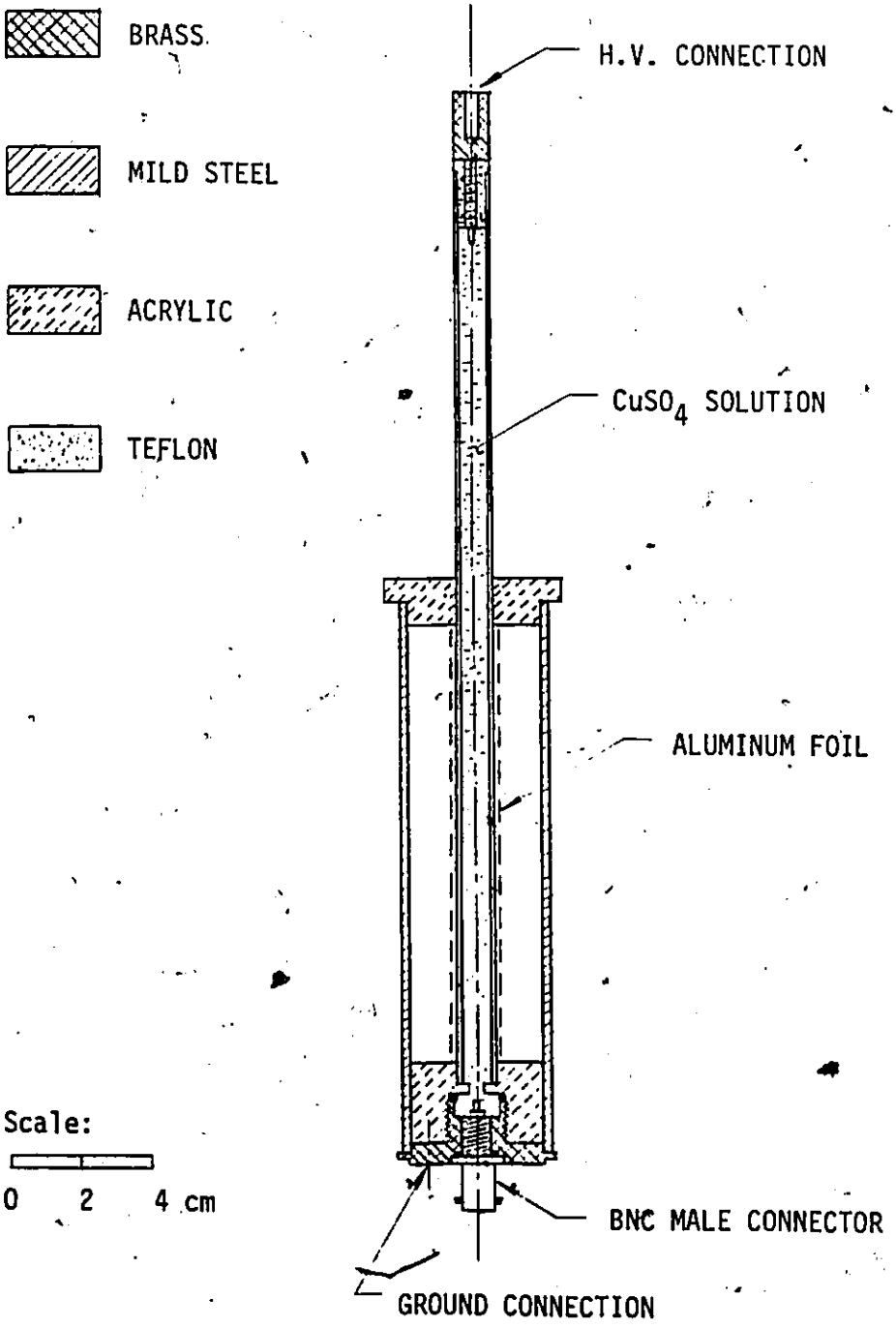
BRASS
MILD STEEL
ACRYLIC
TEFLON
H.V. CONNECTION
$CuSO_4$ SOLUTION
ALUMINUM FOIL
BNC MALE CONNECTOR
GROUND CONNECTION
Scale:
0 2 4 cm

Fig. 3-21

Pulse response of several high-voltage probes. The time axis is 10 ns/division (large square). In each photograph, the upper trace is the observed output pulse from the pulse generator (E-H 127); the lower trace is the corresponding output from

(a) an "unshielded" $CuSO_4$ voltage divider,

(b) a "half-shielded" $CuSO_4$ voltage divider,

(c) an "unshielded" $Na_2S_2O_3$ voltage divider, and

(d) a "compensated" resistor voltage-divider probe.

(a)

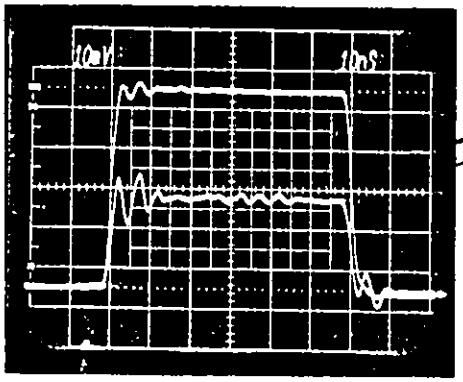

(b)

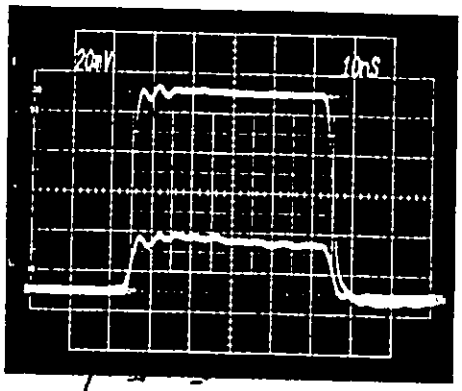

(c)

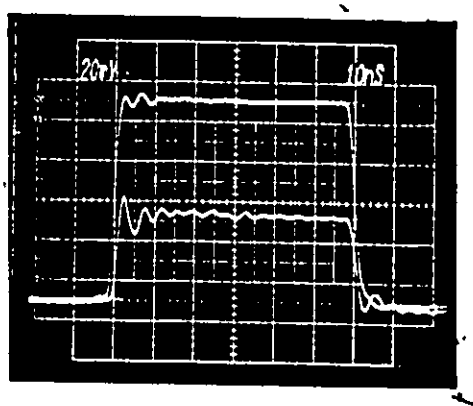

(d)

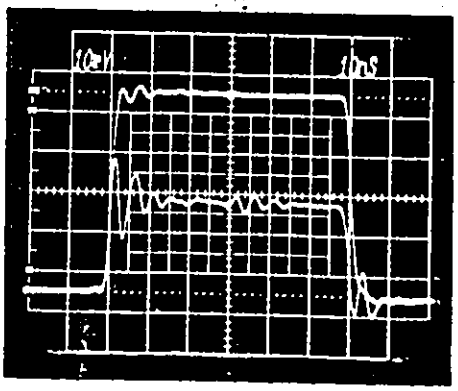

Fig. 3-22

Measured dc attenuation factor for a Tektronix P6015 high-voltage probe.

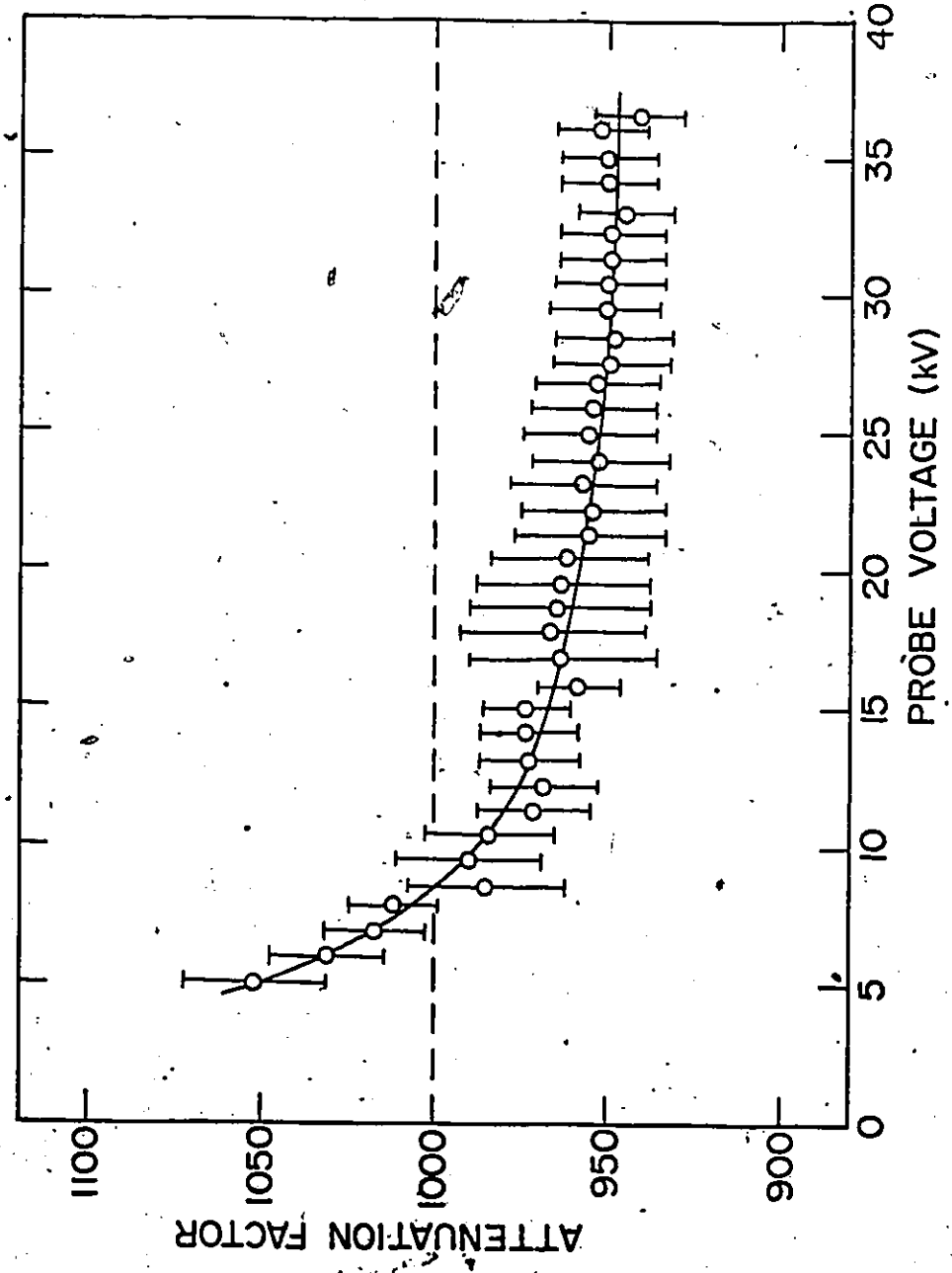
ATTENUATION FACTOR
1100
1050
1000
950
900
0
5
10
15
20
25
30
35
40
PROBE VOLTAGE (kV)

Fig. 3-23

Calibration curve for a "half-shielded" $CuSO_4$ high-voltage probe used together with two ÷10 attenuators.

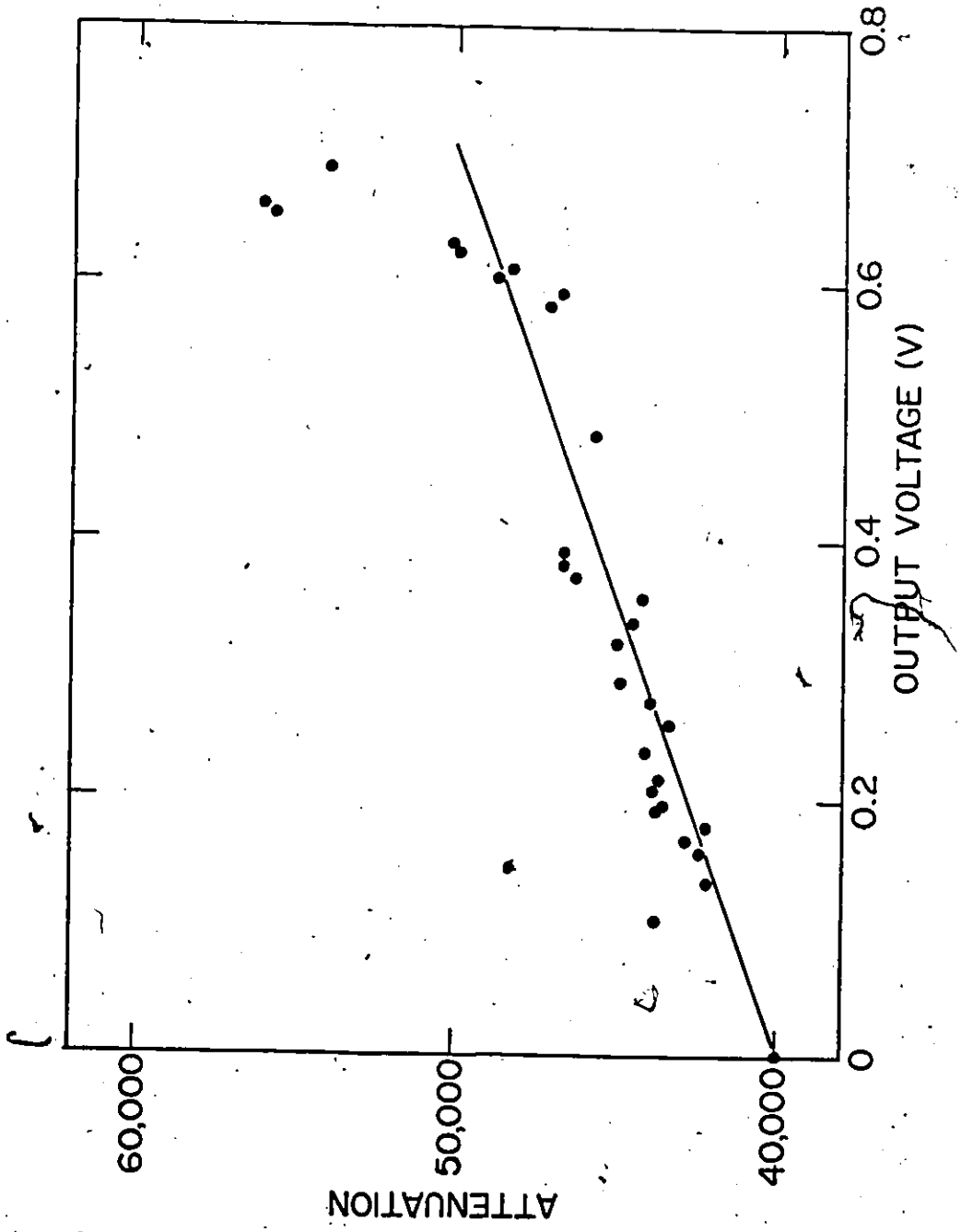
ATTENUATION
60,000
50,000
40,000
0
0.2
0.4
0.6
0.8
OUTPUT VOLTAGE (V)

Fig.3-24

Pulse response of a commercial current transformer (Ion Physics CM-10-M). This data is typical for both transformers employed. The upper trace is the voltage applied across a 50-Ω resistor; the lower trace is the current in the resistor measured using the current transformer. The time scale is 10 ns/division (large square).

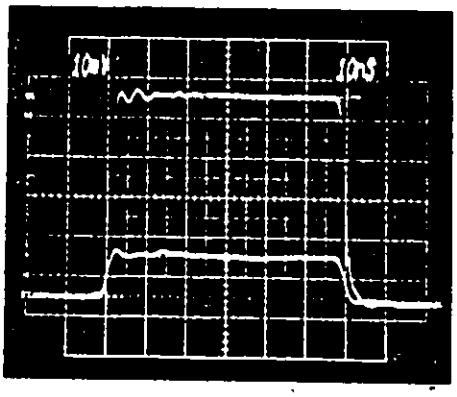
10mV
10mS

low voltages, to 50000 at ~35 kV. Typical results of measurement using this probe are shown in Figs.3-25(b) and (d), 3-26(b) and (d), and 3-27 (b) and (d).

Seven high-voltage probes of different design were compared and found to be very similar. Figure 3-21 shows the low-voltage pulse response for some of these probes. For high-voltage measurements, the sodium thiosulphate ($Na_2S_2O_3 \cdot 5H_2O$) voltage divider performed exceptionally well, and produced the minimum noise. However, this probe had a very limited lifetime (<50 pulses) resulting from rapid deterioration of the solution under high-voltage operation. In contrast, both the "half-shielded" and the "unshielded" $CuSO_4$ probe had much longer operating lifetimes. Furthermore, both probe produced similar discharge-voltage waveform, which indicates that capacitance coupling to surrounding elements was too small to affect risetime significantly. The commercial probe (Tektronix P6015), and the "compensated" resistance probe (using twenty resistors in series) both required substantial shielding when used with high-voltage discharges. A capacitance voltage divider, and a high-voltage probe based on the design of Sarjeant and Alcock [103] were included in the tests. However, these probes were designed for use at voltages below 20 kV, and could not be applied to our high-voltage measurements.

Current transformers (Ion Physics CM-10-M and CM-10-S) were employed to monitor individually the discharge-circuit current (i'), the main discharge current, and the current through one of the preionizers. These transformers both have a sensitivity of 0.1 V/A when terminated into 50 Ω. However, these were always used with two ÷10 attenuators.

Fig. 3-25

Discharge characteristics of the laser system employing a He/0.5% Xe /0.2% HCl mixture at 2957-Torr pressure and 35-kV charging voltage. The time scale (corresponding to one small square) is given at the upper right corner of each oscillogram.

(a) Upper trace: main discharge current (i)
Lower trace: di/dt.

(b) Upper trace: current in the discharge circuit (i')
Lower trace: voltage across the electrodes (v') measured external to the discharge chamber.

(c) Extended time scale for the discharge current (i') waveform.

(d) Extended time scale for the electrode voltage (v') waveform.

(a)

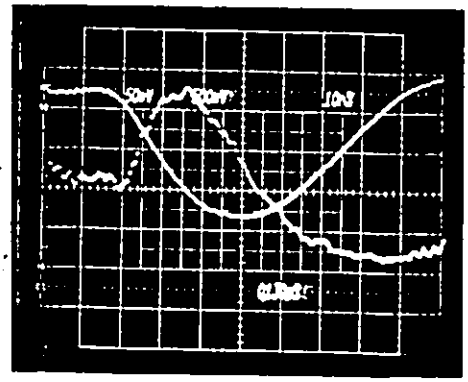

(b)

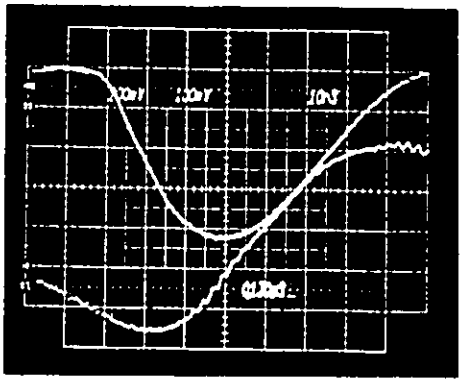

(c)

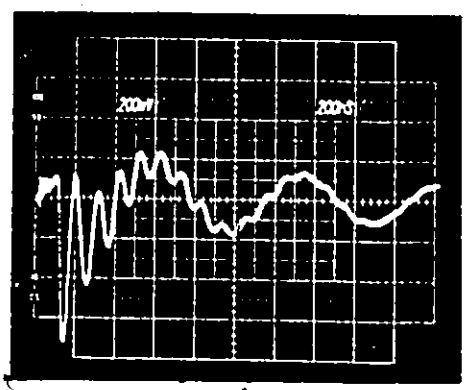

(d)

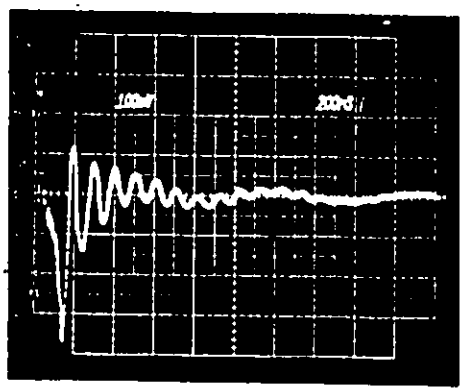

Fig. 3-26

Discharge characteristics of the laser system employing a He/0.5% Xe /0.2% HCl mixture at 2880-Torr pressure and 35-kV charging voltage. The time scale (corresponding to one small square) is given at the upper right corner of each oscillogram.

(a) Upper trace: main discharge current (i)
Lower trace: di/dt.

(b) Upper trace: current in the discharge circuit (i')
Lower trace: voltage across the electrodes (v') measured external to the discharge chamber.

(c) Extended time scale for the discharge current (i') waveform.

(d) Extended time scale for the electrode voltage (v') waveform.

(a)

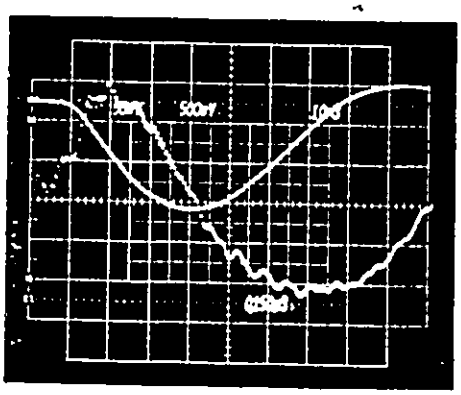

(b)

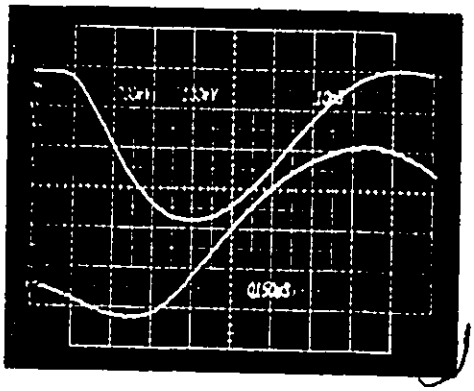

(c)

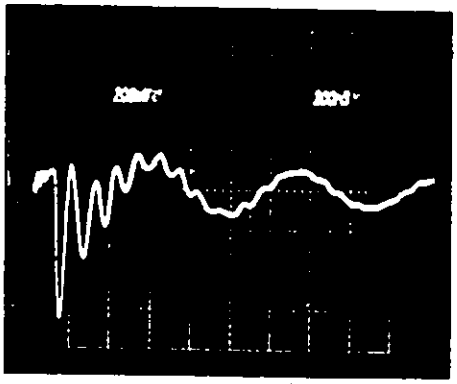

(d)

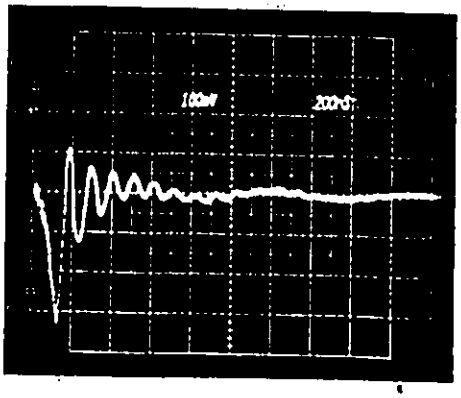

Fig. 3-27

Discharge characteristics of the laser system employing a He/0.5% Xe /0.2% HCl mixture at 2570-Torr pressure and 30-kV charging voltage. The time scale (corresponding to one small square) is given at the upper right corner of each oscillogram.

(a) Upper trace: main discharge current (i)
Lower trace: di/dt.

(b) Upper trace: current in the discharge circuit (i')
Lower trace: voltage across the electrodes (v') measured external to the discharge chamber.

(c) Extended time scale for the discharge current (i') waveform.

(d) Extended time scale for the electrode voltage (v') waveform.

(a)

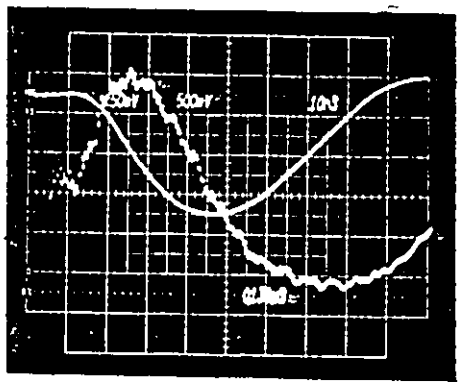

(b)

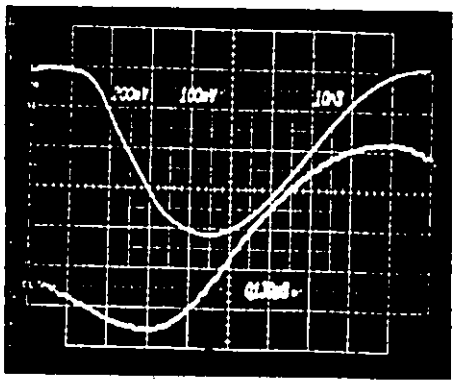

(c)

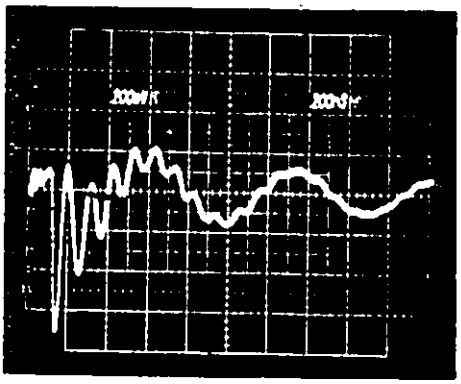

(d)

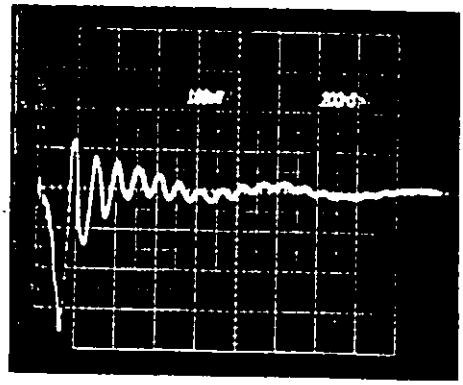

Figure 3-24 illustrates the typical response of a current transformer when monitoring a current produced in a 50-Ω resistor by an applied pulse of 10 V. The actual main discharge current was measured by shunting a small portion of the current through a small current transformer (CM-10-S) using a short length of braided wire. The ends of this wire were attached to the top and bottom of the plate (G in Fig.3-6) connecting the ceramic capacitors to the electrode feed-throughs. Typical current oscillograms are shown in Figs.3-25(a), 3-26(a) and 3-27(a). These can be compared with the oscillograms of the current in the discharge circuit (shown in Figs.3-25(b) and (c), 3-26(b) and (c), and 3-27(b) and (c)), which were obtained using a current transformer (CM-10-M) in one of the sixteen connecting rods (M in Fig.3-6). These latter oscillograms also show some current flow through the supporting structure during charging of the ceramic capacitors. The magnitude of the main discharge current was estimated using values for the stray inductances determined from LC measurements of the discharge-circuit resonances, and values for the total current in the discharge circuit (taking current flow in all sixteen connecting rods into account). However, the amplitude of the preionizer current, an example of which is shown in Fig.3-28, was measured directly using a CM-10-S current transformer, with an estimated error of 10%.

The electrical characteristics of the main discharge can be approximated by the simple circuit shown in Fig.3-29. Capacitances C_s and C, measured using a digital capacitance meter (B & K 820), are 94.5 ± 0.5 nF and 43.0 ± 0.5 nF, respectively. The stray inductances given in the figure were determined from measurements of circuit

Fig. 3-28

A current waveform for the preionizer circuit. The time scale (corresponding to one small square) is 200 ns/division.

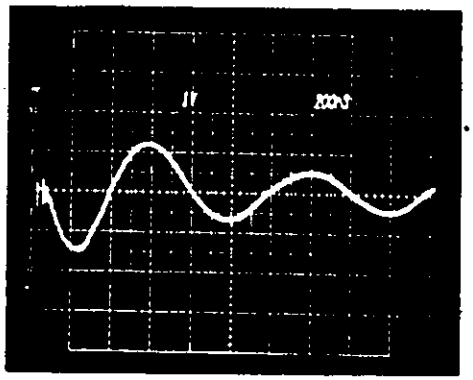

Fig. 3-29

Basic equivalent-circuit diagram for the laser discharge. SG represents the spark gap, V_0 the charging voltage, and R the discharge resistance. The latter varies with the discharge current.

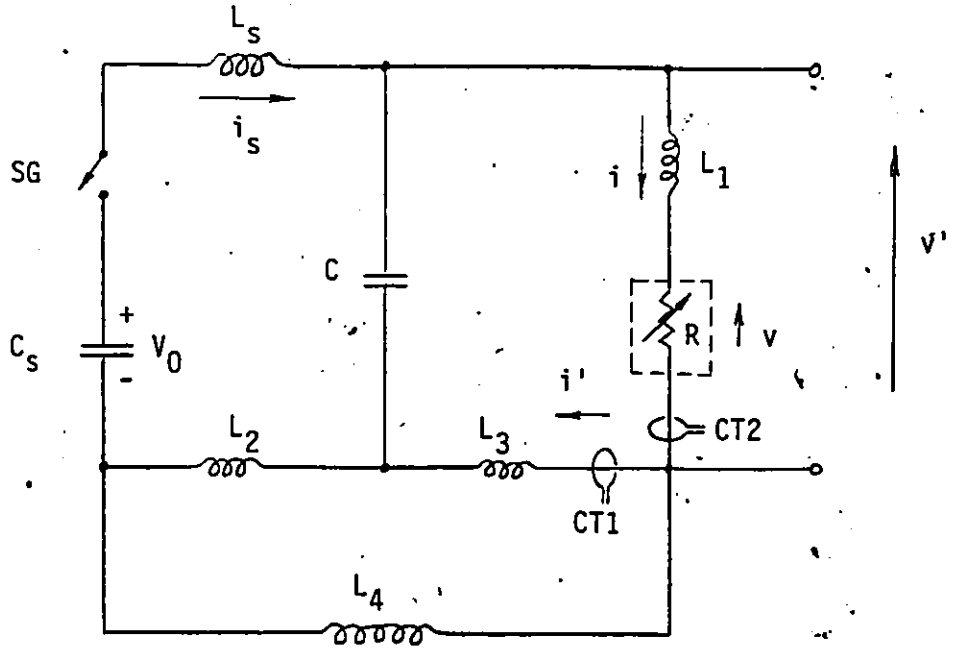

C_s = 94.5 nF

C = 43.0 nF

L_s = 455 nH

L_1 = 16.0 nH

L_2 = 8.4 nH

L_3 = 11.2 nH

L_4 = 19.6 nH

CT1, CT2 = current transformers

resonances employing a high-frequency signal generator (Hewlett-Packard 8640B) as source and an oscilloscope (Tektronix 547) as detector [104]. It is estimated that the inductance values are accurate to within 10%.

The storage capacitor (C_s) is initially charged to voltage V_0. After the spark-gap (SG) conducts, energy is transferred from the storage capacitor to the "voltage-peaking" capacitor array C, which is used to produce the main discharge. Time delays between SG breakdown and discharge breakdown, due mainly to L_s = 455 nH, are shown in Fig.3-30. These ranges from 220 ns to 285 ns for charging voltages from 35 kV to 23 kV, respectively. Similar data for fixed voltages, measured as functions of pressure, are shown in Fig.3-31. Delays range from ~205 ns, for a system operating at a high charging voltage and a low pressure (conditions for best efficiency), to ~315 ns for a similar system operating at low charging voltage and high pressure. Figures 3-30 and 3-31 also show time delays to the start of optical (laser) emission. Over a wide range of operating conditions, the laser output is delayed 30-42 ns relative to the initial breakdown of the main discharge.

During pulse-charging of capacitor C (i.e., at $-t_0 \leq t \leq 0$), the resistance of the discharge medium, R(t), is very large ($R(t<0) \approx 10 k\Omega$, which is solely the resistance of the $CuSO_4$ voltage probe). Therefore, before breakdown the main discharge current is $i(t \leq 0) \approx 0$. The current

$$i'(t \leq 0) \approx \frac{-L_2 i_s(t)}{L_2+L_3+L_4} \quad , \qquad (3\text{-}1)$$

which is measured using CT1 (CM-10-M), can be calculated employing

Fig. 3-30

Time delays as functions of charging voltage. These delays, which are taken with reference to spark-gap breakdown, are for the main discharge breakdown (--●--●--) and for the start of optical emissions, with (--⊖--⊖--) and without (--△--△--) a rear (98%) reflector. The laser employs an electrode spacing of 1.65 cm, and a He/0.5% Xe/0.2% HCl mixture at 2957-Torr pressure.

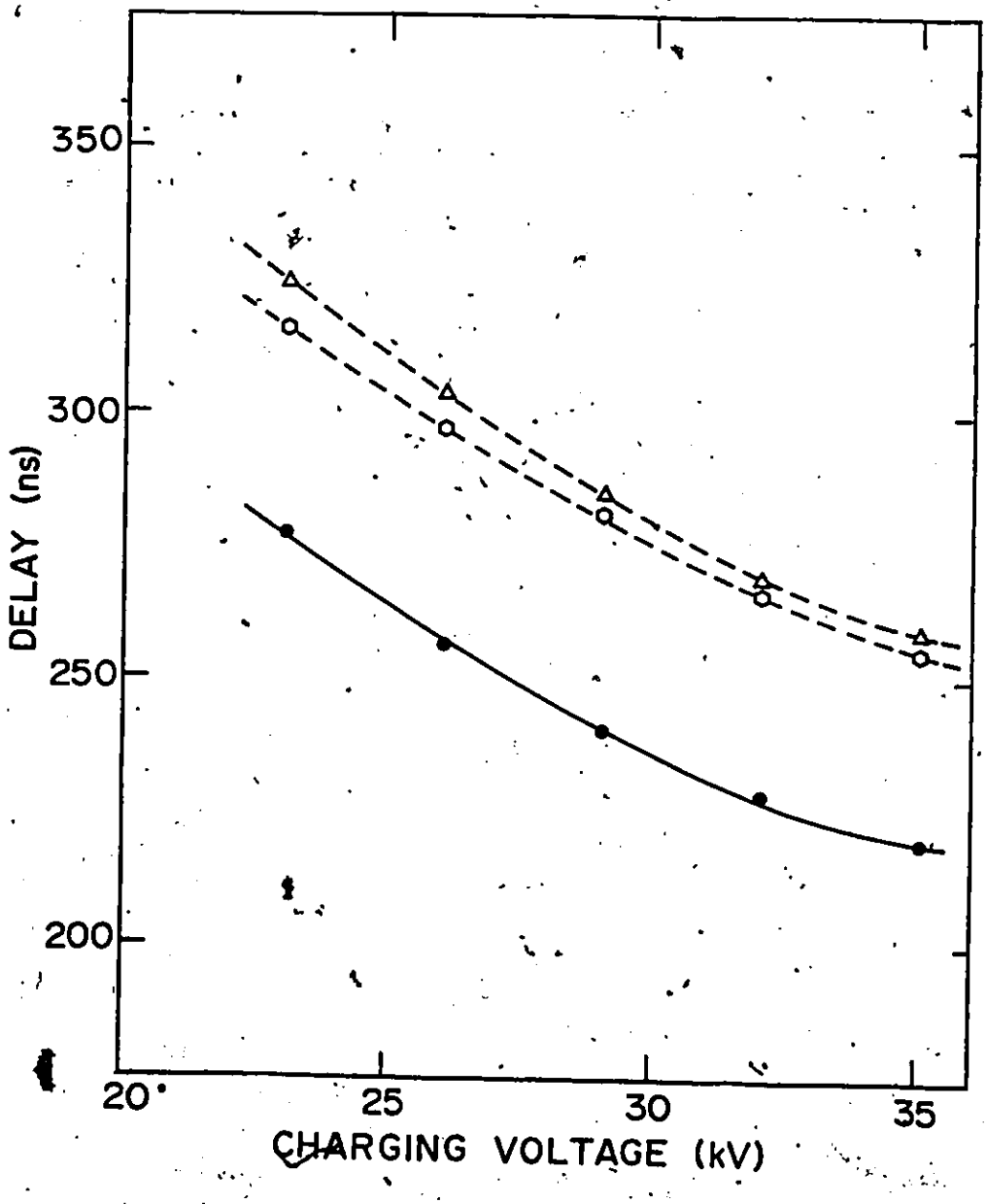
350
300
250
200
DELAY (ns)
20
25
30
35
CHARGING VOLTAGE (kV)

Fig. 3-31

Time delays as functions of gas pressure for charging voltages of 25 kV (●,o), 30 kV (▲,Δ) and 35 kV (■,□). These delays, which are taken with reference to the initial breakdown of the spark gap, are for the main discharge and for the optical emission. The laser employs an electrode spacing of 1.65 cm, and a He/0.5% Xe/0.2% HCl mixture.

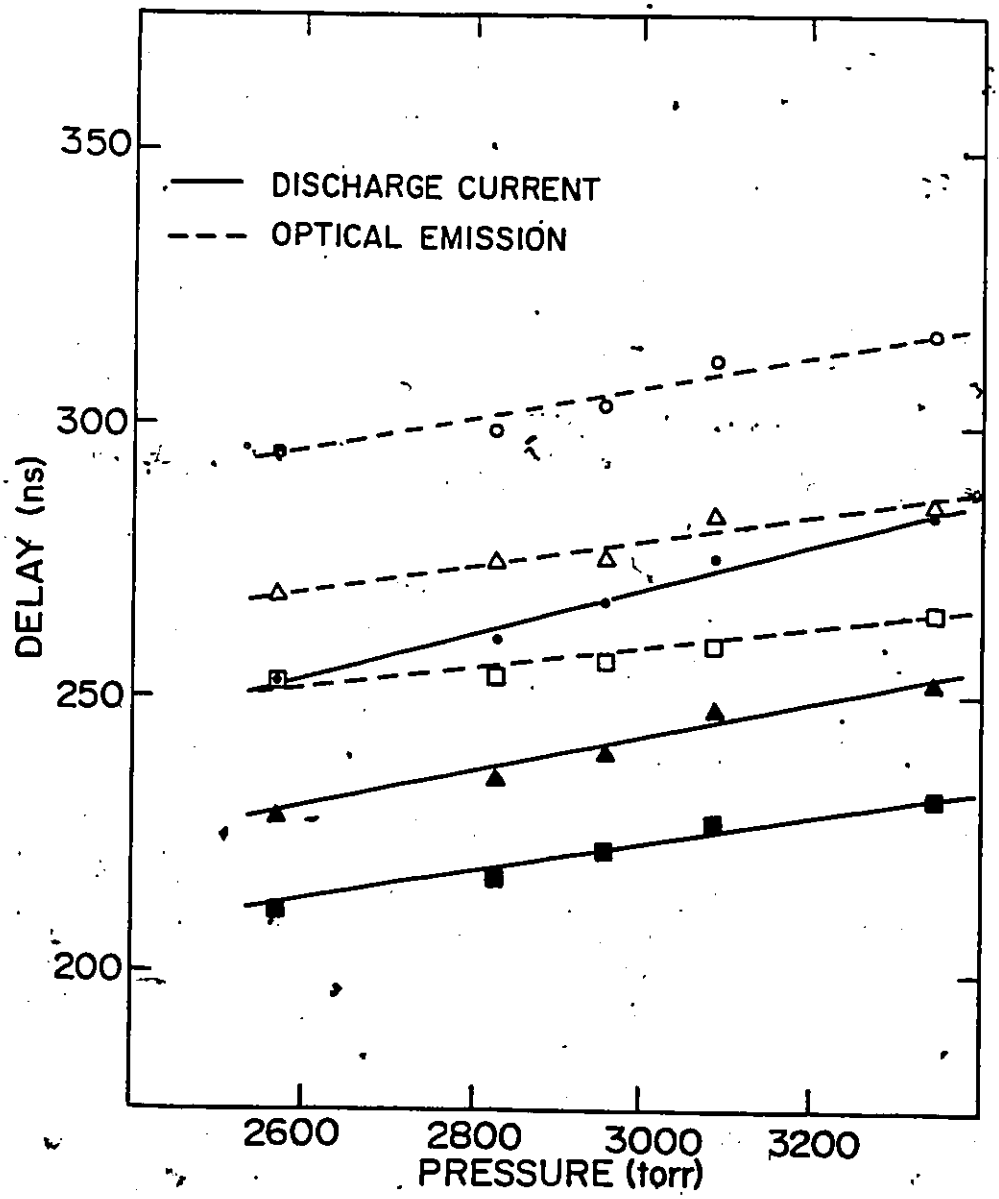
DISCHARGE CURRENT
OPTICAL EMISSION
DELAY (ns)
350
300
250
200
2600
2800
3000
3200
PRESSURE (torr)

$$\left[L_s + \frac{L_2(L_3+L_4)}{L_2+L_3+L_4}\right] \frac{di_s(t)}{dt} + \left(\frac{1}{C_s} + \frac{1}{C}\right)\int_{-t_0}^{t} i_s(t)dt + V_0 \cong 0 \quad , \quad (3\text{-}2)$$

where $i_s(t)$ is the current due to the energy transfer from the storage capacitor. The capacitance C in Eq.(3-2) varies significantly with the applied voltage given by

$$v_c(t) = \frac{1}{C}\int_{-t_0}^{t} [i_s(t)-i(t)]dt \quad . \quad (3\text{-}3)$$

According to the manufacturer's specifications, the low-voltage capacitance value of the ceramic capacitors employed for C (Murata series DHS) can decrease ~40% at the rated dc voltage (40 kV). Capacitance change with frequency is relatively insignificant. Figure 3-32 illustrates the variation of capacitance with voltage. These data were obtained by measuring the discharge time of the capacitor through the resistance (99.2±1.4 MΩ) of a high-voltage probe (Tektronix P6015), employing a storage oscilloscope (Tektronix 466) for observation. An appropriate voltage-dependent capacitor (C) was always used for the solution of Eq.(3-2).

During discharge ($t \geq 0$), the current in the circuit can be evaluated from

$$i'(t) = \frac{(L_2+L_4)i(t)-L_2 i_s(t)}{L_2+L_3+L_4} \quad . \quad (3\text{-}4)$$

The currents $i(t)$ and $i_s(t)$ can be determined from solution of

$$\left[L_s + \frac{L_2(L_3+L_4)}{L_2+L_3+L_4}\right] \frac{di_s(t)}{dt} + \left(\frac{1}{C_s} + \frac{1}{C}\right)\int_{-t_0}^{t} i_s(t)dt + V_0$$

Fig. 3-32

Capacitance multiplier factor for a Murata 909A ceramic capacitor (2700 pF) as a function of voltage.

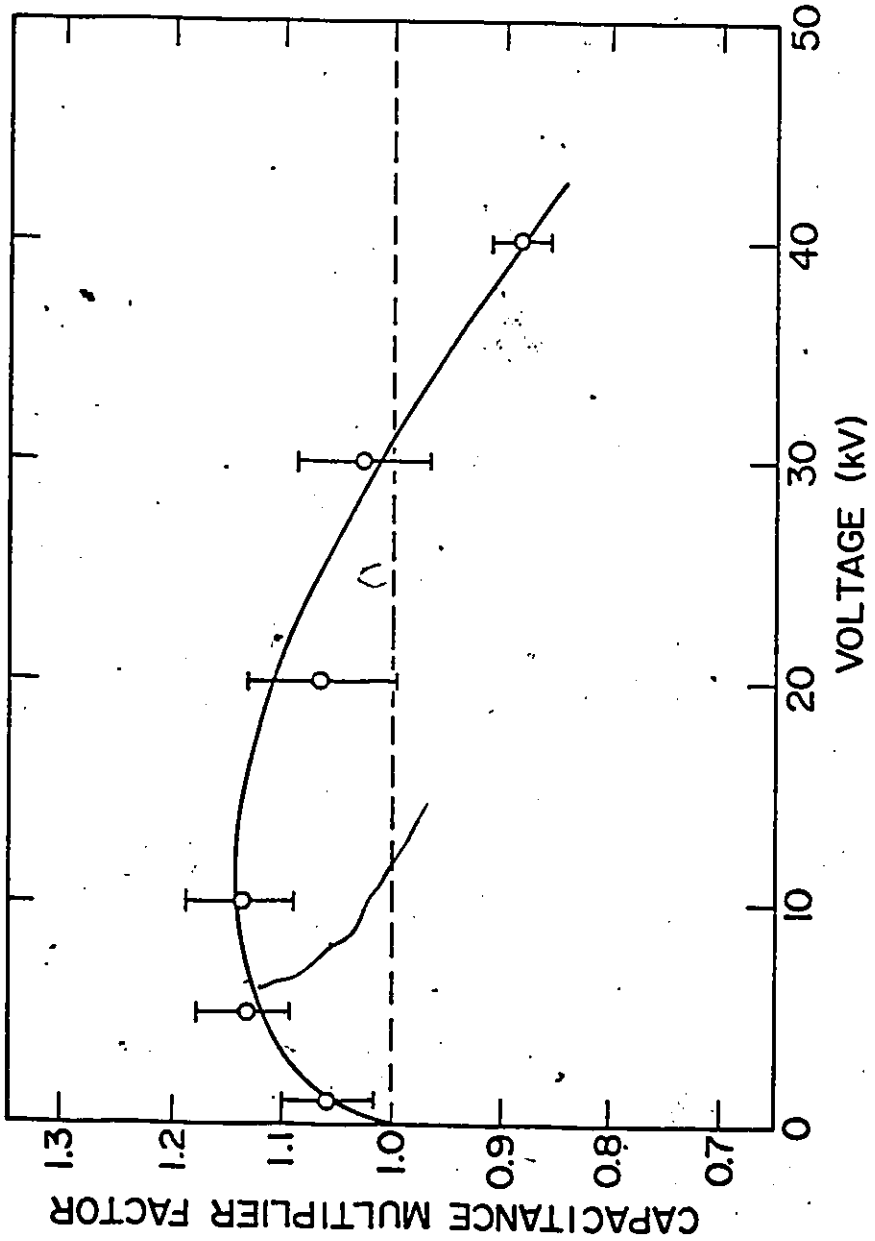
CAPACITANCE MULTIPLIER FACTOR
1.3
1.2
1.1
1.0
0.9
0.8
0.7
0
10
20
30
40
50
VOLTAGE (kV)

$$= \frac{L_2 L_3}{L_2+L_3+L_4} \frac{di(t)}{dt} + \frac{1}{C} \int_{-t_0}^{t} i(t)dt \qquad (3\text{-}5)$$

and

$$\left[L_1 + \frac{L_3(L_2+L_4)}{L_2+L_3+L_4}\right] \frac{di(t)}{dt} + i(t)R(t) + \frac{1}{C} \int_{-t_0}^{t} i(t)dt$$

$$= \frac{L_2 L_3}{L_2+L_3+L_4} \frac{di_s(t)}{dt} + \frac{1}{C} \int_{-t_0}^{t} i_s(t)dt \quad . \qquad (3\text{-}6)$$

As the main discharge current conducts, the discharge impedance (which is mostly resistive),

$$R(t) = v(t)/i(t) \quad , \qquad (3\text{-}7)$$

drops rapidly (~10 ns) to below 1 Ω. For practical reasons, the discharge voltage, v(t), cannot be measured directly. The $CuSO_4$ voltage probe, located external to the discharge, measures

$$v_1(t) = v(t) + L_1 \frac{di(t)}{dt} \quad . \qquad (3\text{-}8)$$

The inductance L_1, due to the electrodes and their connections through the discharge chamber, is estimated to be 16 nH. The oscillograms of observed voltage waveforms, in Figs.3-25(b) and (d), 3-26(b) and (d), and 3-27(b) and (d), reveal no evidence of an abrupt drop in v_1 at gas breakdown. The computed voltage pulses, presented in Figs.3-33(a), 3-34(a) and 3-35(a), show only a gradual decrease when the main discharge current does not increase too rapidly (as is the case at high gas pressures). These gradual changes in both voltage and current result from a relatively slow drop in the discharge impedance, as demonstrated in Figs.3-33(b), 3-34(b) and 3-35(b). Moreover, the

Fig. 3-33

Electrical characteristics of the main discharge, as functions of time, for the laser system employing an electrode spacing of 1.65 cm, a 35-kV charging voltage, and a He/0.5% Xe/0.2% HCl mixture at 2957-Torr pressure. The transient discharge voltage and current are shown in (a), and the electrical power deposited into the gas medium and the discharge impedance (voltage/current) are shown in (b). The experimental curves (solid lines) were obtained from the oscillograms in Fig.3-25. The calculated curves (dashed lines) were evaluated using the circuit in Fig.3-29.

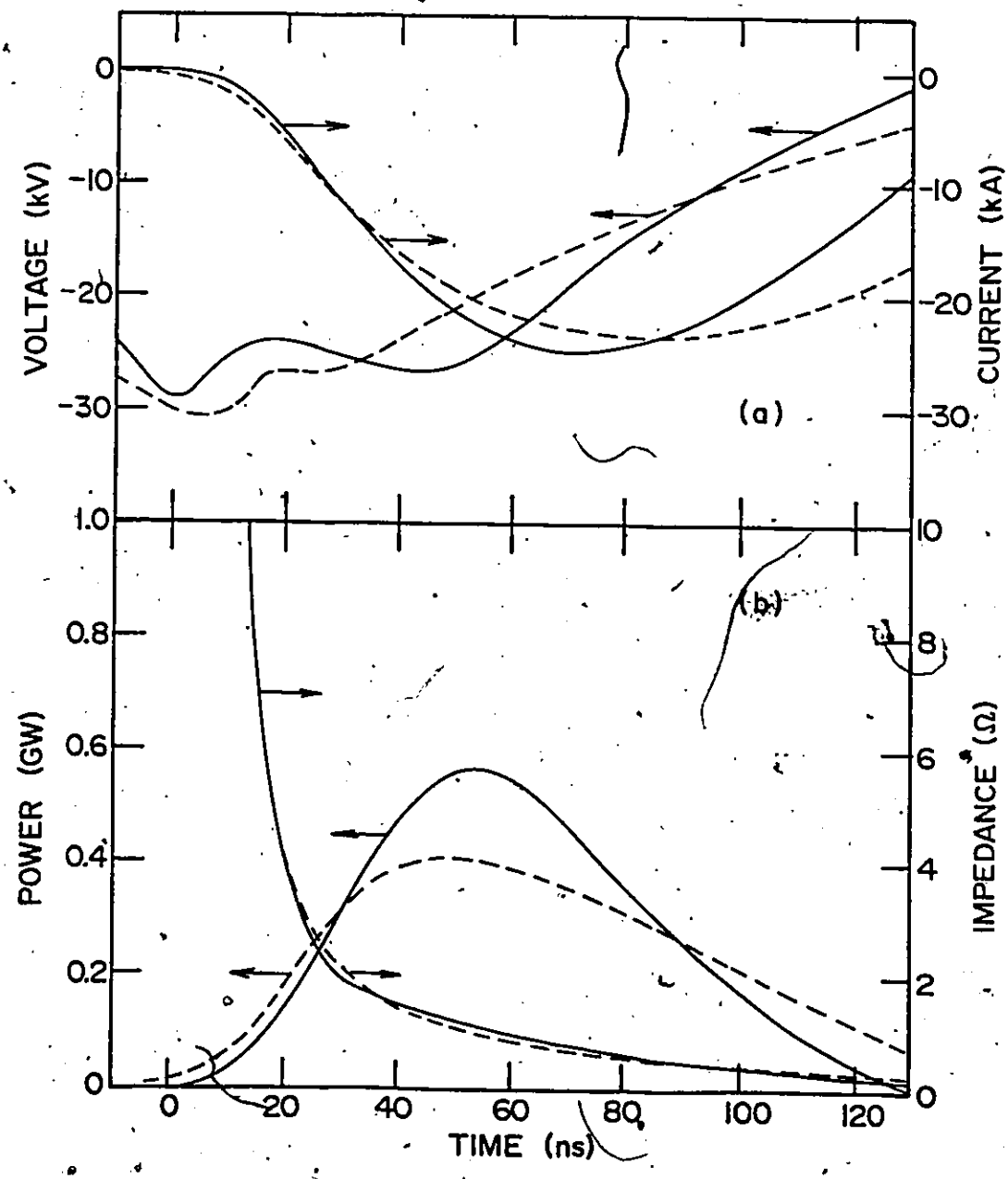
VOLTAGE (kV)
CURRENT (kA)
(a)
POWER (GW)
IMPEDANCE (Ω)
(b)
TIME (ns)
0
-10
-20
-30
1.0
0.8
0.6
0.4
0.2
0
10
8
6
4
2
0
20
40
60
80
100
120

Fig. 3-34

Electrical characteristics of the main discharge, as functions of time, for the laser system employing an electrode spacing of 1.65 cm, a 35-kV charging voltage, and a He/0.5% Xe/0.2% HCl mixture at 2880-Torr pressure. The transient discharge voltage and current are shown in (a), and the electrical power deposited into the gas medium and the discharge impedance (voltage/current) are shown in (b). The experimental curves (solid lines) were obtained using the oscillograms in Fig.3-26. The calculated curves (dashed lines) were evaluated using the circuit in Fig.3-29.

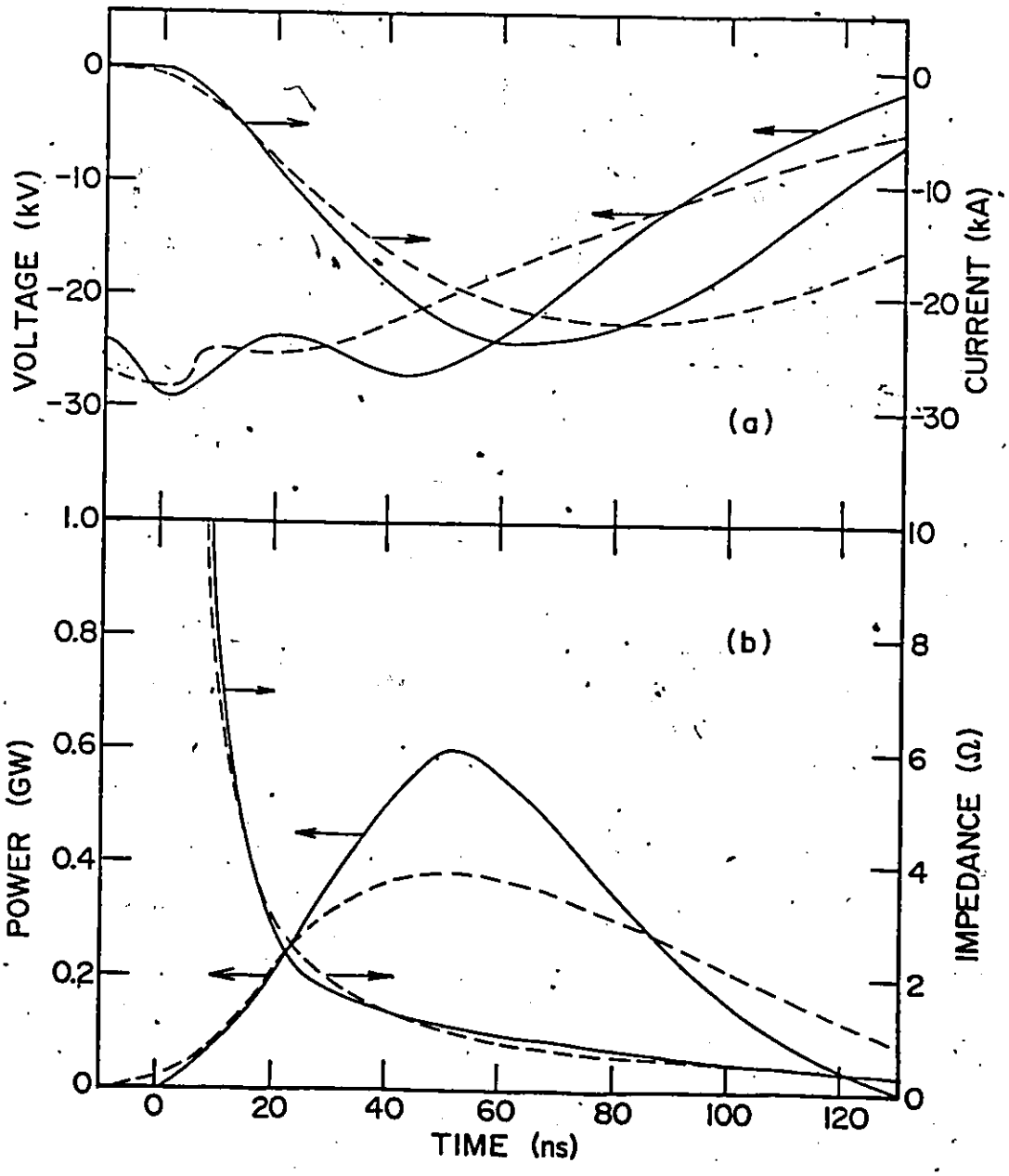
0
-10
-20
-30
VOLTAGE (kV)
0
-10
-20
-30
CURRENT (kA)
(a)
1.0
0.8
0.6
0.4
0.2
0
POWER (GW)
10
8
6
4
2
0
IMPEDANCE (Ω)
(b)
0
20
40
60
80
100
120
TIME (ns)

Fig. 3-35

Electrical characteristics of the main discharge, as functions of time, for the laser system employing an electrode spacing of 1.65 cm, a 30-kV charging voltage, and a He/0.5% Xe/0.2% HCl mixture at 2570-Torr pressure. The transient discharge voltage and current are shown in (a), and the electrical power deposited into the gas medium and the discharge impedance (voltage/current) are shown in (b). The experimental curves (solid lines) were obtained using the oscillograms in Fig.3-27. The calculated curves (dashed lines) were evaluated using the circuit in Fig.3-29.

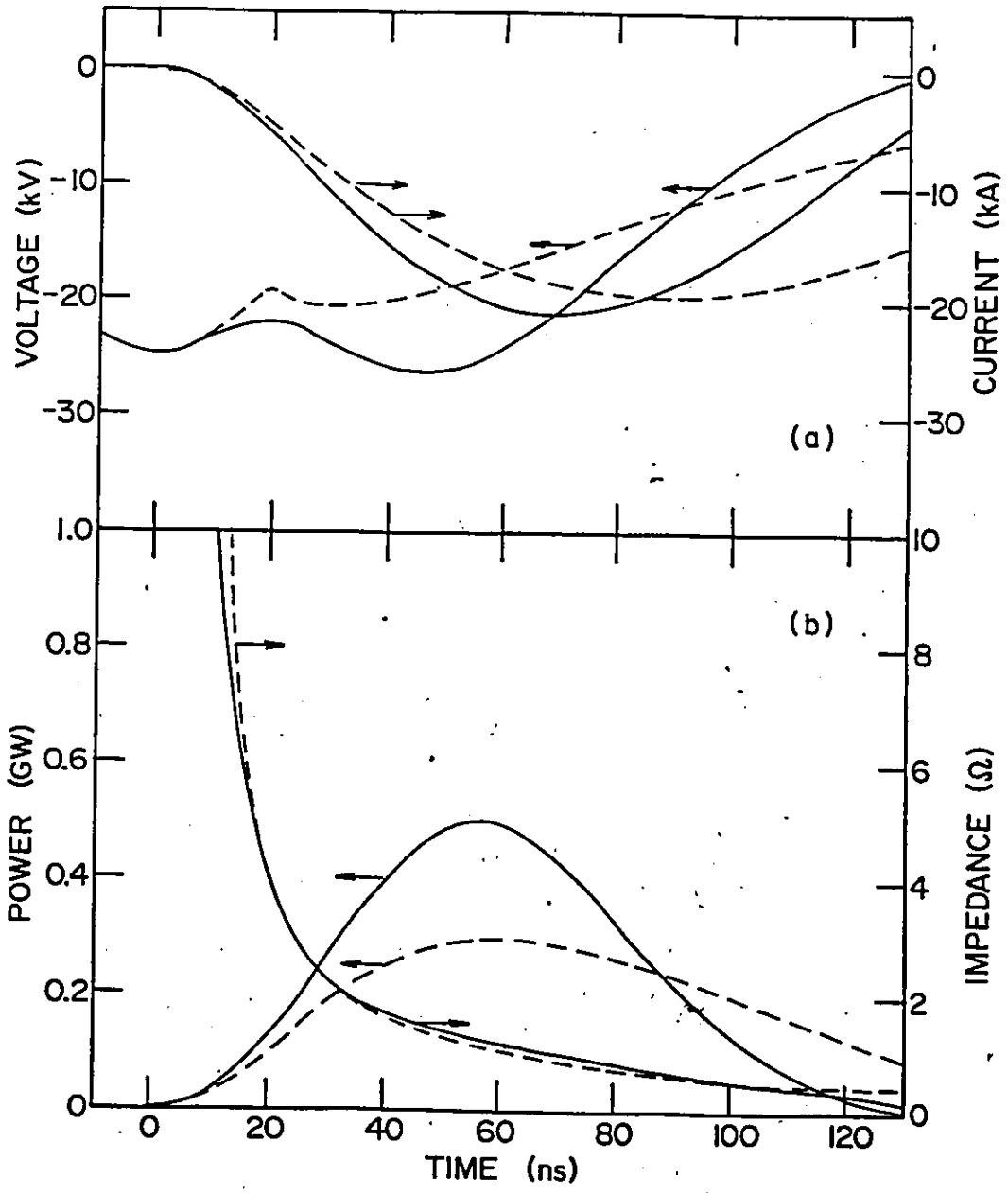
VOLTAGE (kV)
CURRENT (kA)
0
-10
-20
-30
(a)
1.0
0.8
0.6
0.4
0.2
0
10
8
6
4
2
(b)
POWER (GW)
IMPEDANCE (Ω)
0
20
40
60
80
100
120
TIME (ns)

the second peak in the discharge voltages (Figs.3-33(a), 3-34(a) and 3-35(a)) is due to the continuing transfer of energy from the storage capacitor. For low-pressure discharges, however, one may expect an abrupt drop in the discharge voltage corresponding to a rapid rise in the main discharge current.

The time-dependent electrical power deposited into the discharge, calculated using v(t) x i(t), and the corresponding discharge impedance, are shown in Figs.3-33(b), 3-34(b) and 3-35(b). For the first two sets of results, approximately 35 J of the 58-J energy initially stored in C is deposited into the discharge. Although this energy transfer has good efficiency, only ~0.32% of the stored energy is converted into photon energy (see Fig.3-18).

3.3.3 Optical Characteristics

The temporal evolution of laser output pulses was measured with a fast-response (sub-nanosecond) biplanar photodiode (Hamamatsu R1193U). Typical operation was with 250 V from a regulated power supply (Fluke 415B). A combination of pin-holes and fused-silica diffusers was placed in front of the detector to attenuate the laser irradiation. The detector output was displayed on a 400-MHz bandwidth storage oscilloscope (Tektronix 7834).

Optical pulse measurements, employing a 1.65-cm electrode spacing and mixtures (i) He/0.5% Xe/0.2% HCl, (ii) He/1.0% Xe/0.2% HCl, (iii) He/2.5% Xe/0.2% HCl and (iv) He/5.0% Xe/0.2% HCl, are shown in Figs.3-36 to 3-39. These oscillograms are typical of the laser pulses obtained using close to the optimum operating pressure for a particular mixture. In all cases, the peak output power and pulsewidth (FWHM) increase as

Fig. 3-36

Oscillograms of discharge-circuit currents and optical output pulses for the laser system employing an electrode spacing of 1.65 cm, charging voltages of 25 kV, 30 kV and 35 kV, and a He/0.5% Xe/0.2% HCl mixture at 2570-Torr, 2828-Torr, 2957-Torr, 3087-Torr and 3345-Torr pressures. The discharge current and the output power are represented by (i) and (ii), respectively. The time scale (corresponding to one small square) is 10 ns/division. The traces start after a delay time, from SG breakdown, of 55 ns plus the time given below the lower trace in each oscillogram.

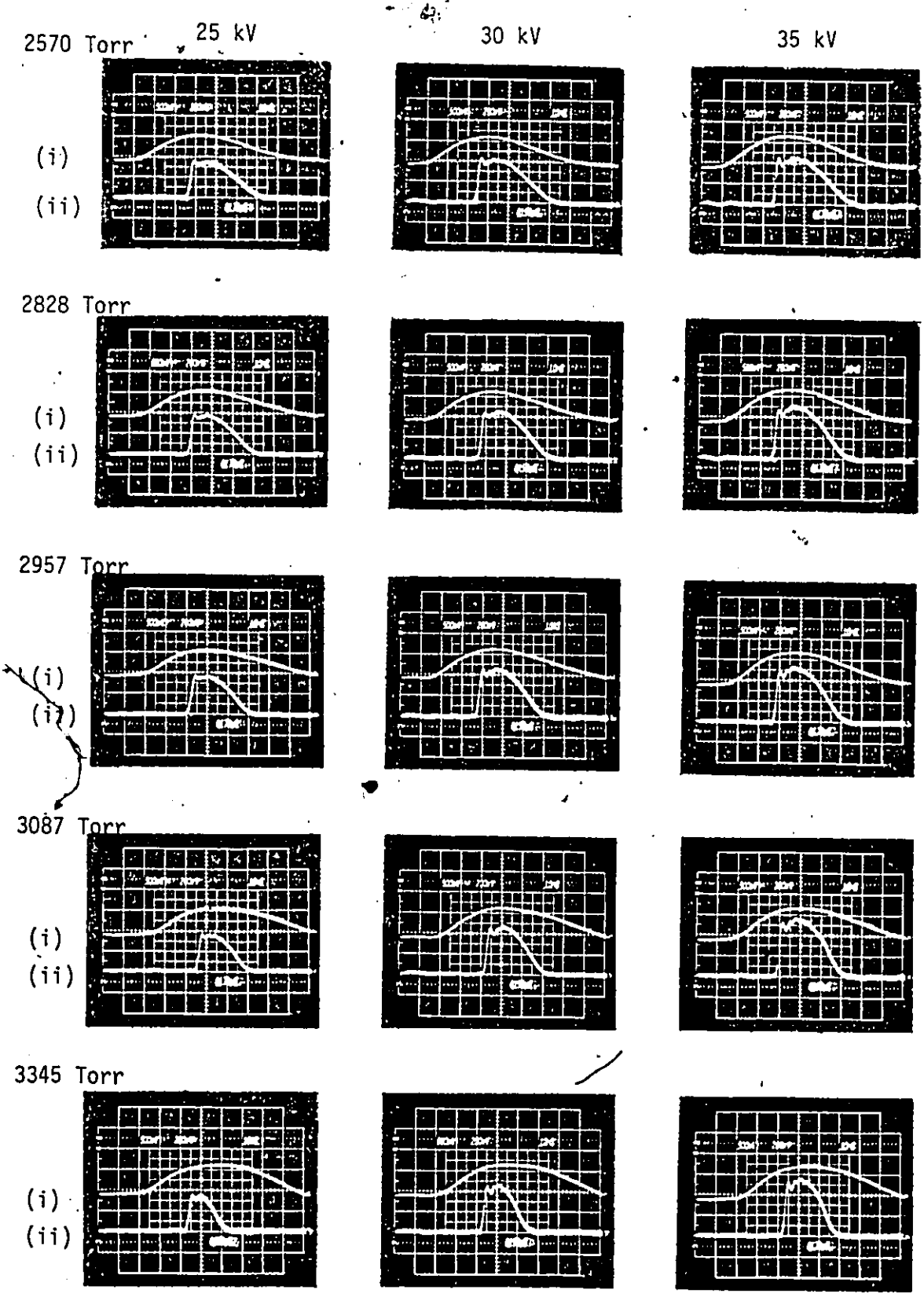
25 kV
30 kV
35 kV
2570 Torr
(i)
(ii)
2828 Torr
(i)
(ii)
2957 Torr
(i)
(ii)
3087 Torr
(i)
(ii)
3345 Torr
(i)
(ii)

Fig. 3-37

Oscillograms of discharge-circuit currents and optical output pulses for the laser system employing an electrode spacing of 1.65 cm, charging voltages of 25 kV, 30 kV and 35 kV, and a He/1.0% Xe/0.2% HCl mixture at 2311-Torr, 2570-Torr ane 2828-Torr pressures. The discharge current and output power are represented by (i) and (ii), respectively. The time scale (corresponding to one square) is 10 ns/division. The traces start after a delay time, from SG breakdown, of 55 ns plus the time given below the lower trace in each oscillogram.

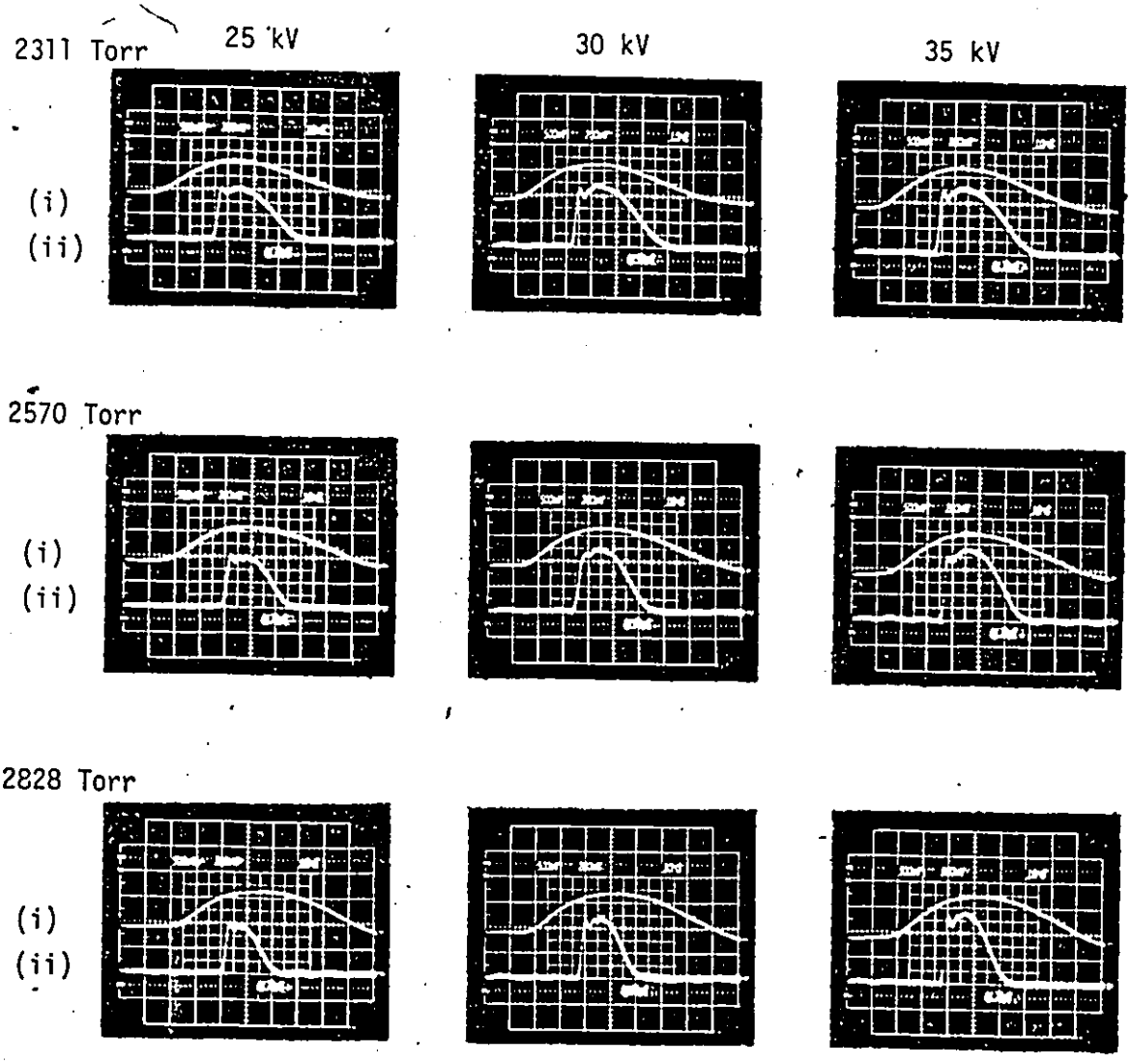
2311 Torr
25 kV
30 kV
35 kV
(i)
(ii)
2570 Torr
(i)
(ii)
2828 Torr
(i)
(ii)

Fig. 3-38

Oscillograms of discharge-circuit currents and optical output pulses for the laser system employing an electrode spacing of 1.65 cm, charging voltages of 25 kV, 30 kV and 35 kV, and a He/2.5% Xe/0.2% HCl mixture at 1794-Torr, 2053-Torr and 2311-Torr pressures. The discharge current and output power are represented by (i) and (ii), respectively. The time scale (corresponding to one small square) is 10 ns/division. The traces start after a delay time, from SG breakdown, of 55 ns plus the time given below the lower trace in each oscillogram.

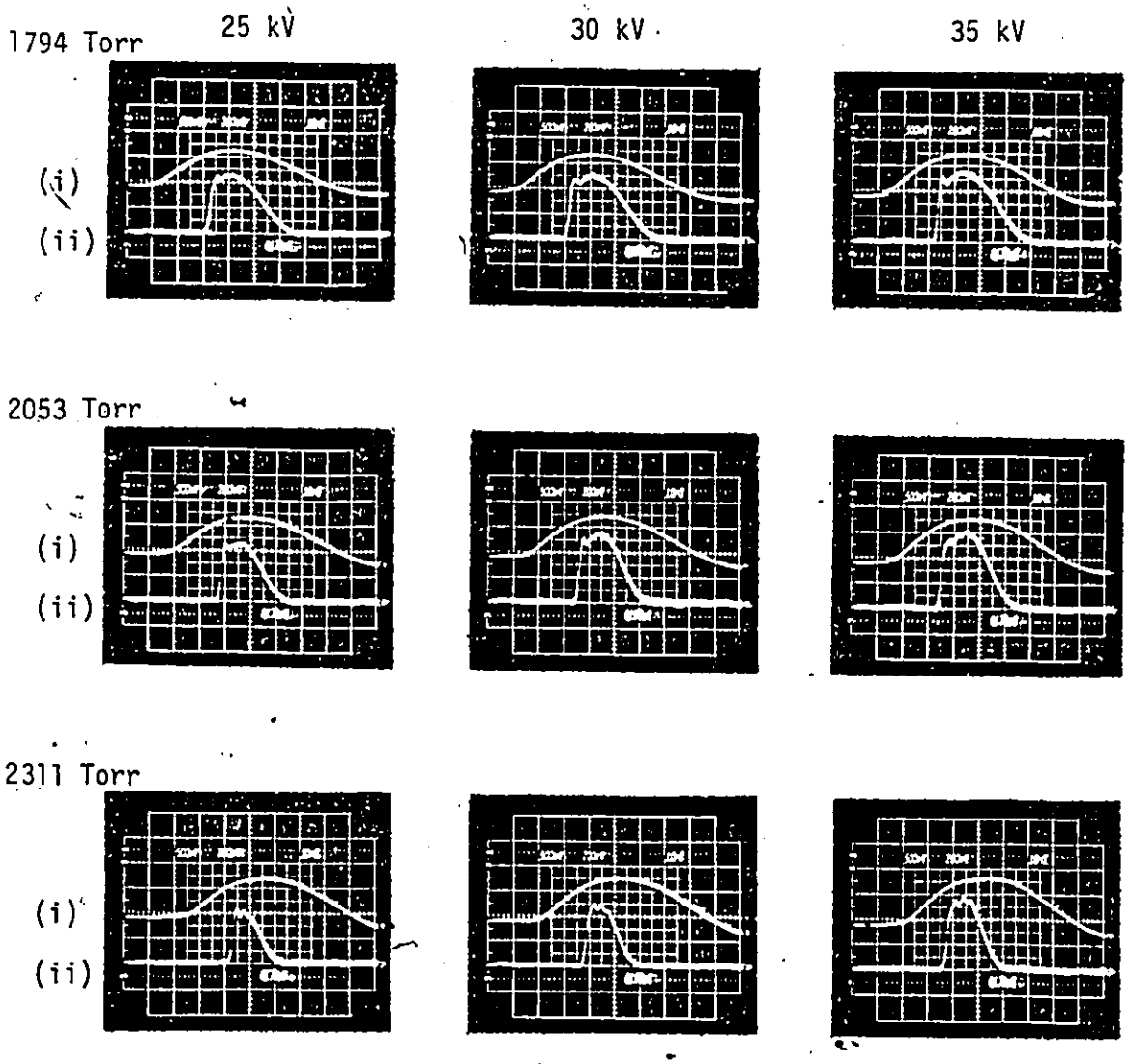
1794 Torr
25 kV
30 kV
35 kV
(i)
(ii)
2053 Torr
(i)
(ii)
2311 Torr
(i)
(ii)

Fig. 3-39

Oscillograms of discharge-circuit currents and optical output pulses for the laser system employing an electrode spacing of 1.65 cm, charging voltages of 25 kV, 30 kV and 35 kV, and a He/5.0% Xe/0.2% HCl mixture at 1536-Torr, 1794-Torr and 2053-Torr pressures. The discharge current and output power are represented by (i) and (ii), respectively. The time scale (corresponding to one small square) is 10 ns/division. The traces start after a delay time, from SG breakdown, of 55 ns plus the time given below the lower trace in each oscillogram.

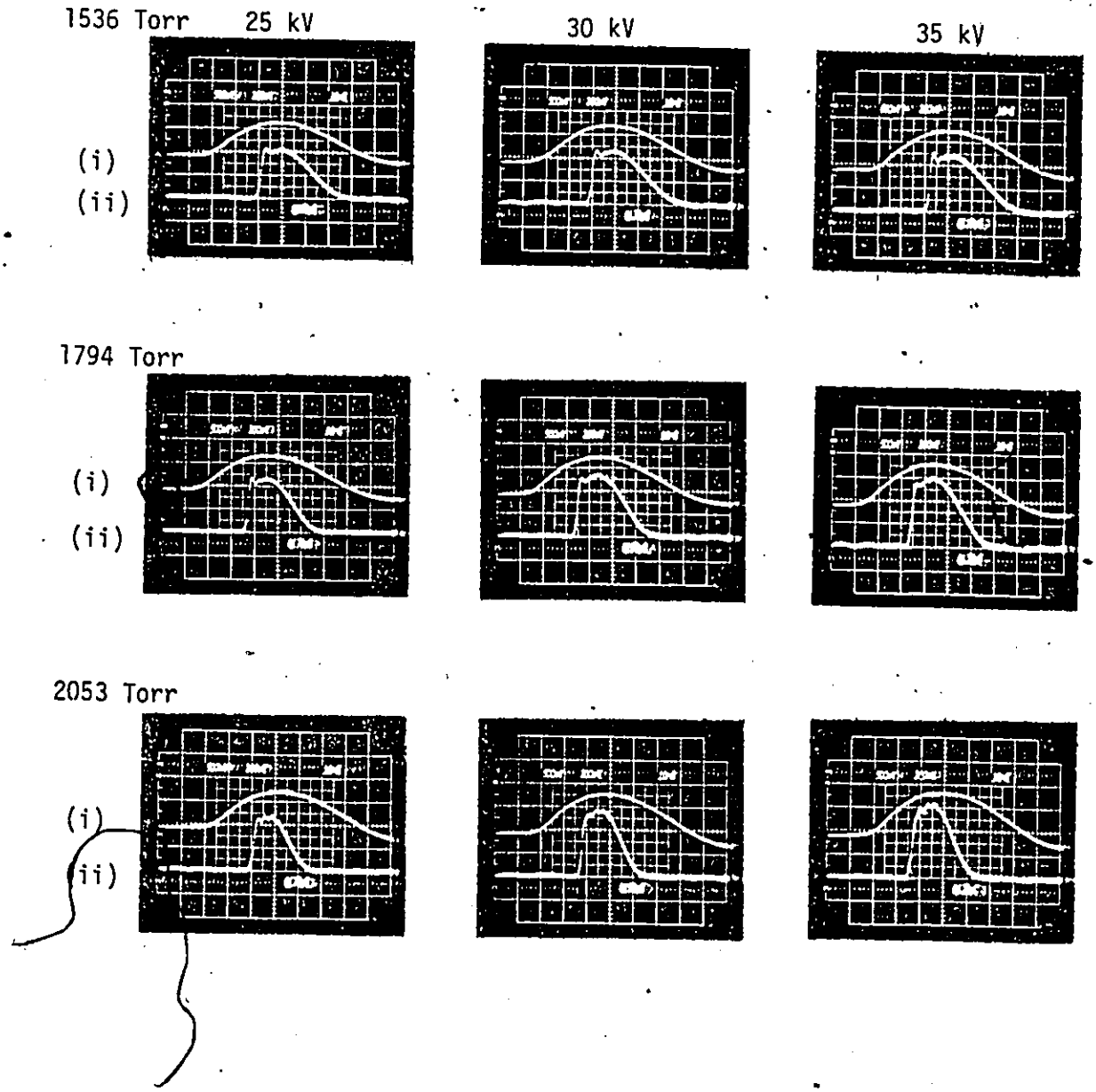
1536 Torr
25 kV
30 kV
35 kV
(i)
(ii)
1794 Torr
(i)
(ii)
2053 Torr
(i)
(ii)

the input energy is increased. The peak power also depends on the gas mixture, and increases with increased Xe content. With increasing gas pressure, there is increased peak power, but at the sacrifice of reduced pulsewidth. In order to maintain the same pulsewidth, additional energy must be deposited into the high-pressure medium. The relationships between optical pulsewidth and operating pressure for a typical He/0.5% Xe/0.2% HCl mixture, at charging voltages of 25 kV, 30 kV and 35 kV, are shown in Fig.3-40. The increase in pulsewidth with decreasing pressure is evident from the figure. At low pressure, the pulsewidth changes very little with increases in charging voltage. Although a long-duration pulse is obtained at low pressures, the system operating efficiency is low because the output saturates very rapidly. This results in low output energy and peak power.

Pulsewidth usually increases fairly linearly with charging voltage. However, the pulsewidth "saturates", at a reduced value, with increasing voltage when the rear reflector is removed. This situation is illustrated in Figs.3-41(b) and 3-42 for the above He/0.5% Xe/0.2% HCl mixture at 2957-Torr pressure. At 23 kV, the pulsewidth, in the absence of the reflector, is reduced by ∿26%. As charging voltage increases, the pulse becomes broadened. The amount of broadening, however, increases very little at high voltage. Above ∿29 kV, for example, the pulsewidth is constantly ∿90% of that obtained when a rear (98%) reflector is used. The output energy characteristics of the system equipped without and with the reflector are compared in Fig.3-41(a). At low charging voltage, the ratio of their energy

Fig. 3-40

Optical pulsewidth (FWHM) as a function of total gas pressure for the laser system employing an electrode spacing of 1.65 cm, charging voltages of 25 kV (●), 30 kV (▲) and 35 kV (■), and a He/0.5% Xe/0.2% HCl mixture. The anomalous data point in circle corresponds to the "flat-topped" pulse shown in Fig.3-45(c).

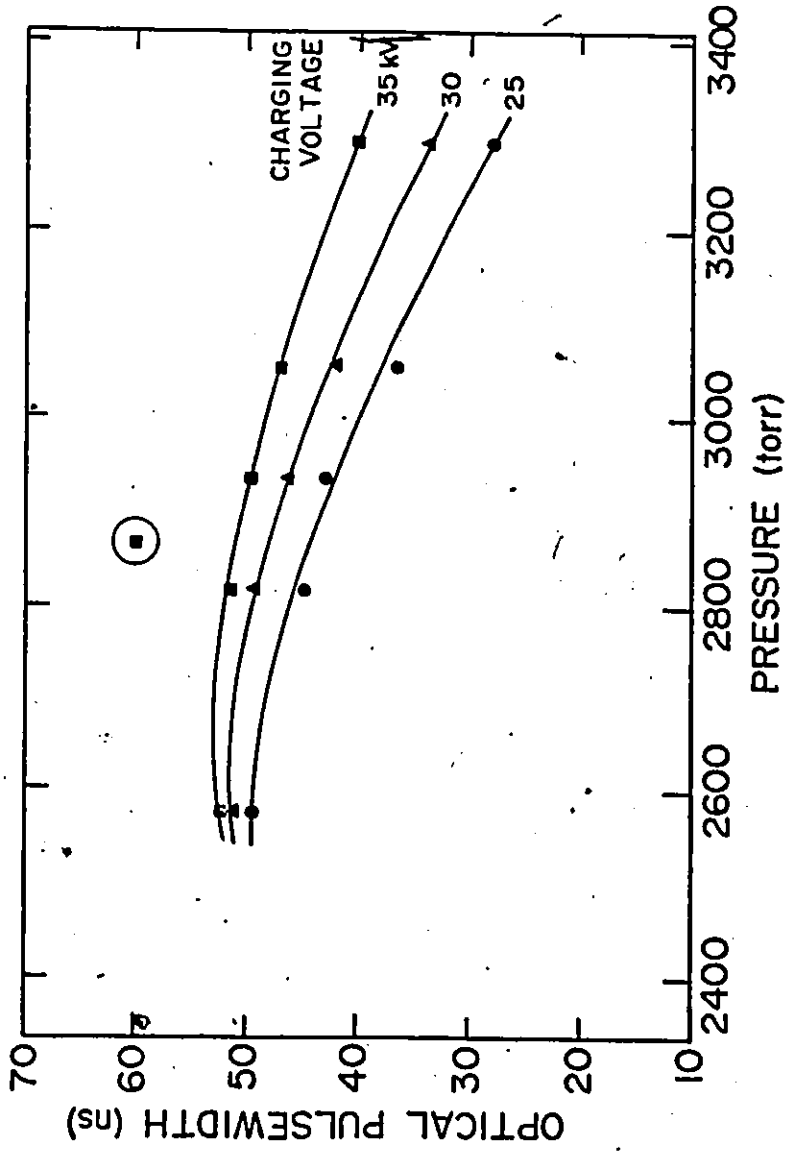
OPTICAL PULSEWIDTH (ns)
70
60
50
40
30
20
10
2400
2600
2800
3000
3200
3400
PRESSURE (torr)
CHARGING VOLTAGE
35 kV
30
25

Fig. 3-41

Comparisons of (a) the optical output energies and (b) the optical pulsewidth (FWHM), as functions of charging voltage, in the presence (●) and the absence (▲) of an external rear (98%) reflector. The laser system employed an electrode spacing of 1.65 cm, and a He/0.5% Xe/0.2% HCl mixture at 2957-Torr pressure. Data points denoted by (▽) in (a) and (b) correspond to the ratio of the data taken without, and with, the reflector.

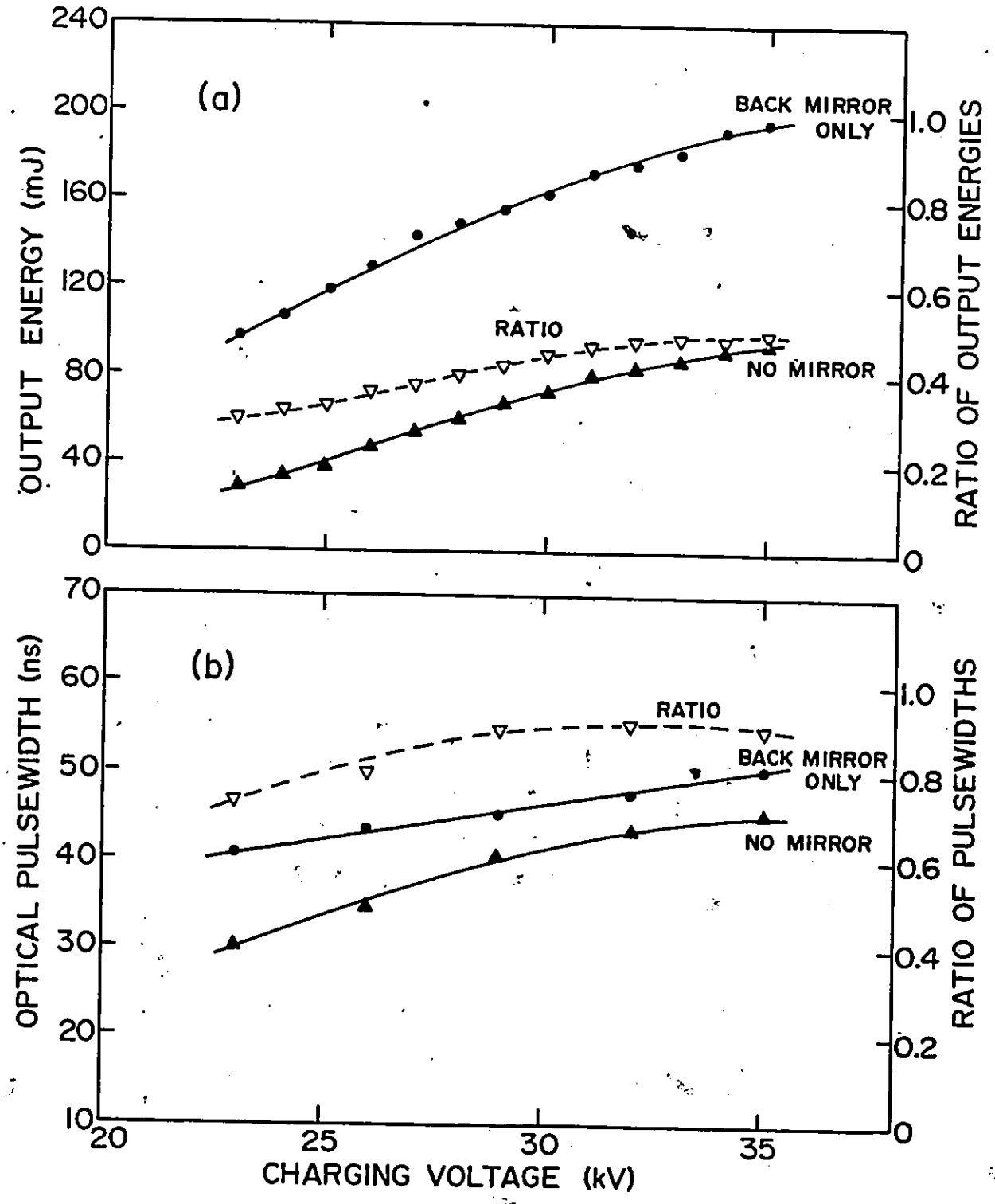
(a)
BACK MIRROR ONLY
RATIO
NO MIRROR
OUTPUT ENERGY (mJ)
RATIO OF OUTPUT ENERGIES
240
200
160
120
80
40
0
1.0
0.8
0.6
0.4
0.2
0
(b)
RATIO
BACK MIRROR ONLY
NO MIRROR
OPTICAL PULSEWIDTH (ns)
RATIO OF PULSEWIDTHS
70
60
50
40
30
20
10
1.0
0.8
0.6
0.4
0.2
0
20
25
30
35
CHARGING VOLTAGE (kV)

Fig. 3-42

Oscillograms of preionizer current (i), discharge-circuit current (ii), and optical output pulses obtained with (iii), and without (iv) an external rear (98%) reflector. The laser system employed an electrode spacing of 1.65 cm, charging voltages of 23 kV, 26 kV, 29 kV, 32 kV and 35 kV, and a He/0.5% Xe/0.2% HCl mixture at 2957-Torr pressure. The vertical-scale factor for (iv) (100 mV/division) is half that for (iii). The time scale (corresponding to one small square) is 10 ns/division. The traces start after a delay time; from SG breakdown, of 55 ns plus the time given below the lower trace in each oscillogram.

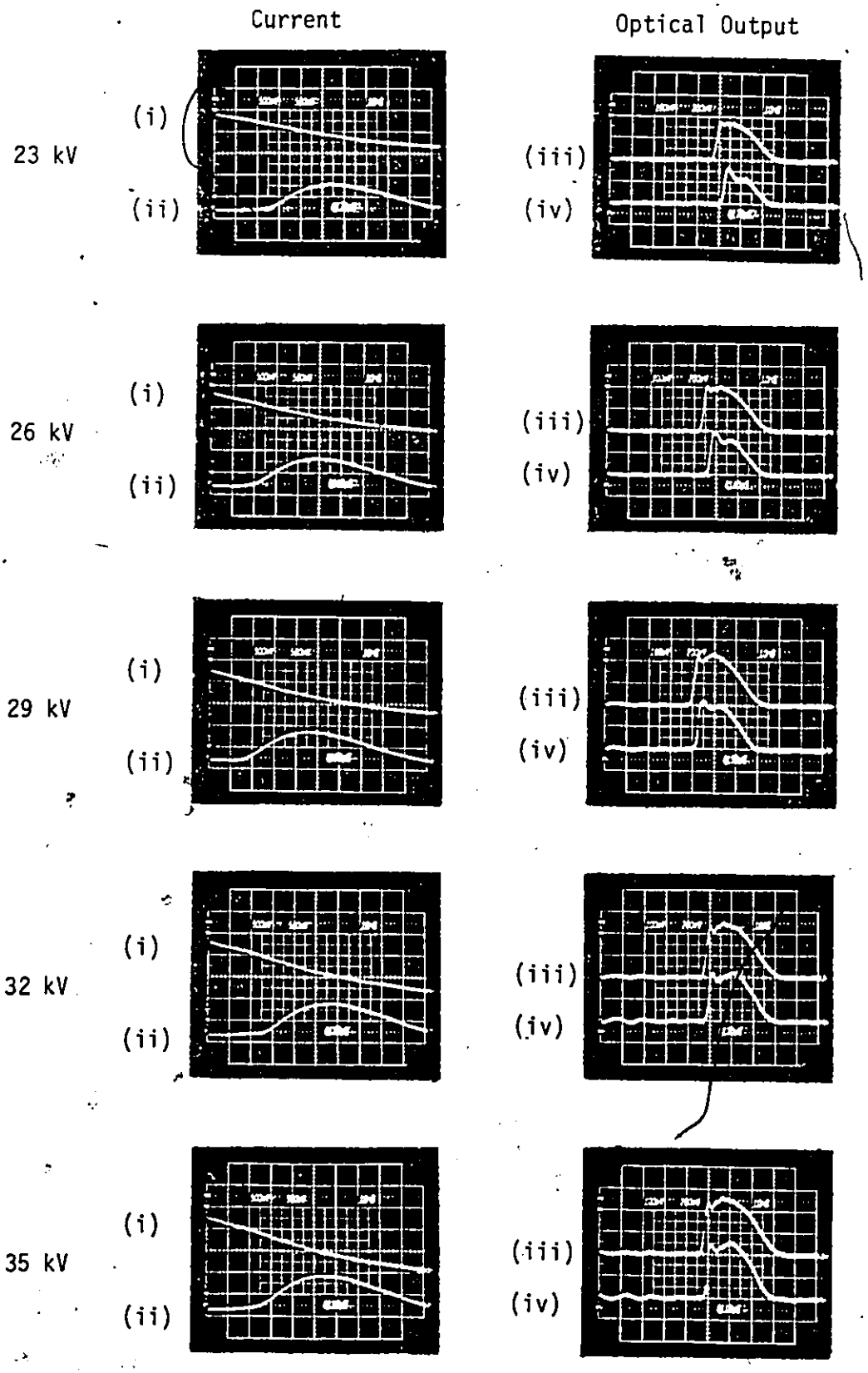
Current
Optical Output
23 kV
(i)
(ii)
(iii)
(iv)
26 kV
(i)
(ii)
(iii)
(iv)
29 kV
(i)
(ii)
(iii)
(iv)
32 kV
(i)
(ii)
(iii)
(iv)
35 kV
(i)
(ii)
(iii)
(iv)

Fig. 3-43

Oscillograms of discharge-circuit currents and optical output pulses for the laser system employing an electrode spacing of 1.97 cm, charging voltages of 25 kV, 30 kV and 35 kV, and a He/1.0% Xe/0.2% HCl mixture at 2311-Torr, 2828-Torr and 3345-Torr pressures. The discharge current and output power are represented by (i) and (ii), respectively. The time scale (corresponding to one small square) is 10 ns/division. The traces start after a delay time, from SG breakdown, of 55 ns plus the time given below the lower trace in each oscillogram.

	25 kV	30 kV	30 kV
2311 Torr (i)	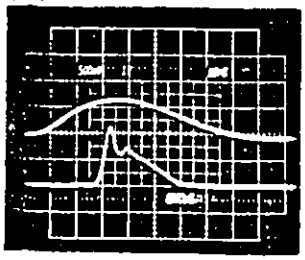	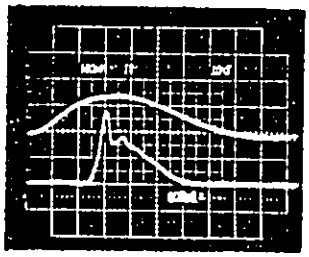	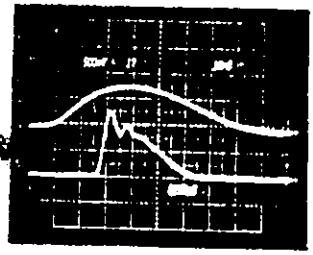
2311 Torr (ii)			
2828 Torr (i)	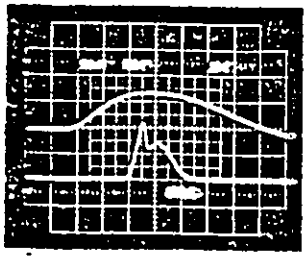	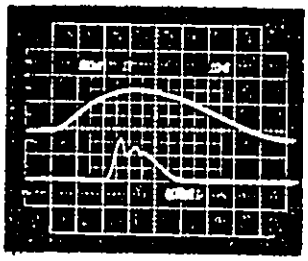	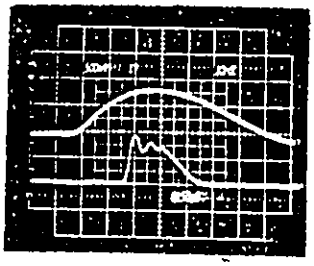
2828 Torr (ii)			
3345 Torr (i)	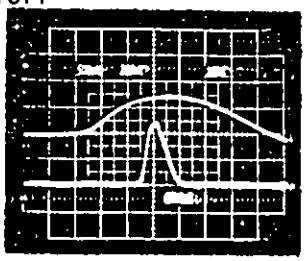	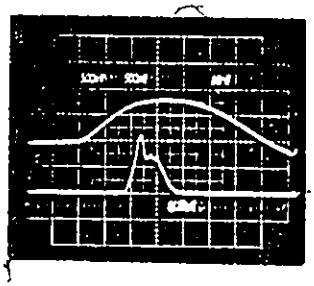	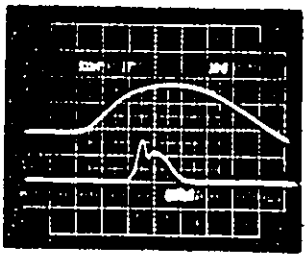
3345 Torr (ii)			

Fig. 3-44

Oscillograms of optical output pulses, employing a 2.29-cm electrode spacing, 25-kV, 30-kV and 35-kV charging voltages, and a He/2.5% Xe /0.3% HCl mixture at 1277-Torr, 1536-Torr, 1794-Torr, 2053-Torr and 2311-Torr pressures. The power scale (corresponding to a small square) is variable and appears on the upper left corner of each trace. The time scale (corresponding to a small square) is 10 ns/division. An individual trace starts after a delay time, from SG breakdown, of 55 ns plus the time given below the lower trace in each oscillogram.

	25 kV	30 kV	35 kV
1277 Torr	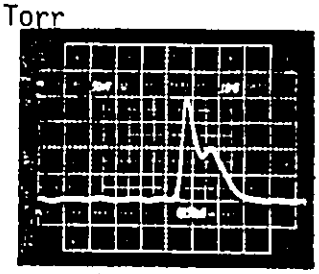	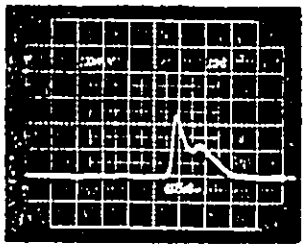	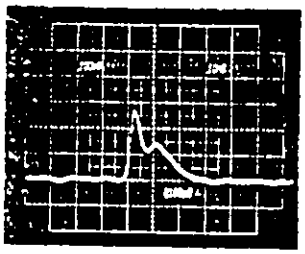
1536 Torr	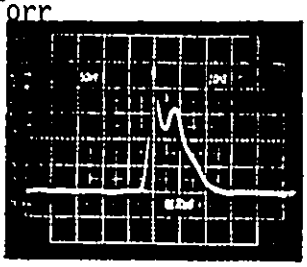	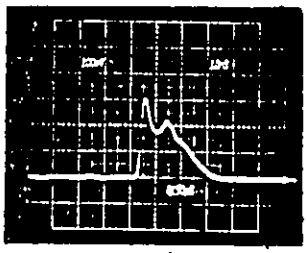	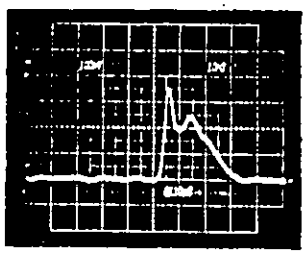
1794 Torr	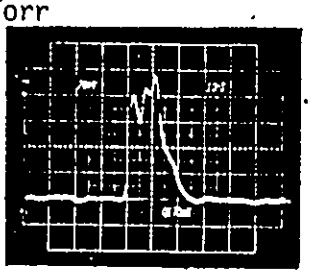	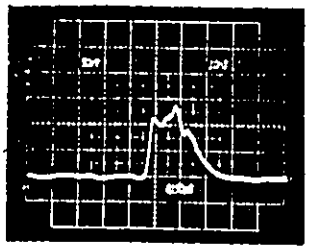	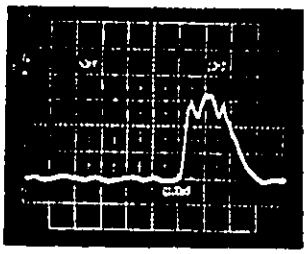
2053 Torr	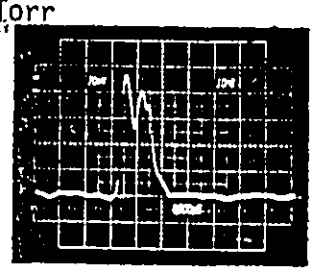	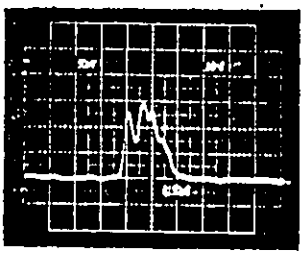	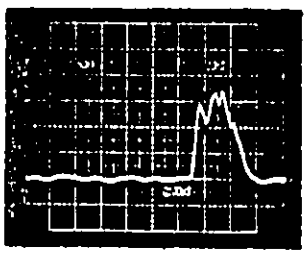
2311 Torr	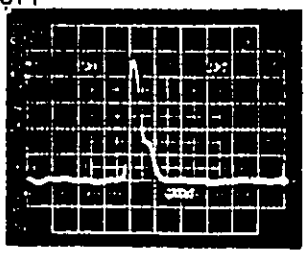	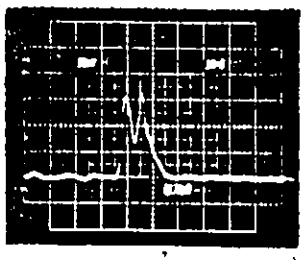	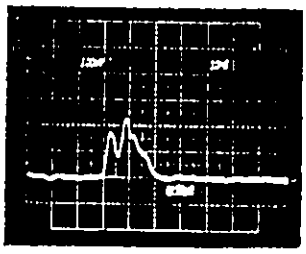

outputs is ∿0.3. The ratio at high voltage is asymptotic to ∿0.5.

Optical outputs from the laser system employing a range of electrode spacings have been investigated. The oscillograms shown in Fig.3-43 were recorded for a 1.97-cm electrode separation and a He/1.0% Xe/0.2% HCl mixture. These illustrate the change in optical pulseshapes at various charging voltages as operating pressure increases. At 3345-Torr pressure, the pulsewidth is reduced and its second peak collapses as charging voltage is reduced. The pulse becomes "triangular" when the voltage approaches 25 kV, with reduced peak power and an energy of ∿5.6 mJ. Similar "triangular" pulse has also been observed employing an electrode spacing of 2.29 cm and a He/2.5% Xe/0.3% HCl mixture. This occurs at a filling pressure of ∿2311 Torr, which is above the optimum operating pressure of ∿1794 Torr, and at a low charging voltage of 25 kV. Oscillograms for this system, recorded at 1277-Torr, 1536-Torr, 1794-Torr, 2053-Torr and 2311-Torr pressures, and 25-kV, 30-kV and 35-kV voltages, are given in Fig.3-44. The multi-peaked structures of these pulses, particularly at pressures above 1794 Torr, results from insufficient energy being deposited into the system because of a wide electrode separation.

A typical "saturated" pulseshape is achieved when the laser system employs a 1.65-cm electrode gap, a 35-kV charging voltage, and a He/0.5% Xe/0.2% HCl mixture at 2880-Torr pressure. The "flat-topped" pulseshape shown in Fig.3-45(c) is 60 ns wide and represents an optical energy of ∿200 mJ. The various pulseshapes in Fig.3-45 are arranged in ascending order of the cavity loss factor, $-\ell n\sqrt{r_1 r_2}$, where r_1 and

Fig. 3-45

Comparison of various optical output pulses produced from a laser system employing a 1.65-cm electrode spacing, a 35-kV charging voltage, and a He/0.5% Xe/0.2% HCl mixture at 2880-Torr pressure. These pulses were obtained using a range of external output couplers and in-cavity attenuators (neutral density filters). The rear and front external elements are, respectively,

(a) 98% reflector and 92% reflector,

(b) 98% reflector and fused-silica flat,

(c) 98% reflector and nil,

(d) 98% reflector plus 0.32 density filter and nil,

(e) 98% reflector plus 0.48 density filter and nil,

(f) 98% reflector plus 1.09 density filter and nil,

(g) 98% reflector plus 2.02 density filter and nil,

(h) 98% reflector plus 3.21 density filter and nil, and

(i) nil and nil.

The optical pulse in (c) has ~200-mJ total energy and a 60-ns duration (FWHM).

(a)

(i)
(ii)

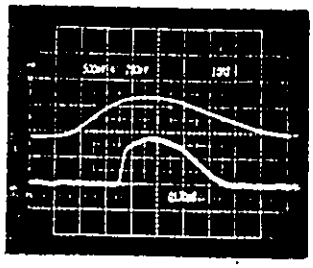

(b)

(i)
(ii)

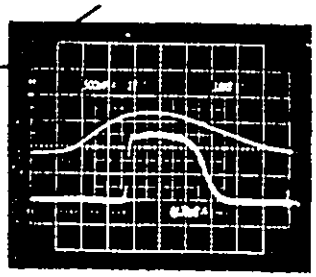

(c)

(i)
(ii)

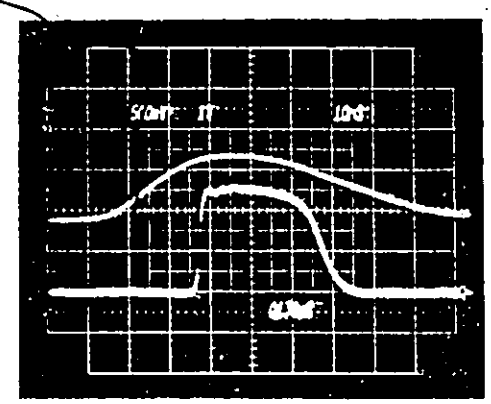

(d)

(i)
(ii)

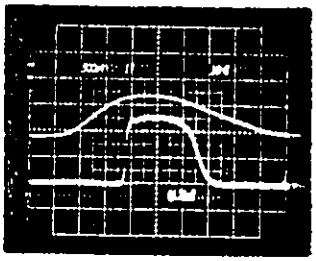

(e)

(i)
(ii)

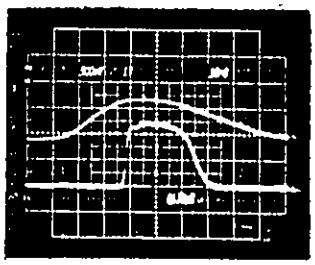

(f)

(i)
(ii)

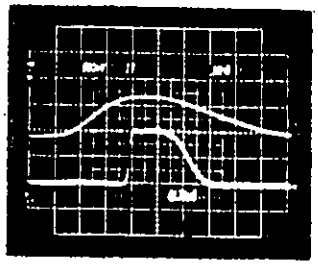

(g)

(i)
(ii)

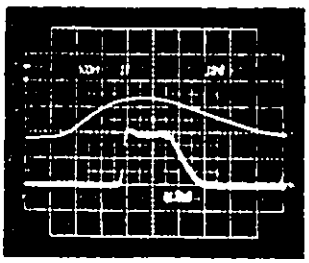

(h)

(i)
(ii)

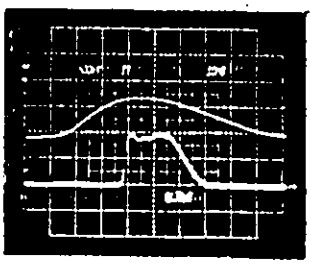

(i)

(i)
(ii)

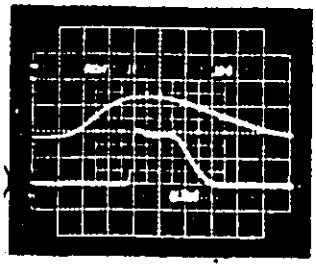

r_2 are the effective reflectances of the rear and front mirrors. The external elements, described in the figure caption of Fig.3-45, are in addition to the reflectors formed by the windows (∿9.5% reflectance). The optical output energy and pulsewidth, as functions of the loss factor, are plotted in Fig.3-46. Maximum energy output occurs for a loss factor ∿1.1. Therefore, for $r_1 = 0.98$, $r_2 \approx 0.11$, which is reasonably close to the 9.5% window reflectance.

Similar experiments have been carried out employing a 1.97-cm electrode separation, a 35-kV charging voltage, and a He/1.0% Xe/0.2% HCl mixture at 2311-Torr pressure. Results of two sets of measurements, performed ∿3 hr apart, but in the same mixture, are shown in Fig.3-47. The oscillograms in Figs.3-47(a)-(d) are for the first experiment. Those in Figs.3-47(e)-(m) are for the second experiment, and are arranged in order of increasing cavity loss, similar to the data in Fig.3-45. The two sets of pulseshapes are very similar (in particular, (a) and (e), (b) and (f), (c) and (g), and (d) and (m)), indicating that the discharge mixture did not significantly change over the time interval between measurements (∿3 hr). The output characteristics are summarized in Fig.3-48. The optimum optical energy is ∿193 mJ for a cavity loss factor of ∿1.0. In contrast to the situation represented by Fig.3-46(b), the optical pulse is not broadest in the region of maximum output. The longest-duration pulse is obtained with a high-reflectance output coupler (plus the rear (98%) reflector). As cavity loss increases, the pulse becomes narrower.

Experiments were performed, at three separate instants, using

Fig. 3-46

Optical output energy (a) and pulsewidth (b), as functions of cavity loss, for the laser system employing an electrode spacing of 1.65 cm, a charging voltage of 35 kV, and a He/0.5% Xe/0.2% HCl mixture at 2880-Torr pressure.

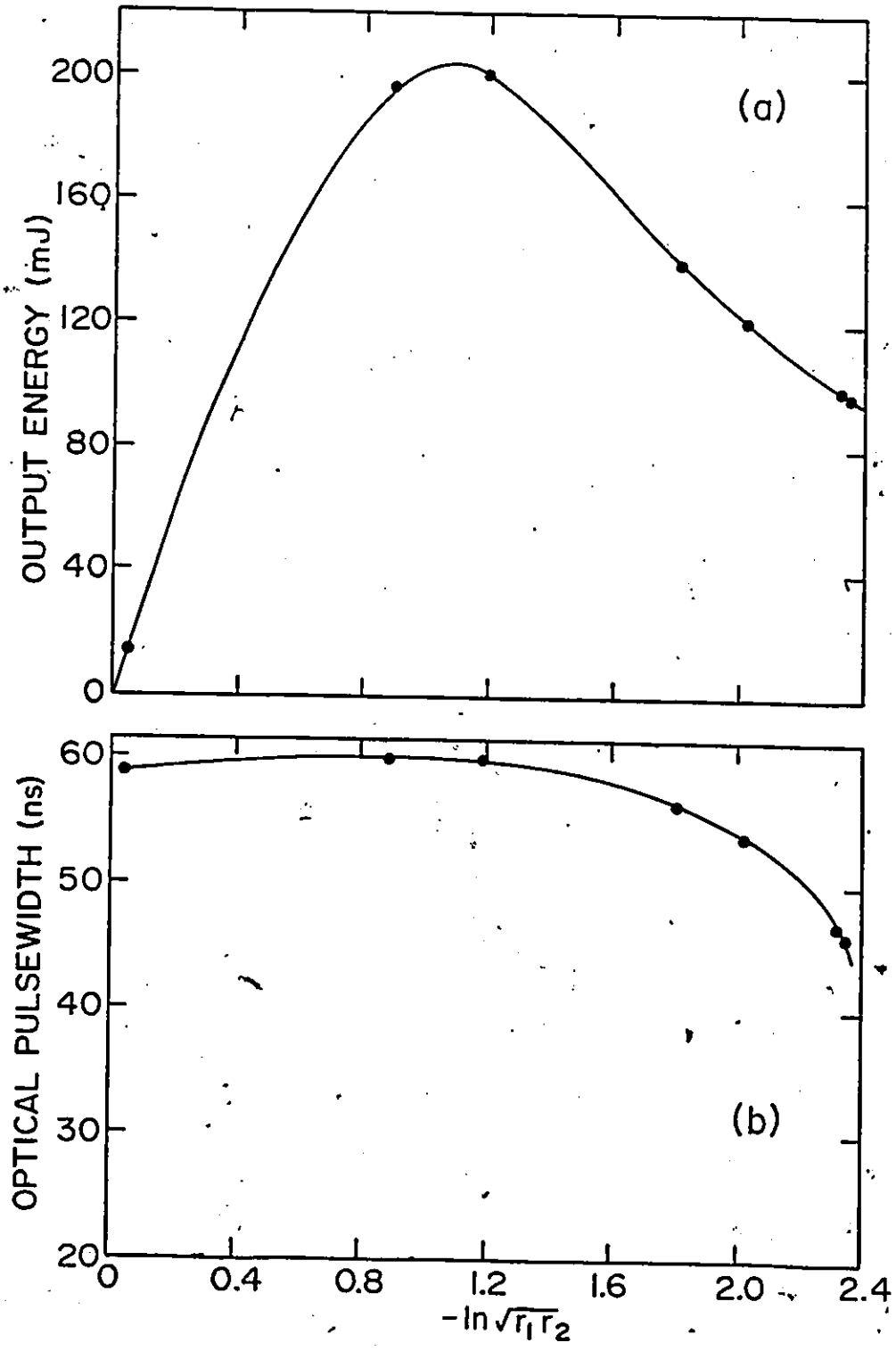
200
160
120
80
40
0
OUTPUT ENERGY (mJ)
(a)
60
50
40
30
20
OPTICAL PULSEWIDTH (ns)
(b)
0
0.4
0.8
1.2
1.6
2.0
2.4
$-\ln\sqrt{r_1 r_2}$

Fig. 3-47

Comparison of various optical output pulses produced from a laser system employing a 1.97-cm electrode spacing, a 35-kV charging voltage, and a He/1.0% Xe/0.2% HCl misture at 2311-Torr pressure. These pulses were obtained using a range of external output couplers and in-cavity attenuators (neutral density filters). Two separate sets of experimental results, (a)-(d) and (e)-(m), are presented. The respective rear and front external elements are

(a), (e) 98% reflector and 92% reflector,

(b), (f) 98% reflector and fused-silica flat,

(c), (g) 98% reflector and nil,

(h) 98% reflector plus 0.32 density filter and nil,

(i) 98% reflector plus 0.48 density filter and nil,

(j) 98% reflector plus 1.09 density filter and nil,

(k) 98% reflector plus 2.02 density filter and nil,

(l) 98% reflector plus 3.21 density filter and nil, and

(d), (m) nil and nil.

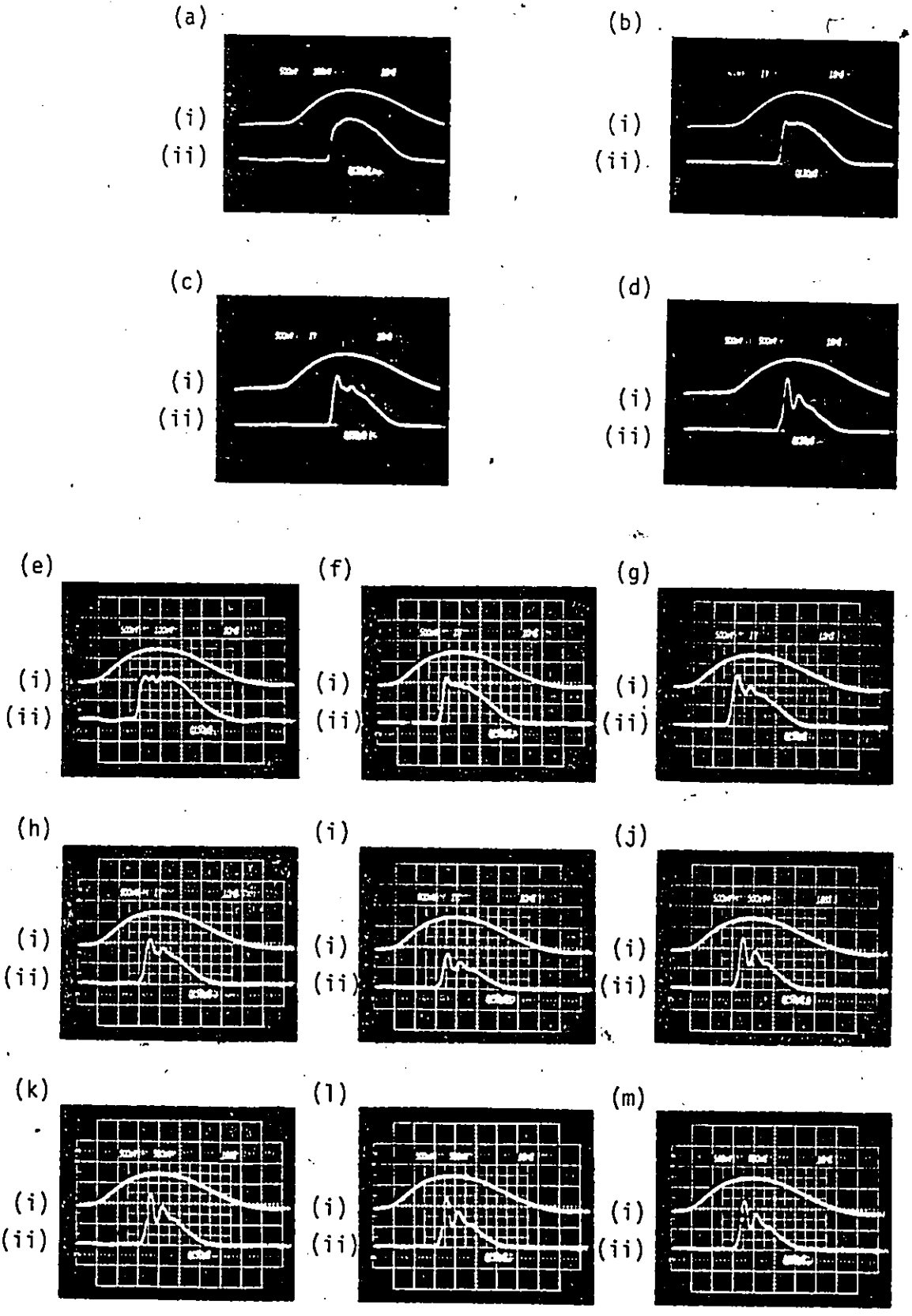
(a)
(i)
(ii)
(b)
(i)
(ii)
(c)
(i)
(ii)
(d)
(i)
(ii)
(e)
(i)
(ii)
(f)
(i)
(ii)
(g)
(i)
(ii)
(h)
(i)
(ii)
(i)
(i)
(ii)
(j)
(i)
(ii)
(k)
(i)
(ii)
(l)
(i)
(ii)
(m)
(i)
(ii)

Fig. 3-48

Optical output energy (a) and pulsewidth (b), as functions of cavity loss, for the laser system employing a 1.97-cm electrode spacing, a 35-kV charging voltage, and a He/1.0% Xe/0.2% HCl mixture at 2311-Torr pressure.

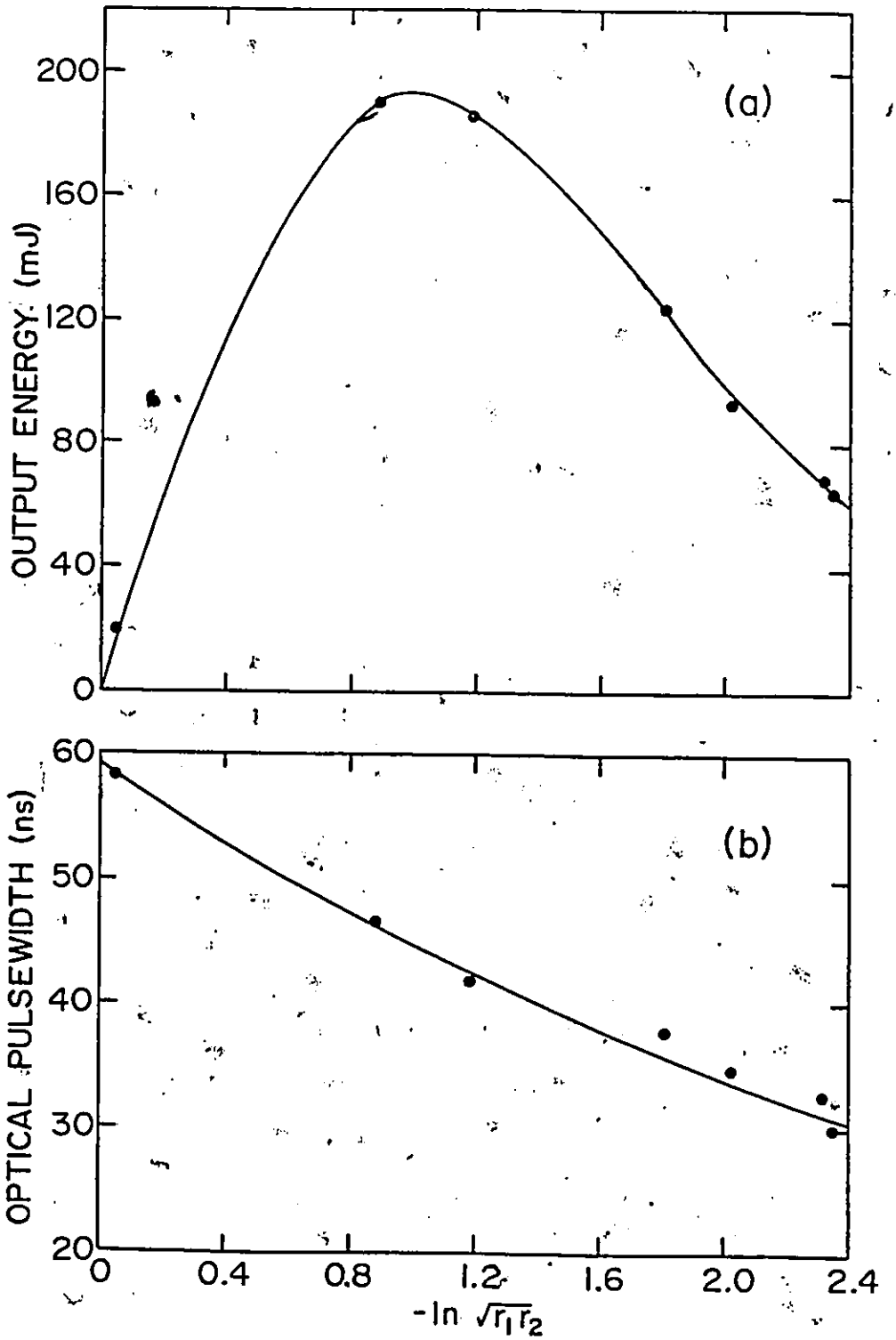
200
160
120
80
40
0
OUTPUT ENERGY (mJ)
(a)
60
50
40
30
20
OPTICAL PULSEWIDTH (ns)
(b)
0
0.4
0.8
1.2
1.6
2.0
2.4
$-\ln \sqrt{r_1 r_2}$

a 2.29-cm electrode spacing, a 30-kV charging voltage, and the same mixture (He/2.5% Xe/0.3% HCl) and pressure (1794 Torr). The optical pulses are compared in Figs.3-49(a), (b) and (f) for the case where only the rear (98%) reflector was used. There are substantial differences in the pulseshapes. However, the pulse durations (FWHM) and total gain periods (~durations of the pulse bases) are similar. The pulses obtained without an external mirror, shown in Fig.3-49(c) and (l), are quite similar to each other, except that the width of the latter pulse is ~15% smaller. The oscillograms of Figs.3-49(d)-(l), arranged similarly to the previous two figures (Figs.3-45 and 3-47), show the effect of cavity loss on optical output. These data are presented in different formats in Fig.3-50. An optimum energy of ~87 mJ in a 38-ns pulse can be extracted from this system using a cavity with a loss factor of ~1.1.

Figure 3-51 displays a waveform of the fluorescence obtained from a typical discharge operating below laser threshold. Also displayed in the figure is the "complete" history of the discharge current. Note that the fluorescence is sustained in the continuing excitation of the medium. Furthermore, the half-width of the fluorescence peak is about the same as the half-width of the excitation current peak. A long-duration current pulse is accompanied by a correspondingly long optical pulse. In our laser system the laser output is limited to ≅100 ns, which is a typical value for the current-pulse duration.

3.4 Summary

A photoionized, avalanche discharge laser system has been

Fig. 3-49

Comparison of various optical output pulses produced from a laser system employing a 2.29-cm electrode separation, a 30-kV charging voltage, and a He/2.5% Xe/0.3% HCl mixture at 1794-Torr pressure. These pulses were obtained using the range of external output couplers and in-cavity attenuators (neutral density filters). The oscillograms of (a), (b) and (f) show different pulseshapes obtained from the same cavity configuration (an external rear-end 98% reflector alone), but at three different times. A slight difference in pulseshape is also found in the oscillograms (c) and (l) for the case where no external reflectors were used. Shown in other oscillograms are pulseshapes for cavities consisting of the respective rear and front elements

(d) 98% reflector and 92% reflector,

(e) 98% reflector and fused-silica flat,

(g) 98% reflector plus 0.32 density filter and nil,

(h) 98% reflector plus 0.48 density filter and nil,

(i) 98% reflector plus 1.09 density filter and nil,

(j) 98% reflector plus 2.02 density filter and nil, and

(k) 98% reflector plus 3.21 density filter and nil.

(a)

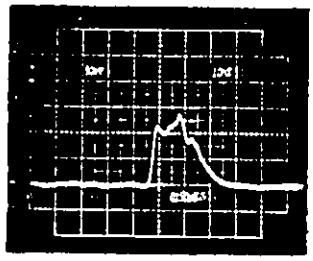

(b)

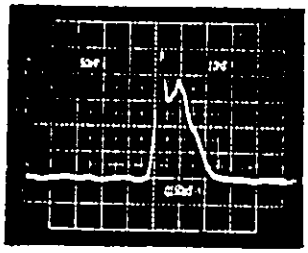

(c)

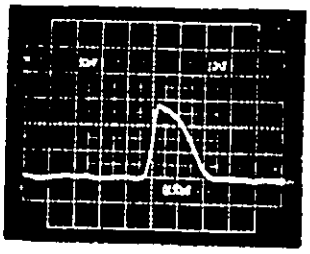

(d)

(i)

(ii)

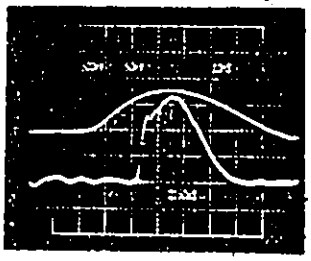

(e)

(i)

(ii)

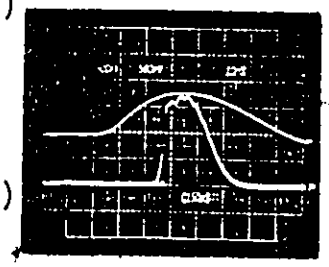

(f)

(i)

(ii)

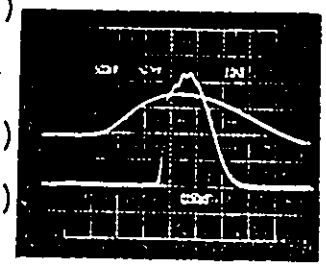

(g)

(i)

(ii)

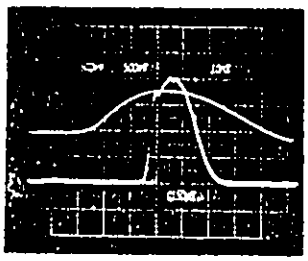

(h)

(i)

(ii)

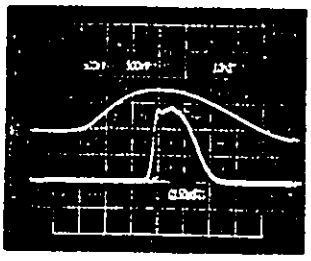

(i)

(i)

(ii)

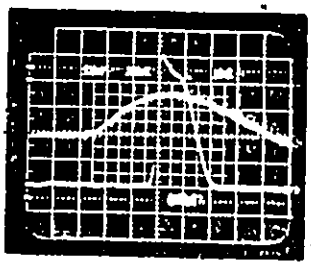

(j)

(i)

(ii)

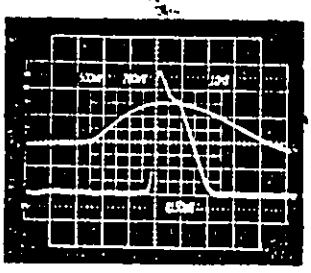

(k)

(i)

(ii)

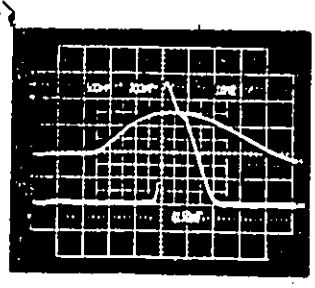

(l)

(i)

(ii)

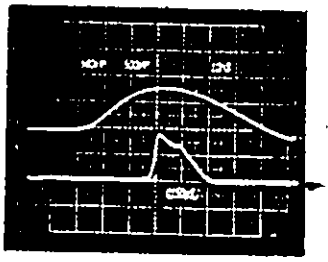

Fig. 3-50

Optical output energy (a) and pulsewidth (b), as functions of cavity loss, for the laser system employing a 2.29-cm electrode spacing, a 30-kV charging voltage, and a He/2.5% Xe/0.3% HCl mixture at 1794-Torr pressure.

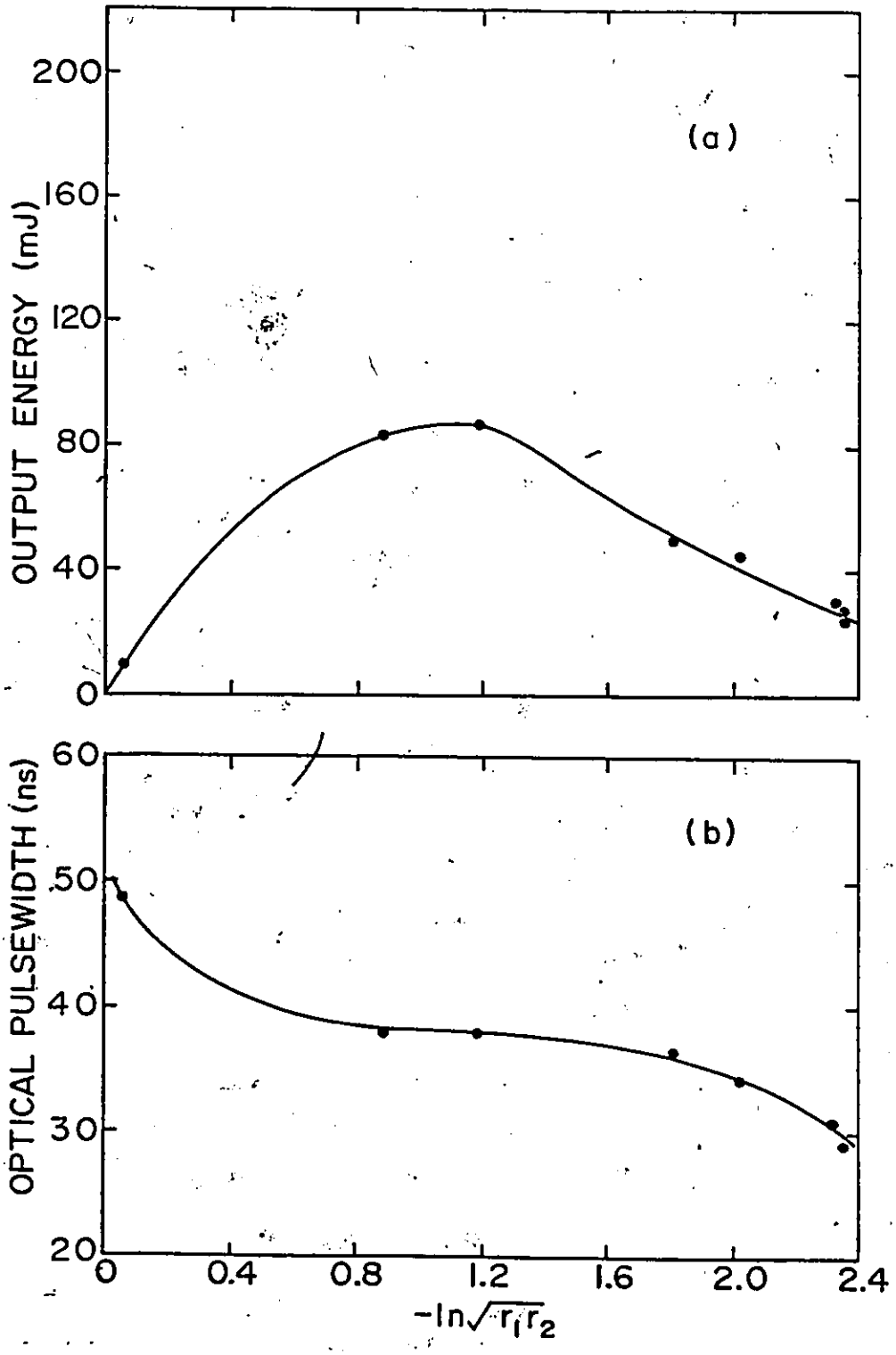
200
160
120
80
40
0
OUTPUT ENERGY (mJ)
(a)
60
50
40
30
20
OPTICAL PULSEWIDTH (ns)
(b)
0
0.4
0.8
1.2
1.6
2.0
2.4
$-\ln\sqrt{r_1 r_2}$

Fig. 3-51

Oscillogram of the fluorescence from a discharge employing a He/0.5% Xe /0.2% HCl mixture at 2957-Torr pressure and a 16-kV charging voltage. The upper and lower traces show the current in the discharge circuit and the fluorescence waveform, respectively. The time scale (corresponding to one small square) is 500 ns/division.

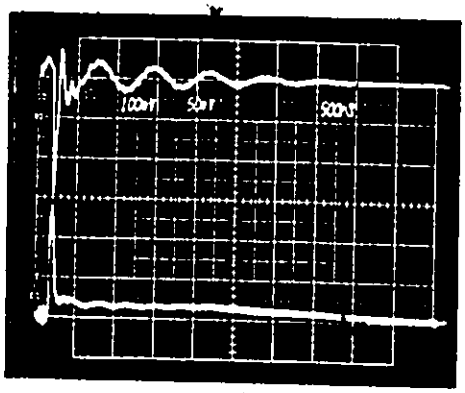
100mV
50nT

designed, constructed, and successfully operated with various He/Xe/HCl mixtures. Over the range of charging voltage (23-25 kV) investigated in our experiments, the system employing a 1.65-cm electrode separation produced the best optical outputs, both in pulse energy and pulsewidth. At 35-kV charging voltage, the most efficient gas mixture for this system (He/0.5% Xe/0.2% HCl at 2957 Torr) provided ~195-mJ output energy in a ~50-ns pulse (Fig.3-36). However, a later experiment using the same mixture composition at 2880-Torr pressure, yielded an almost "flat-topped" pulse with 60-ns duration (FWHM) and ~200-mJ energy (Fig.3-45(c)). This pulse, the first long-duration "flat-topped" pulse ever obtained for any avalanche discharge system, did not relate to other experimental data (see, e.g., Fig.3-40). It may be noted that not long after this pulse (and similar ones) was achieved, one of the preionizer rods "collapsed". The anomalously wide pulse may therefore be due to special discharge operating conditions.

A kinetic model is developed in the following chapters to analyze and compare the above pulses. This model also enables us to understand the dynamics of the XeCl laser operation. Furthermore, results of cavity-loss experiments associated with the broad pulse, and shown in Figs.3-45 and 3-46, are used in combination with Rigrod's theory in Chapter 5 to determine the gain and loss factors governing long-pulse operation.

CHAPTER 4

ELECTRON TRANSPORT SIMULATION OF INITIAL AVALANCHE DEVELOPMENT IN He/Xe/HCl DISCHARGES

4.1 Introduction

When electrons are accelerated towards the anode in an electric discharge, they lose energy through excitation and ionization of the gas medium, and by heating through momentum transfer in elastic scattering. Slow secondary electrons are generated during ionization. Some of these slow electrons attach to atoms and molecules with high electron affinities, to form negative ions. But others, gaining energy from the field, further excite and ionize the gas, and develop into avalanche discharges. The production rates for the excited particles and the ions depend on the availability of electrons, and on the electron energies necessary for inelastic scattering. These rates are commonly determined by taking the product of collisional cross-section and electron velocity $\overline{(\sigma v)}$, which is averaged over a macroscopic electron energy distribution function. This function characterizes the collective behaviour of electrons under the influence of an applied electric field, and can be derived from a solution of the energy continuity-equation for electrons, generally using available information on the appropriate collisional cross-sections.

In most theoretical studies on electron kinetics, the electron

distribution function is determined by solving, in the energy space, a linearized Boltzmann transport equation which incorporates the Lorentzian approximation [105,106]. Usually, only the first two terms in the Legendre expansion of the distribution function are adopted. In this approximation, it is assumed that electrons do not collide with each other, but only with gas particles. Consequently, collisions are principally of the elastic kind, with little loss in energy per collision. However, this assumption is inappropriate if electrons drift in a dense medium in the presence of a high electric field, where the mean-free-path for collisions is small, and high-energy electrons lose a significant fraction of their energy in inelastic collisions. Therefore, it becomes necessary to include higher-order terms in the functional expansion, with the result that the solution of the Boltzmann equation becomes a laborious task[†]. The extended calculation is necessary in electron kinetic studies of high-pressure RGH lasers, which usually operate at an electric field-to-pressure ratio (E/p) near 10 V/cm-Torr.

A different approach, bypassing the usual two-term spherical harmonics expansion in the distribution function, is claimed by Kitamori et al. [108] to be successful for high values of E/p. They integrate

---

[†]An extended Boltzmann analysis, employing up to six terms in the Legendre series, has been developed recently by Pitchford et al. [107]. These authors show that, in calculations of swarm parameters at high E/N ($\leq$24 Td) for the particular case of nitrogen (N_2), a significant difference ($\lesssim$35%) exists between the traditional two-term Legendre expansion solution and the multi-term solution. In addition, they show that at least four to eight terms in the Legendre series are generally required in order to achieve convergency.

the simplified Boltzmann equation (in the velocity and time domains) along the characteristic velocity curve. The basic approach taken by these authors is recommendable. However, according to our early computations, their finite difference scheme underestimates the electron-collision term. Even when we adopted a higher-order expansion for this term, it was found that the numerical method was inefficient for evaluating the XeCl system. This is a consequence of the very small time step required for convergency in the Taylor's expansion of the velocity distribution function. As an alternative approach, we derived an exact solution for the generalized Boltzmann transport equation in the spatial, velocity and temporal coordinates. This approach is discussed briefly in Appendix E. However, further research is needed to establish the approach using an exact solution.[¶]

It is evident, from the exact expression for the generalized distribution function given by Eq.(E-15), that the evolution of the electron velocity (energy) distribution is a direct consequence of collisions involving electrons moving along a classical trajectory. Therefore, the logical method of determining the electron energy distribution is to keep track of the electron motion under typical experimental conditions. One method, employed in this chapter, applies

---

[¶]Recently, Braglia [109] has discussed and appraised various means of obtaining velocity distribution functions and rate coefficients in physical situations of practical interest, where the conventional (first-order) transport theory is inadequate. His views on the status and the development of electron transport analyses are very similar to ours. He has also carried out a detailed analysis of the transport theory of electrons (and ions) using the integral-equation approach.

random-walk theory to a group of electrons in an excited XeCl laser mixture, where electrons are released at the cathode with arbitrary initial velocities. The electron parameters are statistically sampled at various times, and then collectively analyzed to provide a simulated energy distribution which is subsequently used to calculate the reaction rates of the electron collision processes.

The validity of the Monte-Carlo method for use in our work has to be considered. The composite electron-impact cross-sections that are employed in our calculations are obtained from many different sources. When experimental cross-sections are lacking or unreliable, theoretical values based on quantum-mechanical scattering are adopted. Some of the experimental cross-sections are deduced from analyses of electron transport data, assuming a Maxwellian or Druyvestyn distribution function. There are also cross-sections that are determined from a comparison between the calculated transport coefficients using assumed cross-sections in an approximate solution of the Boltzmann equation, and the transport coefficients measured from electron mobility experiments. Although the distribution function calculated using the comparision method may be inaccurate, the argument is usually made in favour of the Boltzmann approach because the cross-sections are made to correspond with the observed transport data. It should be noted, however, that the formulae derived for calculating the electron swarm parameters also invoke a second approximation, and that the normalized distribution function, particularly at its high-energy tail where excitation and ionization predominate, is considerably distorted. Moreover, the

cross-sections for inelastic collision processes are seldom determined by the Boltzmann method. Even though the Monte-Carlo approach requires substantial computer time, this electron simulation is preferred because it can provide reliable information on the electron energy distribution.

The apparent major disadvantage of using the Monte-Carlo method is that it cannot be coupled conveniently with simultaneous gas kinetic calculations. Fundamentally, the method provides a statistical analysis, on a microscopic scale, of a large number of randomly sampled electrons undergoing collisions with various particle species. These species are constantly created and annihilated in the discharge medium. However, particle transformation takes place during excitation and ionization by electrons, and during heavy-particle encounters. The presence of particles can only be evaluated macroscopically by solving a set of kinetic equations involving many chemical reactions and electron inelastic-scattering processes. Changing particle concentrations in the plasma affect the behaviour of electrons (electron kinetics), but much less than the formation and loss of particles (particle kinetics), because elastic-scatterings are predominant with electrons. Therefore, it is possible to assume average rate coefficients for electron kinetic processes, which vary with the electric field or with the average electron energy. These rate coefficients, which can be evaluated from the microscopic electron transport simulation, are subsequently used in particle calculations. This approach allows independent calculations of electron and gas kinetics, without the need for simultaneous coupling of the relevant equations.

There are further reasons for considering the electron and the gas kinetics in the XeCl system separately. The exciplex system uses a recombination plasma as the active medium. In a usual gas laser, stimulated emission takes place when the electron temperature is high during the ionization of the gas mixture. In contrast, an exciplex laser radiates in a decaying plasma which favours the formation of excited complex molecules, especially in a dense medium. This radiation occurs when the characteristic temperature drops below the effective equilibrium temperature corresponding to the degree of ionization, at which time the electrons are supercooled. There is a certain time lag, corresponding to the formation of exciplex species and the buildup of population inversion in the system, between gas breakdown and the onset of laser action. Therefore, the time history of exciplex formation consists of two distinctive periods, the subnanosecond relaxation of electrons, followed by the recombination of the plasma. These periods can be examined separately. Moreover, most cross-sections for electron collisions with metastable atoms and molecules in the He/Xe/HCl mixture are not properly known. Hence the dependence of electron temperature on these processes cannot be correctly accounted for. Only average rate coefficients, based on available data, can be estimated. In this regard, separate electron-kinetic studies should be sufficient to provide valuable electron rates for use in discharge kinetic studies.

4.2 Monte-Carlo Simulation of Electron Transport

The use of a random-walk (Monte-Carlo) procedure to simulate

the motion of electrons, in a gas excited between a pair of parallel electrodes, has been investigated extensively [110-123]. The procedure has also been applied to calculations of electron energy distributions in electron-beam-pumped rare-gas mixtures of Ar-Kr, and of Ar-Xe [124]. Different approaches can be used for deciding the occurrence of an electron collision. However, the general principle of employing a stochastic model exists in all cases. The following simulation of electron transport in the XeCl system incorporates the Coulomb effect, which is generally neglected in calculations for low electron densities.

4.2.1 Principle of Calculation

Ultraviolet radiation at the cathode liberates electrons with different initial velocities, randomly oriented. In the presence of a static, uniform electric field $\vec{E}$ in the $-\hat{z}$ direction indicated in Fig.4-1, these electrons travel in parabolic orbits towards the anode. If gas particles are homogenously dispersed in the electron-transit space, an individual electron is allowed to traverse a free-path (ℓ) prior to a collision with a particle. This distance is usually shorter than the mean-free-path for collisions (λ), and depends on the probability of an electron-particle encounter.

The classical equation of motion for an electron in the field $\vec{E} = -E\hat{z}$ is

$$m \frac{d^2\vec{r}}{dt} = -e\vec{E} \quad , \tag{4-1}$$

where $\vec{r}$ is the displacement vector (x, y, z), and e and m are the

Fig. 4-1

Coordinate systems employed in a random-walk simulation of electron motion in a gas. In (a) and (b), the fixed frame (rectangular coordinates x, y and z) and the moving frame (spherical coordinates v_0, θ and ϕ) have origins at the cathode and the electron, respectively. (b), in addition, shows the positions and velocities of the electron in traversing a free-path (ℓ) between collisions. ρ and Δz are the corresponding transverse and prependicular displacements of the electron in a plane parallel to the electrodes, which are separated by d.

(a)

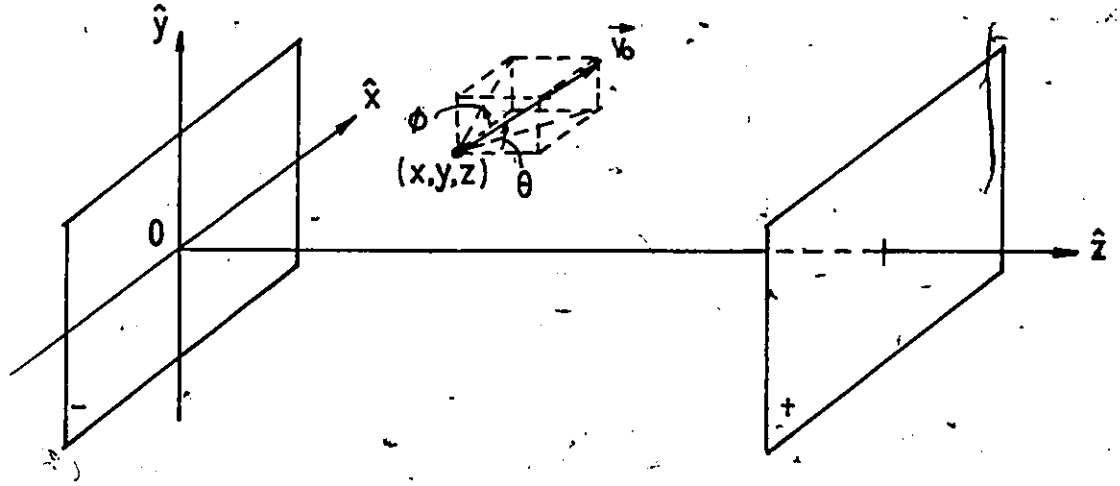

(b)

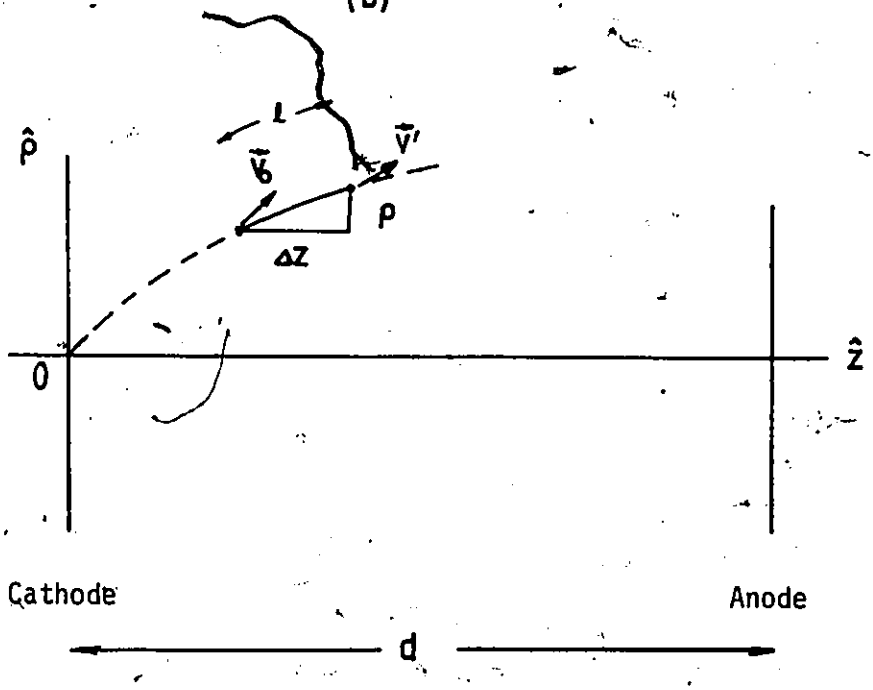

charge and the mass of the electron, respectively. If the electron has an initial velocity $\vec{v}_0 \equiv (v_0, \theta, \phi)$, expressed in spherical coordinates, then ~~after~~ a collisionless (i.e., transit) time, τ, it is displaced by

$$\Delta x = v_0 \cos\theta \sin\phi \, \tau \quad , \tag{4-2a}$$

$$\Delta y = v_0 \sin\theta \sin\phi \, \tau \quad , \tag{4-2b}$$

and $$\Delta z = v_0 \cos\theta \, \tau + \frac{eE}{2m} \tau^2 \quad . \tag{4-2c}$$

The electron trajectory is parabolic, as can be seen from

$$\Delta z = \frac{1}{2} a\rho^2 + b\rho \quad , \tag{4-3}$$

where $$\rho \equiv [(\Delta x)^2 + (\Delta y)^2]^{1/2} \quad , \tag{4-4a}$$

$$a = \frac{eE/m}{(v_0 \sin\theta)^2} \quad , \tag{4-4b}$$

and $$b = \cot\theta \quad . \tag{4-4c}$$

At the end of a trajectory and before a collision, the electron has acquired a velocity $\vec{v}'$ of magnitude

$$v' = [v_0^2 + 2v_0 \cos\theta \frac{eE}{m} \tau + (\frac{eE}{m} \tau)^2]^{1/2} \tag{4-5}$$

and directional cosines

$$\alpha' = \frac{v_0}{v'} \sin\theta \cos\phi \quad , \tag{4-6a}$$

$$\beta' = \frac{v_0}{v'} \sin\theta \sin\phi \quad , \tag{4-6b}$$

and $$\gamma' = \frac{1}{v'} (v_0 \cos\theta + \frac{eE}{m} \tau) \quad . \tag{4-6c}$$

The energy of the electron is then

$$\varepsilon = \frac{1}{2} m v'^2 \qquad (4\text{-}7)$$

The probability of a collision, in terms of the transit time τ, is expressed by

$$P_c(\tau) = \exp\{- \frac{v'}{\lambda(v')} \tau + \frac{eE}{2m} \tau^2 \cos\theta \frac{d}{dv}[\frac{v}{\lambda(v)}]\Big|_{v=v_0} \} \qquad (4\text{-}8)$$

If a random number R_1, with value between 0 and 1, is used to represent the probability, then the free time between collisions,

$$\tau' = \rho / (v_0 \sin\theta) \quad , \qquad (4\text{-}9)$$

can be obtained by solving Eq.(4-8). This time is also related to the free path via the relationship

$$\ell = \int_0^{\tau} |\frac{d\vec{r}}{dt}| \, dt \quad . \qquad (4\text{-}10)$$

A second random number R_2 is used to select the kind of collision. In the present calculations for the XeCl system, the only allowed kinds are elastic collisions by momentum transfer, and inelastic collisions involving excitation and ionization (of ground-state He, Xe and HCl), and dissociative attachment (of HCl into products Cl^-+H and H^-+Cl). The electron-electron interactions are also considered. The cross-sections for these processes, described in the next section, are employed in the form of scattering probabilities (L_i cm^{-1}-$Torr^{-1}$), which are related to the mean-free-path by

$$\lambda = (\sum_i L_i p_i)^{-1} \quad , \qquad (4\text{-}11)$$

where p_i is the partial pressure of the gas involved in the i^{th} scattering process. If the n^{th} collision process takes place, the random number R_2

must fall into the range

$$0 < R_2 \leq \lambda \sum_{i=1}^{n} L_i p_i \quad , \qquad \text{for } n=1$$

$$\lambda \sum_{i=1}^{n-1} L_i p_i < R_2 \leq \lambda \sum_{i=1}^{n} L_i p_i \quad , \qquad \text{for } n \geq 2 \qquad (4\text{-}12)$$

After the collision, the amount of electron energy lost to the gas depends on the type of collision (see Table 4-1). In the case of elastic scattering with a particle of mass M, the electron, with much smaller mass m, loses only a small fraction of its energy by momentum transfer. For a scattering angle ψ, the fractional energy loss is

$$-\left(\frac{\Delta\varepsilon}{\varepsilon}\right)_{eM,elastic} = \frac{4mM}{(M+m)^2}\sin^2\psi \quad , \qquad (4\text{-}13)$$

which is obtained by assuming that M is initially stationary. The mean value for the fractional energy loss is

$$-\left(\overline{\frac{\Delta\varepsilon}{\varepsilon}}\right)_{eM,elastic} = \frac{2mM}{(M+m)^2} \cong \frac{2m}{M} \quad . \qquad (4\text{-}14)$$

If the scattering partner is also an electron, the exact situation is very complex, and depends on the energies of both the incident electron and the scattering electron in the electron cloud. The determination of the latter energy is complicated by the energy distribution of the electron cloud. Figure 4-2 illustrates typical Coulomb scattering of an electron, having velocity $\vec{v}'$, by a scattering electron, of velocity $\vec{u}$. χ is the impact angle of the two colliders. Their relative speed of encounter, which is unchanged both before and after the colloision, is

Table 4-1

Electron energy losses in elastic and inelastic collisions with He, Xe, HCl and electrons. The mean energy-loss value, denoted by *, depends on the electron energy just before a collision.

Electron Scatterer	Type of Collision	Energy Loss (eV)
He	Elastic	$2.74 \times 10^{-4}\ \varepsilon$ *
	Excitation to $2\ ^3S$ level	19.82
	$2\ ^1S$	20.62
	$2\ ^3P$	20.96
	$2\ ^1P$	21.22
	$3\ ^1P$	23.07
	Ionization	24.59
Xe	Elastic	$8.36 \times 10^{-6}\ \varepsilon$ *
	Excitation to $2\ ^3P_2$ level	8.32
	$2\ ^3P_1$	8.44
	Ionization	12.13
HCl	Elastic	$3.01 \times 10^{-5}\ \varepsilon$ *
	Excitation to $v = 1$ level	0.36
	2	0.70
	3	1.03
	4	1.35
	5	1.66
	Ionization	13.64
	Dissociative attachment: Cl^-/H	ε
	H^-/Cl	ε
e	Elastic	see text

Fig. 4-2

Vector diagrams illustrating the scattering of two colliding electrons.

(a) Relative velocity between electrons before collision.

(b) Relative velocity between electrons after collision.

(c) Velocity of the incident electron scattered by the electron cloud.

(a)

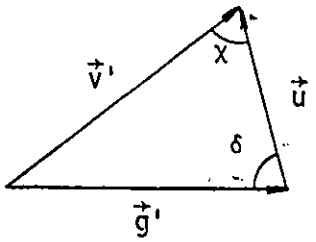

$g = |\vec{g}'| = |\vec{g}''|$

(b)

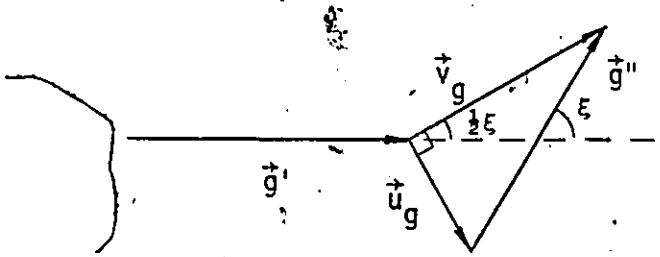

$|\vec{v}_g| = g \cos(\xi/2)$

$|\vec{u}_g| = g \sin(\xi/2)$

(c)

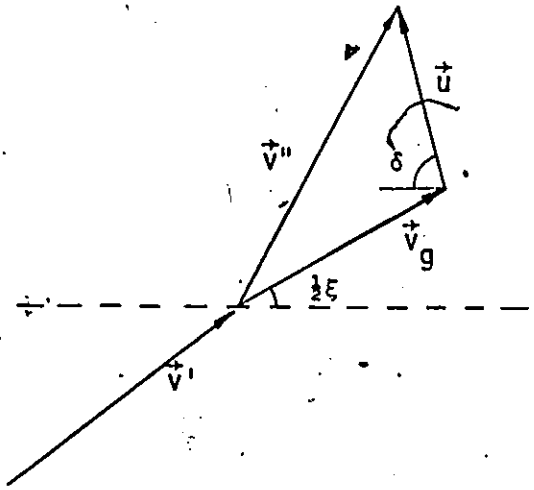

$$g = [v'^2 + u^2 - 2v'u\cos\chi]^{1/2} \quad . \tag{4-15}$$

Parameters χ and u can be selected by evaluating

$$\cos\chi = 1-2R_a \tag{4-16}$$

and $$R_b = \int_0^{\frac{1}{2}mu^2} F(\varepsilon)\, d\varepsilon \quad , \tag{4-17}$$

where R_a and R_b are two different random numbers between 0 and 1. The electron-energy distribution function in Eq.(4-17) assumes the general form

$$F(\varepsilon) = N\,\varepsilon^h \exp[-\beta\varepsilon^k] \quad , \tag{4-18}$$

where the constants $h \cong 0.5$ and $1 \leq k \leq 2$ (see Figs.4-12 and 4-13). The normalized value of N and the parameter β depend on the average energy $\bar{\varepsilon}$ of the electron cloud, through the relationships

$$N = \frac{k\,[\Gamma(\frac{h+1}{k})/\bar{\varepsilon}\,]^{h+2}}{[\Gamma(\frac{h+2}{k})]^{h+1}} \quad , \tag{4-19}$$

and $$\beta = [\frac{\Gamma(\frac{h+2}{k})}{\bar{\varepsilon}\Gamma(\frac{h+1}{k})}]^k \quad , \tag{4-20}$$

where $\Gamma()$ is the gamma function. For the special case of $h = 0.5$ and $k = 1.5$, Eq.(4-17) simplifies to

$$\tfrac{1}{2}mu^2 = \bar{\varepsilon}\,[-\ell n(1-R_b)]^{2/3}/\Gamma(5/3) \quad . \tag{4-21}$$

The relative deflection angle of the scattering electrons, shown in Fig.4-2(b), is determined from [125]

$$\xi = 2 \tan^{-1}(b_0'/b) \quad , \tag{4-22}$$

where b_0 is the impact parameter for 90° deflection. The impact distance can be selected using a random number R_c as

$$b = \lambda_D \sqrt{R_c} \quad , \tag{4-23}$$

where the Debye length λ_D is defined by Eq.(4-35). The velocity of the incident scatterer after the collision can now be evaluated using

$$v'' = \{u^2+g^2 \cos^2(\xi/2)-2ug \cos(\xi/2) \cos(\xi/2+\delta)\}^{1/2} \quad , \tag{4-24}$$

where δ is the angle between the vectors $\vec{u}$ and $\vec{g}'$ prior to collision, as indicated in Fig.4-2(a). A knowledge of the scattering angle ψ, defined by Eq.(4-27), together with an additional random number, allows evaluation of a new orientation (θ'',ϕ'') for the scattered electron. The fractional energy loss, due to the Coulomb collision, is simply

$$-\left(\frac{\Delta\varepsilon}{\varepsilon}\right)_{ee} = 1 - \left(\frac{v''}{v'}\right)^2 \quad . \tag{4-25}$$

The electron-energy loss in an inelastic collision is ~~very~~ substantial. Whenever a ground-state atom or molecule is excited to a higher state, the total energy difference between states must be transferred from the colliding electron. In the rare gases, this represents an electron-energy loss of >8.3 eV per excitation, and requires an energetic electron. A low-energy electron (e.g., <1 eV) may excite the ground state in an easily attachable gas, such as HCl, to a higher vibrational level, and lose most of its energy. Moreover, during ionization, an electron-ion pair is produced. The secondary

electron shares the kinetic energy remaining after collision with the primary electron. For example, if the energy partition is equal, the additive energy loss by the original electron is

$$-(\Delta\varepsilon)_{\text{ionization}} = (\varepsilon+\varepsilon_i)/2 \quad , \tag{4-25}$$

where ε_i is the ionization level of the heavy particle in collision. In our calculations, a random number (R_3) is generated to correspond to the fraction of energy shared out by the simulated (primary) electron. As a result of ionization, the new (secondary) electron and the simulated electron have energies

$$\varepsilon_s'' = (\varepsilon-\varepsilon_i)\, R_3 \quad , \tag{4-26a}$$

and

$$\varepsilon'' = (\varepsilon-\varepsilon_i)(1-R_3) \quad , \tag{4-26b}$$

respectively. Note that electron attachment to HCl causes the most severe loss of electron energy, because the electron is "consumed".

In the course of a collision, the deflection angle of the trajectory is determined by

$$\psi = \cos^{-1}\left(\frac{\vec{v}'\cdot\vec{v}''}{v'v''}\right)$$

$$= \cos^{-1}(\alpha'\alpha'' + \beta'\beta'' + \gamma'\gamma'') \quad . \tag{4-27}$$

The electron, after the collision, is characterized by a new speed,

$$v'' = (2\,\varepsilon''/m)^{1/2} \quad , \tag{4-28}$$

with direction cosines (α'', β'', γ''). The latter parameters are obtained by generating a pair of random numbers R_4 and R_5 so that

$$\gamma'' = 1-2R_4 \quad , \tag{4-29a}$$

$$\alpha'' = (1-\gamma''^2)^{1/2}\cos(2\pi R_5) \quad , \tag{4-29b}$$

and

$$\beta'' = (1-\gamma''^2-\alpha''^2)^{1/2} \tag{4-29c}$$

4.2.2 Cross-Sections for Electron Collision Processes

The cross-sections for the various electron processes in a He/Xe/HCl discharge are required in order to determine both the type of, and the mean-free-path for, collisions in Eq.(4-11). Only those interactions which have a significant influence on the electron-transport calculations are considered (i.e., those between electrons and ground-state atoms or molecules). This expediency, justified above, simplifies the computational procedure and reduces the required computer storage, while still acquiring adequate information on the kinetic rates for use in kinetic modelling. Other electron processes involving by-products of the gas discharge are discussed separately later in this chapter. All cross-sections used in the actual simulation (and given below) are based on the "sectional" fitting of data to appropriate functions and polynomials. In addition, different segments of a composite curve are made to connect continuously. Negative cross-section values, resulting from, for example, curve-fitting in the region near the Ramsauer-Townsend minimum, are removed by additional fits about the appropriate regions.

A. Helium

In view of the high excitation threshold ($\gtrsim$19.8 eV) for helium, considerable experimental effort has been invested into deriving accurate elastic-scattering data from the gas at low electron energies. There is good agreement (better than 4%) between the momentum-transfer cross-sections obtained by the cross-beam measurements [126] and those obtained from the analyses of electron swarm data [127,128]. Equally significant is the good agreement with theoretical cross-sections derived from calculations of the scattering phase shifts [126,129-131]. The He data are generally reliable, and therefore are suitable for use in normalizing electron-beam data taken for other gases.

The momentum-transfer cross-sections for electron-helium collisions, employed in the simulation, are evaluated in three energy regions. For energies below 1 eV, the O'Malley formula [132], structured on the modified effective range theory of O'Malley et al. [133], is adopted. In this situation,

$$\sigma_m = 4\pi[A^2 + (\frac{4\pi}{5})\alpha A k + (\frac{8}{3})\alpha A^2 k^2 \ell n\, k + Ck^2] \quad , \qquad (4\text{-}30)$$

where $\alpha = 1.395$, $A = 1.181$, $C = -0.727$ and $k = 0.2711\sqrt{\varepsilon}$. The relevant cross-sections (σ_m) are expressed in units of a_0^2 (a_0 is the Bohr radius), and can be extrapolated to zero energy ($\varepsilon = 0$ eV) for helium, yielding

$$\sigma_m^0 = 4.91\ \text{Å}^2 \quad . \qquad (4\text{-}31)$$

The experimental data of Crompton et al.[127], and of Milloy and Crompton [128], are used in the range 1 eV $< \varepsilon <$ 12 eV. Beyond 12 eV,

we employ the computed cross-sections of LaBahn and Callaway [129], who use the method of phase shifts in the "dynamic exchange" approximations.

Lowke et al. [134] summarize the inelastic cross-sections of the metastable $2\ ^3S$, $2\ ^1S$ and $2\ ^1P$ levels in He. These are measured by Schulz and Fox [135], Schulz [136], Schulz and Philbrick [137], and Jobe and St. John [138], using different techniques. St. John et al. [139] have, in addition, determined the absolute apparent electron excitation functions (uncorrected for polarization, cascade and transfer effects) for 18 additional metastable states of He up to energies of 400-450 eV. The latter data have not been included by Lowke et al. These authors provide approximate cross-section values only for electron energies >30 kV. De Heer and Jansen [140] have evaluated a set of semi-empirical total cross-sections for excitation to the singlet and triplet levels using energies to 4 keV. Their values are in good agreement with those in [138,139], and with the experimental cross-section data of Jost and Möllenkamp [141]. The latter claim an accuracy of ~5% in the limited energy range of 150-500 eV. For the calculations, we use the cross-sections of de Heer and Jansen [140] in the high energy range (>30 eV), and the collective experimental data [135-139] for low energies (<30 eV).

Rapp and Englander-Golden [142] have carried out a very comprehensive study of the total ionization cross-sections for helium (and other gases), at energies ranging from the ionization threshold to 1 keV. There is excellent agreement with the early measurements of Smith [143] at energies below 80 eV. At 600 eV, the He cross-section

of Rapp and Englander-Golden is about 7% and 20% higher than those of Smith and Schram et al. [144], respectively. Although more accurate experimental cross-sections for ionization of helium atoms have been claimed [141], the results of Rapp and Englander-Golden are sufficiently accurate for our calculations at energies below 100 eV. Moreover, it is possible to closely fit these data with a 10^{th} degree polynomial. Thomas [145] has also suggested an empirical formula of the form

$$\sigma_i(\varepsilon) = A(\varepsilon - \varepsilon_0)^m \exp[-\alpha(\varepsilon - \varepsilon_0)] \quad , \qquad (4\text{-}32)$$

where A, m and α are constants, and ε_0 is the threshold ionization energy, for use over the same range.

All of the electron collision cross-sections for helium used in our computations are presented in Figs.4-3(a) and (b).

B. Xenon

The momentum-transfer cross-section curve of Frost and Phelps [146] is used, in conjunction with the elastic seattering data of de Heer et al. [147], for our calculations. The composite cross-section curve is shown in Fig. 4-4(a). There exists a scarcity of truly reliable data concerning the cross-sections for the electronic excitation of xenon atoms. The experimental results of Schaper and Scheibner [148] appear to be more reliable than those of Dixon and von Engel [146], for energies below 20 eV. The former results are also consistent with the semi-empirical values of de Heer et al. [147] at high energies. After taking into account the error limits quoted in Ref. [147], the two sets

Fig. 4-3

Cross-sections for electron collisions with helium.

(a) Momentum-transfer cross-section.

(b) Inelastic scattering cross-sections: (i) excitation and (ii) ionization.

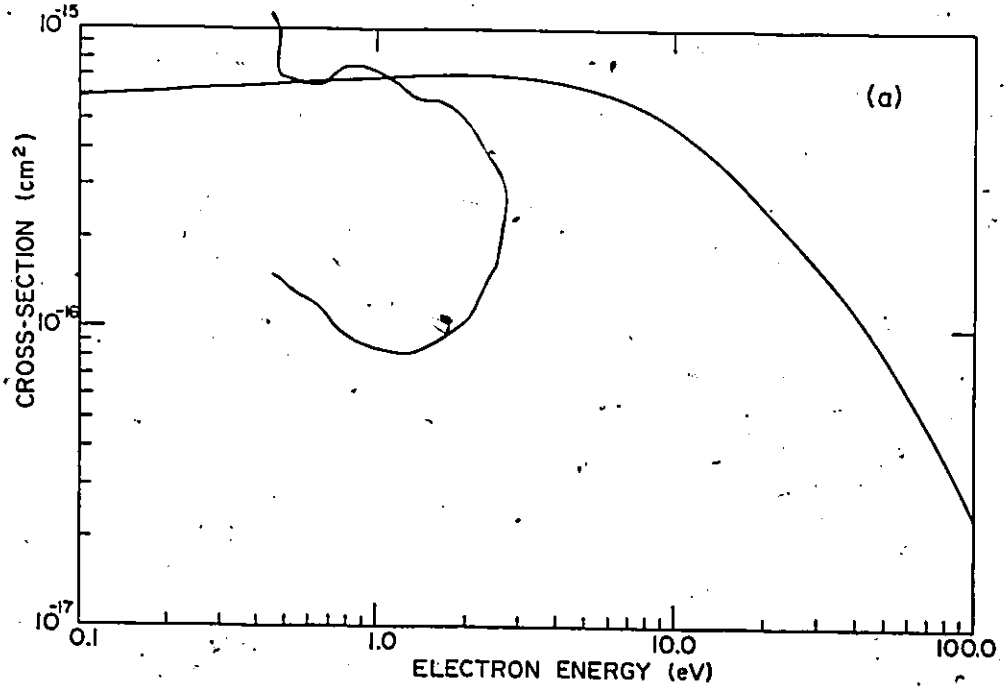
(a)
CROSS-SECTION (cm²)
10⁻¹⁵
10⁻¹⁶
10⁻¹⁷
0.1
1.0
10.0
100.0
ELECTRON ENERGY (eV)

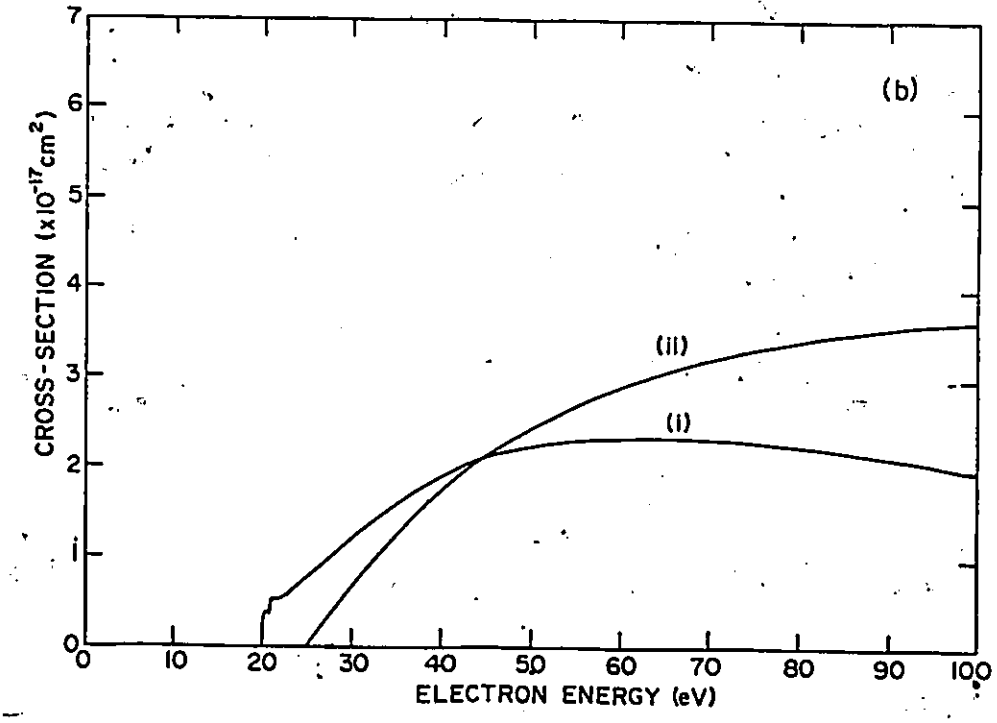
(b)
CROSS-SECTION (x10⁻¹⁷cm²)
0
1
2
3
4
5
6
7
(II)
(I)
0
10
20
30
40
50
60
70
80
90
100
ELECTRON ENERGY (eV)

Fig. 4-4

Cross-sections for electron collisions with xenon.

(a) Momentum-transfer cross-section.

(b) Inelastic scattering cross-sections: (i) excitation and (ii) ionization.

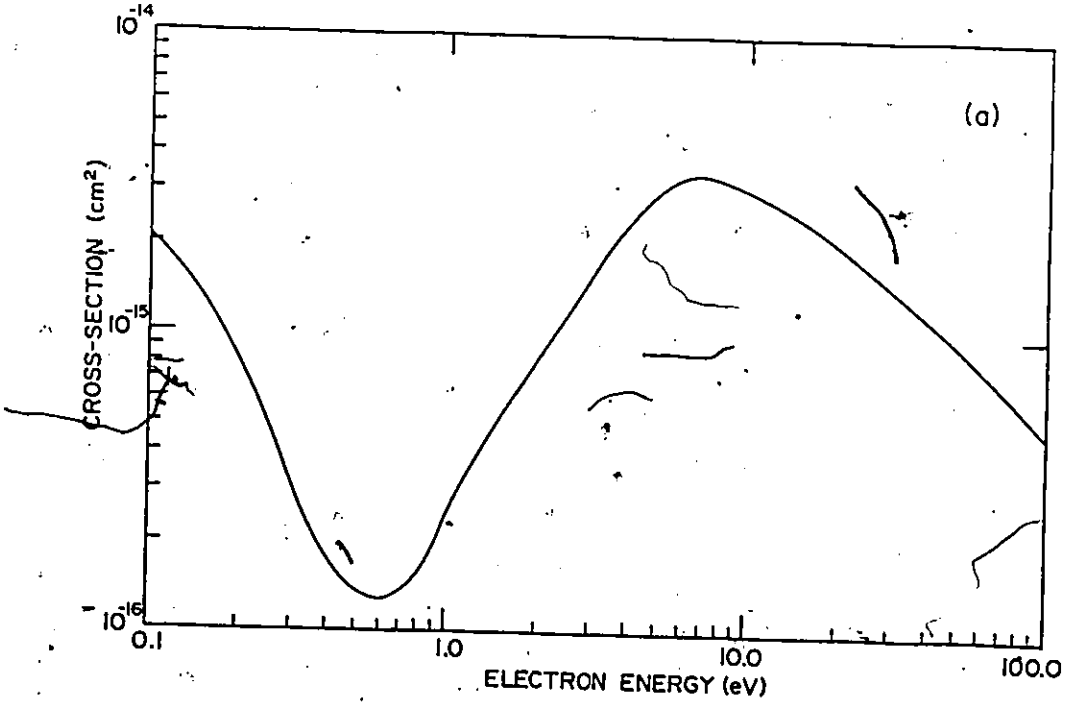
(a)
CROSS-SECTION (cm²)
10⁻¹⁴
10⁻¹⁵
10⁻¹⁶
0.1
1.0
10.0
100.0
ELECTRON ENERGY (eV)

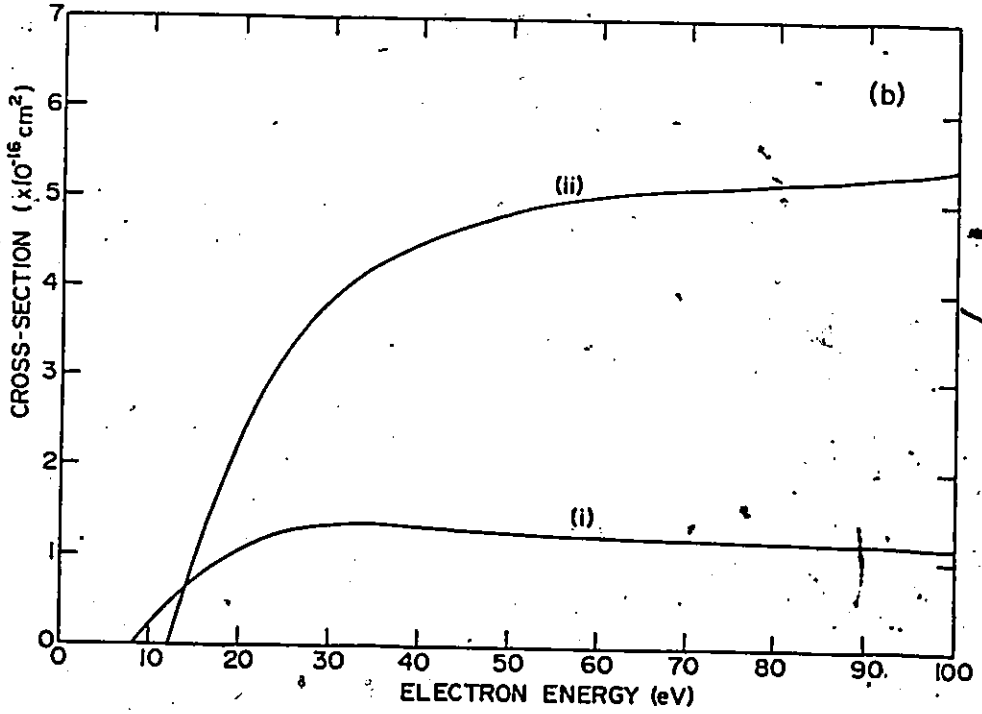
(b)
CROSS-SECTION (x10⁻¹⁶cm²)
(ii)
(i)
0
1
2
3
4
5
6
7
10
20
30
40
50
60
70
80
90
100
ELECTRON ENERGY (eV)

of data [147,148] are adjusted to connect smoothly before being fed into the computer for a least-squares fit. The resulting curve appears in Fig.4-4(b), along with the ionization cross-section curve due to Rapp and Englander-Golden [142]. De Heer et al. [147] evaluate ionization cross-sections using the experimental results of Rapp and Englander-Golden [142], and of Schram et al. [144], and the adjusted data of Tozer and Craggs [150], and of Asundi and Kurepa [151]. The evaluated cross-sections [147] are not adopted in our calculations because the values differ significantly from what we believe are more reliable (e.g., those given in Refs.[142] and [144]).

C. Hydrogen Chloride

Information is lacking on the momentum-transfer cross-sections for hydrogen chloride. However, it is possible to estimate the cross-sections using the experimental data of Rohr and Linder [152] concerning the differential cross-sections for elastic scattering of HCl (up to ~10 eV). The total elastic scattering cross-sections computed from this set of data agrees very well with the elastic collision cross-section curve of Brüche [153], in regions where the energies overlap. It therefore seems reasonable to adjust Brüche's curve to agree with the curve derived by Rohr and Linder, and to use the resulting curve to extend the range of the momentum-transfer cross-sections. For lack of experimental data beyond ~35 eV, we arbitrarily let the cross-section curve in Fig. 4-5(a) decay exponentially. The situation is different for the inelastic scattering cross-sections for ionization of the gas,

Fig. 4-5

Cross-sections for electron collisions with hydrogen chloride.

(a) Momentum-transfer cross-section.

(b) Inelastic scattering cross-sections: (i) excitation and (ii) ionization.

(c) Dissociative attachment cross-sections.

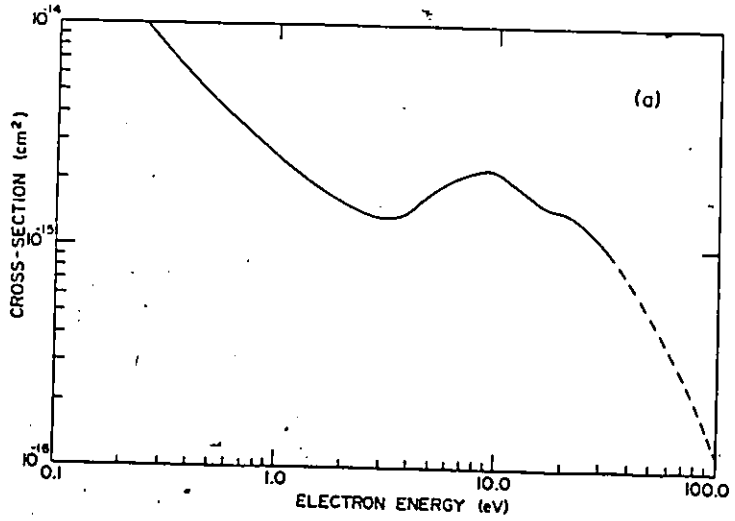
(a)
CROSS-SECTION (cm²)
ELECTRON ENERGY (eV)
0.1
1.0
10.0
100.0

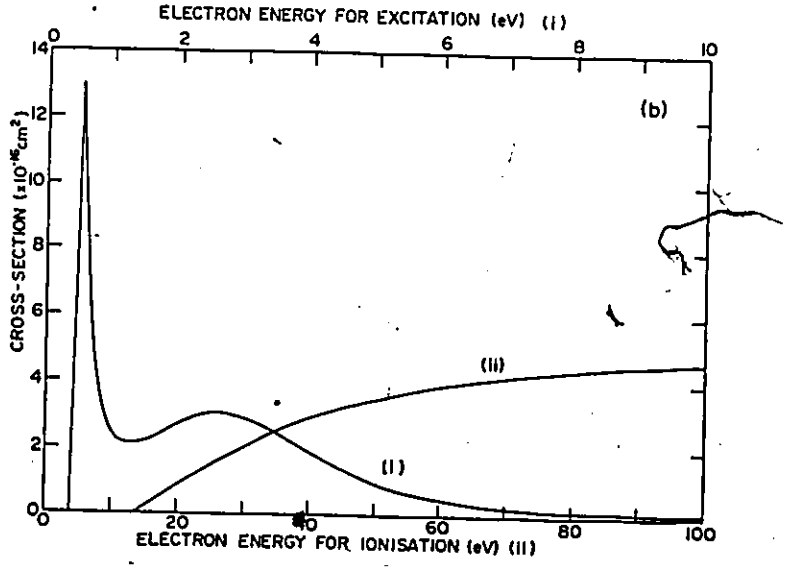
ELECTRON ENERGY FOR EXCITATION (eV) (I)
(b)
CROSS-SECTION (×10⁻¹⁶cm²)
(II)
(I)
ELECTRON ENERGY FOR IONISATION (eV) (II)

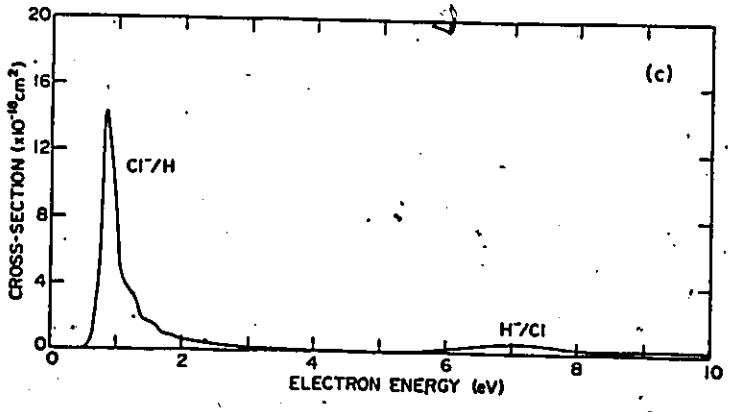
(c)
CROSS-SECTION (×10⁻¹⁸cm²)
Cl⁻/H
H⁻/Cl
ELECTRON ENERGY (eV)

shown in Fig.4-5(b-ii). This curve, taken from Compton and Van Voorhis [154], covers the energy range from threshold to 325 eV.

Vibrational excitation ($e + HCl(v=0) \rightarrow e + HCl(v,j)$) and dissociative attachment ($e + HCl \rightarrow Cl^- + H$, or $H^- + Cl$) are closely affiliated low-energy scattering processes. These processes, together with associative detachment ($Cl^- + H \rightarrow HCl(v,j) + e$), which is not used in the electron simulation, proceed via the formation of an intermediate short-lived state (HCl^-). The total cross-sections for vibrational excitation of the polar molecule (HCl) are deduced from the cross-sections for excitation to the v=1 and v=2 levels, taken from the integral excitation functions obtained experimentally by Rohr and Linder [152,155]. These authors evaluate the absolute cross-section values, at the threshold peaks of the two lowest excitation exit channels, by normalizing their excitation functions to the Cl^-/HCl dissociative attachment data of Christophorou et al.[156]. The normalized values are 18 $\mathring{A}^2$ and 1.4 $\mathring{A}^2$, respectively, with an estimated accuracy of ~50%. There is good agreement with the corresponding values of 12.5 $\mathring{A}^2$ and 1.3 $\mathring{A}^2$ obtained by Ziesel et al.[157]. A maximum Cl^-/HCl dissociative attachment cross-section value of 0.198 $\mathring{A}^2$, obtained by Christophorou et al., differs considerably from other values, which include 0.089 $\mathring{A}^2$ and 0.039 $\mathring{A}^2$ measured by Azria et al.[158] and Buchel'nikova [159], respectively. It is not clear which set of data is the most reliable. The first two sets of data for the attachment cross-sections have been quoted frequently in the literature [155,157,160,161]. We choose to take the average of these two values, which yields a maximum attachment cross-section of

0.14 $\mathring{A}^2$ for Cl^- formation. Consequently, the maximum threshold cross-sections for vibrational excitation to the v=1 and v=2 levels become 12.8 $\mathring{A}^2$ and 1.04 $\mathring{A}^2$, respectively. Moreover, and contrary to the electron distribution for elastic scattering, which peaks in the forward direction, the angular dependence of scattered electrons, for this inelastic process, is isotropic over the entire resonance region. Since the intensity ratio for the first three excited states is ~1.0:0.18:0.08, it is possible to "construct" the total excitation cross-section curve, shown in Fig.4-5(b-i), by including contributions from higher excited levels on the basis of the results given in [152,155], [157] and [162].

The electron attachment cross-sections for the formation of the Cl^- and H^- ions from HCl, appearing in Fig.4-4(c), are based on the results of Azria et al. [158], Abouaf and Teillet-Billy [160], and Azria et al. [163].

D. Electrons

The contribution from the Coulomb interaction between electrons is incorporated into our calculations through the collisional cross-section[¶¶] [164]

$$\sigma_{ee} = 4\pi b_0^2 \ln \Lambda \quad . \qquad (4\text{-}33)$$

[¶¶]Note that the cross-section given by Eq.(4-33) can be replaced by the average Coulomb cross-section of either Shkarofsky et al. [165] ($\langle\sigma_{ee}\rangle = \sqrt{96\pi}\ \overline{b_0}^2 \ln \overline{\Lambda}$) or Mitchner and Kruger [164] ($\langle\sigma_{ee}\rangle = 6\pi\ \overline{b_0}^2 \ln \overline{\Lambda}$). In these cases, $\overline{b_0} = e^2/(8\pi\epsilon_0\bar{\epsilon})$ and $\overline{\Lambda} = \lambda_D/\overline{b_0}$.

The impact parameter for 90° deflection adopted here is

$$b_0 = \frac{e^2}{4\pi\varepsilon_0 \mu g^2} \quad , \tag{4-34}$$

where e is the electron charge, ε_0 the vacuum permittivity, $\mu = m/2$ the reduced mass of electrons (m is the electron mass), and g the relative speed at collision. The impact parameter, at the minimum scattering angle, is usually taken as the Debye shielding length for electrons, defined by

$$\lambda_D = \left(\frac{2\varepsilon_0 \bar{\varepsilon}}{3ne^2}\right)^{1/2} \quad , \tag{4-35}$$

where $\bar{\varepsilon}$ is the average energy of the electron cloud, with electron density n. The parameter Λ in Eq.(4-33) is expressed in terms of the ratio of the Debye length to the impact parameter for right-angle scattering by

$$\Lambda = [1 + (\lambda_D/b_0)^2]^{1/2} \quad . \tag{4-36}$$

4.3 Application to He/Xe/HCl Discharges: Determination of Electron Energy Distributions and Reaction Rates

The Monte-Carlo method was employed to study the early stage of electron avalanches in a typical He/0.5% Xe/0.2% HCl laser mixture at 3000-Torr pressure. A uniform dc electric field was applied between a pair of electrodes having a 1.65-cm separation. The discharge medium was considered to be spatially homogeneous, and any electron scatterings were assumed to be isotropic. The purpose of this study was to derive energy distribution functions suitable for evaluating rate coefficients

for the electron collision processes. These processes control the subsequent formation of $XeCl^*$ species.

In simulations, the probabilities for electron collisions are usually determined using cubic-spline or similar approximations to fit discrete cross-section data over the neighbouring region of a particular energy. However, this approach was not used in our calculations because it often leads to hidden errors. In our computer program for the simulation, the cross-sections for the various scattering processes were in the form of "continuous" functions of electron energies in the range 0-100 eV. Therefore, the probabilities for electron collisions could be easily calculated at any energy in this range. Furthermore, the random numbers in the program were pseudo floating-point numbers uniformly distributed in the (0,1) interval. These were constantly generated for computation using the available subroutine function RANF for the CDC Cyber 170/730 system. This function was initiated by selecting a random time of computation according to the sequence CALL TIME (TX) and CALL RANSET (TX). There are several equivalent library subprograms, such as FRANDN, GGUBS and RANDU, which could also have been used.

Electron-electron collisions were ignored during preliminary runs of the simulation program. An electron, subject to motion by the applied field, was released initially from rest at the cathode (z=0 cm). At each 10^{-11}-s time interval, the instantaneous electron energy ε, velocity $\vec{v}=(v,\theta,\phi)$, position $\vec{r}=(x,y,z)$, mean energy for all previous times $\bar{\varepsilon}$, fractional energy loss over all previous collisions $(\overline{\Delta\varepsilon/\varepsilon})$, and the occurrence frequency of various collisions, were recorded.

Moreover, in the event of an ionization, the initial properties of the new electron (origin, initial velocity, orientation, and time of formation) were stored in the computer memory. The path of the primary electron was traced for 10 ns and then the procedure was repeated for a secondary electron. The computational procedure was terminated either when all electrons in the avalanche had been examined or when the allotted time for the program execution was reached. The simulation was repeated for several runs in order to study avalanches from randomly-oriented primary electrons possessing zero initial energy. For a typical discharge at E/p_0=5.0 V/cm-Torr, the average electron-energy is 5.44 eV, with a probable error of 0.2% determined from [166]

$$\delta_{prob} = \frac{0.675}{\bar{\varepsilon}} \left[\frac{\bar{\varepsilon}^2 - \bar{\varepsilon}^2}{N}\right]^{1/2} \qquad (4\text{-}37)$$

using a set of N=2250 data. At this electron energy, the mean-free-path for electron collisions is 1.48×10^{-5} cm, as shown in Fig.4-6. Therefore, in 10 ns, an average electron only drifts 2.55×10^{-2} cm towards the anode, encountering ~73500 collisions, which are occasionally inelastic. Furthermore, the average fractional energy loss per collision is 4.78×10^{-4}, which can be compared with the fractional elastic scattering loss of 2.74×10^{-4} in pure helium.

In order to determine the equilibrium electron-energy distribution, it was necessary to study primary electrons possessing a range of initial energies. These energies were sampled uniformly over the energy distribution functions obtained from the preliminary simulation. The best method for initiating a typical set of velocity parameters (v_0, θ, ϕ) made use of quasi-random numbers generated by employing bases of an

Fig. 4-6

Mean-free-path for electron collisions, as a function of electron energy, in a He/0.5% Xe/0.2% HCl mixture at 3000-Torr pressure. The Coulomb contribution is ignored.

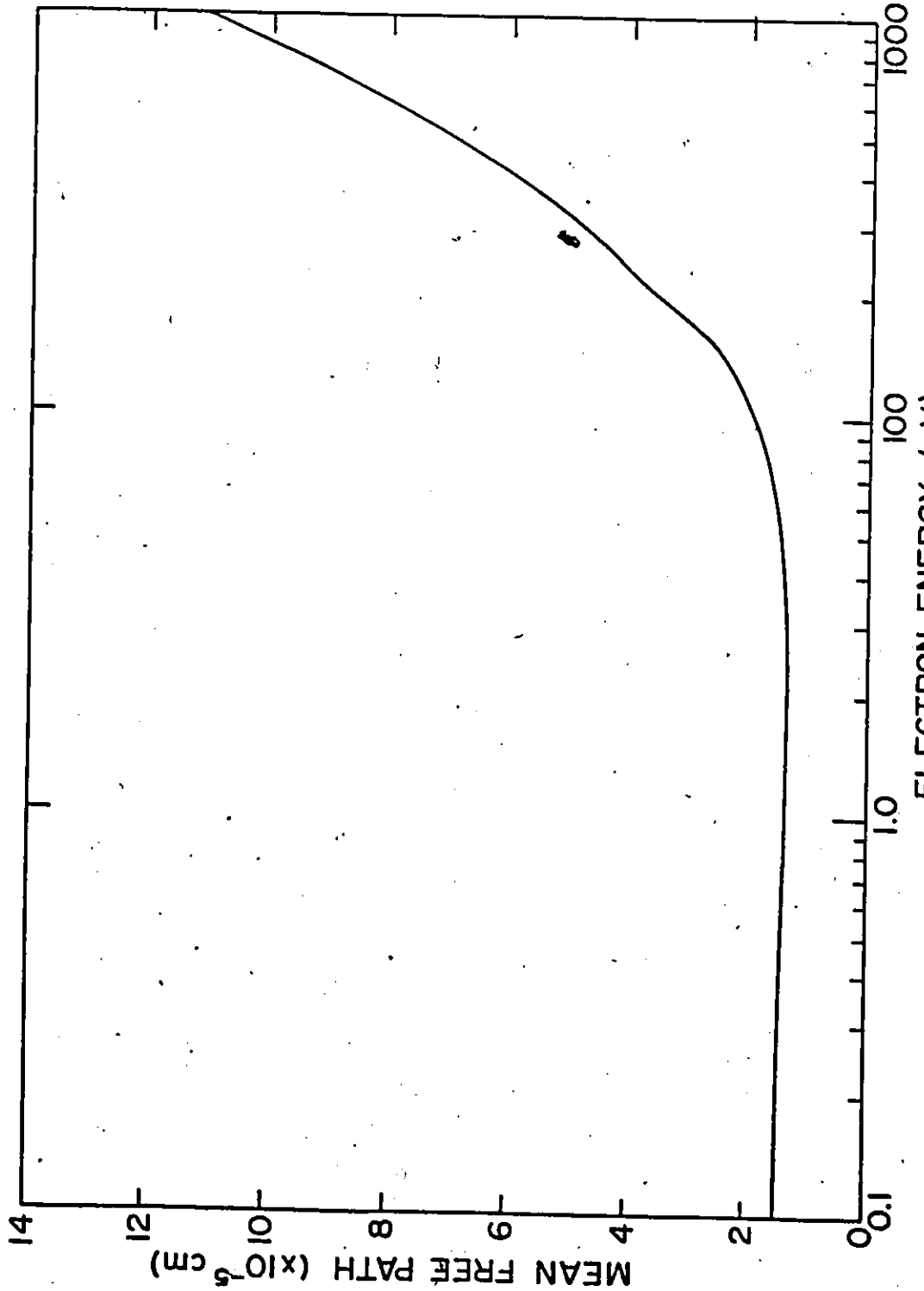
MEAN FREE PATH (x10⁻⁵ cm)
0
2
4
6
8
10
12
14
0.1
1.0
10
100
1000
ELECTRON ENERGY (eV)

algebraic field of order 3 (such as the real cyclotomic field $R(2\cos\frac{2\pi}{7})$[167]), or by employing the optimal coefficients derived by Korobov [168]. The computational procedure was repeated several times, using the last calculated energy distribution function, until a stable distribution was obtained. In order to avoid excessive computation time, the electron avalanches were usually traced for 1ns, which is still far in excess of the relaxation time (estimated to be ~0.1 ns). Note that the computation time for this method is substantially less than that required when the Coulomb scattering is included, as is done below. Using the same E/p_0 = 5.0 V/cm-Torr as previously, the average electron energy and the average fractional energy loss per collision are changed to 5.48 eV (from 5.44 eV) and 5.51×10^{-4} (from 4.78×10^{-4}), respectively.

In the principal simulation program, the Coulomb effect was included by assuming a degree of ionization. The maximum degree of ionization, estimated from experimental curves of the main discharge current (Figs.3-25 to 3-27, and Figs.3-33 to 3-35), is in the range $2\text{-}3 \times 10^{-5}$. Figures 4-7 and 4-8 show simulation results for the average electron energy and the average fractional electron energy loss per collision, for various degrees of ionization and for various values of E/p_0. At a high ionization level, the total electron collision frequency becomes large, primarily due to increased occurrence of Coulomb scattering by electrons. In this scattering process, electrons equilibrate their energy either by releasing excess energy, or by gaining energy from the electron cloud. In a typical discharge medium,

Fig. 4-7

Average electron energy for a He/0.5% Xe/0.2% HCl discharge mixture. The energy is shown as a function of (a) degree of ionization for different E/[redacted]lues, and (b) E/p_0 for two ionization levels.

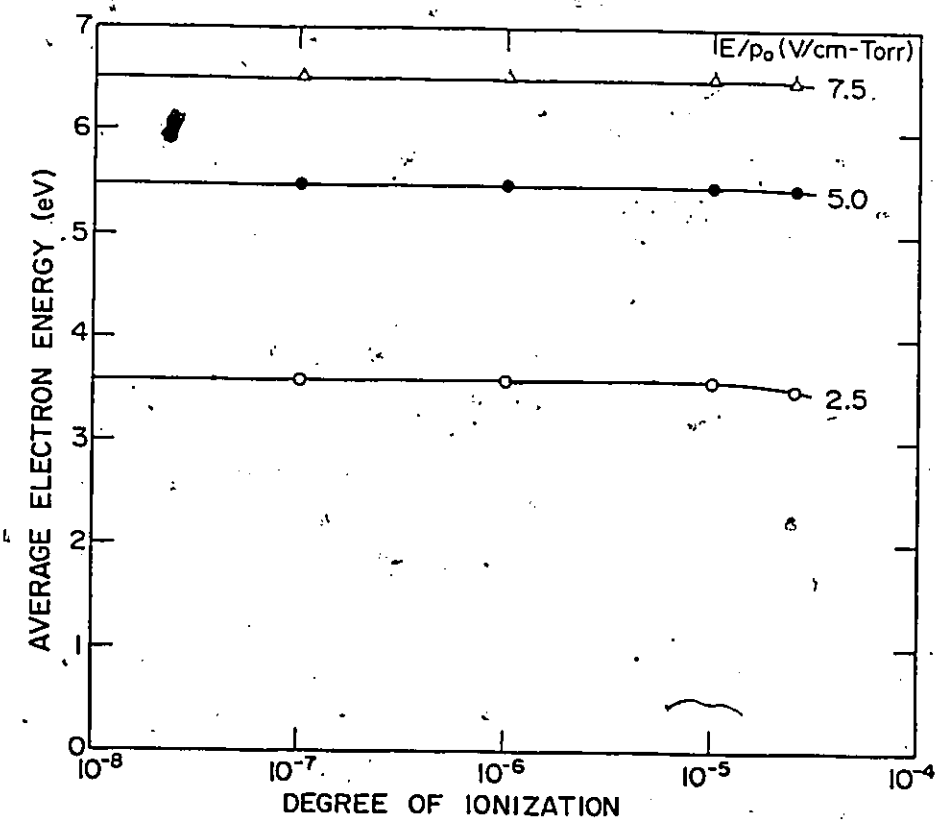
E/p₀ (V/cm-Torr)
7.5
5.0
2.5
AVERAGE ELECTRON ENERGY (eV)
DEGREE OF IONIZATION
0
1
2
3
4
5
6
7
10⁻⁸
10⁻⁷
10⁻⁶
10⁻⁵
10⁻⁴

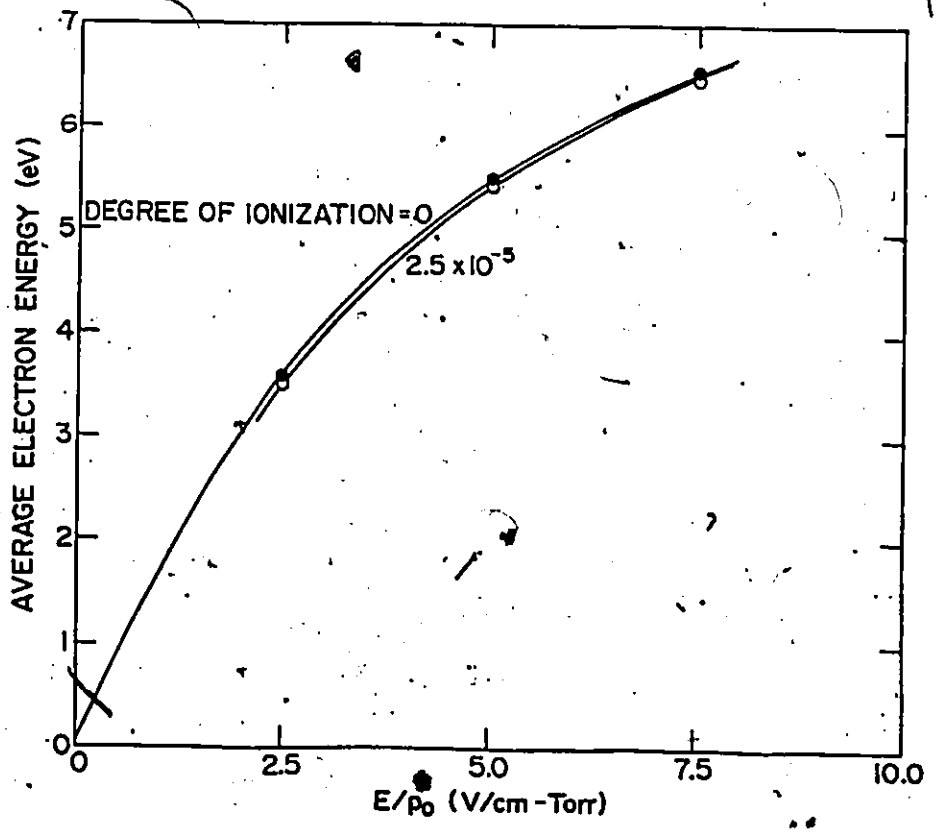
DEGREE OF IONIZATION = 0
2.5 x 10⁻⁵
AVERAGE ELECTRON ENERGY (eV)
E/p₀ (V/cm-Torr)
0
1
2
3
4
5
6
7
0
2.5
5.0
7.5
10.0

Fig. 4-8

Average fractional energy loss for a He/0.5% Xe/0.2% HCl discharge mixture. The energy loss is shown as a function of (a) degree of ionization for different E/p_0 values, and (b) E/p_0 for different ionization levels.

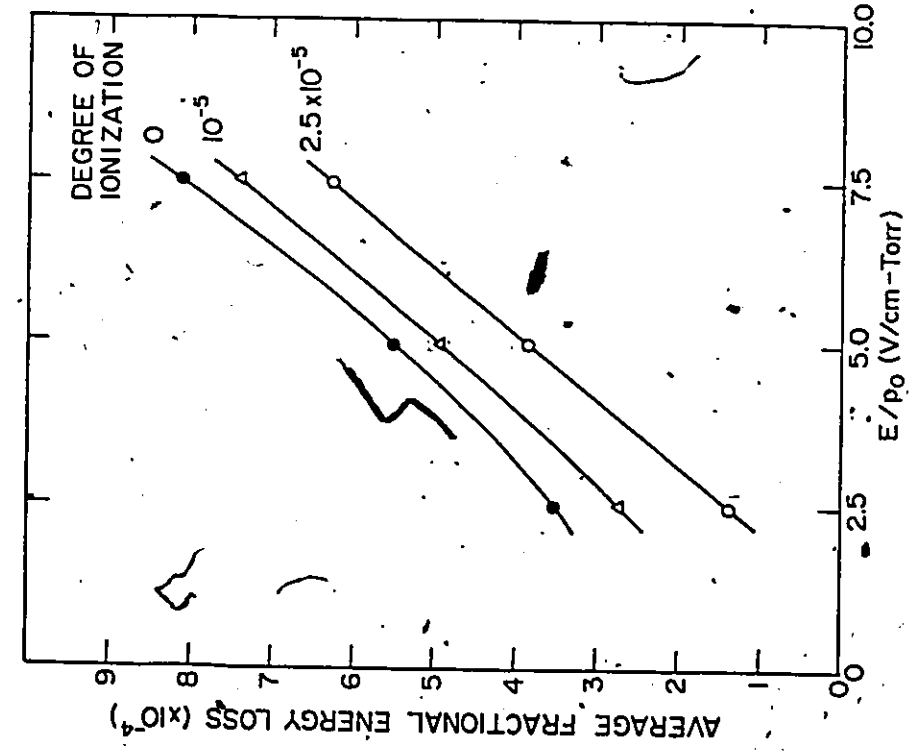
DEGREE OF IONIZATION
0
10^{-5}
2.5×10^{-5}
AVERAGE FRACTIONAL ENERGY LOSS ($\times 10^{-4}$)
E/p_0 (V/cm-Torr)
0.0
2.5
5.0
7.5
10.0

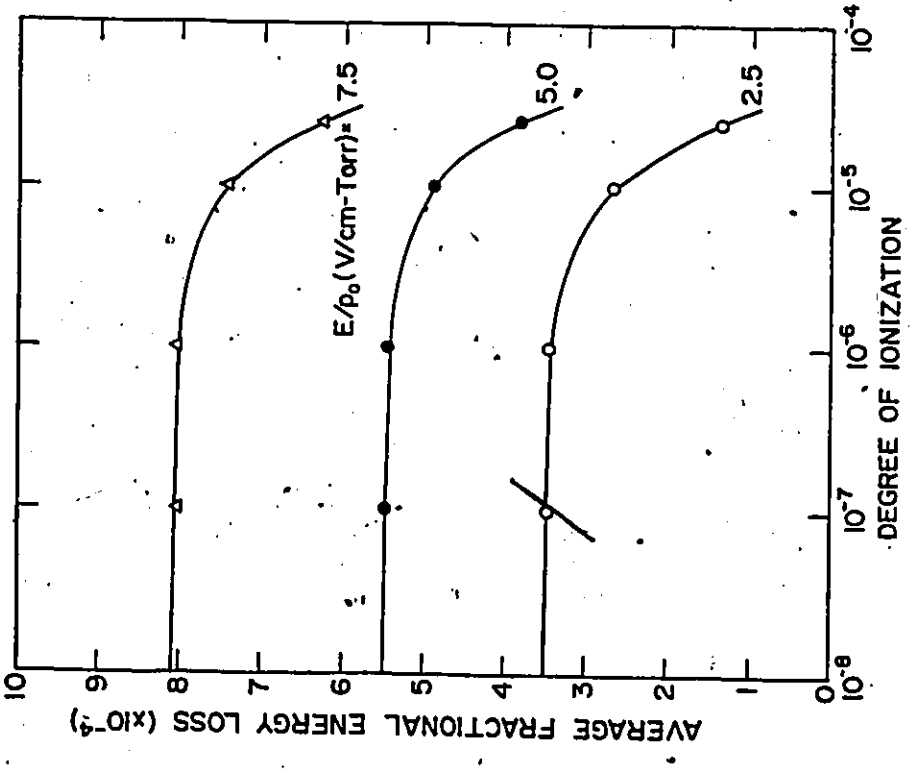
E/p_0 (V/cm-Torr)
7.5
5.0
2.5
AVERAGE FRACTIONAL ENERGY LOSS ($\times 10^{-4}$)
DEGREE OF IONIZATION
10^{-8}
10^{-7}
10^{-6}
10^{-5}
10^{-4}

there are more low-energy electrons than electrons with energies higher than the mean energy of the distribution. Therefore, the average fractional energy loss per collision is reduced, with little change to the average electron energy.

The critical degree of ionization, at which the influence of Coulomb collisions becomes important, can be estimated from the expression [169]

$$\left(\frac{n}{N}\right)_{crit} = \frac{4\pi\varepsilon_0{}^2E^2\lambda}{Ne^2\ell n\Lambda} , \qquad (4\text{-}38)$$

where

$$\Lambda \cong \frac{12\pi}{\sqrt{n}} \left(\frac{\varepsilon_0\bar{\varepsilon}}{1.5e^2}\right)^{1.5} . \qquad (4\text{-}39)$$

Here, n and N are the electron and gas densities, e is the electron charge, ε_0 is the permittivity of free space, E is the magnitude of the applied field, λ is the mean-free-path for collisions with gas particles, and $\bar{\varepsilon}$ is the mean electron energy. The condition given by Eq.(4-38) is derived by balancing the electron energy gained, between collisions, from the applied field, and the average energy exchange at electron collision. For the discharge mixture given, the critical ionization levels are estimated to be 3.4×10^{-6}, 1.4×10^{-5} and 3.1×10^{-5} at E/p_0 = 2.5 V/cm-Torr, 5.0 V/cm-Torr and 7.5 V/cm-Torr, respectively. These values were usually reached in our laser discharges.

In a typical simulation, it was not feasible to study a large number of electron avalanches. It was also not practicable to examine the complete path of a primary electron to the anode. These procedures

required computation times exceeding the maximum allocated user time of 9000 s on the McMaster Cyber 170 computer. However, it was fruitful to sample energy data periodically from a limited number of avalanches. These avalanches were initiated by electrons with energies selected uniformly over an assumed distribution. The equilibrium electron-energy distribution was considered satisfactory when there was good agreement with the results obtained from a separate simulation, under similar excitation conditions, using relaxing avalanches (i.e., primary electrons with zero initial energy). Furthermore, the amount of sampled data was considered adequate if the addition of the last group of data into the previous data collection did not affect either the collective properties of the electrons, or the energy distribution, by more than a few percent.

The instantaneous electron energies sampled from a simulation were grouped at 0.1-eV or 0.2-eV intervals, depending on the amount of data available, and on the range of energies covered. These energy distribution data were than least-squares fitted to a function of the form given by Eq.(4-18)[§]. Figure 4-9 shows typical Monte-Carlo results for the energy distribution obtained using E/p_0 = 5.0 V/cm-Torr, degree of ionization = 10^{-5}, and a set of 12166 data. The curve is based on N = 118.234, β = 0.057, h = 0.484 and k = 1.557. In general, the distribution function can be normalized using

---

[§]The energy distribution function, $F(\varepsilon)$, is related to the velocity distribution function, $f(v)$, defined in Appendix E, by $F(\varepsilon) = vf(v)$, where $\varepsilon = \frac{1}{2}mv^2$, and m is the electron mass.

Fig. 4-9

Electron energy distribution at $E/p_0 = 5.0$ V/cm-Torr for a He/0.5% Xe/0.2% HCl mixture at 3000-Torr pressure. The degree of ionization is assumed to be 10^{-5}.

(i) Statistical results of Monte-Carlo simulation.

(ii) Least-squares fitted function given by Eq.(4-18).

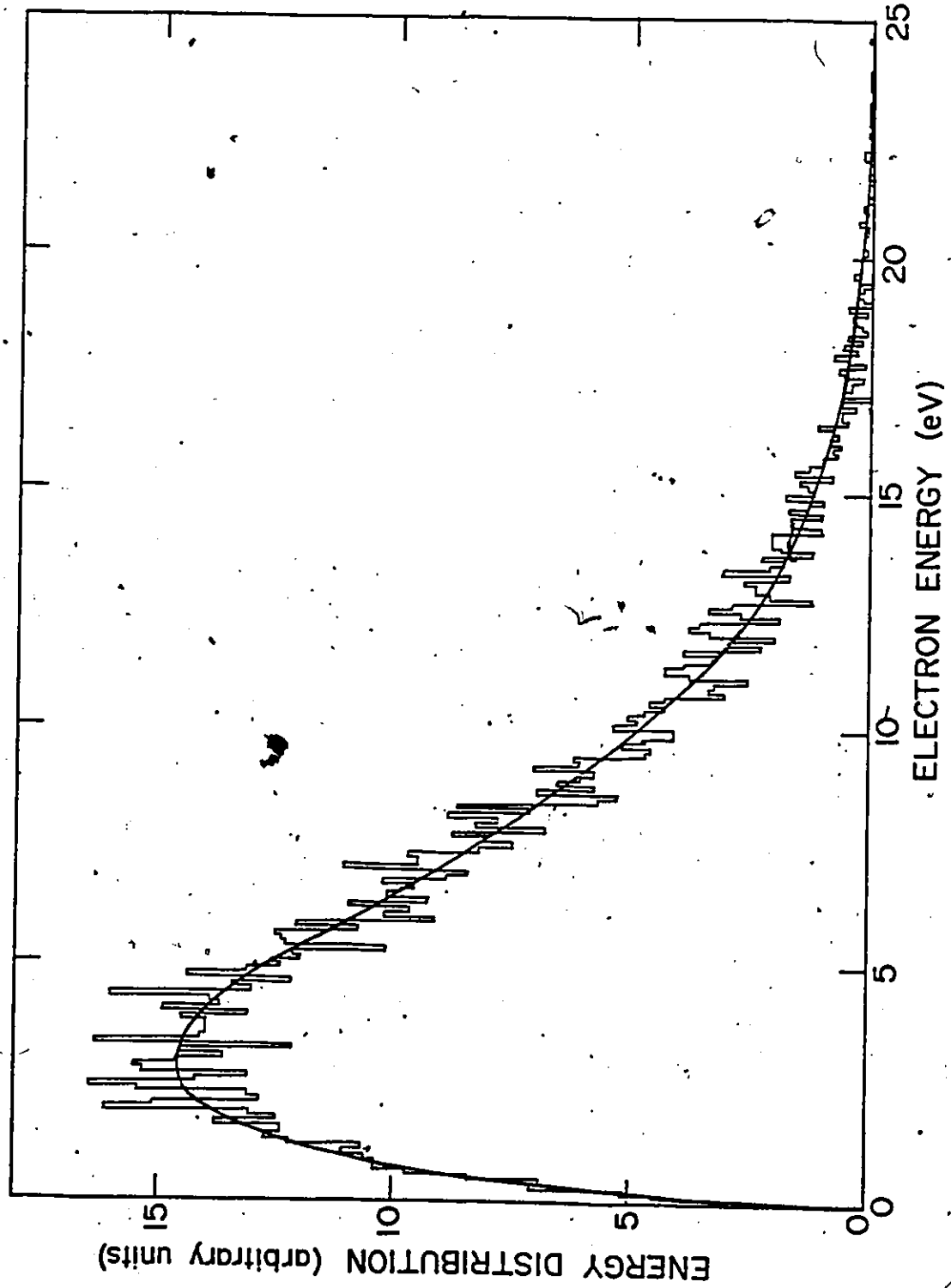
ENERGY DISTRIBUTION (arbitrary units)
0
5
10
15
0
5
10
15
20
25
ELECTRON ENERGY (eV)

$$\int_0^\infty F(\varepsilon)\, d\varepsilon = 1 \quad . \tag{4-40}$$

The normalization factor N (Eq.(4-19)) then assumes the value of 0.099. In addition,

$$\bar{\varepsilon} = \int_0^\infty \varepsilon F(\varepsilon)\, d\varepsilon \tag{4-41}$$

gives the mean electron energy of the distribution. A value of $\bar{\varepsilon}$ = 5.43 eV, found in the simulation, has been adopted for the above curve fitting. The fitting discrepancy is well within 5%, and the statistical sampling error (the probable error) in energy is ±0.23%. In some of our simulations, the sampling error was as low as ±0.04%.

In Fig.4-10, the present energy distribution function (Eq.(4-18)) is compared with those due to Maxwell-Boltzmann,

$$F_{MB}(\varepsilon) = (2.073/\bar{\varepsilon})\ (\varepsilon/\bar{\varepsilon})^{1/2}\ \exp[-1.5(\varepsilon/\bar{\varepsilon})] \quad , \tag{4-42}$$

and to Druyvestyn,

$$F_D(\varepsilon) = (1.038/\bar{\varepsilon})\ (\varepsilon/\bar{\varepsilon})^{1/2}\ \exp[-0.547(\varepsilon/\bar{\varepsilon})^2] \quad . \tag{4-43}$$

A mean electron energy, $\bar{\varepsilon}$ = 5.43 eV, is used as before. If statistical equilibrium can be assumed for the electrons and gas molecules, then a Maxwell-Boltzmann distribution applies. The Druyvestyn energy distribution prevails if both the mean fractional energy loss for electrons and the mean-free-path for collisions vary very slowly with energy. In general, a discharge medium is seldom in thermal equilibrium, and elastic scattering of electrons is not the only energy-loss process. Energy-dependent inelastic scattering processes, such as ionization, excitation and attachment, necessarily induce an abrupt loss of electron

Fig. 4-10

Comparison of various electron energy distribution functions. These functions are given by Eqs.(4-18), (4-42) and (4-43).

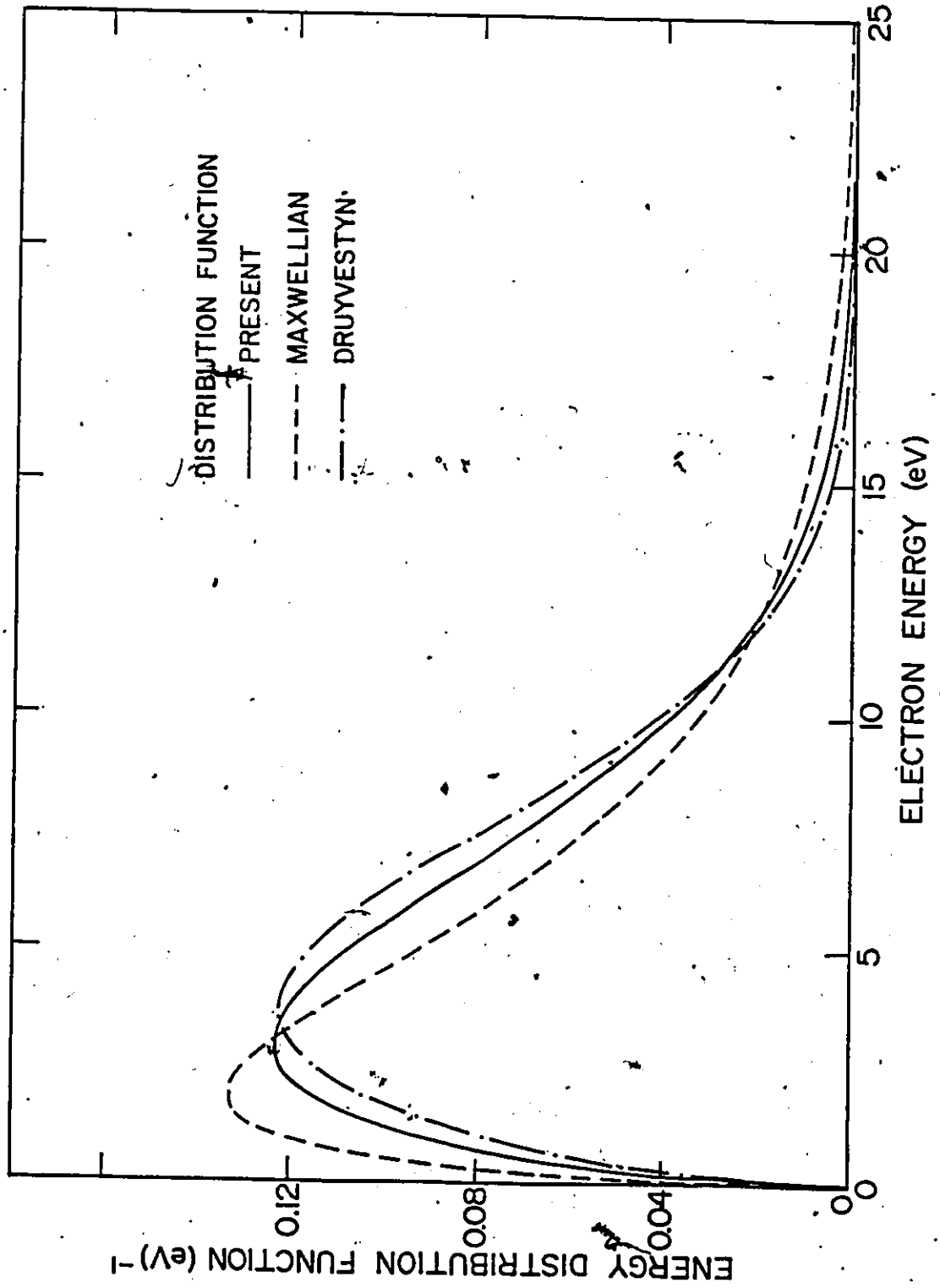
DISTRIBUTION FUNCTION
PRESENT
MAXWELLIAN
DRUYVESTYN
ENERGY DISTRIBUTION FUNCTION (eV)⁻¹
0.12
0.08
0.04
0
0
5
10
15
20
25
ELECTRON ENERGY (eV)

energy. The present energy distribution function, which is intermediary between the two theoretical functions represented by Eqs.(4-42) and (4-43), clearly illustrates the combined effect due to inelastic collisions and to the dominant elastic collisions (including the Coulomb scattering between electrons). From Fig.4-11, it can be seen that the Coulomb effect (e.g., at a high ionization level of 2.5×10^{-5} and at E/p_0 = 5.0 V/cm-Torr) influences the energy distribution by transferring low-energy electrons to the tail of the distribution in the process of "Maxwellization". Figures 4-12 and 4-13 illustrate how the parameters h and k (in the distribution function represented by Eq.(4-18)) vary with the applied fields, at high ionization levels of 10^{-5} and 2.5×10^{-5}, respectively. These are typical values for the XeCl laser discharge. Parameter h appears to have a constant value of ∿0.5. The variation of parameter k, from ∿2.0 to ∿1.0, illustrates the transition from a Druyvestyn to a Maxwell-Boltzmann distribution. Figure 4-14 compares the energy distribution functions (using Eq.4-18) for E/p_0 = 2.5 V/cm-Torr, 5.0 V/cm-Torr and 7.5 V/cm-Torr, assuming the same degree of ionization (10^{-5}).

In order to study the relaxation of the discharge, the production of secondary electrons, and the loss of electrons due to attachment in HCl, it was necessary to trace a relatively large number of avalanches for a sufficiently long drift time (typically 0.5 ns). Zero-energy primary electrons were assumed. The relaxation in energy distribution, for an ionization level of 10^{-5} and for E/p_0 = 5.0 V/cm-Torr, is shown in Fig.4-15. Clearly, the electron distribution is close to equilibrium after an electron drift of only 0.5 ns. Further confirmation is given

Fig. 4-11

Electron energy distribution functions for a He/0.5% Xe/0.2% HCl mixture at E/p_0 = 5.0 V/cm-Torr, (a) when the Coulomb effect is neglected and (b) when the degree of ionization is 2.5×10^{-5}. These functions are least-squares fitted to the results of the Monte-Carlo simulations.

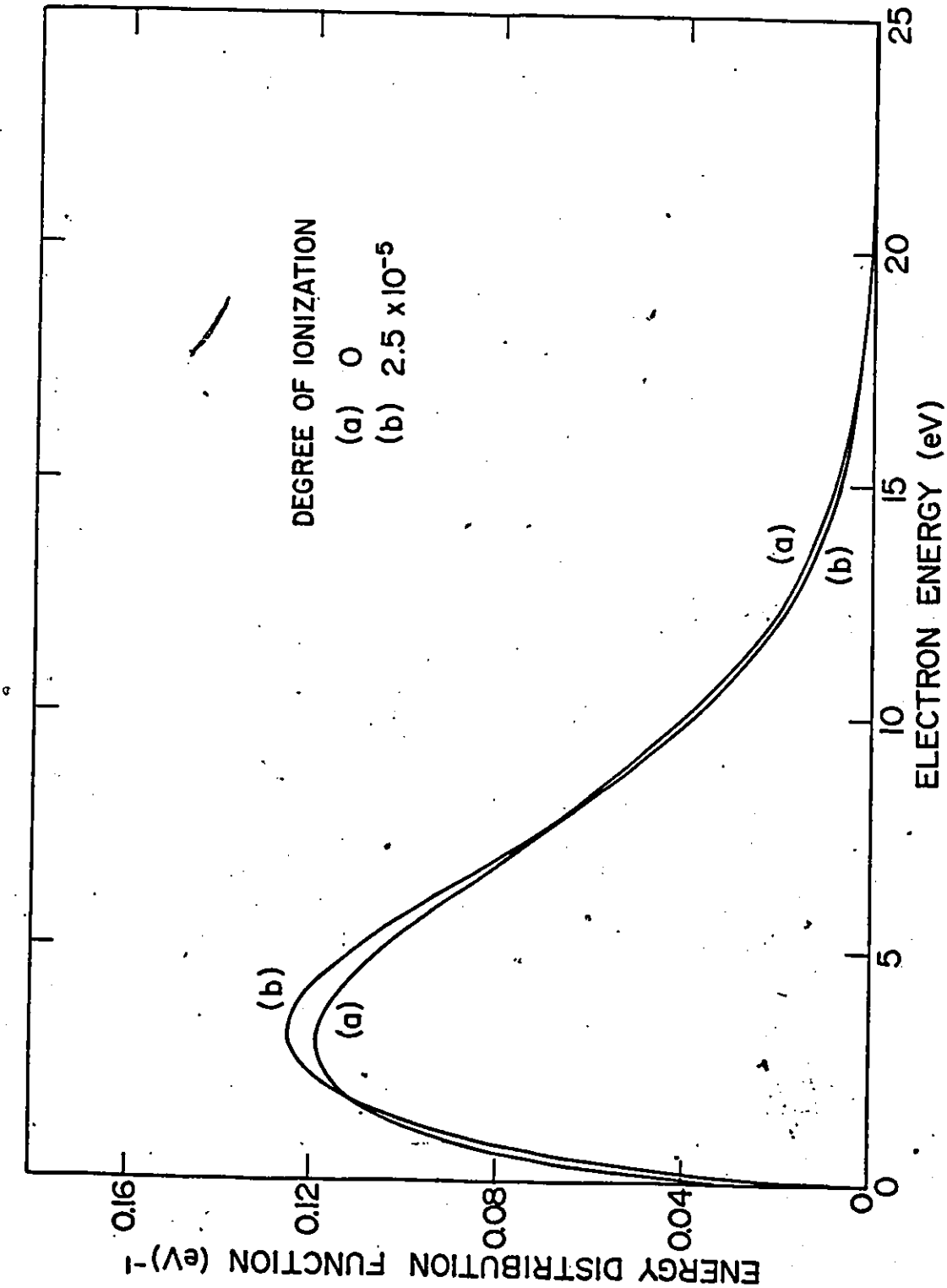
ENERGY DISTRIBUTION FUNCTION (eV)-1
0.16
0.12
0.08
0.04
0
5
10
15
20
25
ELECTRON ENERGY (eV)
DEGREE OF IONIZATION
(a) 0
(b) 2.5 x10-5
(a)
(b)
(a)
(b)

Fig. 4-12

Variation of the parameters h and k, as a function of E/p_0, for a He/0.5% Xe/0.2% HCl mixture at an ionization level of 10^{-5}. These parameters are used in Eq.(4-18).

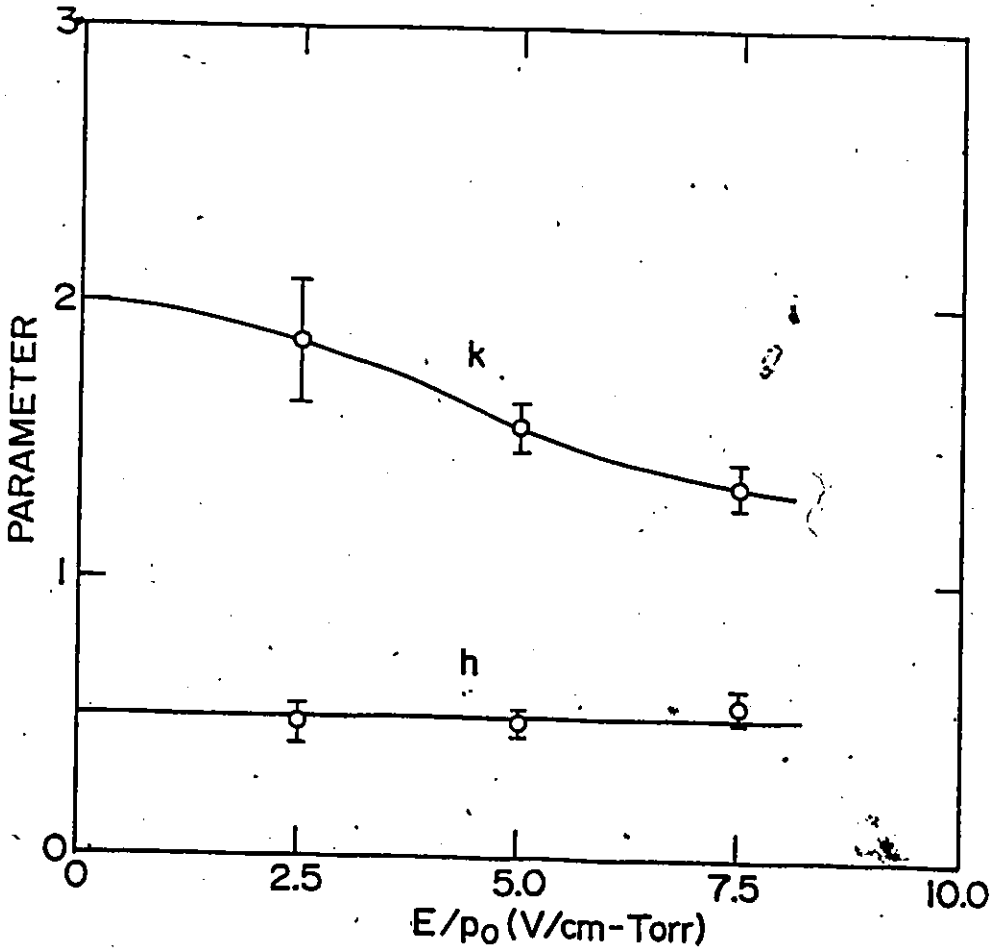
PARAMETER
3
2
1
0
k
h
0
2.5
5.0
7.5
10.0
E/p0 (V/cm-Torr)

Fig. 4-13

Variation of the parameters h and k, as a function of E/p_0, at an ionization level of 2.5×10^{-5}. The discharge mixture is the same as in Fig.4-12.

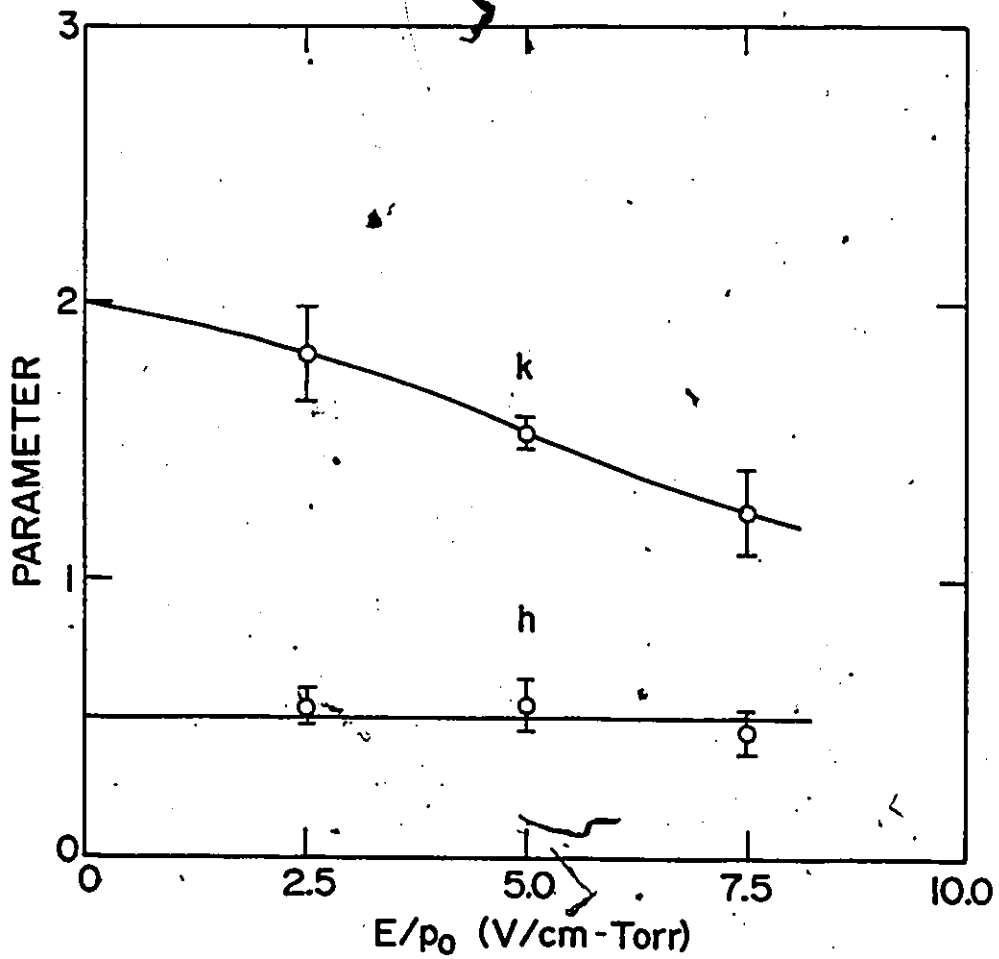
3
2
1
0
PARAMETER
k
h
0
2.5
5.0
7.5
10.0
E/p0 (V/cm-Torr)

Fig. 4-14

Electron energy distribution function for a He/0.5% Xe/0.2% HCl mixture at an ionization level of 10^{-5} and for E/p_0 equal to (a) 2.5 V/cm-Torr, (b) 5.0 V/cm-Torr and (c) 7.5 V/cm-Torr. These functions are least-squares fitted to the results of the Monte-Carlo simulations.

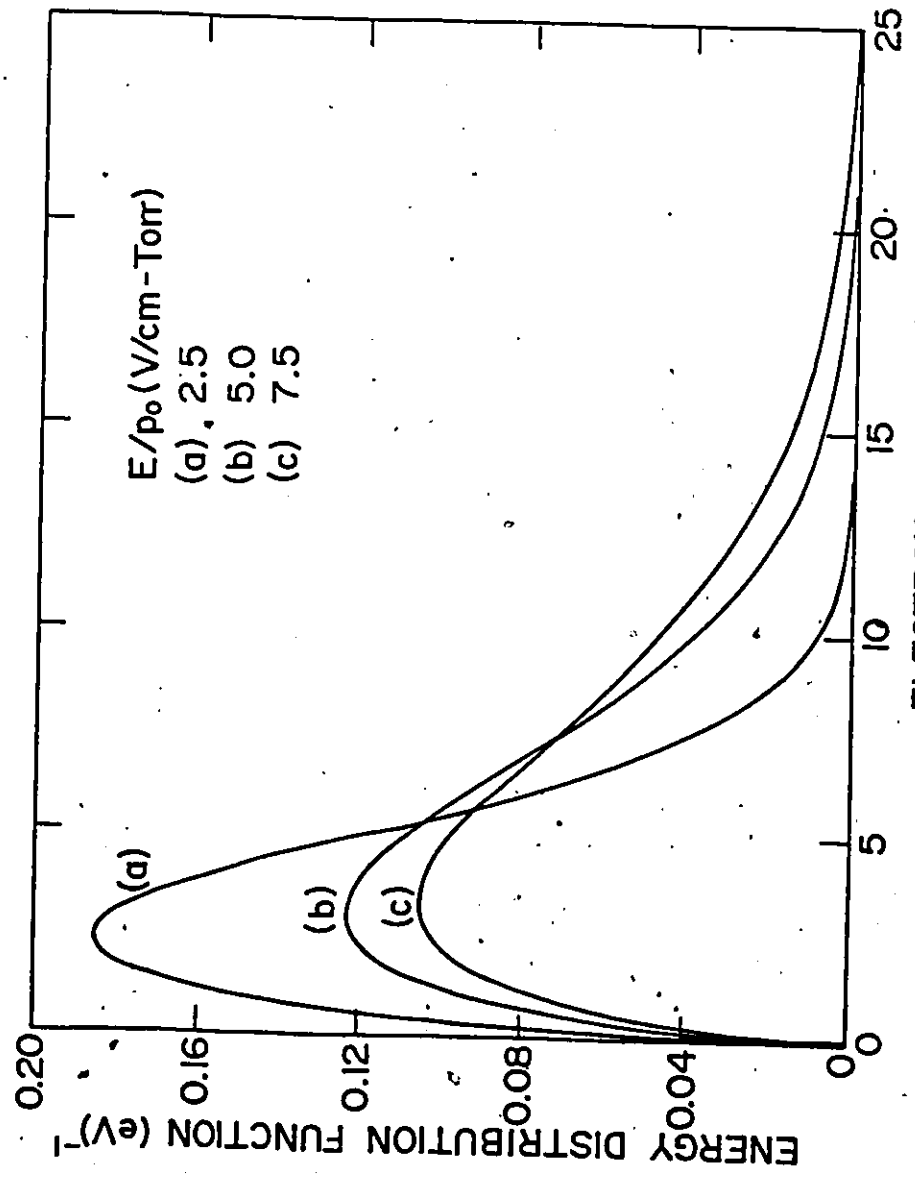
ENERGY DISTRIBUTION FUNCTION (eV)⁻¹
0.20
0.16
0.12
0.08
0.04
0
0
5
10
15
20
25
ELECTRON ENERGY (eV)
E/p₀ (V/cm-Torr)
(a) 2.5
(b) 5.0
(c) 7.5
(a)
(b)
(c)

Fig. 4-15

Relaxation of electron energy distribution for a He/0.5% Xe/0.2% HCl mixture at E/p_0 = 5.0 V/cm-Torr and an ionization level of 10^{-5}. The distribution functions, at times (a) 0.1 ns and (b) 0.5 ns, and (c) at equilibrium, are least-squares fitted to the results of the Monte-Carlo simulations.

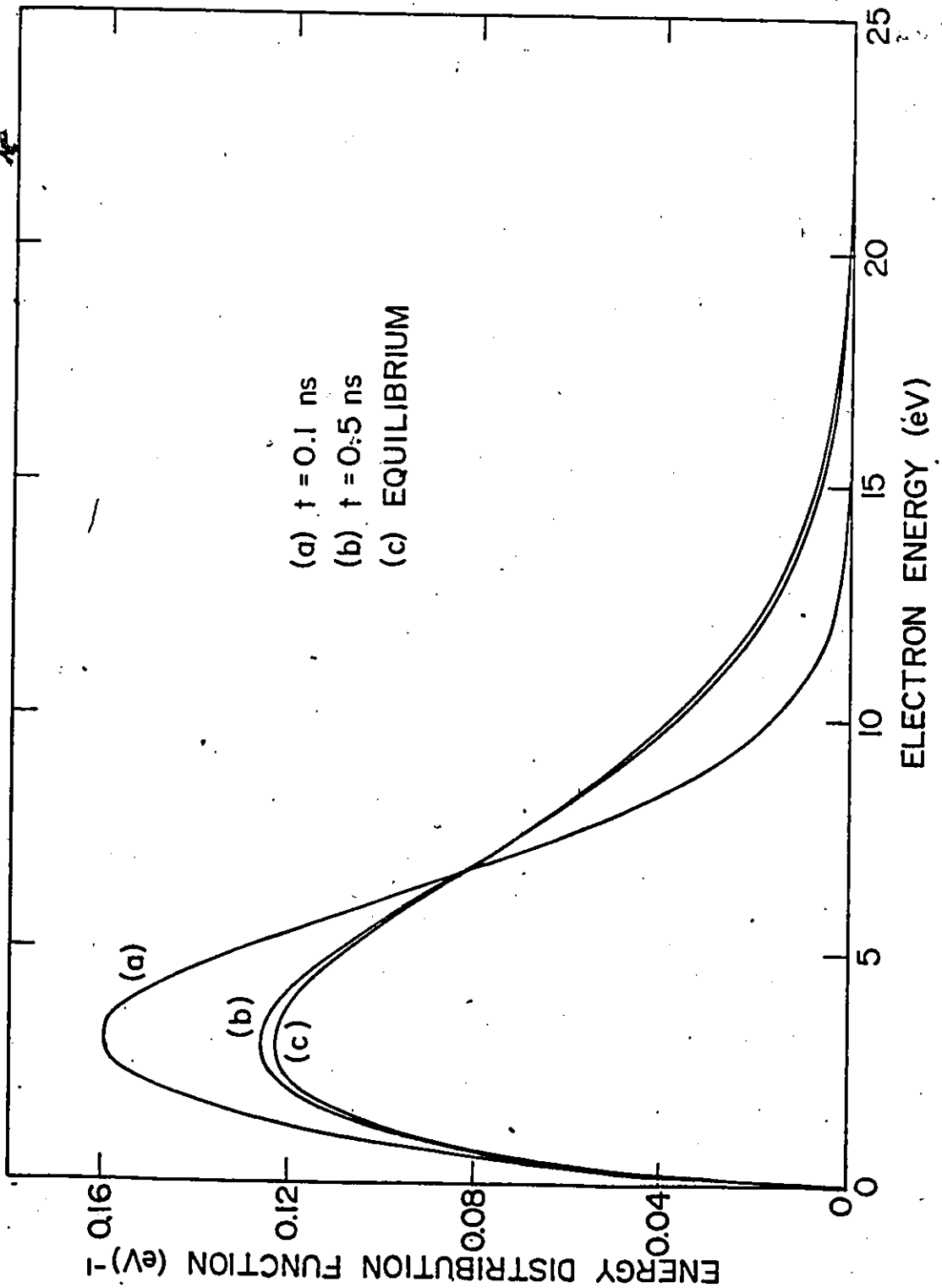
ENERGY DISTRIBUTION FUNCTION (eV)-1
0.16
0.12
0.08
0.04
0
0
5
10
15
20
25
ELECTRON ENERGY (eV)
(a) t = 0.1 ns
(b) t = 0.5 ns
(c) EQUILIBRIUM
(a)
(b)
(c)

by Fig.4-16, which compares the mean-energy relaxation for various discharges but at the same ionization level. The observed relaxation time, which is typically a few tenths of a nanosecond, depends on the discharge operating conditions and on the number of electrons present in the system.

Electrons collide frequently with gas particles. The number of collisions encountered by an electron varies with the instantaneous electron energy and with the strength of the applied field. Figure 4-17 gives the collision frequencies of a typical zero-energy electron during relaxation, for several values of E/p_0. Collision frequencies for different types of electron collisions, for E/p_0 = 5.0 V/cm-Torr and a degree of ionization of 10^{-5}, are given in Fig.4-18. The dominant electron collision processes are elastic scatterings by gas particles; the least dominant process is the ionization of helium atoms, which requires electron energies above 24.6 eV. Electron dissociative attachment in HCl occurs only occasionally.

Figure 4-19 describes the lateral and longitudinal development of a relaxing avalanche drifting towards the anode. The drift velocity can be determined from the slope of the curve giving the average electron position (from the cathode) as function of time (Fig.4-19(b)), using

$$v_d = \frac{\bar{z}(t_1) - \bar{z}(t_0)}{t_1 - t_0} \qquad (4\text{-}44)$$

A reliable result is obtained when only the drift data for both t_1 and $t_0 > \tau_r$ (the relaxation time) are considered. For a discharge at E/p_0 = 5.0 V/cm-Torr and at an electron concentration of 10^{-5}, v_d approaches

Fig. 4-16

Energy relaxation of a 0-eV primary electron for a He/0.5% Xe/0.2% HCl mixture, for an ionization level of 10^{-5}, and for E/p_0 equal to (a) 7.5 V/cm-Torr, (b) 5.0 V/cm-Torr and (c) 2.5 V/cm-Torr.

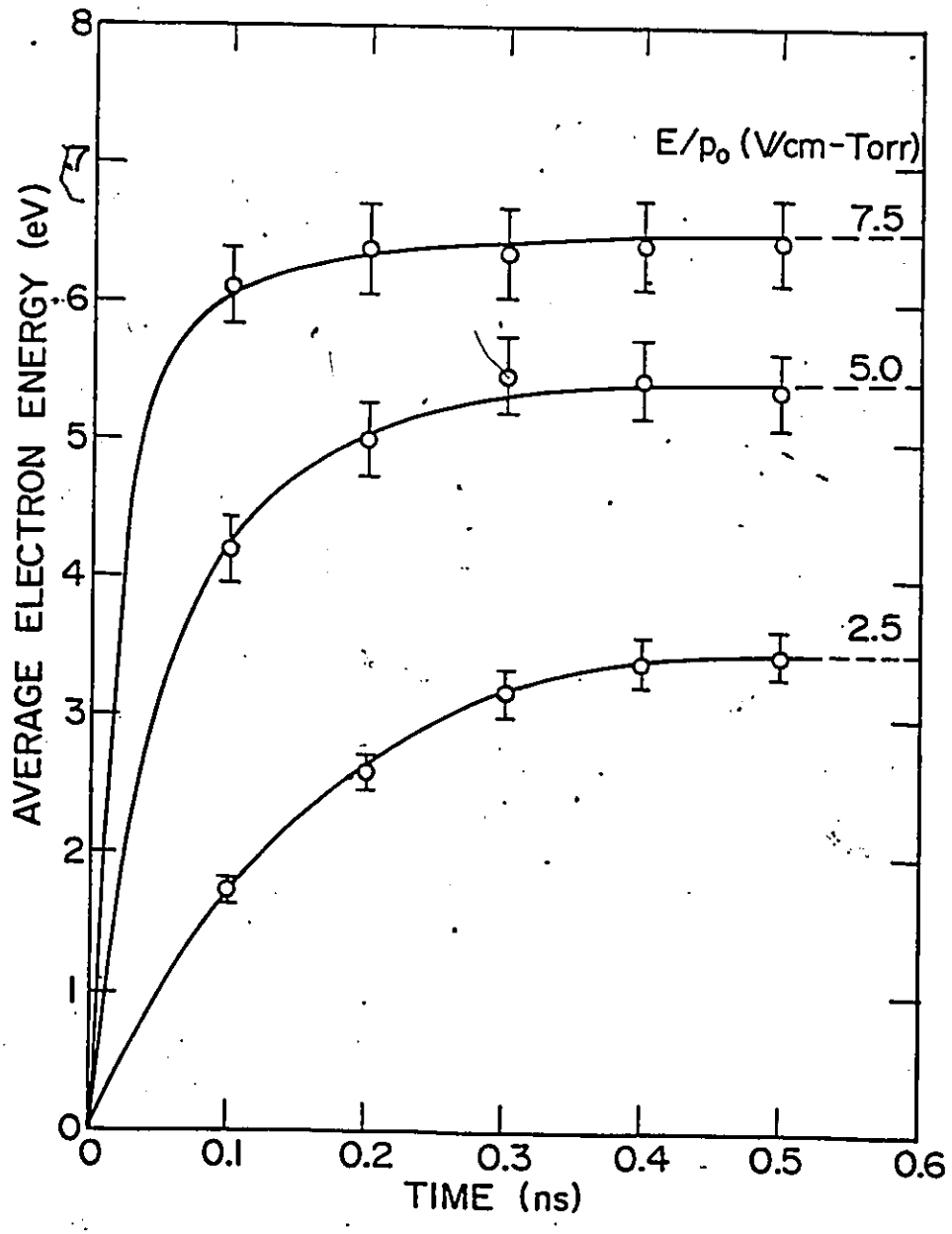
AVERAGE ELECTRON ENERGY (eV)
TIME (ns)
E/p₀ (V/cm-Torr)
7.5
5.0
2.5
0
1
2
3
4
5
6
7
8
0
0.1
0.2
0.3
0.4
0.5
0.6

Fig. 4-17

Variation of average electron-collision frequency, with time, for a 0-eV primary electron drifting in a He/0.5% Xe/0.2% HCl discharge medium at an ionization level of 10^{-5}, and for E/p_0 = 7.5 V/cm-Torr (Δ), 5.0 V/cm-Torr (●) and 2.5 V/cm-Torr (o).

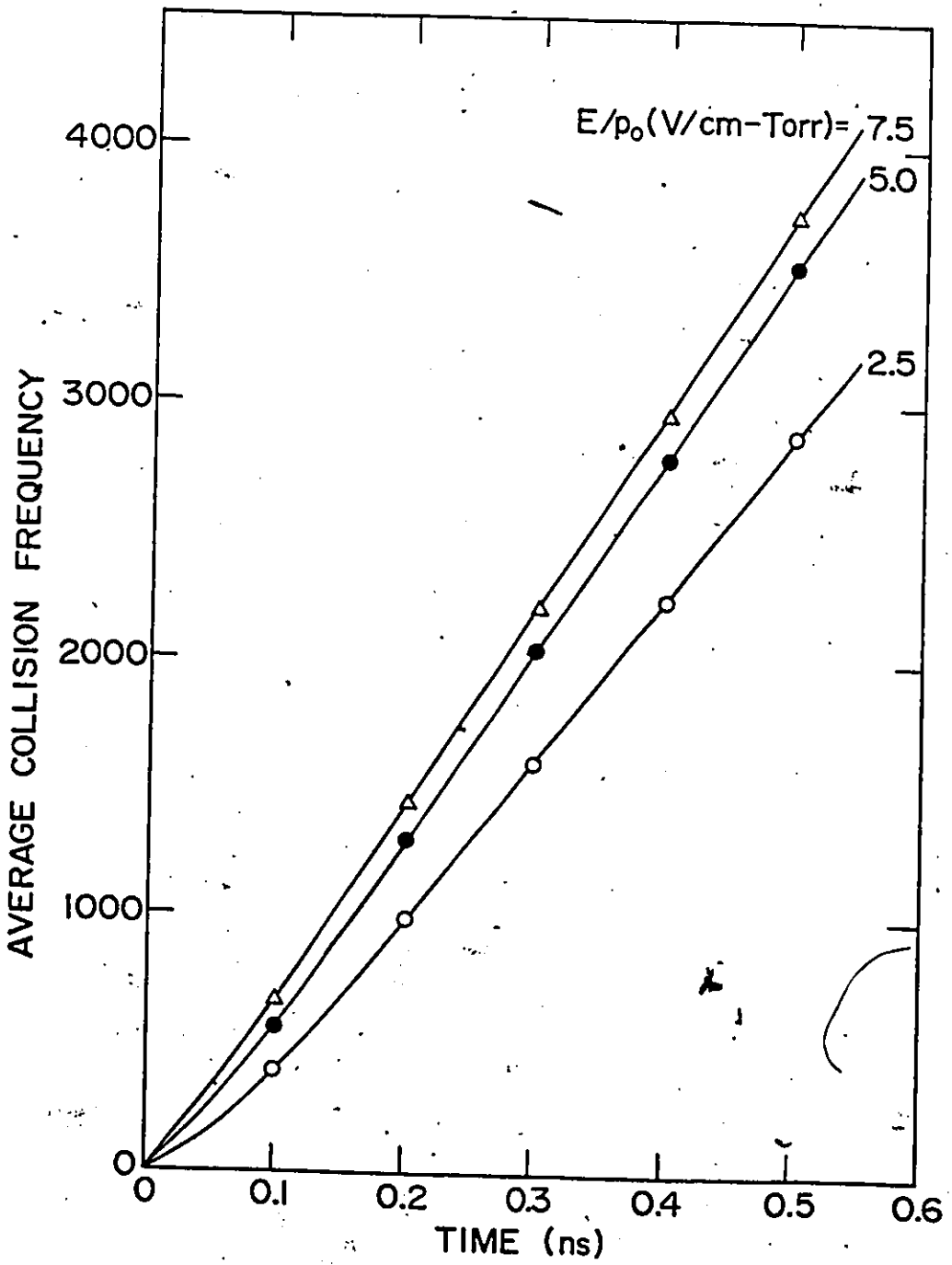
E/p₀(V/cm-Torr)=
7.5
5.0
2.5
AVERAGE COLLISION FREQUENCY
4000
3000
2000
1000
0
0
0.1
0.2
0.3
0.4
0.5
0.6
TIME (ns)

Fig. 4-18

Occurrence frequencies for various electron collision processes in a discharge derived from simulations of a He/0.5% Xe/0.2% HCl mixture at 3000-Torr pressure, and for E/p = 5.0 V/cm-Torr. The degree of ionization is assumed to be 10^{-5}.

(i) Elastic collision of an electron with He.

(ii) Elastic collision of an electron with Xe.

(iii) Elastic collision of an electron with HCl.

(iv) Electron-impact excitation of Xe.

(v) Vibrational excitation of HCl by electron impact.

(vi) Electron-impact ionization of Xe.

(vii) Electron-electron collision.

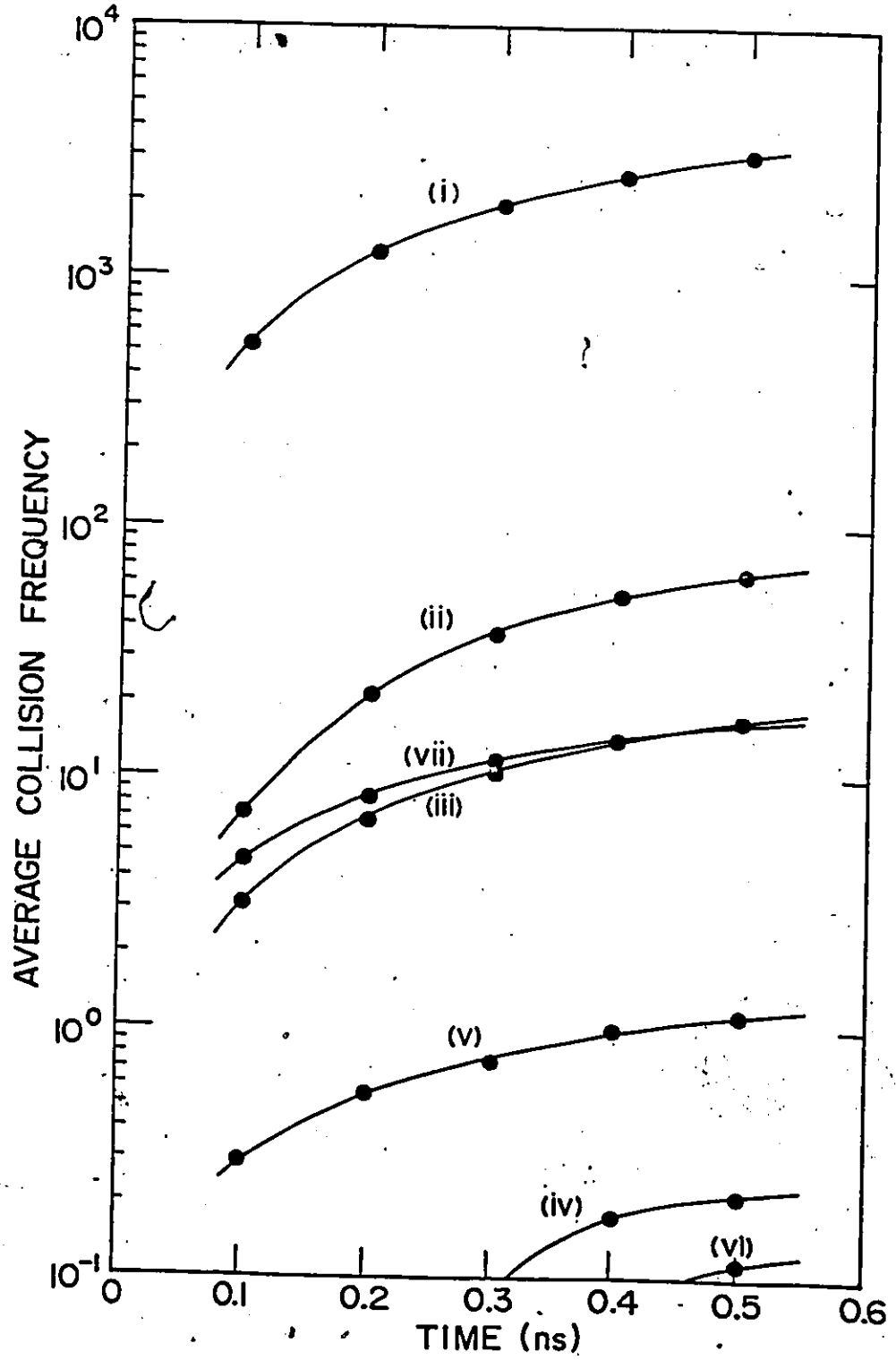
AVERAGE COLLISION FREQUENCY
10^4
10^3
10^2
10^1
10^0
10^{-1}
(i)
(ii)
(vii)
(iii)
(v)
(iv)
(vi)
0
0.1
0.2
0.3
0.4
0.5
0.6
TIME (ns)

Fig. 4-19

Spatial development of an avalanche from a 0-eV primary electron, in a He/0.5% Xe/0.2% HCl discharge medium at an ionization level of 10^{-5}, and for E/p_0 = 7.5 V/cm-Torr (Δ), 5.0 V/cm-Torr (•) and 2.5 V/cm-Torr (o).

(a) Radial development.

(b) Longitudinal drift.

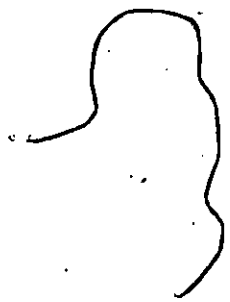

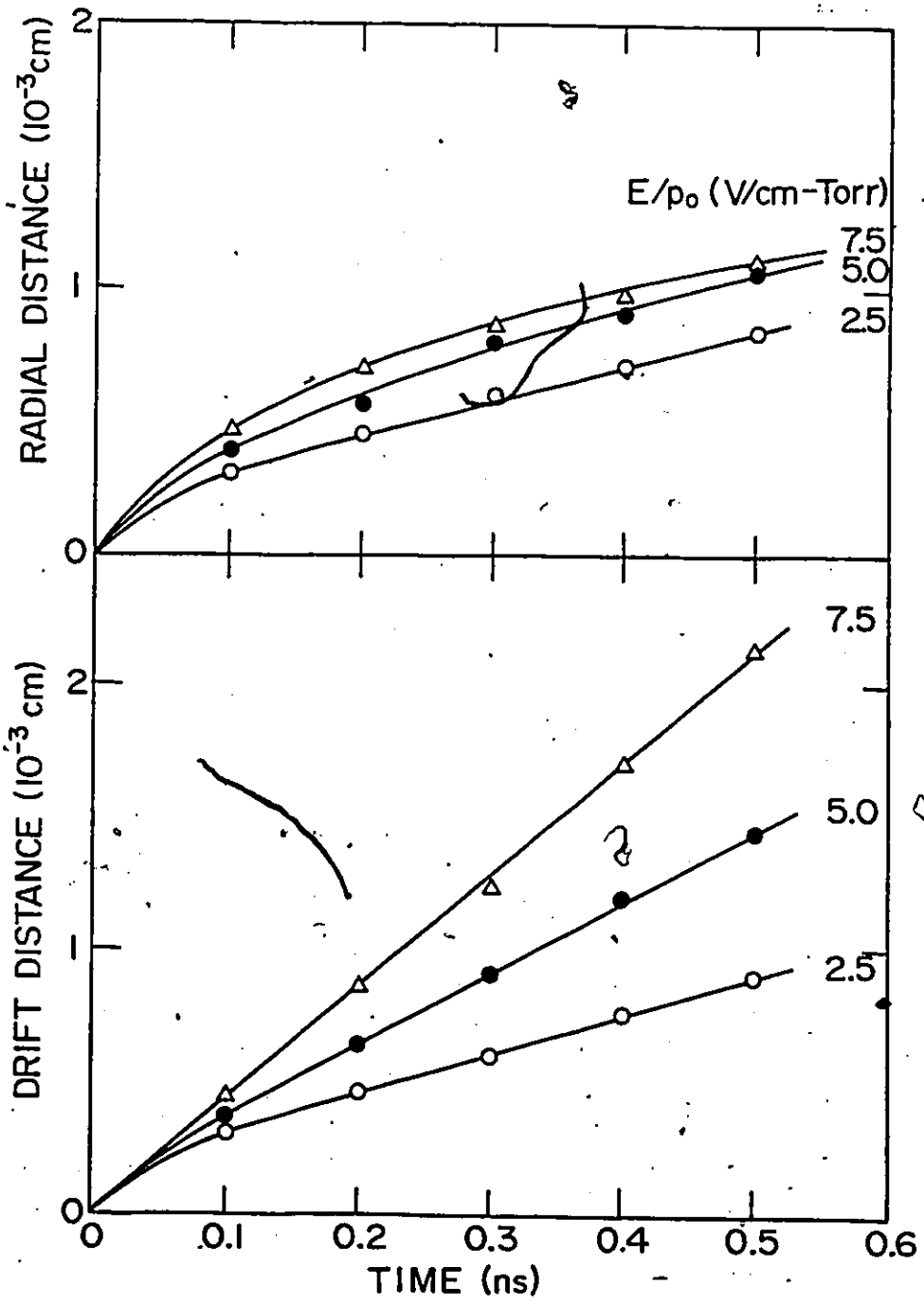
RADIAL DISTANCE (10⁻³cm)
E/p₀ (V/cm-Torr)
7.5
5.0
2.5
DRIFT DISTANCE (10⁻³ cm)
7.5
5.0
2.5
0
1
2
0
0.1
0.2
0.3
0.4
0.5
0.6
TIME (ns)

3.03×10^6 cm/s. In addition, the first Townsend coefficient can be estimated from

$$\alpha_T = \frac{\ell n[N_e(z_1)/N_e(z_0)]}{z_1 - z_0} \quad , \tag{4-45}$$

where the ratio $[N_e(z_1)/N_e(z_0)]$, which defines the electron multiplication between two transit distances z_0 and z_1, is shown in Fig.4-20. For this discharge, $\alpha_T = 98.7$ cm^{-1}, resulting in $\alpha_T/p = 0.033$ ionizations/cm-Torr.

An enormous amount of data must be sampled in order to obtain reliable production rates for excitation and ionization of gas particles directly from the simulation. Alternatively, the reaction rate of an electron collision process can be evaluated as a product of the electron velocity and the corresponding cross-section averaged over the appropriate energy distribution function. Therefore, for the i^{th}-type process,

$$(\overline{\sigma v})_i = \int_0^\infty (2\varepsilon/m)^{1/2} \sigma_i(\varepsilon)\, F(\varepsilon)\, d\varepsilon \quad . \tag{4-46}$$

Table 4-2 shows the calculated reaction rates for the electron collision processes included in the simulation. The calculations are based on a deduced distribution function with $\overline{\varepsilon} = 4.6$ eV and on the cross-sections for those electron processes described in Section 4-2. Also listed in the table are additional reaction rates for other electron processes considered in the kinetic model described in the next chapter.

Fig. 4-20

Multiplication of a 0-eV primary electron in a He/0.5% Xe/0.2% HCl discharge medium at an ionization level of 10^{-5} and at E/p_0 = 7.5 V/cm-Torr (Δ), 5.0 V/cm-Torr (•) and 2.5 V/cm-Torr (o).

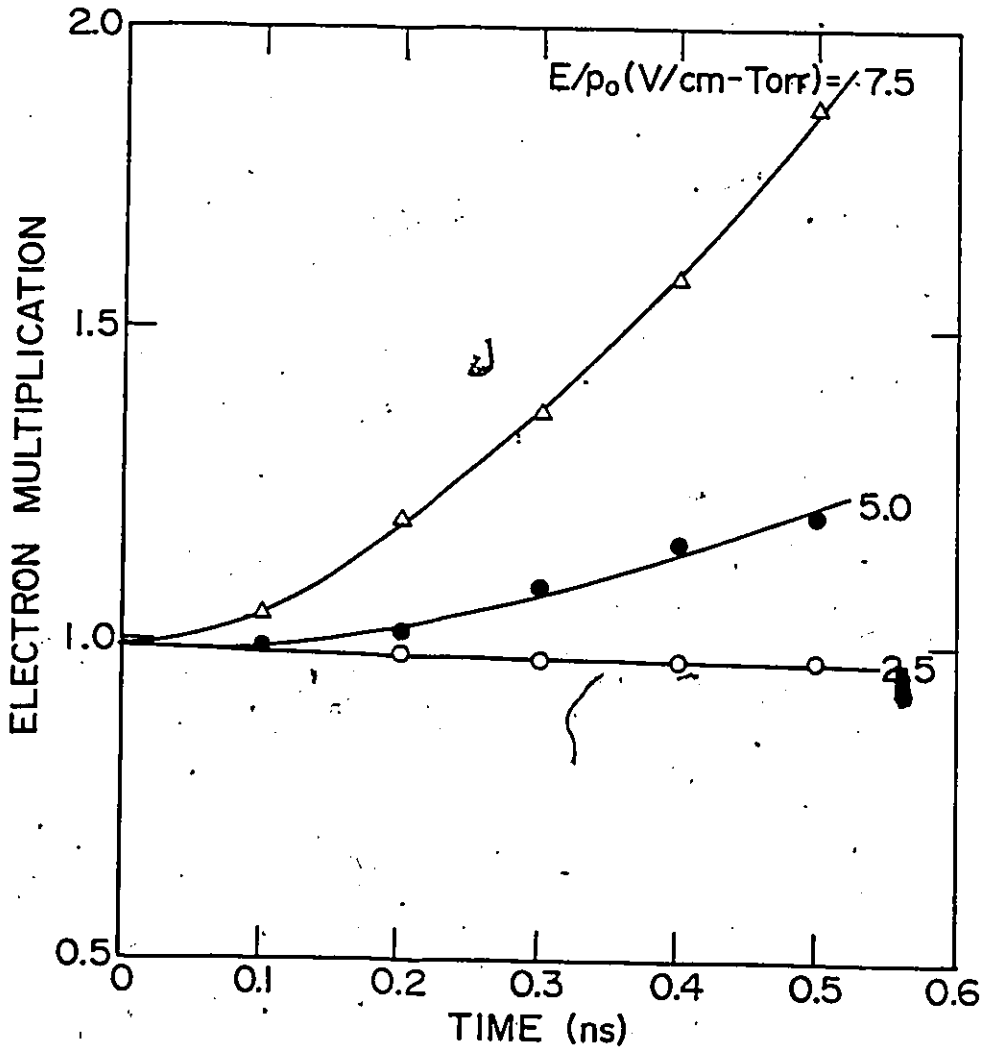
2.0
1.5
1.0
0.5
ELECTRON MULTIPLICATION
E/p₀(V/cm-Torr)=7.5
5.0
2.5
0
0.1
0.2
0.3
0.4
0.5
0.6
TIME (ns)

Table 4-2

Rate coefficients of electron collision processes used in kinetic studes of the XeCl exciplex system. These coefficients are calculated for an average electron energy of 4.6 eV.

		Reaction	Rate Coefficient (cm^3/s; cm^6/s)	Reference
*	A.1	$e + He \rightarrow He + e$	7.0×10^{-8}	[124-126,129]
*	A.2	$e + He \rightarrow He^* + e$	2.4×10^{-13}	[132-137]
*	A.3	$e + He \rightarrow He^+ + 2e$	4.7×10^{-15}	[139]
*	A.4	$e + Xe \rightarrow Xe + e$	3.4×10^{-7}	[143,144]
*	A.5	$e + Xe \rightarrow Xe^* + e$	1.8×10^{-10}	[144,145,167]
*	A.6	$e + Xe \rightarrow Xe^{**} + e$	1.1×10^{-10}	"
*	A.7	$e + Xe \rightarrow Xe^{***} + e$	3.0×10^{-10}	"
*	A.8	$e + Xe \rightarrow Xe^+ + 2e$	3.0×10^{-10}	[139]
*	A.9	$e + HCl \rightarrow HCl + e$	1.7×10^{-7}	[149,150]
*	A.10	$e + HCl \rightarrow HCl^* + e$	1.3×10^{-8}	[149,152]
*	A.11	$e + HCl \rightarrow HCl^{**} + e$	3.5×10^{-9}	"
*	A.12	$e + HCl \rightarrow HCl^+ + 2e$	6.5×10^{-11}	[151]
*	A.13	$e + HCl \rightarrow Cl^- + H$	5.0×10^{-11}	[153,155]
*	A.14	$e + HCl \rightarrow H^- + Cl$	1.6×10^{-11}	"
	A.15	$e + He^* \rightarrow He + e$	4.2×10^{-9}	[168]
*	A.16	$e + He^* \rightarrow He^+ + 2e$	3.3×10^{-8}	[169,170]
	A.17	$e + He^+ \rightarrow He + h\nu$	8.8×10^{-14}	[171]
	A.18	$e + He^+ \rightarrow He^* + h\nu$	8.7×10^{-14}	"
	A.19	$2e + He^+ \rightarrow He^* + e$	2.8×10^{-28}	
	A.20	$e + He^+ + He \rightarrow 2He$	3.6×10^{-34}	[172]
	A.21	$e + He^+ + He \rightarrow He^* + He$	1.8×10^{-29}	
	A.22	$e + He_2^* \rightarrow 2He + e$	3.8×10^{-9}	[168]
*	A.23	$e + He_2^* \rightarrow He_2^+ + 2e$	9.5×10^{-7}	
	A.24	$e + He_2^+ \rightarrow He^* + He$	2.9×10^{-12}	[168]
	A.25	$e + He_2^+ \rightarrow He_2^* + h\nu$	8.2×10^{-13}	"
	A.26	$2e + He_2^+ \rightarrow He^* + He + e$	1.3×10^{-28}	"
	A.27	$2e + He_2^+ \rightarrow He_2^* + e$	3.7×10^{-29}	"
	A.28	$e + He_2^+ + He \rightarrow He^* + 2He$	2.9×10^{-29}	"
	A.29	$e + He_2^+ + He \rightarrow He_2^* + He$	8.2×10^{-30}	"

*	A.30	$e + Xe^{*} \rightarrow Xe + e$	5.4×10^{-10}	
	A.31	$e + Xe^{*} \rightarrow Xe^{***} + e$	3.1×10^{-10}	[173]
*	A.32	$e + Xe^{*} \rightarrow Xe^{+} + 2e$	5.5×10^{-8}	[174]
	A.33	$e + Xe^{**} \rightarrow Xe + e$	5.9×10^{-10}	
	A.34	$e + Xe^{**} \rightarrow Xe^{***} + e$	2.2×10^{-10}	
	A.35	$e + Xe^{**} \rightarrow Xe^{+} + 2e$	5.5×10^{-8}	[174]
	A.36	$e + Xe^{***} \rightarrow Xe + e$	1.3×10^{-12}	
	A.37	$e + Xe^{***} \rightarrow Xe^{*} + e$	4.7×10^{-13}	
	A.38	$e + Xe^{***} \rightarrow Xe^{**} + e$	1.9×10^{-13}	
*	A.39	$e + Xe^{***} \rightarrow Xe^{+} + 2e$	5.5×10^{-8}	
	A.40	$2e + Xe^{+} \rightarrow Xe + e$	3.5×10^{-32}	
	A.41	$2e + Xe^{+} \rightarrow Xe^{*} + e$	2.1×10^{-30}	
	A.42	$2e + Xe^{+} \rightarrow Xe^{**} + e$	1.2×10^{-30}	
	A.43	$2e + Xe^{+} \rightarrow Xe^{***} + e$	1.4×10^{-27}	
*	A.44	$e + Xe_2^{*} \rightarrow Xe_2^{+} + 2e$	1.6×10^{-8}	
*	A.45	$e + Xe_2^{+} \rightarrow Xe^{***} + Xe$	1.7×10^{-7}	[175]
	A.46	$2e + Xe_2^{+} \rightarrow Xe_2^{*} + e$	3.3×10^{-29}	
	A.47	$e + Xe_3^{+} \rightarrow Xe^{***} + 2Xe$	1.4×10^{-6}	[176]
*	A.48	$e + HCl^{*} \rightarrow HCl + e$	7.8×10^{-9}	
*	A.49	$e + HCl^{*} \rightarrow HCl^{**} + e$	5.8×10^{-9}	
*	A.50	$e + HCl^{*} \rightarrow HCl^{+} + 2e$	1.1×10^{-10}	
*	A.51	$e + HCl^{*} \rightarrow Cl^{-} + H$	9.3×10^{-9}	[177]
*	A.52	$e + HCl^{*} \rightarrow H^{-} + Cl$	1.7×10^{-11}	
*	A.53	$e + HCl^{**} \rightarrow HCl + e$	8.5×10^{-10}	
*	A.54	$e + HCl^{**} \rightarrow HCl^{*} + e$	2.3×10^{-9}	
*	A.55	$e + HCl^{**} \rightarrow HCl^{+} + 2e$	2.7×10^{-10}	
*	A.56	$e + HCl^{**} \rightarrow H^{-} + Cl$	1.9×10^{-11}	
	A.57	$2e + HCl^{+} \rightarrow HCl + e$	2.0×10^{-33}	
	A.58	$2e + HCl^{+} \rightarrow HCl^{*} + e$	5.5×10^{-33}	
	A.59	$2e + HCl^{+} \rightarrow HCl^{**} + e$	3.4×10^{-32}	
	A.60	$e + HCl^{+} + He \rightarrow HCl^{**} + He$	1.0×10^{-32}	

	A.61	$e + Cl \rightarrow Cl^-$	3.7×10^{-14}	[178]
*	A.62	$e + Cl^- \rightarrow Cl + 2e$	2.9×10^{-9}	"
	A.63	$e + Cl_2 \rightarrow Cl^- + Cl$	2.1×10^{-10}	[179]
	A.64	$e + Cl_2 \rightarrow Cl_2^-$	4.0×10^{-12}	[180]
	A.65	$e + H \rightarrow H^-$	4.0×10^{-15}	[178]
	A.66	$e + H^+ + He \rightarrow H + He$	8.6×10^{-28}	
*	A.67	$e + H^- \rightarrow H + 2e$	9.7×10^{-7}	[181]
	A.68	$e + H_2 \rightarrow H^- + H$	2.7×10^{-14}	[182]
	A.69	$e + H_2^+ + He \rightarrow H_2 + He$	7.7×10^{-29}	

4.4 Concluding Remarks

In summary, we have applied a Monte-Carlo simulation procedure to study the motion of electrons in a typical gas mixture of He/Xe/HCl, and to obtain information on the electron energy distributions for different discharge conditions and electron concentrations. The statistical data for these energy distributions have been fitted by functions of the general form given by Eq.(4-18). The resulting distribution functions have been used to determine the rate coefficients for various electron collision processes. The simulations assume that only ground-state He, Xe and HCl are involved in the elastic and inelastic electron scattering processes. Therefore, the distribution functions are proper only for describing the early avalanche development in the gaseous discharges, at which time electron collisions with excited species and ions are relatively unimportant. However, these functions can also be good approximations for describing actual gaseous discharges because contributions from the secondary collision processes are minor compared to the Coulomb effect due to electron-electron collisions.

CHAPTER 5

REACTION KINETICS AND EXCIPLEX FORMATION

5.1 Introduction

This chapter analyzes the operation of the XeCl exciplex laser system containing a particular, but typical gas mixture (He/0.5% Xe/0.2% HCl). The particle dynamics of the gaseous discharge are theoretically modelled. The model is used to compute pulseshapes, which are then compared with the observed laser output pulses. In the detailed kinetic model discussed in Section 5.3, a set of 245 reactions (involving 34 neutral, excited and charged species) is investigated. The model takes into account the kinetic processes involving particles which directly or indirectly influence the formation and decay of $XeCl^*$, together with the electron collision processes discussed in the preceeding chapter. After judiciously selecting the important processes, a concise kinetic scheme, employing an abridged set of 115 reactions (involving 31 species), is then developed. This scheme enables us to carry out a relatively simple steady-state analysis of the saturation in the laser system, and to derive useful formulae for evaluating parameters associated with the optical gain. These gain parameters are compared with the estimates based on experimental data empiricially fitted to the conventional gain formula.

It is possible to understand the elaborate kinetic model by

delineating the basic processes in the reaction chains leading to exciplex formation and to subsequent exciplex radiation and decay. As a first approximation, the XeCl laser dynamics can be explained by a simple kinetic flow-diagram involving only those dominant reactions illustrated in Fig.5-1. The exciplex $XeCl^*$ is formed primarily by an ionic recombination process via the collision of a third body, namely,

$$Xe^+ + Cl^- + He \longrightarrow XeCl^* + He \quad . \qquad (5\text{-}1)$$

The positive ion Xe^+ is produced as a result of electron-impact excitation and subsequent, or direct ionization of the phyletic rare-gas atom Xe. Whenever a positive ion is formed, a slow electron is released. This electron may attach to a ground-state or vibrationally-excited electrophilic HCl molecule, which then dissociates to form Cl^-. Reaction (5-1) usually proceeds at a high rate (especially in a dense rare-gas medium) with a rate coefficient in the order of 10^{-27} cm^6/s [186,187]. Moreover, according to the observed discharge current (Fig. 3-20), the electron production at the beginning of the gas breakdown, is mainly initiated by photoionization of rare-gas atoms (principally He) by an external radiation source (e.g., preionization). These photo-electrons assist rapid production of Xe^+ species (and also the Cl^- ions), so that formation of $XeCl^*$ via the ionic recombination channel is particularly efficient.

The exciplex $XeCl^*$ may either decay to its ground state through the ultraviolet emission process

Fig. 5-1

A schematic diagram for the simplified XeCl laser kinetics in a He/Xe/HCl mixture. Φ and Ψ denote the fluxes due to radiation at 308 nm and photoionization, respectively, and τ is the characteristic lifetime of $XeCl^*$.

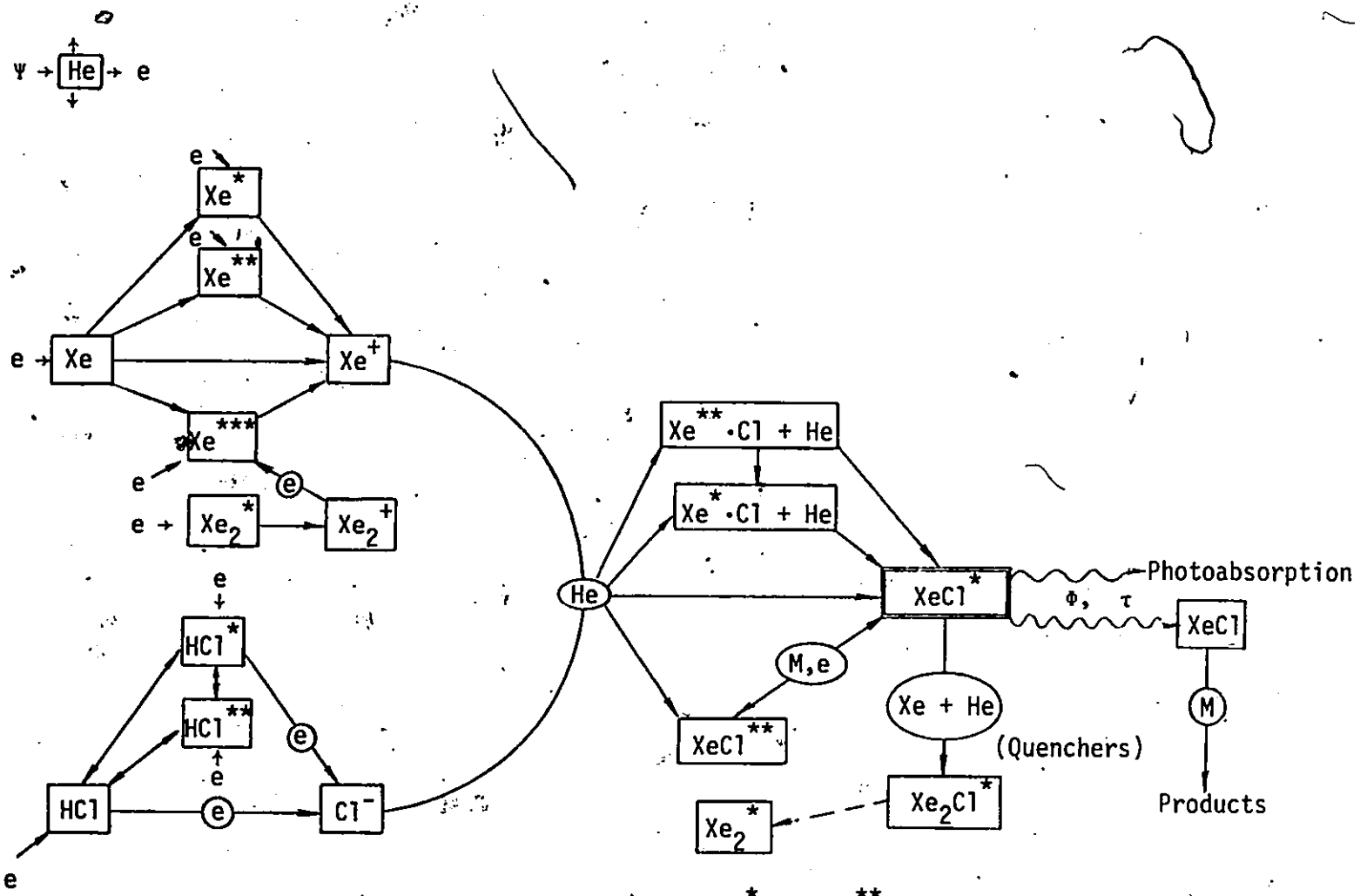

M = He, Xe, HCl, HCl* or HCl**

$$XeCl^* \longrightarrow XeCl + h\nu_L \quad , \qquad (5\text{-}2)$$

where $h\nu_L$ is the photon energy (4.025 eV for the 308 nm laser transition), or be quenched by a discharge particle (predominantly a neutral particle, or an electron). After collision with a gas particle, the ground-state XeCl molecule eventually dissociates into its atomic fragments.

The long-duration pulses observed in our experiments can be modelled if the "harpooning" mechanisms involving the association of $Xe^*(^3P_2)$ and $Xe^{**}(^3P_1)$ with Cl are included in the model. These mechanisms for exciplex formation are particularly important during the late stage of the discharge, when production of ions is reduced. The reactions proceed predominantly via the three-body collision processes

$$Xe^{**} + Cl + He \longrightarrow (Xe^{**}\cdot Cl) + He \longrightarrow XeCl^* + He \qquad (5\text{-}3)$$

and

$$Xe^{*} + Cl + He \longrightarrow (Xe^{*}\cdot Cl) + He \longrightarrow XeCl^* + He \quad . \qquad (5\text{-}4)$$

The intermediate Rydberg molecules are formed because of the presence, in the discharge medium, of a substantial concentration of Cl atoms. These result from exciplex decay and ground-state quenching before atomic recombination occurs at the walls. In addition, the "harpooning" processes effectively delay exciplex formation because of the following mechanisms. The exciplex species which are initially formed from the ionic channel predissociate to atomic fragments corresponding to the molecular Rydberg states. Recombination to the Rydberg states can occur via three-body collisions, followed by transformation back to

exciplex species.

The following loss processes are closely associated with exciplex formation:

(i) Three-body association to form the triatomic Xe_2Cl^*,

$$XeCl^* + Xe + He \longrightarrow Xe_2Cl^* + He \quad . \qquad (5\text{-}5)$$

(ii) Electron quenching (superelastic collision) of $XeCl^*$,

$$XeCl^* + e \longrightarrow XeCl + e \quad . \qquad (5\text{-}6)$$

(iii) Exciplex quenching by gas particles,

$$XeCl^* + M \longrightarrow XeCl^{**} + M \quad , \qquad (5\text{-}7)$$

where M = He, Xe, HCl(v=0), HCl^*(v=1,2) or HCl^{**}(v≥3), and $XeCl^{**}$ is an excited molecular state other than the B-state. The results of our kinetic modelling indicate that these loss channels, together with relatively slow depletion of the ground state, prevail over photoabsorption by Cl, Xe_2^+, Xe_2Cl^*, Xe^*, Xe^{**}, Xe^{***}(atomic states higher than $^3P_1$), and He^*.

5.2 Production of Photoelectrons

Preconditioning of a He/Xe/HCl discharge mixture by photoelectrons not only initiates a volume-stabilized glow discharge at over-atmospheric pressures, but also maintains a high level of electron production. At the onset of laser action, this level represents an electron density in excess of 10^{15} cm^{-3}. These photoelectrons are particularly useful for enchancing the production of ions involved in recombination, at a much higher level than possible in a straight discharge. Low-energy electrons

become easily attached to HCl and HCl^* to produce Cl^- ions. Electron energies $\gtrsim$4 eV participate in the ionization of excited Xe atoms (for $\gtrsim$12 eV energies, ground-state Xe atoms) to produce Xe^+ ions and additional low-energy electrons. To achieve laser action, the population of the upper laser level must be inverted. This requires a large $XeCl^*$ species production from Xe^+ and Cl^- recombination. This production must occur soon after the discharge impedance drops, but long before the impedance "collapses".

In our model, the time-varying photon flux $\Psi(t)$ (irradiance, expressed in photons/cm^2-s), resulting from operation of a pair of auxillary spark arrays, is considered to be proportional to the power deposited into the pair of preionizers. From measured data,

$$\Psi(t) \cong \Psi_0 \exp(-6.66 \times 10^5\ t)\ \sin^2(4.189 \times 10^6\ t)\ , \qquad (5\text{-}8)$$

where Ψ_0 is the maximum flux level. Our kinetic calculations employ the estimated value $\Psi_0 = 1.0 \times 10^{19}$ photons/cm^2-s for a charging voltage of 35 kV. A time lag of 220 ns is assumed from preionizer breakdown to main discharge breakdown. Therefore, the photoionization flux at the beginning of the main discharge is 6×10^{18} photons/cm^2-s. This corresponds to a photoelectron density of 2×10^8 cm^{-3}.

The high photoionization level, which is about four orders of magnitude greater than that required for initiating a volumetric glow discharge in a UV-preionized TEA CO_2 laser, can be evaluated using the theoretical model for photoinitiated discharges given by Palmer [188]. In this model, the Raether's breakdown criterion, which describes streamer breakdown initiated by a single primary avalanche,

is modified to include a large number of photoinitiated primary avalanches. These overlap spatially after propagating a critical distance z_{crit}, at which location initial streamer breakdown occurs. Thus,

$$\alpha_T z_{crit} = \ell n(4\pi\epsilon_0 E_0 \bar{\lambda}/e) + \ell n\, z_{crit} \quad , \qquad (5\text{-}9)$$

where α_T is the first Townsend coefficient for ionization (defined in Section 4.3), E_0 is the applied field with which the space-charge field of an individual avalanche balances, $\bar{\lambda}$ is the electron mean-free-path, and $e/(4\pi\epsilon_0) = 1.44 \times 10^{-9}$ V-m. The first term on the RHS of Eq.(5-9) is usually $\simeq 20$. The distance z_{crit} has a value of 0.135 cm for α_T = 90 cm^{-1}, E_0 = 13.7 kV/cm and $\bar{\lambda} = 1.5 \times 10^{-5}$ cm. Moreover, the condition for the spatial overlaps of adjacent primary avalanches,

$$n_0^{-1/3} \lesssim (\bar{\lambda}\, z_{crit})^{1/2} \quad , \qquad (5\text{-}10)$$

requires that the average lateral separation of the avalanches ($\sim n_0^{-1/3}$) is not greater than the radius of the spherical head of an avalanche. Accordingly, the photoelectron density for a glow discharge (the equivalent to the density of primary avalanches, n_0) is estimated to be 3.5×10^8 cm^{-3}. Therefore $\Psi(t = 220\ ns)$ is $\sim 10^{19}$ photons/cm^2-s. These agree with previously estimated values of 2×10^8 cm^{-3} and 6×10^{18} photons/cm^2-s, respectively.

No detailed measurements have been made on the photoionization emission spectrum. It is therefore difficult to identify the probable photoactive species, and to determine the initial rates for the formation of the various positive ions and electrons which contribute to the gas kinetics. Therefore, some parameters have to be judiciously

selected in order to construct an analytic kinetic model (for the photoinitiated discharge) which agrees with experimental results. For example, it is reasonable to assume that preionization emission is near the 100-nm wavelength region, and therefore that only the ground-state Xe atoms can be directly ionized. Assuming a photoabsorption cross-section of $\sim 5 \times 10^{-17}$ cm^2 for Xe [189], at a density of 4.8×10^{17} cm^{-3} for a He/0.5% Xe/0.2% HCl mixture at 3000-Torr pressure, and the irradiance previously stated, primary electrons are photoreleased at a rate of $\sim 1.4 \times 10^{20}/cm^3$-s. This estimate is far below the expected rate of $\sim 10^{21}$-$10^{22}/cm^3$-s, which is determined by the rise of the measured discharge current ($\frac{di}{dt} \gtrsim 10^{11}$ A/s). Even if all Xe atoms are excited and subsequently ionized, the photoionization demands an unrealistically large absorption cross-section of $> 10^{-15}$ cm^2. More likely, photoionization of ground-state He atoms is involved, because of a large population of $\sim 10^{20}$ cm^{-3}. In addition, hard UV radiation ($\lambda < 50$ nm) is occasional in a He/Xe/HCl discharge, and multi-photon ionization likely takes place. If an absorption cross-section of $\sim 5 \times 10^{-18}$ cm^2 is assumed for He [190] the initial electrons are produced at a rate of $\sim 3 \times 10^{21}$/cm-s, which falls within the experimental estimates. The multi-photon phenomenon is very different from the photoinitiated discharge in a CO_2 laser system, for which plasma absorption occurs in the 105-120 nm wavelength region [191].

In our kinetic model, initial electrons are generated by photoionization of ground-state He, Xe and HCl. The photoionization flux level determines the supply of these electrons for initiating a

stable discharge, and for the electron-impact production of ions taking part in exciplex formation. During the photosustained discharge, electron production also involves other species, e.g., He^*, He_2^*, Xe^*, Xe^{**}, Xe^{***}, Xe_2^*, HCl^*, HCl^{**}, Cl and Cl^-. However, these species generally contribute very little to the total production of electrons and ions. Therefore, our concise kinetic model only includes preionization processes relating to photoionization of rare-gas atoms.

5.3 Particle Dynamics and Exciplex Radiation

This section is devoted to a general discussion of the detailed kinetic model and its application to a He/0.5% Xe/0.2% HCl mixture, with a measured $E/p_0 \sim 5.0$ V/cm-Torr at initial breakdown. Results are presented for operating pressures of 2957 Torr and 2880 Torr, at a charging voltage of 35 kV, and for 2570-Torr pressure at 30-kV charging voltage. The first operating conditions (2957-Torr pressure and 35-kV charging voltage) are typical, and are therefore emphasized for discussion. The temporal species concentrations during the discharge period are determined by solving numerically a large set of rate equations in accordance with the kinetic scheme given in Tables 4-2, and 5-1 to 5-3. The results are described in Fig.5-2. Discharge species with concentrations outside the range 10^{13}-10^{18} cm^{-3} are not shown in the figure. In the following, we select for discussion only those discharge species which are dominant and/or influential in the XeCl laser.

Table 5-1

Intermediate kinetic processes in the XeCl laser discharge. A reaction indicated by an asterisk is selected for the concise kinetic model. Where references are not given, the values are estimated.

		Reaction	Rate Coefficient (s^{-1}; cm^3/s; cm^6/s)	Reference
*	B.1	$He^* + He \rightarrow He_2^+ + e$	7.4×10^{-12}	[192]
	B.2	$He^* + 2He \rightarrow He_2^* + He$	1.6×10^{-34}	[171]
	B.3	$He^* + He^* \rightarrow He^+ + He + e$	2.3×10^{-10}	"
	B.4	$He^* + He^* \rightarrow He_2^+ + e$	5.3×10^{-10}	"
	B.5	$He^* + He_2^* \rightarrow He^+ + 2He + e$	3.8×10^{-10}	"
	B.6	$He^* + He_2^* \rightarrow He_2^+ + He + e$	8.8×10^{-10}	"
*	B.7	$He^* + Xe \rightarrow Xe^+ + He + e$	1.2×10^{-10}	[193-195]
	B.8	$He^* + Xe \rightarrow XeHe^+ + e$	1.7×10^{-11}	[196]
*	B.9	$He(2^3S) + Xe + He \rightarrow \begin{cases} Xe^+ + 2He + e \\ XeHe^+ + He + e \end{cases}$	2.2×10^{-30}	[197]
*	B.10	$He^* + HCl \rightarrow HCl^+ + He + e$	1.3×10^{-9}	[198]
	B.11	$He(2^3S) + HCl + He \rightarrow \begin{cases} HCl^+ + 2He + e \\ He{\cdot}HCl^+ + He + e \end{cases}$	2.9×10^{-30}	[197]
	B.12	$He^* + Cl \rightarrow Cl^+ + He + e$	1.3×10^{-11}	[199]
	B.13	$He(2^3S) + H_2 \rightarrow H_2^+ + He + e$	3.8×10^{-11}	[197]
	B.14	$He(2^3S) + H_2 + He \rightarrow H_2^+ + 2He + e$	1.2×10^{-30}	"
*	B.15	$He^+ + 2He \rightarrow He_2^+ + He$	1.0×10^{-31}	[200]
	B.16	$He^+ + Xe \rightarrow Xe^+ + He$	7.0×10^{-12}	[201]
	B.17	$He^+ + HCl \rightarrow Cl^+ + H + He$	3.3×10^{-9}	[198]
	B.18	$He^+ + Cl \rightarrow Cl^+ + He$	5.3×10^{-10}	[199]
*	B.19	$He^+ + Cl^- + He \rightarrow He^* + Cl + He$	5.9×10^{-26}	
	B.20	$He^+ + H_2 \rightarrow H_2^+ + He$	6.5×10^{-13}	[202]
	B.21	$He^+ + H_2 \rightarrow H^+ + H + He$	1.1×10^{-13}	[203]
	B.22	$He^+ + 2H_2 \rightarrow H^+ + H + He + H_2$	4.4×10^{-31}	[204]
	B.23	$He_2^* + He_2^* \rightarrow He^+ + 3He + e$	2.3×10^{-10}	[171]
	B.24	$He_2^* + He_2 \rightarrow He_2^+ + 2He + e$	5.3×10^{-10}	"
*	B.25	$He_2^* + Xe \rightarrow Xe^+ + 2He + e$	5.9×10^{-10}	[88]
	B.26	$He_2^+ + Xe \rightarrow He^+ + Xe + He$	1.1×10^{-11}	[205]
*	B.27	$He_2^+ + Xe \rightarrow Xe^+ + 2He$	2.6×10^{-10}	"
	B.28	$He_2^+ + Xe \rightarrow XeHe^+ + He$	1.5×10^{-11}	"
*	B.29	$He_2^+ + Xe + He \rightarrow Xe^+ + 3He$	2.0×10^{-29}	

*	B.30	$He_2^+ + HCl \rightarrow \begin{cases} HCl^+ + 2He \\ Cl^+ + H + 2He \end{cases}$	1.8×10^{-9}	[206]
*	B.31	$He_2^+ + HCl + He \rightarrow H^+ + Cl + 3He$	3.0×10^{-29}	"
*	B.32	$He_2^+ + Cl^- + He \rightarrow He_2^* + Cl + He$	3.7×10^{-26}	"
	B.33	$He_2^+ + H_2 \rightarrow H^+ + H + 2He$	4.1×10^{-10}	[206]
	B.34	$He_2^+ + H_2 + He \rightarrow H^+ + H + 3He$	9.0×10^{-30}	"
	B.35	$Xe^* + Xe \rightarrow 2Xe + h\nu$	2.0×10^{-15}	[207]
	B.36	$Xe^* + Xe \rightarrow Xe^{**} + Xe$	1.4×10^{-15}	"
	B.37	$Xe^* + Xe \rightarrow Xe_2^*$	1.6×10^{-15}	[208]
	B.38	$Xe^* + Xe + He \rightarrow Xe_2^* + He$	1.4×10^{-32}	[209]
	B.39	$Xe^* + 2Xe \rightarrow 3Xe$	7.6×10^{-32}	[210]
	B.40	$Xe^* + 2\,Xe \rightarrow Xe_2^* + Xe$	3.2×10^{-32}	[207]
*	B.41	$Xe^* + HCl \rightarrow HCl^{**} + Xe$	5.6×10^{-10}	[11]
*	B.42	$Xe^* + Xe^* \rightarrow Xe^+ + Xe + e$	5.0×10^{-10}	[211]
	B.43	$Xe^* + H_2 \rightarrow H_2 + Xe$	1.6×10^{-11}	[11]
	B.44	$Xe^{**} \rightarrow Xe + h\nu$	1.3×10^{5}	[212]
	B.45	$Xe^{**} + Xe \rightarrow Xe^* + Xe$	2.6×10^{-13}	[207]
	B.46	$Xe^{**} + Xe + He \rightarrow Xe_2^* + He$	1.4×10^{-32}	[209]
	B.47	$Xe^{**} + 2Xe \rightarrow Xe_2^* + Xe$	3.7×10^{-32}	[207]
	B.48	$Xe^{**} + Xe^{**} \rightarrow Xe^+ + Xe + e$	5.0×10^{-10}	[211]
*	B.49	$Xe^{***} \rightarrow Xe^* + h\nu$	7.4×10^{6}	[213]
*	B.50	$Xe^{***} \rightarrow Xe^{**} + h\nu$	1.2×10^{7}	"
*	B.51	$Xe^{***} + Xe \rightarrow Xe_2^+ + e$	8.2×10^{-12}	[214]
*	B.52	$Xe^{***} + Xe^{***} \rightarrow Xe^+ + Xe + e$	5.0×10^{-10}	[211]
*	B.53	$Xe^+ + Xe + He \rightarrow Xe_2^+ + He$	1.1×10^{-31}	[88]
	B.54	$Xe^+ + 2Xe \rightarrow Xe_2^+ + Xe$	2.0×10^{-31}	[215]
*	B.55	$Xe^+ + HCl \rightarrow HCl^+ + Xe$	2.9×10^{-11}	[88]
	B.56	$Xe^+ + Cl_2 \rightarrow Cl_2^+ + Xe$	6.0×10^{-11}	[216]
	B.57	$Xe^+ + Cl_2 \rightarrow XeCl^+ + Cl$	1.0×10^{-9}	
*	B.58	$Xe_2^* \rightarrow 2Xe + h\nu$	1.0×10^{7}	[217]
*	B.59	$Xe_2^* + Xe_2^* \rightarrow Xe^+ + 3Xe + e$	3.5×10^{-10}	[218]
*	B.60	$Xe_2^* + Xe_2^* \rightarrow Xe_2^+ + 2Xe + e$	8.0×10^{-11}	[219]
	B.61	$Xe_2^+ + 2Xe \rightarrow Xe_3^+ + Xe$	9.0×10^{-32}	[220]

*	B.62	$HCl^* + HCl \rightarrow 2HCl$	2.1×10^{-12}	[221]
*	B.63	$HCl^* + Cl \rightarrow Cl + HCl$	4.4×10^{-12}	[222]
	B.64	$HCl^* + H \rightarrow H + HCl$	1.3×10^{-13}	[223]
*	B.65	$HCl^* + H \rightarrow H_2 + Cl$	7.0×10^{-12}	"
*	B.66	$HCl^+ + HCl \rightarrow H_2Cl^+ + Cl$	4.4×10^{-10}	[224]
*	B.67	$HCl^+ + Cl^- + He \rightarrow HCl^{**} + Cl + He$	4.8×10^{-27}	
	B.68	$HCl^+ + H_2 \rightarrow H_2Cl^+ + H$	5.2×10^{-10}	[225]
	B.69	$2Cl + He \rightarrow Cl_2 + He$	4.1×10^{-33}	[226]
	B.70	$2Cl + Cl_2 \rightarrow 2Cl_2$	5.5×10^{-32}	[227]
	B.71	$Cl + H_2 \rightarrow H + HCl$	1.7×10^{-14}	[228]
*	B.72	$Cl^+ + Cl^- + He \rightarrow Cl_2 + He$	3.3×10^{-27}	
	B.73	$Cl^+ + H_2 \rightarrow H + HCl^+$	9.2×10^{-10}	[229]
	B.74	$Cl^+ + H_2 \rightarrow H_2^+ + Cl$	5.5×10^{-12}	[202]
	B.75	$Cl^+ + H_2 \rightarrow 2H^+ + Cl^-$	5.5×10^{-13}	"
*	B.76	$Cl^- + H \rightarrow HCl + e$	9.6×10^{-10}	[230]
	B.77	$Cl_2 + H \rightarrow Cl + HCl$	1.9×10^{-11}	[231,232]
	B.78	$Cl_2 + H \rightarrow Cl + HCl^*$	2.3×10^{-12}	"
	B.79	$Cl_2 + H \rightarrow Cl + HCl^{**}$	4.4×10^{-13}	"
	B.80	$H + HCl \rightarrow H_2 + Cl$	3.8×10^{-14}	[221]
*	B.81	$2H + He \rightarrow H_2 + He$	8.9×10^{-33}	[233]
	B.82	$2H + Xe \rightarrow H_2 + Xe$	1.4×10^{-32}	[234]
	B.83	$2H + H_2 \rightarrow 2H_2$	2.8×10^{-32}	"
	B.84	$2H + H \rightarrow H_2 + H$	1.2×10^{-32}	[235]
	B.85	$H + H^- \rightarrow H_2 + e$	1.7×10^{-9}	[236]
	B.86	$H^+ + Xe \rightarrow H + Xe^+$	5.0×10^{-10}	[237]
*	B.87	$H^+ + Cl^- + He \rightarrow HCl^{**} + He$	7.5×10^{-26}	
	B.88	$H^+ + H_2 \rightarrow H_2^+ + H$	4.6×10^{-11}	[202]
	B.89	$H_2^+ + Cl^- + He \rightarrow HCl^{**} + H + He$	7.3×10^{-26}	
	B.90	$H_2^+ + H_2 \rightarrow H_2 + H^+ + H$	3.8×10^{-12}	[202]

Table 5-2

Kinetic processes for formation and decay of exciplex species. A reaction indicated by an asterisk is selected for the concise kinetic model. Where references are not given, the values are estimated. Levin et al.[85] mention that the rate coefficients for collisional quenching of ground-state XeCl by Xe and HCl (processes C.48, C.49, C.50 and C.51), given in Ref.[238], could be a factor of 50 times larger. Our modelling results indicate that these are ∿38 times larger if the rate coefficient for XeCl quenching by He (process C.43) is assumed to have the value 5.0×10^{-13} cm^3/s.

		Reaction	Rate Coefficient (s^{-1}; cm^3/s; cm^6/s)	Reference
*	C.1	$Xe^* + HCl \rightarrow XeCl^* + H$	$<1.0 \times 10^{-11}$	[38]
*	C.2	$Xe^* + HCl^* \rightarrow XeCl^* + H$	2.0×10^{-10}	[238]
*	C.3	$Xe^* + HCl^{**} \rightarrow XeCl^* + H$	5.0×10^{-10}	
	C.4	$Xe^* + Cl_2 \rightarrow XeCl^* + Cl$	7.2×10^{-10}	[239]
	C.5	$Xe^{**} + HCl \rightarrow XeCl^* + H$	1.0×10^{-11}	
*	C.6	$Xe^{**} + HCl^* \rightarrow XeCl^* + H$	2.0×10^{-10}	
*	C.7	$Xe^{**} + HCl^{**} \rightarrow XeCl^* + H$	5.0×10^{-10}	
	C.8	$Xe^{**} + Cl_2 \rightarrow XeCl^* + Cl$	1.0×10^{-9}	
*	C.9	$XeCl^+ + Cl^- + He \rightarrow XeCl^* + Cl + He$	3.2×10^{-27}	
*	C.10	$XeHe^+ + Cl^- + He \rightarrow XeCl^* + 2He$	3.0×10^{-27}	
*	C.11	$Xe^+ + Cl^- + He \rightarrow XeCl^{**} + He$	2.1×10^{-27}	
*	C.12	$Xe^+ + Cl^- + He \rightarrow XeCl^* + He$	7.5×10^{-28}	
*	C.13	$Xe^+ + Cl^- + He \rightarrow Xe^* + Cl + He$	4.2×10^{-28}	
*	C.14	$Xe^+ + Cl^- + He \rightarrow Xe^{**} + Cl + He$	2.3×10^{-27}	
*	C.15	$Xe^{**} + Cl + He \rightarrow XeCl^* + He$	1.3×10^{-27}	
*	C.16	$Xe^{**} + Cl + He \rightarrow Xe^* + Cl + He$	7.6×10^{-28}	
*	C.17	$Xe^{**} + Cl + He \rightarrow Xe^+ + Cl^- + He$	3.6×10^{-28}	
*	C.18	$Xe^* + Cl + He \rightarrow XeCl^* + He$	5.7×10^{-28}	
*	C.19	$Xe^* + Cl + He \rightarrow Xe^{**} + Cl + He$	6.7×10^{-30}	
	C.20	$Xe^* + Cl + He \rightarrow Xe^+ + Cl^- + He$	5.8×10^{-31}	
*	C.21	$XeCl^{**} + M \rightarrow XeCl^* + M$	1.0×10^{8}	
*	C.22	$XeCl^* \rightarrow XeCl + \phi$	$\tau = 41$ ns	[240]
*	C.23	$XeCl^* + \phi \rightarrow XeCl + 2\phi$	$\sigma_s = 2.4$ Å^2	
*	C.24	$XeCl^* + He \rightarrow XeCl^{**} + He$	5.0×10^{-13}	
	C.25	$XeCl^* + He^* \rightarrow XeCl^+ + He + e$	1.0×10^{-10}	
	C.26	$XeCl^* + He^+ \rightarrow XeCl^+ + He$	1.0×10^{-11}	
	C.27	$XeCl^* + He_2^* \rightarrow XeCl^+ + 2He + e$	1.0×10^{-11}	
	C.28	$XeCl^* + He_2^+ \rightarrow XeCl^+ + 2He$	1.0×10^{-10}	
*	C.29	$XeCl^* + Xe \rightarrow XeCl^{**} + Xe$	3.2×10^{-11}	[102]
	C.30	$XeCl^* + Xe^* \rightarrow XeCl^+ + Xe + e$	5.0×10^{-10}	

	C.31	$XeCl^* + Xe^{**} \rightarrow XeCl^+ + Xe + e$	5.0×10^{-10}	
*	C.32	$XeCl^* + Xe^{***} \rightarrow XeCl^+ + Xe + e$	5.0×10^{-10}	
	C.33	$XeCl^* + Xe^+ \rightarrow XeCl^+ + Xe$	5.0×10^{-11}	
*	C.34	$XeCl^* + Xe_2^* \rightarrow XeCl^+ + 2Xe + e$	1.0×10^{-10}	
	C.35	$XeCl^* + Xe_2^+ \rightarrow XeCl^+ + 2Xe$	1.0×10^{-11}	
*	C.36	$XeCl^* + Xe + He \rightarrow Xe_2Cl^* + He$	5.0×10^{-30}	
*	C.37	$XeCl^* + HCl \rightarrow XeCl^{**} + HCl$	1.4×10^{-9}	[102]
*	C.38	$XeCl^* + HCl^* \rightarrow XeCl^{**} + HCl^*$	1.4×10^{-9}	"
*	C.39	$XeCl^* + HCl^{**} \rightarrow XeCl^{**} + HCl^{**}$	1.4×10^{-9}	"
*	C.40	$XeCl^* + e \rightarrow XeCl + e$	3.5×10^{-8}	
*	C.41	$XeCl^* + e \rightarrow XeCl^+ + 2e$	8.3×10^{-10}	
*	C.42	$XeCl^{**} \rightarrow Xe + Cl + h\nu$	2.0×10^{7}	
*	C.43	$XeCl + He \rightarrow Xe + Cl + He$	3.0×10^{-12}	
	C.44	$XeCl + He^* \rightarrow XeCl^+ + He + e$	1.0×10^{-10}	
	C.45	$XeCl + He^+ \rightarrow XeCl^+ + He$	1.0×10^{-11}	
	C.46	$XeCl + He_2^* \rightarrow XeCl^+ + 2He + e$	1.0×10^{-11}	
	C.47	$XeCl + He_2^+ \rightarrow XeCl^+ + 2He$	1.0×10^{-10}	
*	C.48	$XeCl + Xe \rightarrow 2Xe + Cl$	5.6×10^{-12}	[241]
*	C.49	$XeCl + HCl \rightarrow Xe + Cl + HCl$	2.2×10^{-11}	"
*	C.50	$XeCl + HCl^* \rightarrow Xe + Cl + HCl^*$	2.2×10^{-11}	"
*	C.51	$XeCl + HCl^{**} \rightarrow Xe + Cl + HCl^{**}$	2.2×10^{-11}	"
*	C.52	$XeCl + e \rightarrow XeCl^* + e$	4.6×10^{-9}	
	C.53	$Xe_2^* + Cl_2 \rightarrow Xe_2Cl^* + Cl$	1.0×10^{-9}	
*	C.54	$Xe_2^+ + Cl^- + He \rightarrow Xe_2Cl^* + He$	3.4×10^{-27}	
*	C.55	$Xe_2Cl^* \rightarrow 2Xe + Cl + h\nu$	τ=100ns,135ns	[242,243]
*	C.56	$Xe_2Cl^* + He \rightarrow Xe_2^* + Cl + He$	5.0×10^{-13}	
*	C.57	$Xe_2Cl^* + Xe \rightarrow Xe_2^* + Cl + Xe$	2.0×10^{-11}	
*	C.58	$Xe_2Cl^* + HCl \rightarrow Xe_2^* + Cl + HCl$	1.0×10^{-9}	
*	C.59	$Xe_2Cl^* + HCl^* \rightarrow Xe_2^* + Cl + HCl^*$	1.0×10^{-9}	
*	C.60	$Xe_2Cl^* + HCl^{**} \rightarrow Xe_2^* + Cl + HCl^{**}$	1.0×10^{-9}	
*	C.61	$XeCl^+ + e \rightarrow Xe^{***} + Cl$	1.0×10^{-7}	

Table 5-3

Photoabsorbers in the XeCl laser discharge. The cross-sections are for absorption near 308 nm. An absorbing species indicated by an asterisk is selected for the concise kinetic model. Where references are not given, the cross-section is estimated.

	Species	Cross Section (cm^2)	Reference
D.1	$He(2\ ^1S)$	8.8×10^{-18}	[244]
D.2	$He(2\ ^3P)$	9.3×10^{-18}	[245]
D.3	$He(2\ ^1P)$	5.3×10^{-18}	"
D.4	$He_2(A\ ^1\Sigma^+)$	6.9×10^{-18}	[244]
* D.5	Xe^*	1.6×10^{-18}	"
* D.6	Xe^{**}	1.1×10^{-18}	"
* D.7	Xe^{***}	4.0×10^{-19}	
D.8	$Xe_2^+(A\ ^2\Sigma^+_{1/2u})$	3.5×10^{-17}	[246]
* D.9	Cl^-	2.3×10^{-17}	[247]
D.10	Cl_2	7.5×10^{-20}	[248]
D.11	Cl_2^-	2.0×10^{-17}	[249]
* D.12	Xe_2Cl^*	1.0×10^{-18}	

Fig. 5-2

Temporal evolution of active species in a XeCl laser discharge. The system employs a He/0.5% Xe/0.2% HCl mixture at a 2957-Torr operating pressure, a 35-kV charging voltage and a 1.65-cm electrode separation. The discharge species are stated with the curves in (a), (b) and (c).

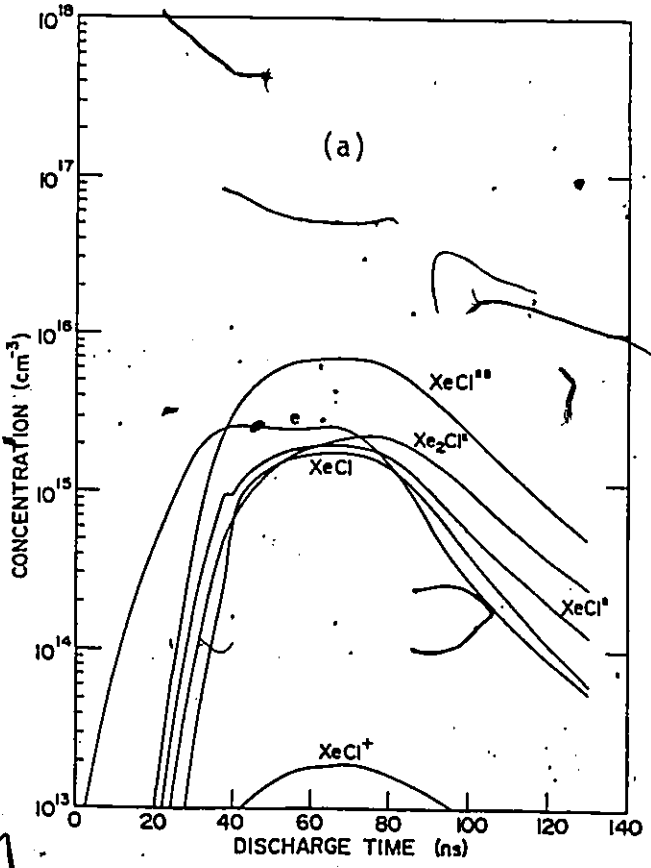
(a)
CONCENTRATION (cm⁻³)
DISCHARGE TIME (ns)
XeCl**
e
Xe₂Cl*
XeCl
XeCl*
XeCl⁺

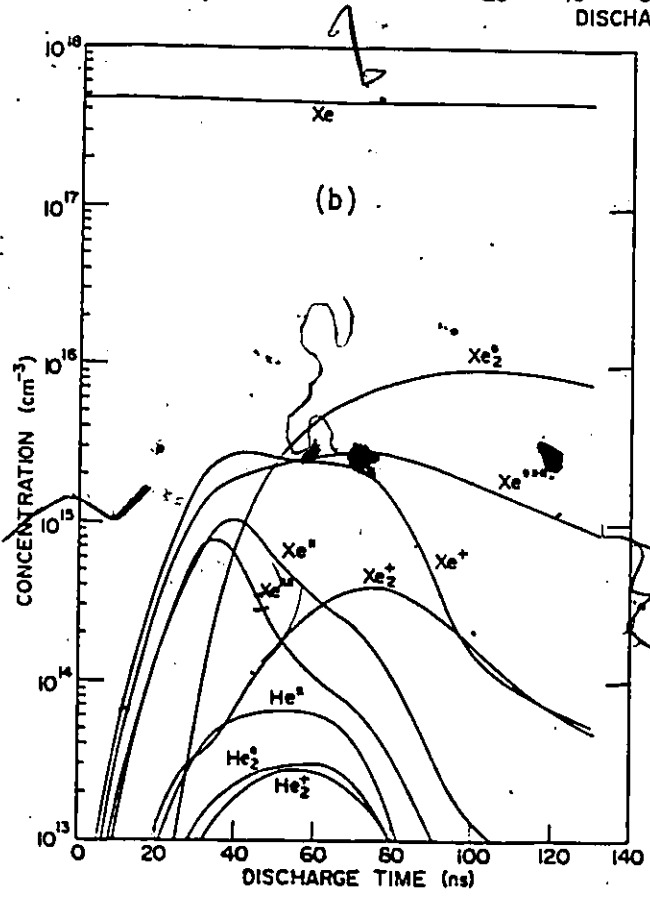
(b)
CONCENTRATION (cm⁻³)
DISCHARGE TIME (ns)
Xe
Xe₂*
Xe**
Xe*
Xe⁺
Xe₂⁺
He*
He₂*
He₂⁺

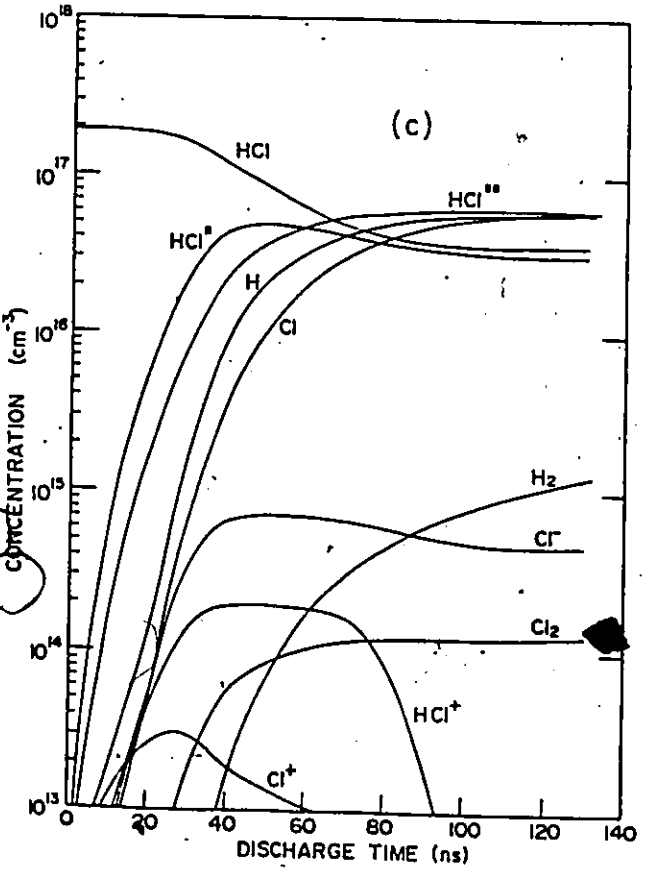
(c)
CONCENTRATION (cm⁻³)
DISCHARGE TIME (ns)
HCl
HCl**
HCl*
H
Cl
H₂
Cl⁻
Cl₂
HCl⁺
Cl⁺

A. Xe^+

The electron is the most important species governing the laser dynamics. This is followed, in importance, by Xe^+ which is the major ionic species present. This species is produced primarily by electron-impact ionization of ground-state and of excited-state Xe atoms. These are efficient channels for ion production because the Xe atoms have the lowest ionization potential (12.127 eV) of all the components in a He/Xe/HCl mixture, and because the ~4 eV energy required to ionize excited Xe atoms is not much different from the average electron energy in the plasma. In addition, the ionic dissociation of $Xe^+ \cdot Cl^-(B)$, which is formed via three-body "harpooning" of $Xe^{**}(^3P_1)$ and $Cl(^2P_{3/2})$ atoms, significantly increases the population of Xe^+ ions. There are also supplementary channels for the Xe^+ production. These are processes involving two- and three-body charge exchange of He_2^+ ions with Xe atoms, and Penning ionization of Xe in collisions with He^* and He_2^* excited species. Of these supplementary channels, the three-body process involving charge exchange between He_2^+ and Xe is most efficient because of the high reaction rate for the process in a He-rich mixture, and because of the relatively high abundance of He_2^+. The latter species is formed mainly as a result of the electron-impact ionization of He_2^*, and the Hornbeck-Molnar reaction associating ground and excited He atoms. Other supplementary processes leading to the Xe^+ production, which are investigated in the kinetic model, include auto-Penning ionization of Xe^*, Xe^{**} and Xe^{***}, and auto-dissociative ionization of Xe_2^*. The model indicates that these processes are unimportant compared to the electron

collision processes. Under ordinary conditions, photoionization of Xe-related discharge species resulting either from photoabsorption of the laser emission or from photo-preionization of the discharge medium, generally contributes little to ion production. However, in the presence of abundant Xe metastable atoms and at a high laser flux level, the contribution may be substantial. Most of the Xe^+ ions produced by the above processes are usefully consumed in forming $XeCl^*$ exciplex species. There is also a significant Xe^+ ion loss in the three-body association with Xe atoms to form Xe_2^+ ions, which are both efficient combiners with Cl^- ions, and strong photoabsorbers near the 308-nm laser wavelength. An additional loss channel is the charge transfer with HCl molecules. All important processes relating to the production and loss of Xe^+ ions are summarized in Fig.5-3.

B. Cl^-

In a gaseous discharge, electrons are the most abundant negatively-charged species. The ratio of electrons to negative ions in a typical discharge-excited XeCl laser mixture is as high as 3:1. For example, the kinetic modelling results given in Fig.5-2(c) indicate that the Cl^- concentration reaches 7×10^{14} cm^{-3}. This concentration is about an order of magnitude larger than the value estimated by Levin et al. [85] for a Ne/Xe/HCl mixture. Our high value is a consequence of the efficient formation of Cl^- via dissociative attachment to ground-state (v=0) and vibrationally-excited (v=1,2) HCl molecules, resulting from low-energy electrons which occur at higher densities in helium than in neon. Some Cl^- ions are also generated from dissociation

Fig. 5-3

A schematic diagram illustrating the important channels for the production and loss of Xe^+ ions in a XeCl laser discharge.

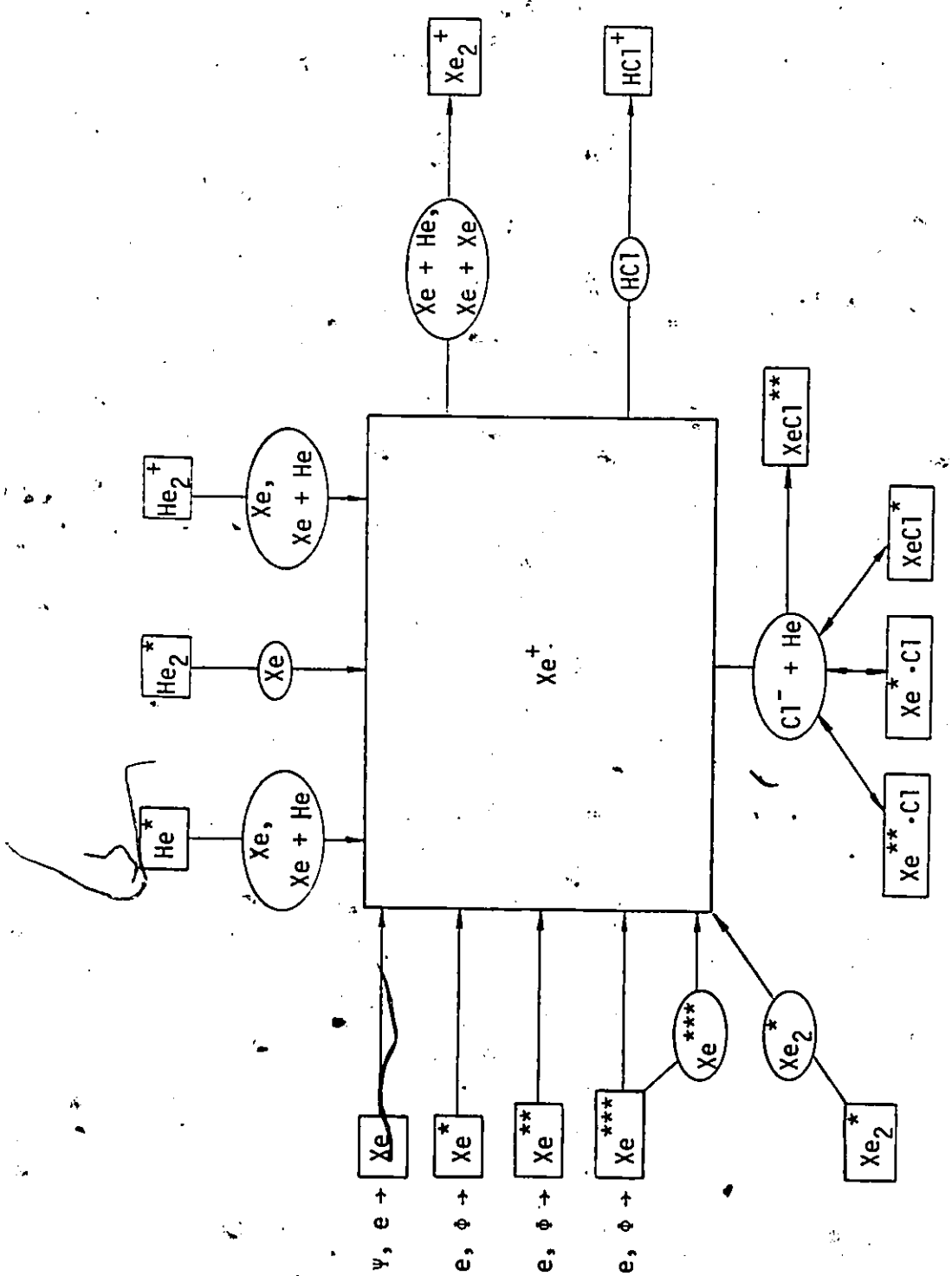
Xe
Xe*
Xe**
Xe***
Xe*2
Xe+2
HCl+
HCl
Xe + He, Xe + Xe
He*2
He+2
Xe
Xe, Xe + He
He*
Xe+
Cl− + He
XeCl**
XeCl*
Xe* ·Cl
Xe** ·Cl
ψ, e →
e, Φ →
e, Φ →
e, Φ →

of $XeCl^*(B)$ formed primarily from the Rydberg molecule $Xe^{**}\cdot Cl$, and less frequently from $Xe^*\cdot Cl$. There are other minor supplementary channels involving electron attachment to Cl atoms, electron dissociative attachment to Cl_2, double electron attachment to Cl^+ by H_2-impact, and photo-dissociation of Cl_2^- ions. These latter processes can be neglected in our kinetic model either because the particle concentrations are low or because the processes themselves are inefficient . Most Cl^- ions are depleted to form exciplex species such as $XeCl^*$, $XeCl^{**}$ and Xe_2Cl^*. In addition, there are secondary losses, shown in Fig.5-4, caused by photo-detachment, electron detachment by impact with electrons and with H atoms, and recombination with various positive ions.

Cl^- ions are consumed predominantly by, and usefully in, $XeCl^*$ formation, and therefore directly influence the laser dynamics. The primary processes which determine the supply of Cl^- ions (dissociative attachment of HCl and HCl^* molecules) are very important. These electron processes are sensitive to discharge variations, and consequently the production rate of Cl^- ions is largely determined by the discharge conditions. At the early stages of a discharge, when HCl molecules are essentially in their ground state, the ion production proceeds via electron attachment to these molecules. During the time that optical emission occurs most of the HCl molecules are vibrationally excited (see Fig.5-2(c)). Consequently, and because the attachment rate for HCl^* (v=1,2) is greater than for HCl (v=0), Cl^- ions are generated more efficiently during optical emission (typically $\geq$ 30 ns after gas breakdown) than immediately after gas breakdown. As the concentration

Fig. 5-4

A schematic diagram illustrating the important channels for the production and loss of Cl^- ions in a XeCl laser discharge.

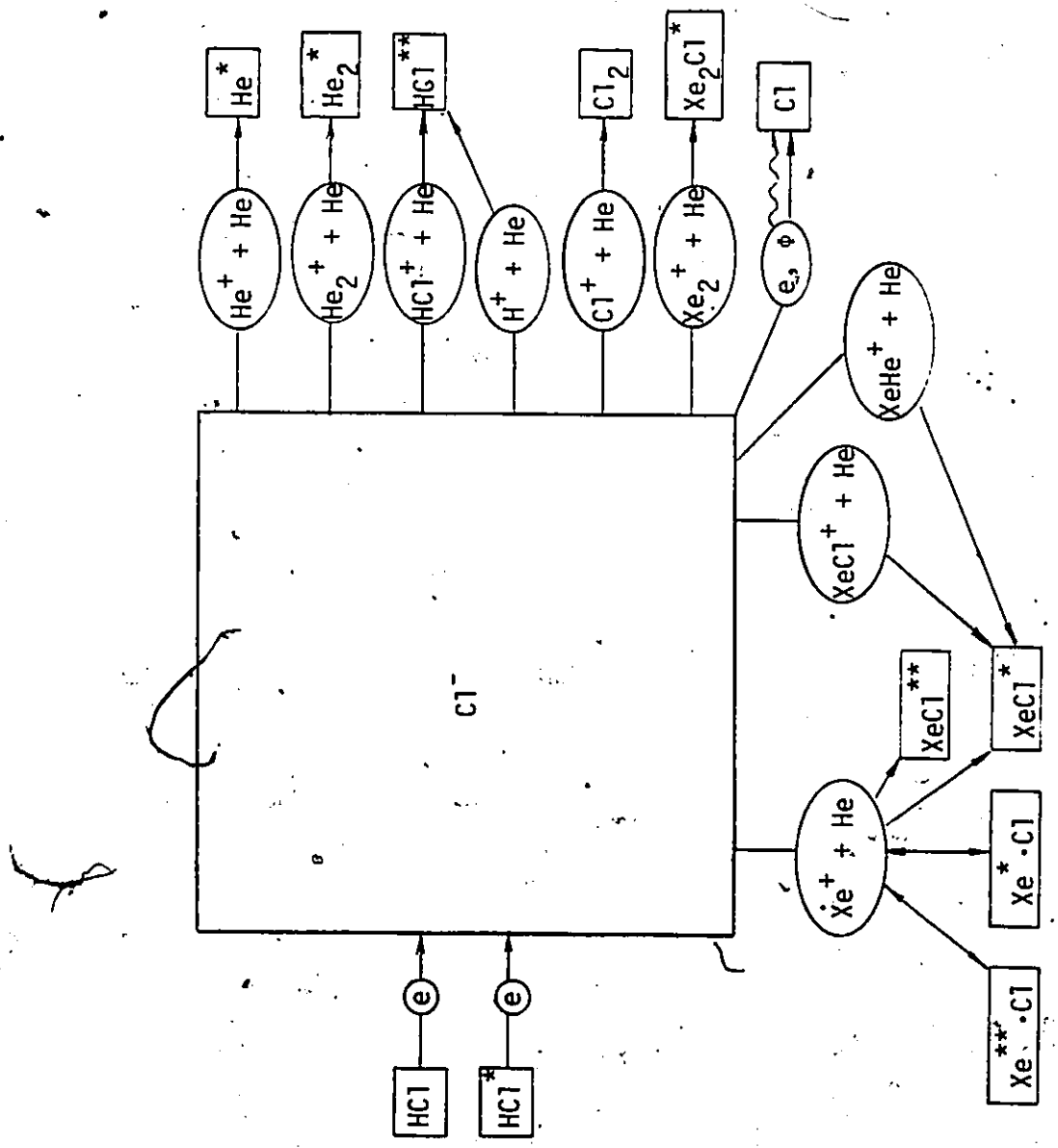
HCl
HCl*
e
e
Cl⁻
He* + He
He₂* + He
HCl** + He
H⁺ + He
Cl₂⁺ + He
Xe₂Cl* + He
e, Φ
He*
He₂*
HCl**
Cl₂
Xe₂Cl*
Cl
XeHe⁺ + He
XeCl⁺ + He
Xe⁺ + He
XeCl**
XeCl*
Xe* + Cl
Xe** + Cl

of Cl^- ions increases, the $XeCl^*$ formation rate increases rapidly. Consequently, the Cl^- ions produced by the various processes given above are quickly depleted until a quasi-equilibrium state is reached, at which time the production and loss rates are balanced. In a typical situation, shown in Fig.5-2(c), this quasi-equilibrium state corresponds to a Cl^- ion concentration of 5-7 x 10^{14} cm^{-3}.

C. Xe^* and Xe^{**}

Three-body ionic recombination dominates the formation of the exciplex $XeCl^*$. The "harpooning" processes, involving the Rydberg molecules Xe^*·Cl and Xe^{**}·Cl, are also efficient channels for the formation of $XeCl^*$. These two latter channels take advantage of the metastable atom $Xe^*(^3P_2)$ and the resonance-trapped atom $Xe^{**}(^3P_1)$. Both atoms are generated primarily by electron-impact excitation of ground-state Xe atoms, and as predissociation products of $XeCl^*$ formed via the ionic channel. Additional processes populating the $^3P_2$ and $^3P_1$ levels in Xe include relaxation, by radiation and by electron-impact, of high-lying excited Xe^{***} atoms. These latter atoms are created in the discharge by electron-impact excitation, or by dissociative recombination of Xe_2^+ and of $XeCl^+$ ions with electrons.

The excited atoms Xe^* and Xe^{**}, described in Figs.5-5 and 5-6, are primarily depleted in useful channels which lead to $XeCl^*$ formation, either indirectly through electron-impact ionization or through further excitation and subsequent ionization, or directly in "harpooning" reactions with ground-state Cl atoms and with vibrationally-excited HCl atoms. Ionization of the Xe^* and Xe^{**} atoms can also occur either in

Fig. 5-5

A schematic diagram illustrating the important channels for the production and loss of Xe^* atomic species in a XeCl laser discharge.

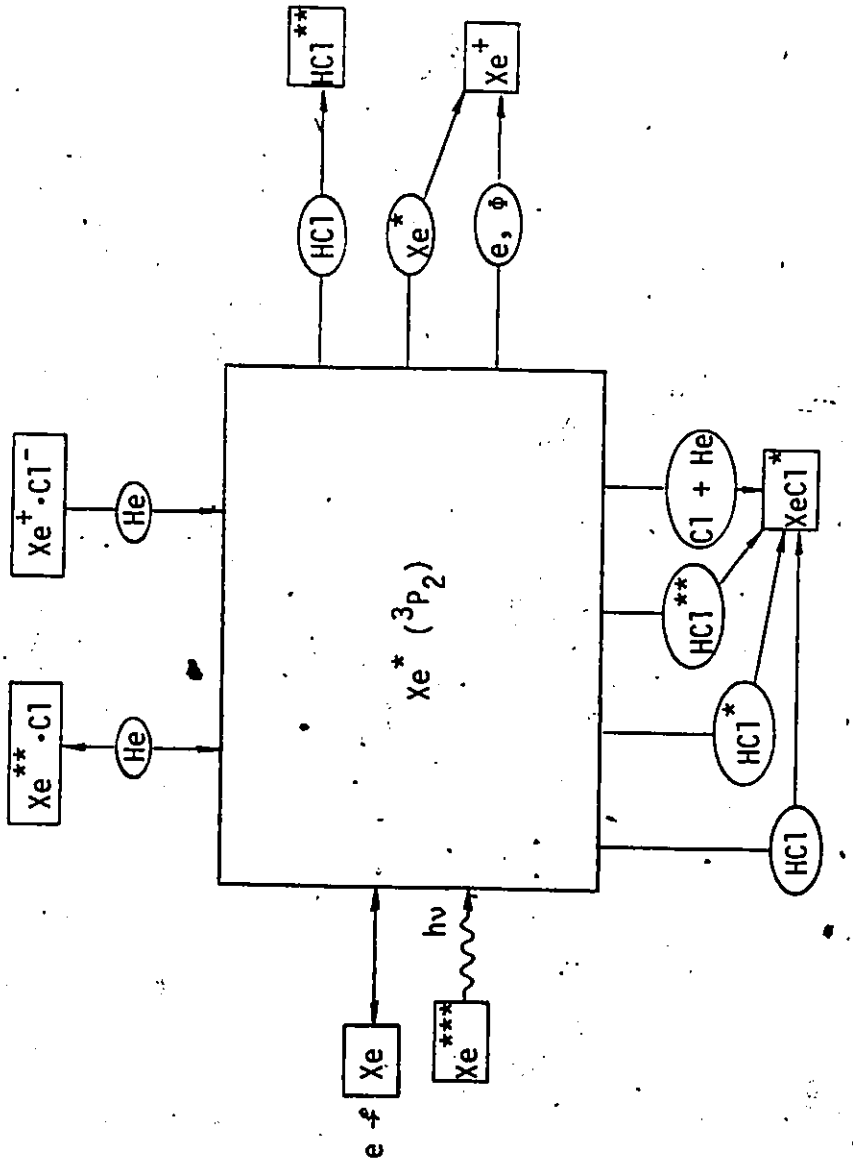
HCl**
Xe+
HCl
Xe*
e, Φ
Xe+·Cl−
He
Xe** ·Cl
He
Xe* (3P2)
C1 + He
XeCl*
HCl**
HCl*
HCl
e
Xe
hν
Xe***

Fig. 5-6

A schematic diagram illustrating the important channels for the production and loss of Xe^{**} atomic species in a XeCl laser discharge.

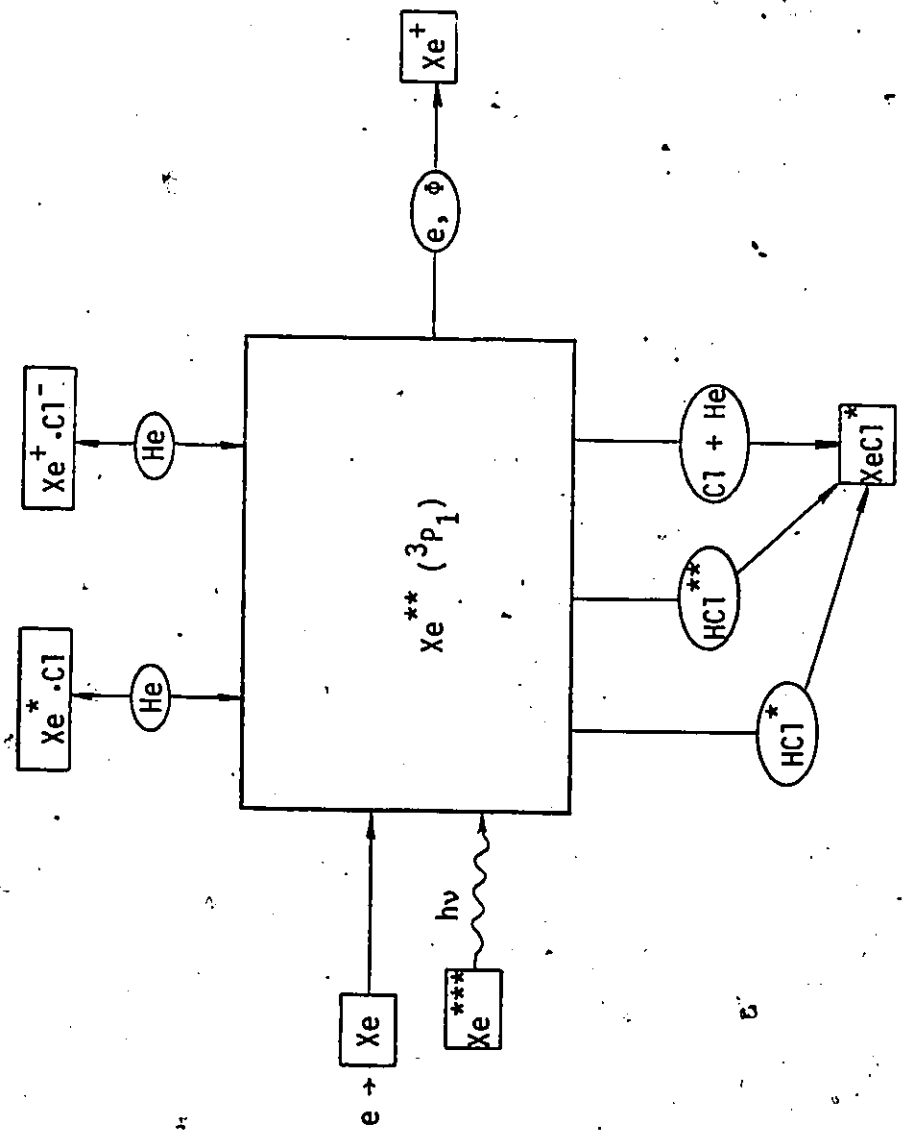
Xe+
e, Φ
Xe+.Cl-
He
Xe*.Cl
He
Xe** (3P1)
Cl + He
XeCl*
HCl**
HCl*
hν
Xe
e +
Xe***

auto-Penning processes or after photoabsorption at the laser wavelength. However, both processes produce significant losses in the gain medium. In addition to ionization, the auto-Penning processes also remove Xe^* and Xe^{**} atoms (by de-excitation to the Xe ground state) which would otherwise directly engage in forming $XeCl^*$ via the Rydberg-state channels. The photoabsorption results in a reduction of laser output. The secondary loss processes for Xe^* and Xe^{**} are superelastic collision, th[illegible]od Phelps-Molnar association with Xe and He to produce the xenon excimer Xe_2^*, and Penning ionization of the exciplex $XeCl^*$. It may be noted that the "harpooning" processes, which associate excited Xe atoms ($^3P_2$ and $^3P_1$ states) with HCl (v=0) and Cl_2, are found to be unimportant in our kinetic studies. The reactions with HCl proceed at low rates during optical emission; those with Cl_2 are greatly reduced by the presence of a small quantity of Cl_2 in the discharge medium.

D. Cl

In the XeCl laser system employing HCl as the halogen donor, a significant number of donor molecules dissociate, via various reaction channels, into Cl and H atomic species. The Cl atoms result mainly from predissociation of energetic $XeCl^*$ species via the Rydberg exit channels, from collisional quenching of the ground-state XeCl molecule and of the Xe_2Cl^* triatomic exciplex. Additional Cl atoms are produced by many other processes. These include photodetachment and electron-impact detachment of Cl^- ions, [illegible]diative dissociation of $XeCl^{**}$ and Xe_2Cl^* exciplex species, ph[illegible]ciation of Xe_2Cl^*, dissociative ionic recombination of Cl^- [illegible] He^+, He_2^+, HCl^+ and $XeCl^+$ in He, electron

dissociative attachment of vibrationally-excited and ground-state HCl molecules, molecular dissociation of HCl^* by H-impact, dissociation of HCl in collision with HCl^+ or He_2^+ ions, and dissociative recombination of $XeCl^+$ ions with electrons. Cl atoms are necessary for the "harpooning" reactions with excited Xe atoms to form $XeCl^*$. However, most of the Cl atoms still remain in the discharge because the re-formation of HCl molecules (e.g., by reaction of Cl with H_2) is slow. The important kinetic processes relating to the production and loss of Cl atoms are summarized in Fig.5-7. The minor Cl loss mechanisms, which are not shown in the figure, include three-body association in He or Cl_2 (to produce Cl_2 molecules), charge transfer from He^+ ions, Penning ionization by collision with He^* species, and electron attachment to yield Cl^- ions.

E. Electrons

Electrons are essential species in the XeCl laser medium. In the discharge, the electrons produce excited species, positive ions, and additional electrons. In particular, the Xe^* and Xe^{**} atomic species and the Xe^+ ions, all resulting from electron-xenon collisions, participate actively in $XeCl^*$ exciplex production. Other excited species such as He^*, He^+, He_2^*, He_2^+, Xe^{***}, Xe_2^* and Xe_2^+, lose either their energies or charges to Xe atoms in collisions, and indirectly supplement exciplex production. Slow electrons released after ionization may attach to ground- and excited-state electrophilic molecules (HCl and HCl^*) to provide Cl^- ions and Cl atoms, which are necessary for the $XeCl^*$ formation. However, the electrons can also have a detrimental

Fig. 5-7

A schematic diagram illustrating the important channels for the production and loss of Cl atoms in a XeCl laser discharge.

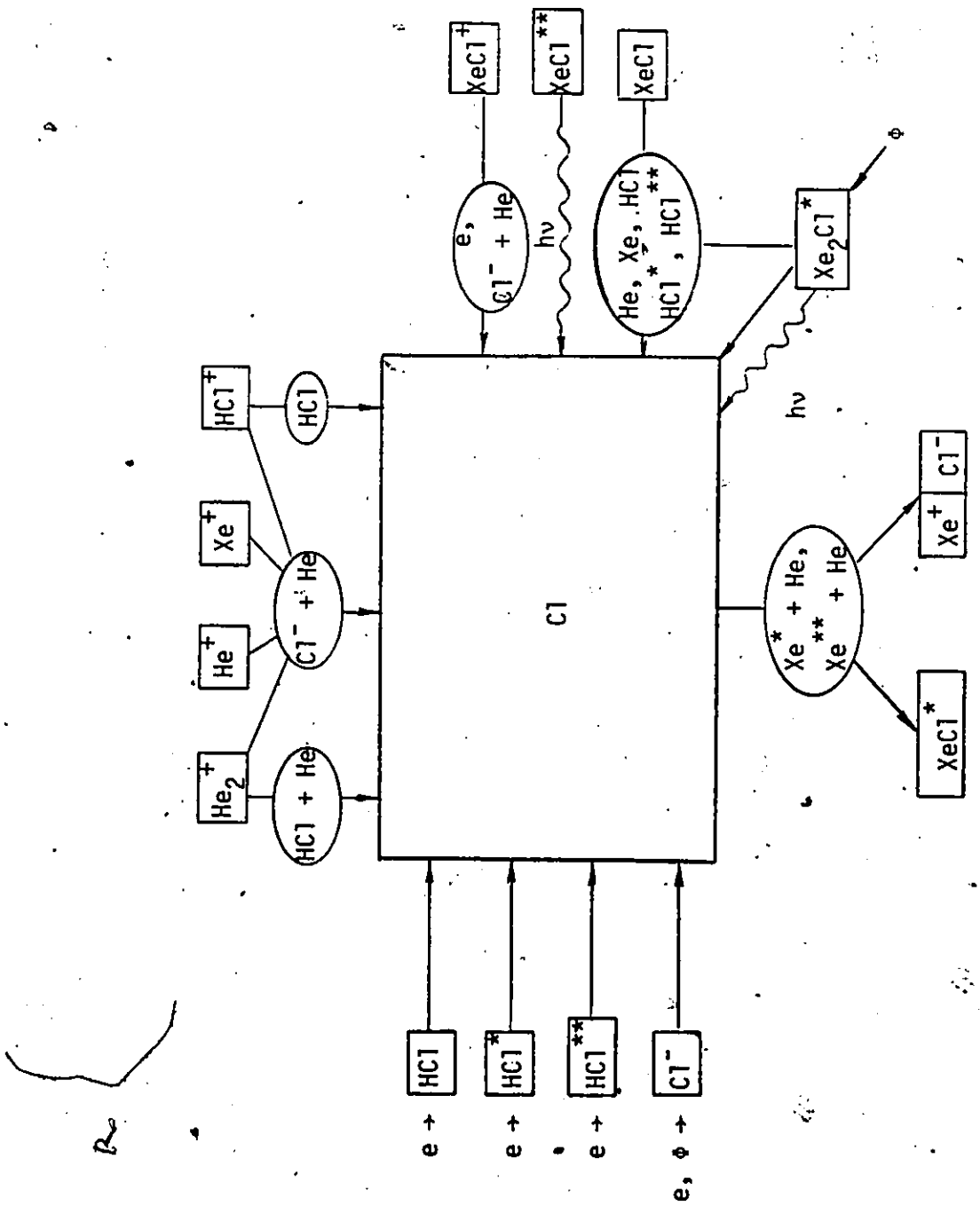
e + HCl
e + HCl*
e + HCl**
e, Φ + Cl⁻
Cl
e, Cl⁻ + He
hν
XeCl⁺
XeCl**
He, Xe, HCl, HCl*, HCl**
XeCl
Xe₂Cl*
Φ
hν
HCl⁺
HCl
Xe⁺
He⁺
He₂⁺
Cl⁻ + He
HCl + He
Xe* + He, Xe** + He
Xe⁺ Cl⁻
XeCl*

effect in the XeCl laser dynamics. The electron quenching (superelastic collision) of the $XeCl^*$ exciplex species generally results in reduction of laser gain and efficiency.

Electrons can exchange energy in collisions with discharge species, and, in addition, can be either produced or depleted in the kinetic processes. The average energy $\bar{\varepsilon}$ of an electron depends on the population of electrons (n) present in the medium, and the gain or loss in electron energy after collision. The latter can be evaluated using the threshold energies of various species listed in Table 5-4. Taking into account the dominant processes that affect electrons only, the energy balance equation for electrons is

$$\frac{\partial(n\bar{\varepsilon})}{\partial t} = \sum\{-(\bar{\varepsilon}-\bar{\varepsilon}_g)(\nu_{el}\frac{2m}{M})n$$ elastic scattering

$$- E_{ex}\overline{(\sigma v)}_{ex}Nn$$ excitation

$$+ E_{ex}\overline{(\sigma v)}_{sup}N^*n$$ superelastic collision

$$- E_{ion}\overline{(\sigma v)}_{ion}Nn$$ ionization

$$+ E_p k_p N_a^* N_b$$ Penning ionization

$$+ E_p K_p N_a^* N_b N_c$$ 3-body Penning ionization

$$- \bar{\varepsilon} k_a Nn$$ electron attachment

$$- \bar{\varepsilon} k_r N^+ n$$ radiative recombination

$$- \bar{\varepsilon} K_r N_a^+ N_b n$$ 3-body electron-ion recombination

$$- \bar{\varepsilon} k_r N_2^+ n$$ dissociative recombination

$$- \bar{\varepsilon} K_r N^+ n^2$$ dielectronic recombination

Table 5-4

Threshold energies of discharge species considered in the kinetic calculations for the XeCl laser system.

Species	Threshold Energy (eV)	Reference
He^*	19.82	[137]
He^+	24.59	[250]
He_2^*	18.26	[251]
He_2^+	22.22	[251]
Xe^*	8.32	[74]
Xe^{**}	8.44	[74]
Xe^{***}	9.45	[74]
Xe^+	12.13	[74]
Xe_2^*	7.25	[49]
Xe_2^+	11.13	[252]
Xe_3	11.9	
HCl^*	0.36	[250]
HCl^{**}	1.03	[250]
HCl^+	12.75	[250]
Cl^+	12.97	[250]
Cl^-	3.62	[78]
Cl_2^-	2.38	[253]
H^+	13.60	[250]
H^-	0.75	[78]
H_2^+	15.43	[254]
$XeHe^+$	16.2	
$XeCl^+$	12.5	
$XeCl^*$	4.02	[12,37]
Xe_2Cl^*	2.50	[255]

$$
\begin{aligned}
&+ E_{AI} k_{AI} N_a^* N_b && \text{associative ionization} \\
&+ E_{AI} K_{AI} N_a^* N_b N_c && \text{3-body associative ionization} \\
&+ E_{PB} k_{PB} N_{a2}^* N_b && \text{Phelps-Brown process} \\
&+ (h\nu - E_N)\sigma\Phi N && \text{photoionization} \\
&+ (h\nu - E_{N^-})\sigma\Phi N^- \} && \text{photodetachment} \\
&+ \frac{(eE)^2}{m\bar{\nu}} n \quad , && \text{source term}
\end{aligned}
\tag{5-11}
$$

where N, N^* (or N_2^*), N^+ and N^- are the concentration of neutral, excited, positive ionic and negative ionic species, respectively, and where k (or K), σ, Φ, $h\nu$, ν_{el}, $\bar{\nu}$, e and E are the appropriate two- (or three-) body rate constants, the photoabsorption cross-sections, the photon flux, the photon energy, the elastic collision frequencies, the average electron collision frequency, the electron charge and the applied electric field, respectively. The average fractional electron-energy loss in an elastic-scattering process is (2m/M), where m and M are the masses of electron and the collider. $\bar{\varepsilon}_g$ and E_X are the average gas energy and the appropriate energy transfer between electrons and particles, respectively. The average energy of a secondary electron, resulting from a Penning or Phelps-Brown process, or from associative ionization, is lower than the energy excess (ΔE) between the metastable level and the ionization potential of the particle. For example, the average energy of a Penning electron is $E_p \cong \frac{5}{8}(\Delta E)_p$ [256]. However, the electron energy change resulting from a Hornbeck-Molnar process is insignificant compared to other processes, and is

therefore neglected in the equation. The rate of change in energy resulting from electron-electron collision, calculated using a single-term approximation and the energy distribution function represented by Eq.(4-18), is vanishingly small and is excluded in Eq.(5-11). The rate of energy loss by diffusion is also excluded because it is several orders of magnitude smaller than any of the terms given in Eq.(5-11). However, errors can exist in the determination of the applied field, and from neglecting (in the kinetic model) contributions from elastic scatterings of electrons by excited and ionic discharge species. The latter are neglected because adequate cross-section data are not available. For these reasons, the source term in Eq.(5-11) is usually multiplied by a factor of order unity.

The energy balance equation for electrons (Eq.(5-11)) is solved simultaneously with the energy balance and the kinetic rate equations for discharge particles. The kinetic calculations determine the time-dependent concentration of electrons (and other discharge species), as shown in Fig.5-2, and the time-dependent average electron energy, as shown in Figs.5-10(c), 5-11(c) and 5-12(c). The results of the model indicate that the electron concentration during laser emission reaches $\sim 3 \times 10^{15}$ particles per cm^3 (degree of ionization $\sim 3 \times 10^{-5}$). The average electron energy rises rapidly to $\sim$4.6 eV shortly after gas breakdown, remains relatively unchanged during laser emission, and then falls with the decreasing gain of the medium.

F. Exciplexes and the B → X Emission

In our kinetic model, only the dominant B → X emission in the

XeCl laser system is analyzed. Only the $XeCl^*(B)$ and XeCl(X) electronic states are employed individually in the model. All the other states ($XeCl^{**}$) are assumed to contribute collectively to the $XeCl^*(B)$ exciplex formation. The C state is allowed to combine with the B state because these two states are close together (within 0.013 eV [75]). Therefore, the effective radiative lifetime (τ) of the combined state can be determined from [257]

$$\frac{g_B + g_C}{\tau} = \frac{g_B}{\tau_B} + \frac{g_C}{\tau_C} \quad , \tag{5-12}$$

where g_B, g_C and τ_B, τ_C are the degeneracy factors and the radiative lifetimes of the two states, respectively. Employing $g_B : g_C = 3 : 1$, $\tau_B = 11$ ns [46] and $\tau_C = 126$ ns [75], the calculated lifetime is $\tau = 35$ns, in reasonable agreement with the experimental value (41 ± 3 ns) obtained recently by Glass et al. [240]. Using the emission ratios for the two states given by Drieling and Setser [258], the calculated τ is in the range 38 ns (for low pressure) to 55 ns (for high pressure).

Most kinetic data concerning exciplex formation and quenching are not available in the literature, and have to be either calculated using conventional theories or estimated by analogy with values for similar processes. For example, the rate coefficients for the dominant three-body recombination of Xe^+ and Cl^- ions in He, and harpooning processes associating excited Xe and ground-state Cl atoms, are calculated using simple formulae described in Appendix F. In addition, the Drawin formulae [259] are used to determine the rate coefficients for electron-impact excitation and ionization of XeCl and $XeCl^*$, and, in conjunction with the calculated partition functions of the two states, to evaluate

the superelastic rate coefficient. In particular, the parameter β_1 in the Drawin formula for excitation has been chosen to be 3 in accordance with the results of the kinetic modelling. Consequently, the superelastic rate coefficient is 3-4 x 10^{-8} cm^3/s, in agreement with the estimate of 2 x 10^{-8} cm^3/s by Morgan and Pound [260] and comparable to the theoretical results for KrF^* and XeF^* due to Hazi et al. [261]. However, all of these values are an order of magnitude lower than the experimentally-based estimate of Sze and Seegmiller [262], and the value adopted by Levin et al. [85]. Our results indicate that exciplex quenching by electrons contributes less than 10% to the total depopulation rate of the excimer B-state, corresponding to ~15% of the quenching by all the discharge species.

Figure 5-8 is a schematic diagram illustrating the important formation and quenching channels for the $XeCl^*(B)$ exciplex, including radiative decay to XeCl(X). Collisional quenching by electrons, He, Xe, HCl, HCl^* and HCl^{**} are the main process depopulating both the excimer and ground states. In our kinetic model, electron quenching of the ground state results in excitation of XeCl to the excimer state, and not in atomic dissociation. This excitation is due to the small transition moments between the XeCl (v"=1,2) and XeCl (v"≥22) levels. The excitation rates for v" = 1 and 2 to v" = 3 are not small (~10^{-7} cm^3/s), which should result in rapid depopulation of the lower levels. However, the superelastic rates are very similar to the excitation rates. Therefore, direct or indirect electron-impact dissociation of XeCl is inefficient. In the model, collisional quenching of the excimer state by gas particles likely leads to populating other electronic states, and not to producing

Fig. 5-8

A schematic diagram illustrating the important channels for the formation and decay of $XeCl^*$ and XeCl in a XeCl laser discharge.

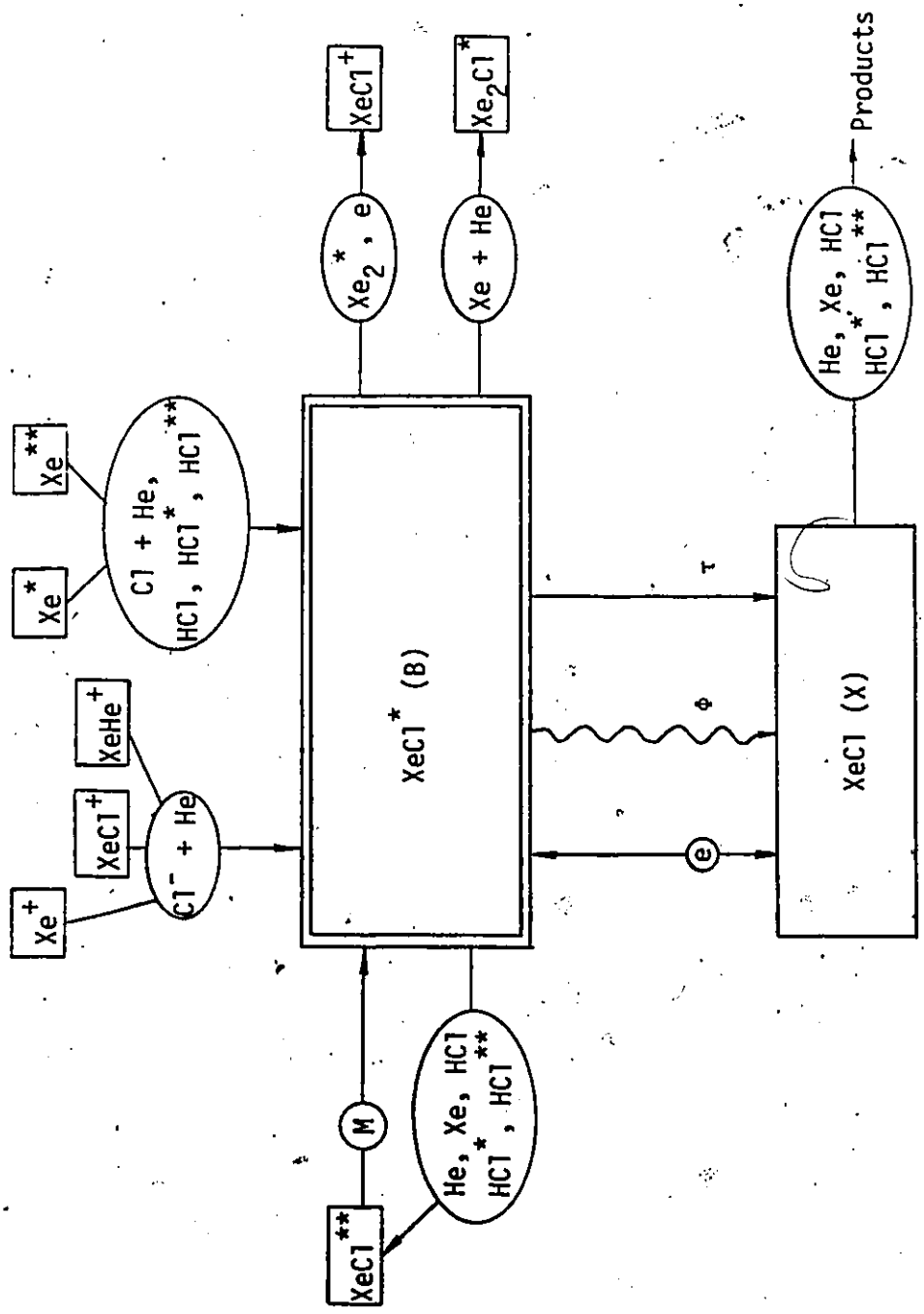
Products
He, Xe, HCl
HCl*, HCl**
XeCl (X)
XeCl* (B)
τ
Φ
e
M
Xe2*, e
XeCl+
Xe + He
Xe2Cl*
Cl + He,
HCl, HCl*, HCl**
Xe**
Xe*
Cl⁻ + He
XeHe+
XeCl+
Xe+
XeCl**
He, Xe, HCl
HCl*, HCl**

ground-state atoms. In addition, exciplex quenching by excited or ionic discharge species, such as He^*, He^+, He_2^*, He_2^+, Xe^*, Xe^{**}, Xe^{***}, Xe^+, Xe_2^* and Xe_2^+, may result in ionization of the exciplex. However, the primary loss of $XeCl^*$ particles is attributed to three-body association with Xe, in the presence of He, to form the triatomic exciplex Xe_2Cl^*. Although the process is reversible, recovery of the $XeCl^*$ is nevertheless slow.

Broad-band (~30-nm FWHM) laser emission from Xe_2Cl^*, centred at 518 nm, has recently been observed in an electron-beam-excited Ar/3.89% Xe/0.02% CCl_4 mixture at ~6.5-atm pressure [39]. Tang et al [242] have determined that the stimulated-emission cross-section and the radiative lifetime of the triatomic exciplex are ~0.08 $Å^2$ and ~100 ns, respectively. The radiative lifetime can be compared to the value 135 ns recently reported by Tittel et al. [242,263], and 330 ns calculated by Stevens and Krauss [255]. This exciplex is predominantly formed in collisions between $XeCl^*$ and Xe, as evidenced by the high xenon concentration (>100-Torr partial pressure) required to produce emission, which is also predicted from the results of our kinetic model for the XeCl system. Although the three-body recombination rate for Xe_2^+ and Cl^- in He is very high (3.4×10^{-27} cm^6/s), the ionic channel for Xe_2Cl^* formation is only of secondary importance in our case. The triatomic exciplex is quenched predominantly by gas particles (He, Xe, HCl, HCl^* and HCl^{**}). In addition, Xe_2Cl^* has a large population in the XeCl laser medium (shown in Fig.5-2(a)), and is therefore a good photoabsorber near λ = 308 nm, even though the estimated cross-section is only ~0.01 $Å^2$. The important kinetic role played by the

triatomic exciplex in the XeCl system is summarized in Fig.5-9.

Based on the results of our kinetic modelling presented in Figs . 5-10 to 5-12, the maximum photoabsorption amounts to $\sim$3.2% cm^{-1} when He is used as the diluent (absorption by $XeCl^*$ is not included). For comparison, the absorption coefficients using Ar and Ne as the diluents, measured by Champagne et al. [264], are typically $\sim$2.9% cm^{-1} and $\sim$1.5% cm^{-1}, respectively. Under our experimental conditions, the laser gain is $\sim$18% cm^{-1} during early optical emission, and therefore the medium absorption of $\sim$2% cm^{-1} is comparatively insignificant. The major photoabsorbers at this early emission period are the Cl^- and Xe_2^+ ionic species, followed in importance by the excited Xe atoms (Xe^* and Xe^{***}). After gain saturation is reached, the gain falls rapidly to a "constant" level of $\sim$5% cm^{-1}. In addition to Cl^- and Xe_2^+, the dominant absorber is the triatomic exciplex Xe_2Cl^*, which is a quenching product of the exciplex $XeCl^*$. Furthermore, other relatively strong absorbers at the laser wavelength, such as Xe^{***}, Xe^*, He_2^*, He^* and Xe^{**}, are also present. Therefore, photoabsorption is expected to be high when the $XeCl^*$ population is large. This results in a reduction of optical emission, particularly during long-pulse operation.

The computed and observed optical pulseshapes are shown in Figs.5-10(a) to 5-12(a). There is generally good agreement between theory and experiment for the output-pulse parameters. These include output power, pulse duration, delay time for onset of emission, and rise- and fall-times. The total optical pulse energies calculated using the kinetic model, and given in Table 5-5, agree very well with

Fig. 5-9

A schematic diagram illustrating the important channels for the formation and decay of the triatomic exciplex Xe_2Cl^* in a XeCl laser discharge.

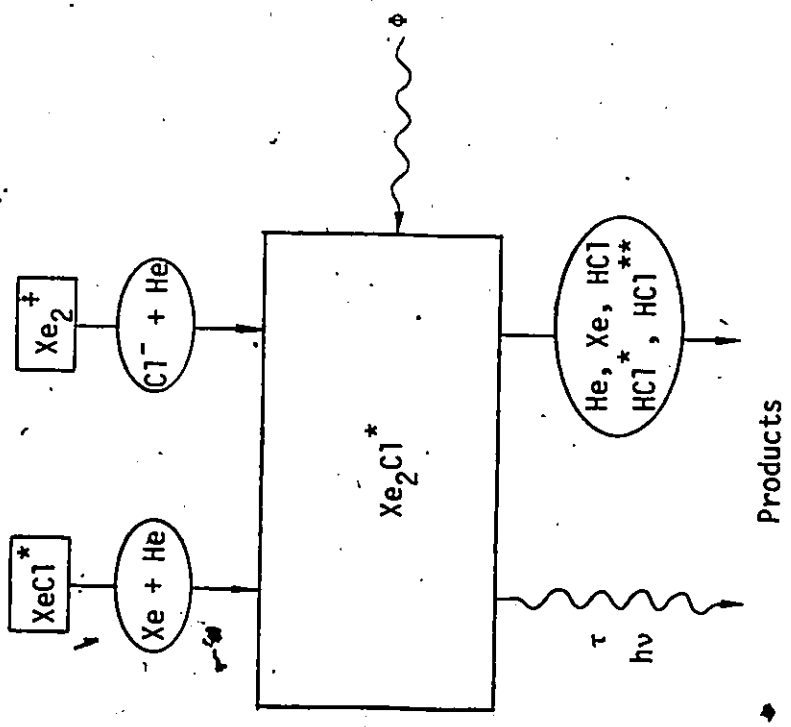
Φ
Xe_2^+
$Cl^- + He$
$XeCl^*$
$Xe + He$
Xe_2Cl^*
He, Xe, HCl
HCl^*, HCl^{**}
Products
τ
hν

Fig. 5-10

Results of kinetic modelling for a He/0.5% Xe/0.2% HCl laser mixture at 2957-Torr operating pressure, 35-kV charging voltage and 1.65-cm electrode separation.

(a) Comparison between computed (solid curve) and observed (dashed curve optical output pulses.

(b) Computed transient gain and absorption coefficients.

(c) Computed unsaturated gain coefficient, and average electron energy.

The computed results are based on the kinetic parameters given in Tables 4-2, and 5-1 to 5-3.

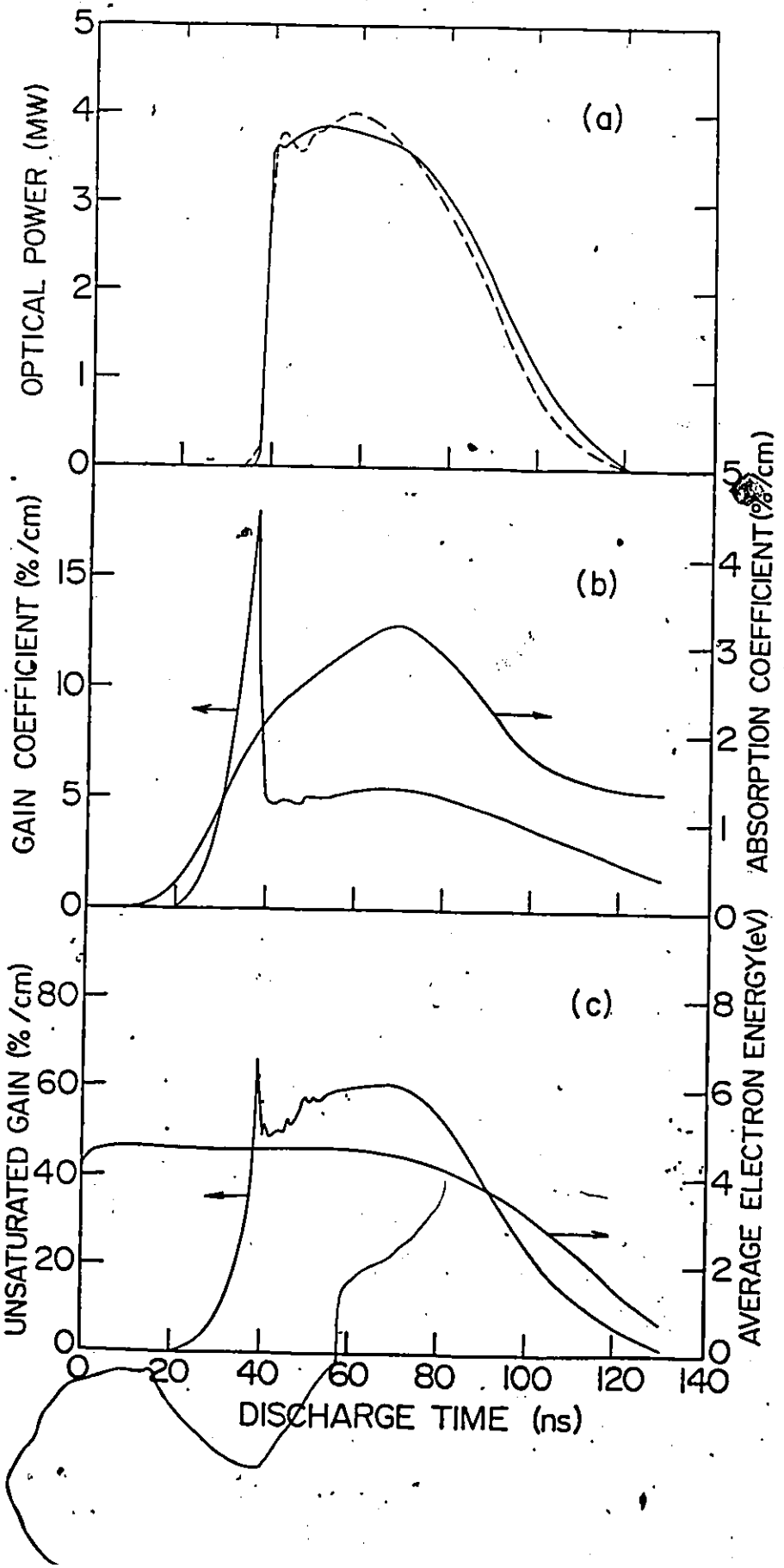
OPTICAL POWER (MW)
(a)
GAIN COEFFICIENT (%/cm)
ABSORPTION COEFFICIENT (%/cm)
(b)
UNSATURATED GAIN (%/cm)
AVERAGE ELECTRON ENERGY(eV)
(c)
DISCHARGE TIME (ns)

Fig. 5-11

Results of kinetic modelling for a He/0.5% Xe/0.2% HCl laser mixture at 2880-Torr operating pressure, 35-kV charging voltage and 1.65-cm electrode separation.

(a) Comparison between computed (solid curve) and observed (dashed curve) optical output pulses.

(b) Computed transient gain and absorption coefficients.

(c) Computed unsaturated gain coefficient, and average electron energy.

The computed results are based on the kinetic parameters given in Tables 4-2, and 5-1 to 5-3.

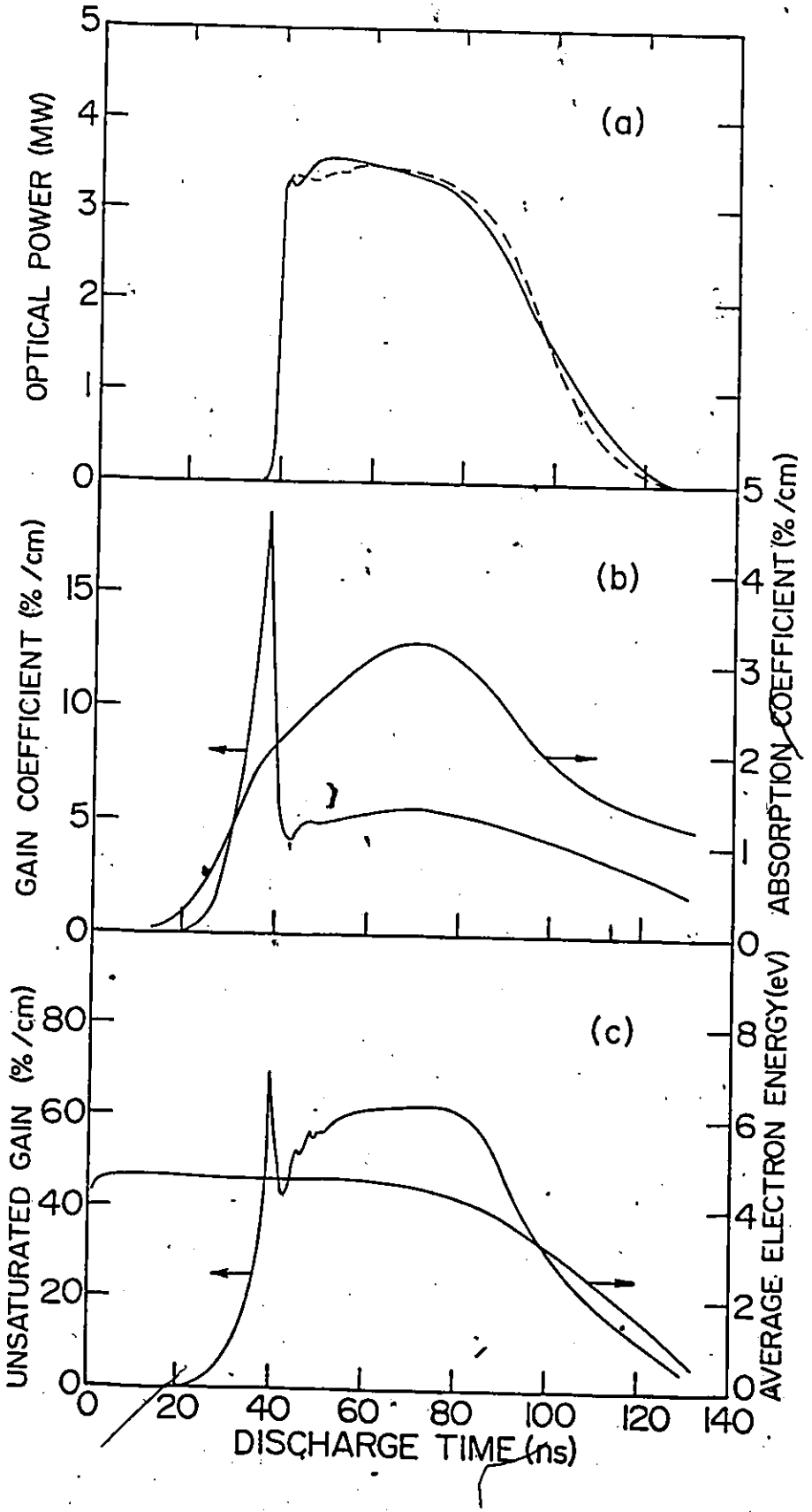
(a)
(b)
(c)
OPTICAL POWER (MW)
GAIN COEFFICIENT (%/cm)
ABSORPTION COEFFICIENT (%/cm)
UNSATURATED GAIN (%/cm)
AVERAGE ELECTRON ENERGY(eV)
DISCHARGE TIME (ns)
0
20
40
60
80
100
120
140

Fig. 5-12

Results of kinetic modelling for a He/0.5% Xe/0.2% HCl laser mixture at 2570-Torr operating pressure, 30-kV charging voltage and 1.65-cm electrode separation.

(a) Comparison between computed (solid curve) and observed (dashed curve) optical output pulses.

(b) Computed transient gain and absorption coefficients.

(c) Computed unsaturated gain coefficient, and average electron energy.

The computed results are based on the kinetic parameters given in Tables 4-2, and 5-1 to 5-3.

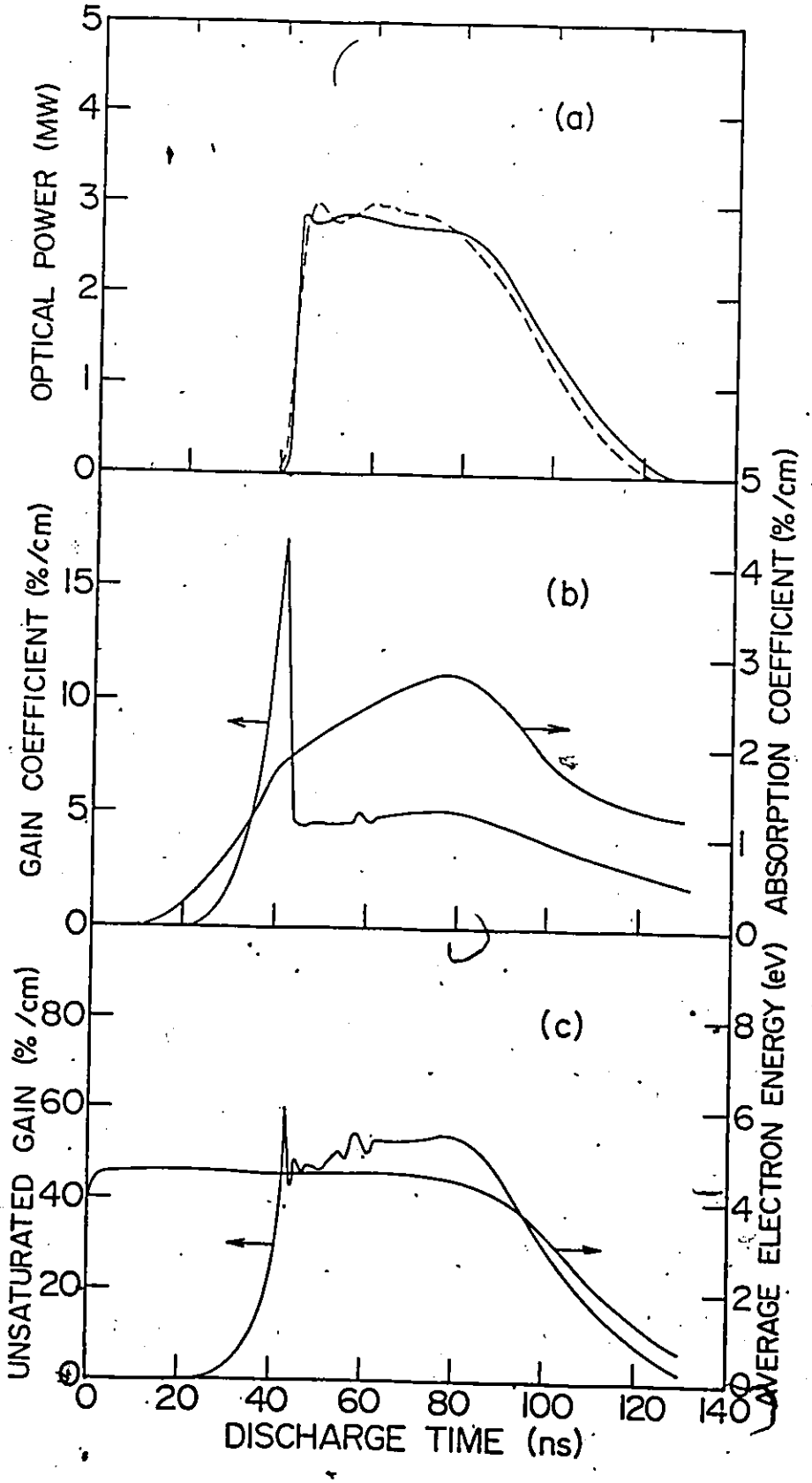
(a)
OPTICAL POWER (MW)
(b)
GAIN COEFFICIENT (%/cm)
ABSORPTION COEFFICIENT (%/cm)
(c)
UNSATURATED GAIN (%/cm)
AVERAGE ELECTRON ENERGY (eV)
DISCHARGE TIME (ns)

Table 5-7

Steady-state laser parameters, for various XeCl laser discharges, determined by the concise kinetic model.

Mixture : He/0.5% Xe/0.2% HCl

Gas Pressure (Torr)	Charging Voltage (kV)	Output Energy (mJ) Experiment (±20%)	Theory
2957	35	195	199.9
2880	35	200	208.2
2570	30	150	164.4

the measured values. The generally good agreement between all the computed and measured laser characteristics demonstrates that the present model is very suitable for describing the performance of the XeCl laser system.

A concise kinetic model has been constructed using the 115 important processes indicated by asterisks in Tables 4-2, and 5-1 to 5-3. These processes are selected by careful analyses of the contributions that the various processes have made to the results of the elaborate model employed for the above computations. The concise model, which is easier to use, and yields results with accuracies comparable to the elaborate model, is applied in the following section.

5.4 Quasi-Steady-State Determination of Laser Gain

The nonlinear gain characteristics of a discharge-excited XeCl laser system are evaluated using the concise kinetic model. The model is used to derive macroscopic parameters, such as the unsaturated gain, g_0, the absorption coefficient α_0 and the saturation irradiance Φ_s, in terms of microscopic kinetic properties of the discharge medium. These parameters permit us to determine the net laser gain (gain minus absorption) and the optical extraction efficiency. The parameters are also used in the study of quasi-cw behaviour (long-pulse operation) of the laser system.

Assuming steady-state conditions, the kinetic rate equations for the XeCl system, given in Table 5-6, can be solved to yield the inversion density

Table 5-6

Some rate equations employed in the concise kinetic model for evaluating laser parameters. The notation used is

Φ = irradiance at 308 nm

c = velocity of light

ℓ = length of active medium

L = cavity length

r_1, r_2 = effective rear and front mirror reflectances

[X] = concentration of discharge species X

n = electron density

σ_s = stimulated-emission cross-section

σ = photoabsorption cross-section

k = 2-body rate coefficient

K = 3-body rate coefficient

γ = decay frequency

τ = decay lifetime

t = discharge time

ρ = fraction of spontaneous emission contributing to output radiation ($\sim 5 \times 10^{-5}$)

$$\frac{1}{c}\frac{d\phi}{dt} = (\sigma_s([XeCl^*]-[XeCl]) - \varepsilon n\sqrt{r_1 r_2} - (\sigma_{D5}[Xe^*] + \sigma_{D6}[Xe^{**}] + \sigma_{D7}[Xe^{***}] + \sigma_{D8}[Xe_2^+] + \sigma_{D9}[Cl^-] + \sigma_{D12}[Xe_2Cl^*]))\phi\ell/L + \rho[XeCl^*]/\tau$$

$$\frac{d}{dt}[XeCl^*] = (k_{C1}[HCl] + k_{C2}[HCl^*] + k_{C3}[HCl^{**}])[Xe^*] + (k_{C6}[HCl^*] + k_{C7}[HCl^{**}])[Xe^{**}] + (K_{C9}[XeCl^+][Cl^-] + K_{C10}[XeHe^+][Cl^-] + K_{C12}[Xe^+][Cl^-] + K_{C15}[Xe^{**}][Cl] + K_{C18}[Xe^*][Cl])[He] + \gamma_{C21}[XeCl^{**}] + k_{C52}[XeCl]n - [XeCl^*]/\tau - \sigma_s([XeCl^*] - [XeCl])\phi - (k_{C24}[He] + k_{C29}[Xe] + K_{C36}[Xe][He] + k_{C37}[HCl] + k_{C38}[HCl^*] + k_{C39}[HCl^{**}] + (k_{C40} + k_{C41})n)[XeCl^*]$$

$$\frac{d}{dt}[XeCl] = [XeCl^*]/\tau + \sigma_s([XeCl^*]-[XeCl])\phi + k_{C40}[XeCl^*]n - (k_{C43}[He] + k_{C48}[Xe] + k_{C49}[HCl] + k_{C50}[HCl^*] + k_{C51}[HCl^{**}] + k_{C52}n)[XeCl]$$

$$\frac{d}{dt}[Xe^*] = k_{A5}[Xe]n + \gamma_{B49}[Xe^{***}] + (K_{C13}[Xe^+][Cl^-] + K_{C16}[Xe^{**}][Cl])[He] - ((k_{A30} + k_{A32})n + (k_{B41} + k_{C1})[HCl] + 2k_{B42}[Xe^*] + k_{C2}[HCl^*] + k_{C3}[HCl^{**}] + (K_{C18} + K_{C19})[Cl][He] + \sigma_{D5}\phi)[Xe^*]$$

$$\frac{d}{dt}[Xe^{**}] = k_{A6}[Xe]n + \gamma_{B50}[Xe^{***}] + (K_{C14}[Xe^+][Cl^-] + K_{C19}[Xe^*][Cl])[He] - (k_{A35}n + k_{C6}[HCl^*] + k_{C7}[HCl^{**}] + (k_{C15} + k_{C16} + k_{C17})[Cl][He] + \sigma_{D6}\phi)[Xe^{**}]$$

$$\frac{d}{dt}[Xe^+] = (k_{A8}[Xe] + k_{A32}[Xe^*] + k_{A35}[Xe^{**}] + k_{A39}[Xe^{***}])n + (k_{B7} + \tfrac{1}{2}K_{B9}[He])[He^*][Xe] + k_{B25}[He_2^*][Xe] + (k_{B27} + K_{B29}[He])[He_2^+][Xe] + k_{B52}[Xe^{***}]^2 + k_{B59}[Xe_2^*]^2 + K_{C17}[Xe^{**}][Cl][He] + (\sigma_{D5}[Xe^*] + \sigma_{D6}[Xe^{**}] + \sigma_{D7}[Xe^{***}]) - (K_{B53}[Xe][He] + k_{B55}[HCl] + (K_{C11} + K_{C12} + K_{C13} + K_{C14})[Cl^-][He])[Xe^+]$$

$$\frac{d}{dt}[HCl^*] = (k_{A10}[HCl] + k_{A54}[HCl^{**}])n - ((k_{A48} + k_{A49} + k_{A50} + k_{A51} + k_{A52})n + k_{B62}[HCl] + k_{B63}[Cl] + k_{B65}[H] + k_{C2}[Xe^*] + k_{C6}[Xe^{**}])[HCl^*]$$

$$\frac{d}{dt}[Cl] = (k_{A14}[HCl] + k_{A52}[HCl^*] + k_{A56}[HCl^{**}] + k_{A62}[Cl^-])n + (K_{B19}[He^+] + K_{B32}[He_2^+] + K_{B67}[HCl^+] + K_{C9}[XeCl^+] + (K_{C13} + K_{C14})[Xe^+])[Cl^-][He] + k_{B31}[He_2^+][HCl][He] + k_{B65}[HCl^*][H] + k_{B66}[HCl^+][HCl] + \gamma_{C42}[XeCl^{**}] + (k_{C43}[He] + k_{C48}[Xe] + k_{C49}[HCl] + k_{C50}[HCl^*] + k_{C51}[HCl^{**}])[XeCl] + (1/\tau_{C55} + k_{C56}[He] + k_{C57}[Xe] + k_{C58}[HCl] + k_{C59}[HCl^*] + k_{C60}[HCl^{**}])[Xe_2Cl^*] + k_{C61}[XeCl^+]n + (\sigma_{D9}[Cl^-] + \sigma_{D12}[Xe_2Cl^*])\phi - ((K_{C15} + K_{C17})[Xe^{**}] + K_{C18}[Xe^*])[Cl][He]$$

$$\frac{d}{dt}[Cl^-] = (k_{A13}[HCl] + k_{A51}[HCl^*])n + K_{C17}[Xe^{**}][Cl][He] - (k_{A62}n + (K_{B19}[He^+] + K_{B32}[He_2^+] + K_{B67}[HCl^+] + K_{B72}[Cl^+] + K_{B87}[H^+] + K_{C9}[XeCl^+] + K_{C10}[XeHe^+] + (K_{C11} + K_{C12} + K_{C13} + K_{C14})[Xe^+] + K_{C54}[Xe_2^+])[He] + k_{B76}[H] + \sigma_{D9}\phi)[Cl^-]$$

$$\Delta N \equiv [XeCl^*] - [XeCl] = \frac{(Q'' - \frac{1}{\tau})[XeCl^*] - F''}{(Q'' + \sigma_s \Phi)} \quad , \qquad (5\text{-}14)$$

where Q" and F" are the total quenching frequency and the formation rate (via superelastic collision of the exciplex by electrons), respectively, for the ground state, τ is the radiative lifetime of the upper emitting (excimer) state, and σ_s is the stimulated-emission cross-section. Equation (5-14) can also be written as

$$\Delta N = \frac{(Q'' - \frac{1}{\tau})F' - (Q' + \frac{1}{\tau})F}{Q''(Q' + \frac{1}{\tau}) + \sigma_s \Phi (Q' + Q'')} \quad , \qquad (5\text{-}15)$$

where Q' and F' are the total quenching frequency and the total formation rate for the excimer B state. In the presence of a laser field, the laser gain, defined by

$$g \equiv \sigma_s \Delta N \quad , \qquad (5\text{-}16)$$

can be expressed as

$$g = \frac{g_0}{1 + \Phi/\Phi_s} \quad . \qquad (5\text{-}17)$$

The net optical gain (gain minus absorption), the unsaturated gain, and the saturation irradiance are calculated from

$$g_{net} = g - \alpha_0 \quad , \qquad (5\text{-}18)$$

$$g_0 = \left(\frac{Q'' - \frac{1}{\tau}}{Q' + \frac{1}{\tau}}\right)\frac{F'}{Q''} - \frac{F''}{Q''} \quad , \qquad (5\text{-}19)$$

and

$$\Phi_s = \frac{Q' + \frac{1}{\tau}}{\sigma_s (1 + Q'/Q'')} \quad , \qquad (5\text{-}20)$$

respectively. Note that the total rate of exciplex formation is determined predominantly by electron-impact excitation and/or ionization of Xe atoms. These electron processes vary directly with the applied field. Therefore, if the quenching rates for the upper and the lower laser levels remain relatively constant, then the unsaturated gain is proportional to the amount of excitation. For this reason, the gain period can be long if the excitation pulse is long. The saturation, however, is affected only by the depopulation rates of the excimer and the ground states.

The absorption coefficient α_0, which takes into account contributions from all photoabsorbers, is given by

$$\alpha_0 = \sum_i \sigma_{ph}^{(i)}[i] \quad , \qquad (5\text{-}21)$$

where $\sigma_{ph}^{(i)}$ is the absorption cross-section of the i^{th} discharge species at the laser wavelength. In Eq.(5-21), the absorption of the laser radiation by $XeCl^*$ species is not included because it is a self-depopulating process. However, it has been considered in the determination of the laser gain.

Numerical results, using the steady-state parameters given by Eqs.(5-17) and (5-19) to (5-21), are presented in Table 5-7 for the same operating conditions used above. The transient "quasi-steady-state" parameter g_0, the computed gain g, and the absorption coefficient α_0 are taken from Figs.5-10 to 5-12. The high gain at high irradiance associated with the XeCl system is typical of the RGH laser family. Alternatively, the intrinsic parameters for the laser system (g_0, α_0

Table 5-5

Comparison of optical output energies determined experimentally and using the kinetic model.

Mixture : He/0.5% Xe/0.2% HCl

Gas Pressure (Torr)	Charging Voltage (kV)	Cavity Irradiance (MW/cm^2)	Saturation Irradiance Φ_s (MW/cm^2)	Unsaturated Gain g_o ($\%cm^{-1}$)	Gain g ($\%cm^{-1}$)	Absorption α_o ($\%cm^{-1}$)
2957	35	3.79	0.582	60.8	5.51	3.28
2880	35	3.39	0.570	61.6	5.56	3.30
2570	30	2.73	0.499	54.1	5.14	3.05

and Φ_s) can be determined from the gain-saturation theory, used together with measurements of the output power.

5.5 Determination of Laser Parameters Using Intracavity Attenuators

Rigrod's gain-saturation theory [45,265] is usually applied, in conjunction with laser output measurements, to determine the intrinsic laser parameters g_0, α_0 and Φ_s, and to determine the optimum output performance of RGH lasers [26,30,40,262]. This approach makes use of the exact solution of the steady-state field equations to relate mirror reflectances to optical output power. The field equations are

$$\frac{1}{\beta_\pm}\frac{d\beta_\pm}{dz} = \frac{\pm g_0}{1+\beta_+ + \beta_-} - \alpha_0 \quad , \tag{5-22}$$

where $\beta_\pm \equiv \Phi_\pm(z)/\Phi_s$ are the normalized irradiances in the forward (+z) and backward (-z) directions of propagation. Assuming constant gain and loss, the field equations yield [266]

$$-\alpha_0 \ell - \ell n\sqrt{r_1 r_2} = \frac{g_0}{g_0-\alpha_0}\frac{1}{\cos(2\lambda)}\ell n\left[\frac{(1-\sqrt{r_1}\tan\lambda)(1-\sqrt{r_2}\tan\lambda)}{(\sqrt{r_1}-\tan\lambda)(\sqrt{r_2}-\tan\lambda)}\right] \quad , \tag{5-23}$$

where ℓ is the active length of the laser, and r_1 and r_2 are the rear and front mirror reflectances. The parameter λ is related to the output power, given by

$$P = \Phi_s A\left(\frac{g_0-\alpha_0}{2\alpha_0}\right)\left(\frac{1-r_2}{\sqrt{r_2}}\right)\sin(2\lambda) \quad , \tag{5-24}$$

where A is the area of the optical beam. The three intrinsic laser

parameters in Eqs.(5-23) and (5-24) are often determined experimentally by measuring the output power for at least three different output couplers. However, in our experiments, we also changed the rear mirror reflectance r_1 by inserting in-cavity attenuators (UV-grade neutral density filters) between the rear cavity window and mirror. The effective reflectance r_1 becomes

$$r_1 = \frac{2r+(1-3r)R_1 \exp(-2D)}{1+r-2rR_1 \exp(-2D)} , \qquad (5\text{-}25)$$

where r and R_1 are the reflectances of a cavity window surface ($r \approx 5\%$) and of the rear mirror, respectively, and D is the optical density of the filter in use. The front-end reflectance, in the absence of an external output coupler, is

$$r_2 = \frac{2r}{1+r} \approx 9.5\% . \qquad (5\text{-}26)$$

When an external fused-silica flat is used as an additional output coupling element,

$$r_2 = \frac{4r}{1+3r} \approx 17.4\% . \qquad (5\text{-}27)$$

Similarly, when a mirror of reflectance R_2 is used,

$$r_2 = \frac{2r+(1-3r)R_2}{1+r-2rR_2} . \qquad (5\text{-}28)$$

Results of optical pulse measurements, taken with in-cavity attenuators, have already been presented in Figs.3-45, 3-47 and 3-49. Of particular interest here are the "flat-topped" pulse (Fig.3-45) observed using a He/0.5% Xe/0.2% HCl mixture at 2880-Torr operating pressure, a 35-kV charging voltage, and a 1.65-cm electrode separation.

For each measurement, the output power is determined directly from Fig.3-45. The scaling factor is calculated using the "flat-topped" pulse shown in Fig.5-11. The curve calculated using Eqs.(5-23) and (5-24) is carefully fitted to the experimental data shown in Fig.5-13. For the particular discharge mixture used; and for ℓ=50 cm and A=1.05 cm^2, g_0=0.50 cm^{-1}, α_0=0.038 cm^{-1} and Φ_s=0.462 MW/cm^2. The model yields g_0=0.616 cm^{-1}, α_0=0.033 cm^{-1} and Φ_s=0.570 MW/cm^2, as given in Table 5-7. The two sets of parameters agree to better than 20%, which is within the experimental error. Note that the saturation irradiance determined from experimental data is somewhat lower than the calculated value. The difference in Φ_s may be due to absorption in the laser windows, which is not included in the saturation theory.

The values of the laser parameters (g_0, α_0 and Φ_s) are very sensitive to the shape of the curve (such as Fig.5-13) and consequently to experimental errors in power measurements. However, the values are relatively insensitive to the absolute powers represented by the curve (see also Ref.[267]). Therefore, the calculation of reliable laser parameters requires relative power measurements considerably more accurate than absolute power measurements.

5.6 Discussion

The kinetic model developed in this chapter is generally applicable for evaluating the performance of a discharge-excited XeCl laser system, and for determining the laser parameters. The results of kinetic calculations, shown in Figs.5-10 to 5-12, are in good agreement with experimental observations, in terms of total energy, peak power,

Fig. 5-13

Application of gain-saturation theory to the determination of laser parameters. Output power is plotted as a function of the cavity loss factor ($-\ell n\sqrt{r_1 r_2}$). The solid curve calculated using Eqs. (5-23) and (5-24) is fitted to the experimental data (o), obtained for a He/0.5% Xe/0.2% HCl laser mixture at a 2880-Torr operating pressure, a 35-kV charging voltage and a 1.65-cm electrode separation.

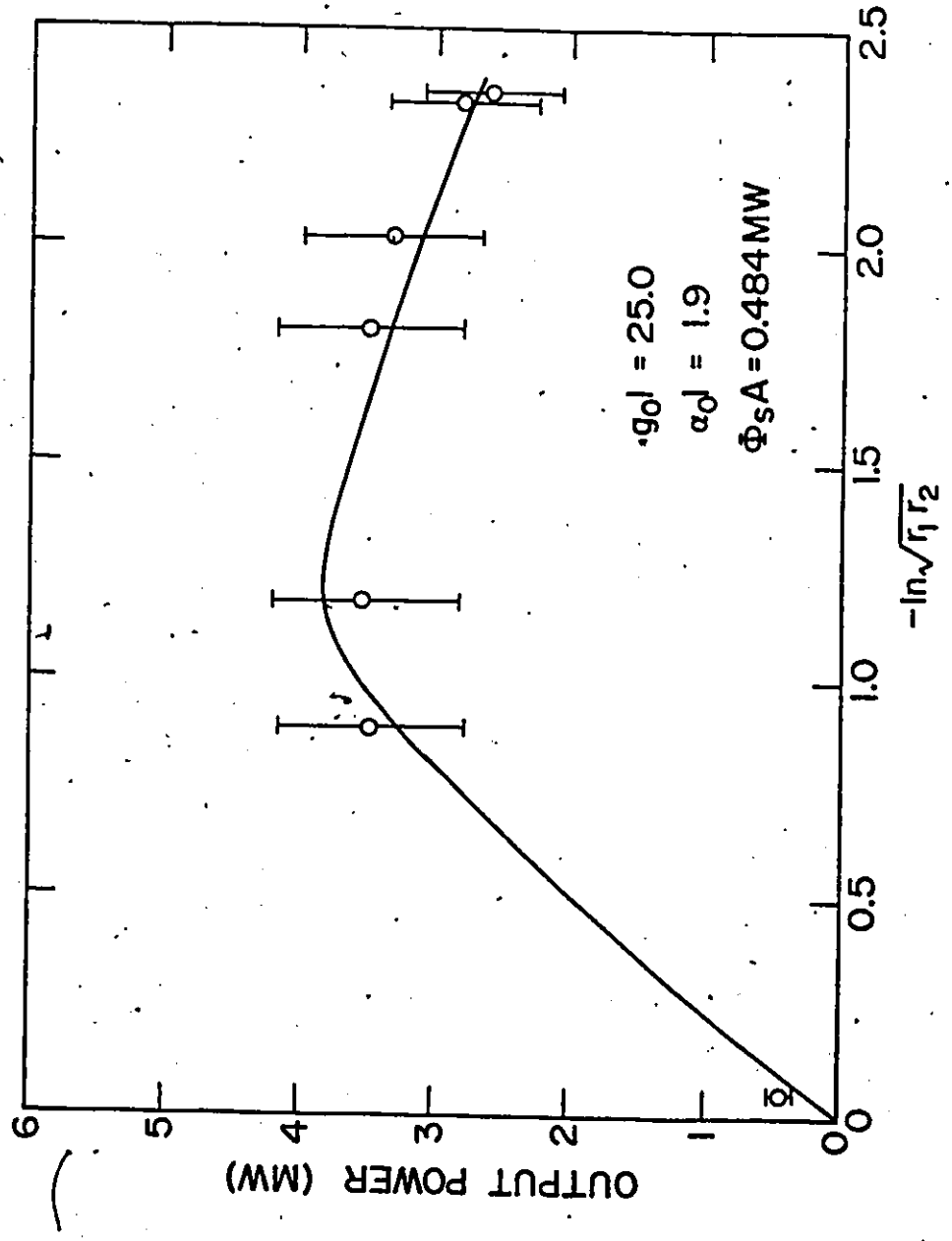
OUTPUT POWER (MW)
0
1
2
3
4
5
6
0
0.5
1.0
1.5
2.0
2.5
$-\ln\sqrt{r_1 r_2}$
$g_0 l = 25.0$
$\alpha_0 l = 1.9$
$\Phi_s A = 0.484\,MW$

pulse-duration, delay to onset of emission, and rise- and fall-times. In addition, the results of these calculations are also in good agreement with the gain and absorption coefficients, and with the saturation irradiance, which are all experimentally-derived results based on gain-saturation theory. Furthermore, the theoretical laser efficiency η_L, defined by Eq.(5-29) below, is ~0.31%, which is in excellent agreement with the experimental efficiency of ~0.32% given in Fig.3-11(e). This comparison employs a He/0.5% Xe/0.2% HCl mixture at a 2957-Torr pressure, a 35-kV charging voltage and a 1.65-cm electrode separation. The laser efficiency is given by

$$\eta_L = \eta_Q \, \eta^* \, \eta_{elec} \, \eta_{ex} \quad . \tag{5-29}$$

The quantum efficiency (η_Q) for the XeCl B → X emission, defined in Chapter 2 (p.42), is 48.4%. The exciplex production efficiency (η^*) is the ratio of the $XeCl^*$ energy to the total energy of all excited and ionic species, including electrons. According to the kinetic results in Fig.5-2, and using the energy-exchange values listed in Table 5-4, $\eta^* \approx 3.4\%$. The electrical efficiency (η_{elect}) is the fractional amount of energy in the storage capacitor deposited into the laser discharge. From Fig.3-34, $\eta_{elect} \sim 35$ J/58 J ≈ 60%. In addition, the power extraction efficiency, calculated using [266]

$$\eta_{ex} = \frac{P}{\Phi_s A g_0 \ell} \quad , \tag{5-30}$$

has a maximum value of ~~~31.9%~~. This is based on the data on page 254 and the maximum power (P) taken from Fig.5-13.

Exciplex quenching by electrons and by rare gases are, in part,

responsible for the relatively low exciplex production efficiency. Under the above discharge conditions (high E/p), electrons are present in high concentration (typically $\sim 2.5 \times 10^{15}$ cm^{-3}), and electron collisions with $XeCl^*$ are frequent. In addition, the exciplex species are removed by dominant three-body association with Xe atoms to form the triatomic exciplex species Xe_2Cl^*. The Xe_2Cl^* density ($\gtrsim 2 \times 10^{15}$ cm^{-3}) is calculated to be higher than the exciplex population. The total rate for the depopulation of the upper emitting state ($XeCl^*$) is $\sim 5.8 \times 10^8$ s^{-1}, and of the ground state (XeCl) is $\sim 3.0 \times 10^8$ s^{-1}. The relatively slow removal of the ground state results in a relatively low $\Delta N \sim 2.3 \times 10^{14}$ cm^{-3}, derived from Fig.5-2(a). Even though the inversion density is ~12% of the exciplex population density, the optical gain associated with the XeCl system is still high because of the large stimulated-emission cross-section.

CHAPTER 6

CONCLUSIONS

Details of the research carried out for this thesis, are presented in the preceeding chapters. In summary, we have developed a comprehensive understanding of the XeCl laser system, which is based on experimental observations and on the formulation of a successful kinetic model for evaluating the overall laser operation. The main conclusions resulting from the research are listed below.

1. The XeCl ground $X\ ^2\Sigma^+_{1/2}$ state has a well-depth of 298.46 cm^{-1} which includes a total of 23 vibrational levels. These are determined using a new potential energy (P.E.) function which is capable of reproducing the experimentally-derived data of Sur et al. [44] to within ~1% accuracy, and demonstrating the "superharmonic" nature of the ground-state molecule. In essence, this new P.E. function is a van der Waals (r^{-6}) potential distorted by a logarithmic-type ($-\ell n\, r/r$) field, and believed to be the first P.E. function applicable to describing an ionic-covalent mixed state.

2. As a result of the Franck-Condon calculations carried out for the radiative $B \rightarrow X$ transition in XeCl, the effective lifetime of the transition and the cross-section for stimulated emission, are estimated to be 35 ns and 2.35 $\mathring{A}^2$, respectively. These estimates are dependent on the value for the electronic transition moment, which is still not known accurately. In addition, the calculations predict that

the strongest emission should be the 0-2 vibrational band of the electronic transition, and not the 0-1 band observed in our experiments. This discrepancy may be attributed to the relatively rapid depopulation of the v" = 1 level of the ground state.

3. In accordance with the molecular structure of XeCl, the exciplex molecules in the B $^2\Sigma^+_{1/2}$ state are primarily formed through the ionic channel in which Xe^+ and Cl^- are recombined. However, two other formation channels are also found to be important. These stem from the curve-crossings of the two lowest Rydberg and the excimer B states, at which locations the "harpooning" reactions involving the Rydberg molecules Xe ($^3P_2$) · Cl ($^2P_{3/2}$) and Xe ($^3P_1$) · Cl ($^2P_{3/2}$) take place. In addition to being the entrance channels for $XeCl^*$, these two formation channels are also exit channels for exciplex predissociation. Therefore, the two Rydberg channels effectively delay the relaxation of the exciplex molecules (formed by ionic recombination) to the lowest vibrational level. Consequently, high optical gain can be maintained for relatively long duration, even though the ion densities may be low.

4. Laser output experiments, using a photo-preionized avalanche-discharge system, have been performed employing a range of He/Xe/HCl mixtures and excitation conditions. The laser system is designed for operation at gas pressures up to 30 atm, with an active volume of 42-83 cm^3, and for charging voltages below 35 kV. Optimum optical output is usually achieved when the laser cavity consists of a rear 98% external reflector and the front laser window as the output coupler. An output energy of ~200 mJ, in an almost flat-topped optical pulse with 60-ns

duration (FWHM), has been extracted from the laser system employing a He/0.5% Xe/0.2% HCl mixture at 2880-Torr pressure, 35-kV charging voltage and 1.65-cm electrode separation. In general, the following laser characteristics have been observed.

(i) High efficiency requires relatively large electrode separation at high charging voltage, and relatively small electrode separation at low charging voltage.

(ii) As the electrode separation is increased, the optimum operating pressure decreases. Typical E/p_0 values at gas breakdown are ~4.5-6.0 V/cm-Torr for a He/1.0% Xe/0.2% HCl mixture and ~5.5-7.0 V/cm-Torr for a He/2.5% Xe/0.2% HCl mixture.

(iii) In order to produce maximum energy, the HCl concentration in a He/Xe/HCl mixture is slightly less than 0.2%. As the ratio of HCl to He increases (or decreases), the optimum gas pressure decreases (or increases) but at reduced energy output. The output energy changes more rapidly with HCl concentration than with total pressure (principally He concentration). This is a consequence of the exciplex quenching rate due to HCl being larger than that due to He.

(iv) A system employing a mixture with a high Xe content is usually efficient because a large number of exciplex species can be formed. However, the optimum gas pressure is reduced with increasing Xe concentration in order to reduce exciplex quenching by Xe.

(v) For a 1.65-cm electrode separation, and at high energy input and optimum operating pressure, the He/0.5% Xe/0.2% HCl mixture provides

higher output energy than the He/5.0% Xe/0.2% HCl mixture. This difference can be attributed to reduced exciplex quenching (at lower Xe concentration) by electrons which are formed together with xenon ions. With suitable data, exciplex quenching by Xe and by electrons can be distinguished.

(vi) Both output peak power and pulsewidth increase with input energy. The peak power depends on the gas mixture, and increases with Xe content. During operation at a low pressure, the peak power is reduced and the pulse duration is long. However, the system efficiency may be low because the output saturates very rapidly.

5. A Monte-Carlo procedure has been applied to study electron transport in He/Xe/HCl mixtures. In addition to electron scatterings by ground-state gas particles (He, Xe and HCl), the procedure considers electron-electron scattering which makes an important contribution in our experiments. Using the results obtained from a series of Monte-Carlo simulations, we derive electron-energy distribution functions which are then used to determine rate coefficients for electron collision processes. Even though electron collisions with excited and ionic particles are neglected in these simulations, the results are still valid for the gas kinetic studies, where the average electron energy is more important than a slightly distorted electron energy distribution.

6. Based on observations of the discharge current, it is found that the primary electrons are mostly generated in the discharge medium as a result of photoionization of He atoms which are present in high concentration. In addition, multi-photon ionization likely takes place

because hard UV radiation (λ < 50 nm) is minimal in the preionization emission.

7. Our elaborate kinetic model takes into account 245 kinetic processes for 34 discharge species (given in Tables 4-2, and 5-1 to 5-3). This comprehensive model is developed on the basis of achieving good agreement between the computed pulseshapes and the observed optical pulses in terms of total energy, peak power, delay time for onset of emission, and rise- and fall-times. The principal results of the modelling are summarized in the following:

(i) The fundamental formation channels of $XeCl^*$ exciplex species are via the three-body recombination of Xe^+ and Cl^-, and the three-body "harpooning" of the $Xe(^3P_2)\cdot Cl(^2P_{3/2})$ and $Xe(^3P_1)\cdot Cl(^2P_{3/2})$ Rydberg molecules.

(ii) The exciplex species are mainly lost in collisional quenching by neutral gas particles. Superelastic quenching by electrons amounts to ~15% of the total depopulation of the exciplex.

(iii) Under "usual" operating conditions, there is only minor absorption of laser radiation by discharge species. However, absorption can be important at high output irradiance and during long-pulse operation. The dominant photoabsorbers are the Cl^- and Xe_2^+ ions, and the triatomic exciplex Xe_2Cl^*.

(iv) There is a relatively slow depopulation of the XeCl ground state, compared to the excimer B state depopulation. As a result, the inversion density is only 2.3×10^{14} cm^{-3}, which can be compared to the exciplex population of $\sim 2 \times 10^{15}$ cm^{-3}.

8. The intrinsic laser parameters (unsaturated gain g_0,

absorption coefficient α_0 and saturation irradiance Φ_s) have been determined by using microscopic kinetic calculations, and by using macroscopic gain-saturation theory employed in conjunction with output power measurements. The usual approach for the latter measurements is to use at least three different output couplers in order to generate adequate data. However, we obtain additional data by inserting in-cavity attenuators (UV-grade neutral density filters) between the rear cavity window and mirror. For the typical He/0.5% Xe/0.2% HCl mixture at 2880-Torr pressure, and a 35-kV charging voltage, the measurements yield $g_0 = 0.50\ cm^{-1}$, $\alpha_0 = 0.038\ cm^{-1}$ and $\Phi_s = 0.462\ MW/cm^2$. These values are in good agreement with $g_0 = 0.616\ cm^{-1}$, $\alpha_0 = 0.033\ cm^{-1}$ and $\Phi_s = 0.570\ MW/cm^2$ calculated using the kinetic model.

On the basis of the generally good agreement between the model calculations and the experimental results, we conclude that the fundamental dynamical processes in a pulsed He/Xe/HCl discharge have been identified. Consequently, the kinetic model can be used to study the dynamics of the XeCl exciplex system, and to evaluate XeCl laser performance over a reasonable range of operating conditions. Note that the present model requires an accurate knowledge of the discharge characteristics and operating conditions. Laser output measurements taken at different times, but without changing the gas mixture, are usually different. These differences are caused by changes in the gas mixture with time. In particular, there is a gradual deterioration of HCl, which is the most reactive component in the gain medium. Moreover, slow processes not included in our model may be important for modelling very long pulses. Therefore, it is hoped that as more and better

information is developed concerning the long-term operation of the XeCl laser system, the kinetic model can be extended to study quasi-continuous or continuous laser behaviour.

The present work would be enhanced by future research, which includes the following experimental topics:

1. The emission spectrum from sliding-spark-array discharges needs to be characterized. This would provide details of the mechanisms leading to photoelectron production.
2. Other preionization sources (e.g., X-rays) should be implemented and investigated. Such research could result in higher laser efficiency and/or increased output energy.
3. Temporal gain and absorption measurements should be carried out. These could then be compared with the results obtained from kinetic model calculations.
4. Methods for improving laser performance should be investigated. It should be possible to increase substantially the present extraction specific energy of ~4 J/ℓ, the total output energy, the output power, the output pulse duration and the laser efficiency. This research may require re-examination of the discharge conditions, the discharge geometry, the excitation circuitry, and the preionization requirements.
5. Investigations should be carried out on quasi-cw or high-repetition-rate operation, and on long-life (per static gas fill) operation.
6. The laser emission characteristics (spectral and temporal) should be investigated for a range of gas temperatures.
7. The behaviour of the triatomic exciplex Xe_2Cl^* in the discharge medium

should be studied by investigating the broad-band emission near 518 nm.

8. The D → X and C → A systems in XeCl should be investigated as particularly important laser transitions.

Further theoretical research may include the following topics:

1. The electron kinetic calculations, using the method of exact Boltzmann solution or the extended-Boltzmann analysis, should be incorporated into the gas kinetic studies. However, additional data are required for the various electron collision cross-sections.
2. The kinetic model could include the multi-pass analysis of the laser irradiance. This could provide further detail in the computed optical output pulses.
3. The model should be applied to systems considerably different in size and/or operating condition. An example is a miniature XeCl laser.
4. The theoretical spectral analysis should be extended to higher electronic states in the XeCl molecule, particularly the C, the D and the two lowest-lying Rydberg states.
5. The new P.E. function for the XeCl ground state could be applied to characterization of other RGH ground states.

APPENDIX A

A POTENTIAL FUNCTION FOR AN IONIC-COVALENT MIXED STATE

We propose the existence of a potential-field, represented by

$$U(r) = - \exp(1)\, D_e\, \ell n(r/r_0)/(r-r_0) \quad , \tag{A-1}$$

which is characteristically repulsive at close internuclear distances on the left of the equilibrium position ($r_e = r_0 \exp(1)$). This field has a relatively shallow and a very broad well, resembling that of a dissociative state of a weakly-bound ionic molecule. More generally, the amalgamation of a high-order van der Waals field with this new field, i.e.,

$$U(r) = - n \exp(1)\, D_e\, \ell n(r/r_0)/(r-r_0)^n \quad , \tag{A-2}$$

makes the existing van der Waals field more repulsive, draws the equilibrium position much closer ($r_e = r_0 \exp(1/n)$), and produces considerable enhancement of molecular dissociation. All these features correspond to the properties of an ionic-covalent mixed state. Furthermore, the potential function given by Eq.(2-6) can be put in the form

$$U(r) = - D_e \left\{ \frac{a' \ell n\, y}{y^n} + \frac{(b' \cdot \ell n\, y + 1)}{y^p} \right\} \quad , \tag{A-3}$$

where $a' = -a$ and $b' = -b$. This results in an interaction force

$$F(r) = \frac{D_e}{r_e} \left\{ \frac{a'(1 - n \ln y)}{y^{n+1}} + \frac{b'(1 - p \ln y)}{y^{p+1}} - \frac{p}{y^{p+1}} \right\} \quad . \qquad (A\text{-}4)$$

For $r > r_e$, Eq.(A-4) is expected to have a quasi van der Waals behaviour, as can be seen from the following: near equilibrium,

$$F(r \simeq r_e) \simeq \frac{D_e}{r_e} \left\{ \frac{a'}{y^{n+1}} + \frac{b'-p}{y^{p+1}} \right\} \quad , \qquad (A\text{-}5)$$

and at long range

$$F(r >> r_e) \sim \frac{D_e}{r_e} \left\{ \frac{a'}{y^n} + \frac{b'}{y^p} \right\} \left(- \frac{\ln y}{y} \right) \quad . \qquad (A\text{-}6)$$

At short distances, the 'logarithmic' repulsion dominates.

APPENDIX B

AN EXACTLY SOLVABLE WAVE EQUATION FOR A REPULSIVE POTENTIAL

The potential function used in the calculation has the form

$$U(r) = v \exp(-\alpha r) \quad , \tag{B-1}$$

where v and α assume large values for steeply repulsive interactions. This results in the wave equation

$$-\frac{\hbar^2}{2\mu}\frac{d^2\psi}{dr^2} + v \exp(-\alpha r)\,\psi = E\psi \quad , \tag{B-2}$$

where the turning point is located at $r_0 = \alpha^{-1}\,\ell n(v/E)$ and $0 < E << v$. The required wavefunction has the properties that $\psi(r=0) = 0$ and that it is oscillatory[†] at large distances.

Exact Treatment

Upon replacing the wavefunction by

$$\varphi = \psi \exp(-\alpha r/4) \quad , \tag{B-3}$$

and introducing a new variable

$$z = [32\mu v/(\hbar^2\alpha^2)]^{1/2} \exp(-\alpha r/2) \quad , \tag{B-4}$$

[†] It should be noted that $\frac{d\psi}{dr}\big|_{r=0}$ does not vanish, but approaches a very small value as v is made large. The usual requirements for ψ are still satisfied.

Eq.(B-2) can be written in the recognizable form

$$\frac{d^2\varphi}{dz^2} + \left[-\frac{1}{4} + \left(\frac{1}{4} + \frac{8\mu E}{\hbar^2\alpha^2}\right)\frac{1}{z^2}\right]\varphi = 0 \quad ; \tag{B-5}$$

which is commonly known as the Whittaker equation [268]. The general solution, in terms of Whittaker functions, is

$$\varphi(z) = c_1 M_{0,i\beta}(z) + c_2 M_{0,-i\beta}(z) \quad ; \tag{B-6}$$

where c_1 and c_2 are constants, and

$$\beta \equiv [8\mu E/(\hbar^2\alpha^2)]^{1/2} \quad . \tag{B-7}$$

The Whittaker functions, which can be put into an integral form and evaluated, are

$$M_{0,i\beta}(z) = \frac{z^{i\beta+1/2}\ 2^{-i2\beta}}{B(i\beta+1/2, i\beta+1/2)} \int_{-1}^{1} (1-t^2)^{i\beta-1/2}\ e^{zt/2}\ dt$$

$$= I_0(z/2) + 2\sum_{m=1}^{\infty} I_{2m}(z/2)\ \frac{(-1)^m\ B(i\beta+1, i\beta+1)}{B(i\beta+1+m, i\beta+1-m)} \quad , \tag{B-8}$$

where B and I are the Beta function and the modified Bessel function. Note that

$$\frac{B(i\beta+1, i\beta+1)}{B(i\beta+1+m, i\beta+1-m)} = (1+m^2/\beta^2)^{-1/2}\ \exp(i\delta'_m) \quad , \tag{B-9}$$

and

$$\delta'_m \equiv \tan^{-1}\left(\frac{m}{\beta}\right) + 2\sum_{k=1}^{m-1} \tan^{-1}\left(\frac{k}{\beta}\right) \tag{B-10}$$

so that the reduced solution can be written as

$$\varphi(z) = N' z^{1/2}\{I_0(z/2)\sin(\beta \ln z+\delta_0) + 2\sum_{m=1}^{\infty}(-1)^m I_{2m}(z/2)(1+m^2/\beta^2)^{-1/2}\sin(\beta \ln z+\delta_m)\} \quad , \quad (B\text{-}11)$$

where N' and δ_0 are constants, and $\delta_m \equiv \delta_0 + \delta_m'$.

In its final form, the wave function for the repulsive potential is

$$\psi(r) = N \{I_0[\gamma \exp(-\alpha r/2)]\sin(\varepsilon_0-\alpha\beta r/2) + 2\sum_{m=1}^{\infty}(-1)^m I_{2m}[\gamma \exp(-\alpha r/2)](1+m^2/\beta^2)^{-1/2}\sin(\varepsilon_m-\alpha\beta r/2)\} , \quad (B\text{-}12)$$

with $\gamma \equiv [8\mu v/(\hbar^2\alpha^2)]^{1/2}$,

$\varepsilon_0 \equiv \delta_0 + \beta \ln(2\gamma)$,

and $\varepsilon_m = \varepsilon_0 + \delta_m'$. (B-13)

To the right of the turning point ($r > r_0$), the re-defined normalization factor, $N \equiv N'(2\gamma)^{1/2}$, can take the value calculated at a very large distance, namely,

$$N = (\alpha\beta\pi/2)^{-1/2} = (2\mu E\pi/\hbar^2)^{-1/2} \quad . \quad (B\text{-}14)$$

The phase lag ε_0 is evaluated from

$$\tan \varepsilon_0 = -2\sum_{m=1}^{\infty}(-1)^m(1+m^2/\beta^2)^{-1/2}\sin \delta_m' \Big/ [1 + 2\sum_{m=1}^{\infty}(-1)^m(1+m^2/\beta^2)^{-1/2} \cos \delta_m'] \quad . \quad (B\text{-}15)$$

Approximate Treatment

Three separate regions are investigated below. These are on the right of ($r \to \infty$), on the left of ($r \to 0$), and near the turning point ($r \simeq r_0$).

(i) $r \to \infty$

As the potential curve approaches its asymptote to the separated atom limit, the wavefunction is essentially free from perturbation by the external potential. As Eq.(B-12) indicates,

$$\psi(r) \sim (2\mu E\pi/\hbar^2)^{-1/2} \sin[\varepsilon_0 - (2\mu E/\hbar^2)^{1/2} r] \quad . \tag{B-16}$$

An alternate derivation, using the fact that $E \gg U(r)$, gives

$$-\frac{\hbar^2}{2\mu} \frac{d^2\psi}{dr^2} \simeq E\psi \quad . \tag{B-17}$$

In the above limit, high-order contributions to ψ are unimportant since the functions I_{2m} become very small compared to I_0, which approaches unity. This is typical of an unbound-state situation.

(ii) $r \to 0$

In this case, analysis of Eq.(B-12) is complicated by the series representation of ψ, and by the amount of computation required to evaluate ε_0. Alternately, the wave equation (B-2) can be re-examined by letting $v \exp(-\alpha r) \simeq v(1-\alpha r)$. Thus,

$$\psi(r) = \text{constant} \times \{Ai[(\frac{2\mu v}{\hbar^2\alpha^2})^{1/3}(\frac{v-E}{v} - \alpha r)]/Ai[(\frac{2\mu v}{\hbar^2\alpha^2})^{1/3}(\frac{v-E}{v})]$$

$$- \mathrm{Bi}[(\frac{2\mu v}{\hbar^2\alpha^2})^{1/3}(\frac{v-E}{v} - \alpha r)]/\mathrm{Bi}[(\frac{2\mu v}{\hbar^2\alpha^2})^{1/3}(\frac{v-E}{v})]\} \tag{B-18}$$

and is characterized by the Airy functions Ai and Bi.

In the semi-classical approximation, for $E << V(r)$,

$$\psi(r) \longrightarrow [2\mu v \exp(-\alpha r)/\hbar^2]^{-1/4} \exp\{-[8\mu/(\hbar^2\alpha^2)]^{1/2}(v^{1/2}-E^{1/2})\}$$

$$x \sinh\{[8\mu v/\hbar^2\alpha^2]^{1/2}[1-\exp(-\alpha r/2)]\} \quad , \tag{B-19}$$

which grows hyperbolically to the turning point in agreement with Eq.(B-18).

(iii) $r \simeq r_0$

The wave equation (B-2) takes the simple form

$$\frac{d^2\psi}{dr^2} + k^2\alpha(r-r_0)\psi = 0 \quad , \tag{B-20}$$

where $k \equiv (2\mu E/\hbar^2)^{1/2}$ and $\{1- \exp[-\alpha(r-r_0)]\} \simeq \alpha(r-r_0)$. Letting $y = (k^2\alpha)^{1/3}(r-r_0)$, Eq.(B-20) becomes

$$\frac{d^2\psi}{dy^2} + y\psi = 0 \quad , \tag{B-21}$$

which is the Airy equation, yielding the general solution

$$\psi(r) = c_1\, \mathrm{Ai}[-(k^2\alpha)^{1/3}(r-r_0)] + c_2\, \mathrm{Bi}[-(k^2\alpha)^{1/3}(r-r_0)] \quad , \tag{B-22}$$

where c_1 and c_2 are constants. In an alternate form, Eq.(B-20) can be

solved by Laplace transform techniques to give

$$\psi(r) = c_1\, Hi[-(k^2\alpha)^{1/3}(r-r_0)] + c_2\, Hi[\exp(i\pi/6)(k^2\alpha)^{1/3}(r-r_0)]$$
$$+ c_3\, Hi[\exp(-i\pi/6)(k^2\alpha)^{1/3}(r-r_0)] \quad , \qquad \text{(B-23)}$$

where $$c_1 = \frac{\pi}{3^{1/3}}\left[\frac{\psi(r_0)}{\Gamma(1/3)} - \frac{\psi'(r_0)}{3^{1/3}\Gamma(2/3)}\right] ,$$

$$c_2 = \frac{\pi}{2\cdot 3^{1/3}}\left\{\left[\frac{2}{\Gamma(1/3)} + \frac{1}{i3^{1/3}\Gamma(2/3)}\right]\psi(r_0) + \left[\frac{1}{3^{1/3}\Gamma(2/3)}\right]\psi'(r_0)\right\} ,$$

and $$c_3 = \frac{\pi}{2\cdot 3^{1/3}}\left\{\left[\frac{2}{\Gamma(1/3)} + \frac{1}{i3^{1/3}\Gamma(2/3)}\right]\psi(r_0) + \left[\frac{1}{3^{1/3}\Gamma(2/3)}\right]\psi'(r_0)\right\} . \qquad \text{(B-24)}$$

Here ψ' is the first derivative of ψ with respect to r, and Hi is the related Airy function [268].

APPENDIX C

FRANCK-CONDON FACTORS AND DENSITIES FOR THE XeCl B → X SYSTEM

V1	V2	WAVENUMBER CM**(-1)	WAVELENGTH (VACUO) NM	WAVELENGTH (AIR) NM	FRANCK-CONDON FACTOR	FRANCK-CONDON DENSITY CM
0	0	32494.5	307.744	307.655	1.11E-01	3.39E-03
	1	32466.7	308.008	307.919	2.07E-01	6.31E-03
	2	32439.0	308.272	308.177	2.66E-01	8.09E-03
	3	32411.3	308.536	308.436	2.47E-01	7.52E-03
	4	32383.6	308.801	308.701	1.80E-01	5.47E-03
	5	32355.9	309.065	308.965	1.10E-01	3.37E-03
	6	32328.2	309.330	309.229	5.43E-02	1.66E-03
	7	32300.5	309.594	309.493	2.17E-02	6.62E-04
	8	32272.8	309.859	309.758	6.95E-03	2.12E-04
	9	32245.1	310.123	310.022	1.75E-03	5.34E-05
1	10	32217.4	310.388	310.287	3.46E-04	1.06E-05
	11	32189.7	310.653	310.552	5.61E-05	1.72E-06
	12	32162.0	310.917	310.816	7.61E-06	2.33E-07
	13	32134.3	311.182	311.081	8.74E-07	2.68E-08
	14	32106.6	311.447	311.345	8.61E-08	2.64E-09
	15	32078.9	311.712	311.610	7.46E-09	2.29E-10
	16	32051.2	311.977	311.875	5.61E-10	1.72E-11
	17	32023.5	312.242	312.140	3.74E-11	1.15E-12
	18	31995.8	312.507	312.405	2.19E-12	6.73E-14
	19	31968.1	312.772	312.670	1.14E-13	3.51E-15
	20	31940.4	313.037	312.935	5.34E-15	1.64E-16
2	0	32681.0	305.988	305.899	9.01E-02	2.98E-03
	1	32653.2	306.249	306.160	6.73E-02	2.24E-03
	2	32625.5	306.509	306.416	9.21E-03	3.07E-04
	3	32599.8	306.750	306.661	9.41E-03	3.15E-04
	4	32575.0	306.984	306.894	6.42E-02	2.15E-03
	5	32551.8	307.203	307.113	1.13E-01	3.79E-03
	6	32530.2	307.405	307.317	1.38E-01	4.63E-03
	7	32510.4	307.594	307.505	1.27E-01	4.26E-03
	8	32492.3	307.765	307.676	9.96E-02	3.34E-03
	9	32475.9	307.920	307.831	6.94E-02	2.33E-03
	10	32461.3	308.059	307.970	4.42E-02	1.48E-03
	11	32448.6	308.180	308.092	2.65E-02	8.91E-04
	12	32437.2	308.288	308.199	1.43E-02	4.82E-04
	13	32427.5	308.380	308.291	7.45E-03	2.50E-04
	14	32419.4	308.457	308.368	3.96E-03	1.33E-04
	15	32412.7	308.521	308.431	1.91E-03	6.42E-05
	16	32407.6	308.571	308.482	8.44E-04	2.83E-05
	17	32403.3	308.610	308.521	4.02E-04	1.35E-05
	18	32400.4	308.638	308.549	1.77E-04	5.95E-06
	19	32399.4	308.648	308.558	7.89E-05	2.65E-06
	20	32397.1	308.669	308.580	3.30E-05	1.10E-06

V1	V2	WAVENUMBER CM**(-1)	WAVELENGTH (VACUO) NM	WAVELENGTH (AIR) NM	FRANCK-CONDON FACTOR	FRANCK-CONDON DENSITY CM
2	0	32963.5	304.289	304.200	9.51E-02	3.44E-03
	1	32835.7	304.547	304.458	5.93E-02	2.14E-03
	2	32808.5	304.799	304.711	4.82E-03	1.80E-04
	3	32782.4	305.042	304.954	4.93E-03	1.93E-04
	4	32757.6	305.273	305.184	1.51E-02	5.96E-04
	5	32734.3	305.490	305.401	6.75E-02	2.70E-03
	6	32712.8	305.691	305.602	9.44E-02	4.00E-03
	7	32692.9	305.877	305.788	2.44E-01	1.06E-02
	8	32674.8	306.046	305.957	1.44E-01	6.58E-03
	9	32658.5	306.198	306.111	2.00E-01	9.28E-03
	10	32644.8	306.336	306.248	1.27E-01	5.98E-03
	11	32633.0	306.459	306.369	4.94E-02	2.36E-03
	12	32619.7	306.583	306.474	9.92E-03	4.78E-04
	13	32610.0	306.674	306.565	4.60E-03	2.23E-04
	14	32601.9	306.730	306.642	3.98E-03	1.96E-04
	15	32595.3	306.793	306.704	3.25E-03	1.61E-04
	16	32589.9	306.844	306.754	2.64E-03	1.32E-04
	17	32585.8	306.882	306.792	1.88E-03	9.48E-05
	18	32582.9	306.910	306.820	1.33E-03	6.73E-05
	19	32580.9	306.924	306.839	8.24E-04	4.17E-05
	20	32579.7	306.940	306.851	4.46E-04	2.26E-05
3	0	33042.9	302.637	302.548	7.89E-02	2.93E-03
	1	33015.1	302.892	302.804	1.55E-02	5.74E-04
	2	32947.8	303.142	303.054	8.08E-03	3.02E-04
	3	32961.7	303.347	303.256	4.44E-03	1.74E-04
	4	32936.9	303.611	303.522	4.73E-03	1.97E-04
	5	32913.7	303.826	303.737	2.44E-03	1.02E-04
	6	32892.1	304.024	303.936	5.50E-03	2.36E-04
	7	32872.3	304.204	304.119	4.78E-05	2.06E-06
	8	32854.2	304.370	304.287	1.23E-03	5.32E-05
	9	32837.8	304.522	304.438	2.39E-03	1.03E-04
	10	32823.2	304.657	304.574	2.39E-03	1.03E-04
	11	32810.5	304.774	304.694	1.72E-03	7.48E-05
	12	32799.7	304.887	304.798	2.41E-03	1.05E-04
	13	32790.8	304.970	304.883	1.74E-03	7.58E-05
	14	32783.8	305.035	304.948	1.11E-03	4.85E-05
	15	32778.7	305.082	304.995	7.25E-04	3.16E-05
	16	32775.4	305.113	305.025	4.77E-04	2.08E-05
	17	32773.9	305.127	305.039	2.77E-04	1.21E-05
	18	32774.0	305.126	305.038	1.43E-04	6.24E-06
	19	32775.8	305.109	305.021	6.44E-05	2.81E-06
	20	32779.2	305.078	304.990	2.61E-05	1.14E-06

V1	V2	WAVENUMBER CM**(-1)	WAVELENGTH (VACUO) NM	WAVELENGTH (AIR) NM	FRANCK-CONDON FACTOR	FRANCK-CONDON DENSITY CM
4	0	33219.5	301.023	300.941	7.33E-03	2.64E-03
4	1	33209.4	301.114	301.214	4.55E-03	1.76E-03
4	2	33199.4	301.204	301.440	1.49E-02	5.54E-04
4	3	33189.3	301.295	301.678	2.66E-02	1.04E-03
4	4	33179.3	301.386	301.303	7.43E-03	2.98E-03
4	5	33169.3	301.477	302.116	4.13E-04	1.63E-04
4	6	33159.2	301.568	302.313	1.65E-02	7.26E-03
4	7	33149.2	301.659	302.494	4.46E-03	2.00E-03
4	8	33139.1	301.750	302.660	2.04E-03	9.31E-04
4	9	33129.1	301.841	302.810	2.91E-02	1.38E-03
4	10	33119.0	301.932	302.944	1.99E-02	1.45E-03
4	11	33109.0	302.023	303.043	1.14E-02	9.32E-04
4	12	33098.9	302.114	303.166	6.20E-03	5.64E-04
4	13	33088.8	302.205	303.255	2.91E-03	3.28E-04
4	14	33078.8	302.296	303.329	1.22E-03	1.65E-04
4	15	33068.7	302.387	303.391	4.58E-04	7.67E-05
4	16	33058.7	302.478	303.440	4.06E-05	1.19E-05
4	17	33048.6	302.569	303.477	8.44E-06	1.68E-06
4	18	33038.6	302.660	303.505	1.16E-06	3.44E-07
4	19	33028.5	302.751	303.523	6.62E-08	7.35E-08
4	20	33018.5	302.842	303.534	6.62E-08	7.62E-08
5	0	33393.6	299.459	299.372	3.82E-02	1.37E-03
5	1	33383.5	299.550	299.621	4.48E-04	1.62E-05
5	2	33373.5	299.641	299.766	2.41E-02	9.02E-04
5	3	33363.4	299.732	300.101	1.71E-02	6.70E-04
5	4	33353.4	299.823	300.325	9.50E-04	3.96E-05
5	5	33343.3	299.914	300.534	3.26E-03	1.44E-04
5	6	33333.3	300.005	300.730	9.08E-03	4.34E-04
5	7	33323.2	300.096	300.909	7.42E-03	3.91E-04
5	8	33313.2	300.187	301.073	2.33E-03	1.38E-04
5	9	33303.1	300.278	301.222	6.02E-04	3.29E-05
5	10	33293.1	300.369	301.354	1.97E-03	1.14E-04
5	11	33283.0	300.460	301.472	5.13E-03	4.25E-04
5	12	33273.0	300.551	301.574	8.42E-03	8.07E-04
5	13	33262.9	300.642	301.662	1.03E-02	1.16E-03
5	14	33252.9	300.733	301.735	1.07E-02	1.45E-03
5	15	33242.8	300.824	301.796	9.84E-03	1.65E-03
5	16	33232.8	300.915	301.845	8.32E-03	1.78E-03
5	17	33222.7	301.006	301.882	6.50E-03	1.85E-03
5	18	33212.7	301.097	301.909	4.84E-03	1.90E-03
5	19	33202.6	301.188	301.927	3.47E-03	1.92E-03
5	20	33192.6	301.279	301.938	2.41E-03	1.92E-03
5	21	33182.5	301.370	301.943	1.66E-03	1.91E-03

V1	V2	WAVENUMBER CM**(-1)	WAVELENGTH (VACUO) NM	WAVELENGTH (AIR) NM	FRANCK-CONDON FACTOR	FRANCK-CONDON DENSITY CM
6	0	33565.3	297.826	297.840	2.75E-02	9.86E-04
6	1	33537.6	298.173	298.087	3.56E-03	1.29E-04
6	2	33510.3	298.416	298.329	1.08E-02	7.04E-04
6	3	33484.2	298.649	298.562	2.83E-03	1.91E-04
6	4	33459.4	298.870	298.783	4.16E-03	1.73E-04
6	5	33436.2	299.077	298.991	1.70E-02	7.60E-04
6	6	33414.6	299.270	299.184	1.72E-02	8.28E-04
6	7	33394.7	299.448	299.361	8.00E-03	4.26E-04
6	8	33376.6	299.611	299.524	1.35E-03	7.34E-05
6	9	33360.5	299.754	299.671	8.30E-05	5.37E-06
6	10	33345.7	299.889	299.802	1.56E-03	1.01E-04
6	11	33332.8	300.005	299.918	2.94E-03	2.04E-04
6	12	33321.5	300.106	300.019	2.33E-03	2.47E-04
6	13	33311.9	300.193	300.106	1.45E-03	2.19E-04
6	14	33303.8	300.266	300.179	6.85E-04	1.21E-04
6	15	33297.1	300.326	300.239	2.06E-04	2.79E-05
6	16	33291.8	300.374	300.287	1.33E-04	2.22E-05
6	17	33287.7	300.411	300.324	7.89E-04	1.69E-04
6	18	33284.7	300.438	300.351	4.42E-04	1.26E-04
6	19	33282.7	300.456	300.369	2.39E-04	9.56E-05
6	20	33281.5	300.467	300.380	1.22E-04	7.77E-05
6	21	33281.1	300.471	300.384	5.74E-05	6.61E-05

V1	V2	WAVENUMBER CM**(-1)	WAVELENGTH (VACUO) NM	WAVELENGTH (AIR) NM	FRANCK-CONDON FACTOR	FRANCK-CONDON DENSITY CM
7	0	33734.9	296.429	296.343	6.01E-03	2.16E-04
7	1	33707.1	296.673	296.587	7.63E-03	2.76E-04
7	2	33679.9	296.913	296.827	6.87E-03	2.57E-04
7	3	33653.8	297.144	297.057	3.00E-04	1.18E-05
7	4	33629.0	297.363	297.276	7.42E-04	3.09E-05
7	5	33605.8	297.568	297.482	5.80E-03	2.55E-04
7	6	33584.2	297.759	297.673	9.80E-03	4.73E-04
7	7	33564.3	297.935	297.849	8.05E-04	4.77E-05
7	8	33546.2	298.096	298.010	5.85E-03	3.40E-04
7	9	33529.9	298.241	298.155	9.93E-03	6.46E-04
7	10	33515.5	298.370	298.285	1.06E-02	7.71E-04
7	11	33502.9	298.483	298.400	8.78E-03	7.14E-04
7	12	33492.3	298.577	298.493	5.01E-03	5.74E-04
7	13	33483.5	298.655	298.571	2.69E-03	4.09E-04
7	14	33476.7	298.716	298.632	1.97E-03	3.98E-04
7	15	33471.8	298.760	298.676	9.90E-04	2.44E-04
7	16	33468.8	298.787	298.703	4.84E-04	1.36E-04
7	17	33467.7	298.797	298.713	4.10E-04	1.36E-04
7	18	33468.5	298.790	298.705	1.97E-04	7.38E-05
7	19	33471.2	298.765	298.681	1.10E-04	4.64E-05
7	20	33475.8	298.724	298.639	4.13E-05	1.85E-05
7	21	33482.3	298.666	298.582	1.41E-05	6.98E-06
7	22	33490.7	298.591	298.507	3.94E-06	2.00E-06
7	23	33501.0	298.499	298.415	1.02E-06	5.47E-07
7	24	33513.2	298.391	298.307	2.24E-07	1.27E-07
7	25	33527.3	298.265	298.181	4.34E-08	2.58E-08
7	26	33543.3	298.123	298.039	7.49E-09	4.70E-09
7	27	33561.2	297.964	297.880	1.19E-09	7.76E-10
7	28	33581.0	297.788	297.704	1.76E-10	1.19E-10
7	29	33602.7	297.596	297.512	2.46E-11	1.71E-11
7	30	33626.3	297.387	297.303	3.26E-12	2.34E-12
7	31	33651.8	297.161	297.077	4.13E-13	3.06E-13
7	32	33679.2	296.919	296.835	5.04E-14	3.85E-14
7	33	33708.5	296.660	296.576	5.94E-15	4.67E-15
7	34	33739.7	296.384	296.300	6.77E-16	5.43E-16
7	35	33772.8	296.092	296.008	7.46E-17	6.06E-17
7	36	33807.8	295.783	295.699	7.94E-18	6.49E-18
7	37	33844.7	295.457	295.373	8.14E-19	6.67E-19
7	38	33883.5	295.115	295.031	8.01E-20	6.57E-20
7	39	33924.2	294.757	294.673	7.51E-21	6.16E-21
7	40	33966.8	294.382	294.298	6.67E-22	5.47E-22
7	41	34011.3	293.990	293.906	5.57E-23	4.57E-23
7	42	34057.7	293.582	293.498	4.34E-24	3.56E-24
7	43	34106.0	293.157	293.073	3.08E-25	2.53E-25
7	44	34156.2	292.716	292.632	1.92E-26	1.58E-26
7	45	34208.3	292.258	292.174	1.01E-27	8.32E-28
7	46	34262.3	291.784	291.700	4.56E-29	3.75E-29
7	47	34318.2	291.293	291.209	1.72E-30	1.42E-30
7	48	34376.0	290.786	290.702	5.38E-32	4.43E-32
7	49	34435.7	290.262	290.178	1.42E-33	1.17E-33
7	50	34497.3	289.722	289.638	3.04E-35	2.51E-35
7	51	34560.8	289.165	289.081	5.19E-37	4.28E-37
7	52	34626.2	288.592	288.508	7.14E-39	5.89E-39
7	53	34693.5	288.002	287.918	7.94E-41	6.55E-41
7	54	34762.7	287.396	287.312	7.34E-43	6.06E-43
7	55	34833.8	286.773	286.689	5.72E-45	4.72E-45
7	56	34906.8	286.133	286.049	3.72E-47	3.07E-47
7	57	34981.7	285.476	285.392	1.98E-49	1.63E-49
7	58	35058.5	284.803	284.719	8.57E-52	7.07E-52
7	59	35137.2	284.113	284.029	2.84E-54	2.34E-54
7	60	35217.8	283.406	283.322	7.15E-57	5.90E-57
7	61	35300.3	282.682	282.598	1.31E-59	1.08E-59
7	62	35384.7	281.942	281.858	1.66E-62	1.37E-62
7	63	35470.9	281.185	281.101	1.37E-65	1.13E-65
7	64	35559.1	280.411	280.327	6.87E-69	5.67E-69
7	65	35649.2	279.620	279.536	1.87E-72	1.54E-72
7	66	35741.2	278.813	278.729	2.21E-76	1.82E-76

V1	V2	WAVENUMBER CM**(-1)	WAVELENGTH (VACUO) NM	WAVELENGTH (AIR) NM	FRANCK-CONDON FACTOR	FRANCK-CONDON DENSITY CM
8	0	33812.5	295.704	295.878	7.58E-03	9.26E-05
8	1	33974.7	294.293	294.467	7.84E-03	9.43E-04
8	2	34137.4	292.888	293.062	1.56E-03	5.89E-05
8	3	34299.6	291.489	291.663	4.07E-03	1.60E-04
8	4	34462.3	290.096	290.269	4.88E-03	1.98E-04
8	5	34625.1	288.708	288.882	3.55E-03	1.48E-04
8	6	34787.8	287.326	287.500	2.57E-03	1.09E-04
8	7	34950.6	285.950	286.123	3.14E-03	1.36E-04
8	8	35113.3	284.579	284.753	5.88E-03	2.66E-04
8	9	35276.1	283.214	283.388	4.99E-03	3.22E-04
8	10	35438.8	281.854	282.027	2.77E-03	1.75E-04
8	11	35601.5	280.500	280.673	6.17E-04	4.29E-05
8	12	35764.3	279.151	279.324	2.54E-05	2.44E-06
8	13	35927.0	277.808	277.980	4.11E-04	4.71E-05
8	14	36089.8	276.470	276.643	1.47E-04	1.47E-05
8	15	36252.5	275.137	275.310	1.57E-03	2.62E-04
8	16	36415.3	273.810	273.983	1.77E-03	3.69E-04
8	17	36578.0	272.488	272.661	1.59E-03	4.64E-04
8	18	36740.8	271.171	271.344	1.27E-03	5.17E-04
8	19	36903.5	269.860	270.032	9.80E-04	5.59E-04
8	20	37066.3	268.554	268.726	5.00E-04	5.76E-04
9	0	34068.0	293.530	293.445	2.20E-03	7.49E-05
9	1	34230.7	292.127	292.042	1.70E-03	6.14E-05
9	2	34393.5	290.730	290.645	2.40E-03	8.96E-05
9	3	34556.2	289.338	289.253	6.36E-03	2.43E-04
9	4	34719.0	287.951	287.866	8.78E-03	3.56E-04
9	5	34881.7	286.570	286.485	1.78E-03	7.33E-05
9	6	35044.5	285.194	285.109	7.34E-03	3.54E-04
9	7	35207.2	283.824	283.739	7.78E-03	4.10E-04
9	8	35370.0	282.459	282.374	3.86E-03	2.24E-04
9	9	35532.7	281.099	281.014	9.56E-04	6.24E-05
9	10	35695.4	279.745	279.660	9.97E-05	7.24E-06
9	11	35858.2	278.396	278.311	9.99E-04	8.34E-05
9	12	36020.9	277.052	276.967	2.40E-03	2.28E-04
9	13	36183.7	275.713	275.628	2.03E-03	2.04E-04
9	14	36346.4	274.380	274.295	2.40E-03	2.48E-04
9	15	36509.2	273.051	272.966	1.33E-03	1.40E-04
9	16	36671.9	271.728	271.643	1.93E-03	2.13E-04
9	17	36834.6	270.410	270.325	1.42E-03	1.62E-04
9	18	36997.4	269.097	269.012	1.05E-03	1.23E-04
9	19	37160.1	267.789	267.704	5.87E-04	7.04E-05
9	20	37322.9	266.486	266.401	2.14E-04	2.63E-05
10	0	34231.7	292.127	292.042	7.74E-03	2.78E-04
10	1	34393.9	290.730	290.645	1.20E-03	4.67E-05
10	2	34556.7	289.338	289.253	8.45E-03	3.16E-04
10	3	34719.5	287.951	287.866	3.12E-03	1.22E-04
10	4	34882.3	286.570	286.485	9.44E-03	3.97E-04
10	5	35045.1	285.194	285.109	7.23E-03	3.23E-04
10	6	35207.9	283.824	283.739	6.82E-03	3.20E-04
10	7	35370.7	282.459	282.374	1.92E-03	9.03E-05
10	8	35533.5	281.099	281.014	1.93E-03	9.91E-05
10	9	35696.3	279.745	279.660	2.79E-03	1.81E-04
10	10	35859.1	278.396	278.311	5.63E-03	4.09E-04
10	11	36021.9	277.052	276.967	6.59E-03	5.46E-04
10	12	36184.7	275.713	275.628	5.77E-03	5.52E-04
10	13	36347.5	274.380	274.295	4.19E-03	4.73E-04
10	14	36510.3	273.051	272.966	2.66E-03	3.55E-04
10	15	36673.1	271.728	271.643	1.55E-03	2.64E-04
10	16	36835.9	270.410	270.325	8.64E-04	1.85E-04
10	17	36998.7	269.097	269.012	4.57E-04	1.30E-04
10	18	37161.5	267.789	267.704	2.34E-04	9.60E-05
10	19	37324.3	266.486	266.401	1.15E-04	7.39E-05
10	20	37487.0	265.188	265.103	5.34E-05	6.15E-05
11	0	34363.6	290.752	290.668	4.48E-03	3.04E-04
11	1	34526.4	289.357	289.273	2.10E-03	7.40E-05
11	2	34689.2	287.967	287.883	8.21E-04	3.07E-04
11	3	34852.0	286.582	286.498	1.24E-04	4.46E-06
11	4	35014.8	285.202	285.118	5.52E-03	2.20E-04
11	5	35177.6	283.827	283.743	8.52E-03	3.80E-04
11	6	35340.4	282.457	282.373	2.66E-03	1.27E-04
11	7	35503.2	281.093	281.009	7.05E-03	3.71E-04
11	8	35666.0	279.733	279.649	2.98E-03	1.73E-04
11	9	35828.8	278.379	278.295	5.44E-03	3.70E-04
11	10	35991.6	277.030	276.946	2.53E-03	1.99E-04
11	11	36154.4	275.686	275.602	1.34E-03	1.12E-04
11	12	36317.2	274.347	274.263	3.93E-04	3.48E-05
11	13	36480.0	273.013	272.929	1.62E-03	1.48E-04
11	14	36642.8	271.684	271.600	5.80E-04	5.43E-05
11	15	36805.6	270.360	270.276	2.88E-04	2.18E-05
11	16	36968.4	269.041	268.957	1.16E-04	8.53E-06
11	17	37131.2	267.727	267.643	4.11E-05	4.10E-05
11	18	37294.0	266.418	266.334	2.88E-04	3.12E-05
11	19	37456.8	265.113	265.029	2.28E-04	1.18E-04
11	20	37619.7	263.814	263.730	1.34E-04	1.61E-04

V1	V2	WAVENUMBER CM**(-1)	WAVELENGTH (VACUO) NM	WAVELENGTH (AIR) NM	FRANCK-CONDON FACTOR	FRANCK-CONDON DENSITY CM
12	0	34583.7	289.109	289.321	5.34E-03	1.91E-04
12	1	34566.6	289.251	289.464	1.13E-03	1.13E-04
12	2	34549.4	289.394	289.607	4.47E-03	1.68E-04
12	3	34532.2	289.538	289.751	2.02E-03	1.60E-05
12	4	34515.0	289.682	289.895	6.50E-03	2.52E-04
12	5	34497.8	289.826	290.039	3.77E-03	1.53E-04
12	6	34480.5	289.971	290.184	1.51E-05	7.78E-07
12	7	34463.3	290.116	290.329	2.64E-03	1.37E-04
12	8	34446.0	290.261	290.474	6.30E-03	3.96E-04
12	9	34428.7	290.406	290.619	2.44E-03	3.42E-04
12	10	34411.4	290.551	290.764	7.39E-04	2.06E-04
12	11	34394.1	290.697	290.910	2.54E-05	5.62E-06
12	12	34376.8	290.843	291.056	1.54E-04	2.44E-06
12	13	34359.5	290.989	291.202	1.78E-05	1.78E-05
12	14	34342.2	291.135	291.348	5.69E-04	7.71E-05
12	15	34324.8	291.282	291.495	4.76E-04	1.47E-04
12	16	34307.5	291.428	291.641	4.44E-04	2.07E-04
12	17	34290.1	291.575	291.788	8.84E-04	2.62E-04
12	18	34272.7	291.723	291.936	6.69E-04	2.92E-04
12	19	34255.3	291.871	292.084	4.74E-04	3.03E-04
12	20	34237.9	292.019	292.232	2.67E-04	3.07E-04
13	0	34712.1	288.084	288.296	1.27E-03	4.57E-05
13	1	34695.0	288.226	288.438	1.44E-03	5.30E-05
13	2	34677.9	288.368	288.581	1.12E-03	4.21E-05
13	3	34660.8	288.511	288.723	4.82E-04	3.46E-05
13	4	34643.7	288.653	288.866	3.15E-03	1.31E-04
13	5	34626.6	288.796	289.008	7.01E-04	3.13E-05
13	6	34609.5	288.939	289.151	4.55E-04	2.20E-05
13	7	34592.4	289.082	289.294	2.68E-03	1.44E-04
13	8	34575.3	289.225	289.437	2.96E-03	1.72E-04
13	9	34558.2	289.368	289.580	1.36E-03	8.40E-05
13	10	34541.1	289.511	289.723	1.41E-03	1.02E-04
13	11	34524.0	289.654	289.866	1.24E-04	1.32E-05
13	12	34506.9	289.797	290.009	7.64E-04	7.32E-05
13	13	34489.8	289.941	290.153	1.36E-03	1.54E-04
13	14	34472.7	290.084	290.296	1.62E-03	2.19E-04
13	15	34455.6	290.227	290.439	1.55E-03	2.60E-04
13	16	34438.5	290.370	290.582	1.30E-03	2.78E-04
13	17	34421.4	290.513	290.725	9.90E-04	2.82E-04
13	18	34404.3	290.656	290.868	6.91E-04	2.80E-04
13	19	34387.2	290.799	291.011	4.35E-04	2.76E-04
13	20	34370.1	290.942	291.154	2.38E-04	2.69E-04

V1	V2	WAVENUMBER CM**(-1)	WAVELENGTH (VACUO) NM	WAVELENGTH (AIR) NM	FRANCK-CONDON FACTOR	FRANCK-CONDON DENSITY CM
14	0	34458.9	290.013	290.225	4.69E-05	1.68E-05
14	1	34440.8	290.165	290.377	3.01E-05	1.09E-06
14	2	34422.9	290.315	290.527	7.52E-05	2.91E-06
14	3	34407.7	290.443	290.655	5.24E-05	3.23E-06
14	4	34387.9	290.610	290.822	3.16E-04	1.32E-05
14	5	34369.7	290.763	290.975	1.83E-06	8.17E-08
14	6	34351.8	290.914	291.126	4.21E-04	2.03E-05
14	7	34334.1	291.064	291.276	8.53E-04	4.49E-05
14	8	34316.3	291.215	291.427	4.84E-04	2.81E-05
14	9	34298.2	291.368	291.580	3.07E-05	2.57E-06
14	10	34280.3	291.520	291.732	9.18E-05	6.65E-06
14	11	34262.5	291.671	291.883	4.39E-04	3.60E-05
14	12	34244.5	291.824	292.036	6.92E-04	6.64E-05
14	13	34226.5	291.977	292.189	7.38E-04	8.24E-05
14	14	34208.7	292.128	292.340	6.11E-04	8.29E-05
14	15	34190.7	292.281	292.493	4.42E-04	7.39E-05
14	16	34172.9	292.433	292.645	2.83E-04	6.18E-05
14	17	34155.1	292.585	292.797	1.77E-04	5.05E-05
14	18	34137.3	292.737	292.949	1.03E-04	4.17E-05
14	19	34119.5	292.889	293.101	5.64E-05	3.59E-05
14	20	34101.7	293.041	293.253	2.77E-05	3.19E-05
15	0	35024.1	285.514	285.725	4.21E-03	1.51E-04
15	1	35006.8	285.655	285.867	1.62E-03	5.52E-05
15	2	34989.5	285.797	286.008	9.71E-04	3.63E-05
15	3	34972.2	285.938	286.150	1.05E-02	4.12E-04
15	4	34954.8	286.080	286.292	4.83E-04	2.01E-05
15	5	34937.5	286.222	286.433	4.44E-03	2.18E-04
15	6	34920.2	286.363	286.575	7.37E-03	3.85E-04
15	7	34902.8	286.505	286.717	2.24E-03	1.18E-04
15	8	34885.5	286.647	286.858	1.32E-04	7.65E-06
15	9	34868.1	286.789	287.000	3.04E-03	1.97E-04
15	10	34850.8	286.931	287.142	5.37E-03	3.91E-04
15	11	34833.4	287.073	287.284	5.05E-03	4.18E-04
15	12	34816.1	287.215	287.426	3.22E-03	3.04E-04
15	13	34798.7	287.357	287.568	1.45E-03	1.54E-04
15	14	34781.4	287.499	287.710	4.73E-04	5.44E-05
15	15	34764.0	287.641	287.852	7.36E-05	1.73E-05
15	16	34746.7	287.783	287.994	2.21E-07	4.72E-08
15	17	34729.3	287.925	288.136	3.30E-05	9.41E-06
15	18	34712.0	288.067	288.278	6.43E-05	2.11E-05
15	19	34694.6	288.209	288.420	6.30E-05	4.17E-05
15	20	34677.3	288.351	288.562	4.02E-05	5.15E-05

V1	V2	WAVENUMBER CM**(-1)	WAVELENGTH (VACUO) NM	WAVELENGTH (AIR) NM	FRANCK-CONDON FACTOR	FRANCK-CONDON DENSITY CM
16	0	35177.7	284.271	284.159	3.24E-06	1.15E-07
16	1	35144.9	284.535	284.413	2.04E-04	7.23E-06
16	2	35112.7	284.796	284.674	3.89E-04	1.38E-05
16	3	35080.5	285.057	284.936	3.49E-04	1.24E-05
16	4	35048.3	285.319	285.197	1.41E-04	5.03E-06
16	5	35016.1	285.580	285.459	2.15E-05	7.74E-07
16	6	34984.0	285.842	285.720	1.13E-06	4.06E-08
16	7	34951.8	286.104	285.982	6.84E-05	2.46E-06
16	8	34919.6	286.366	286.244	1.43E-04	5.15E-06
16	9	34887.4	286.628	286.506	2.12E-04	7.64E-06
16	10	34855.2	286.890	286.768	1.77E-04	6.38E-06
16	11	34823.0	287.152	287.030	1.13E-04	4.08E-06
16	12	34790.8	287.414	287.292	5.62E-05	2.03E-06
16	13	34758.6	287.676	287.554	2.44E-05	8.81E-07
16	14	34726.4	287.938	287.816	9.37E-06	3.38E-07
16	15	34694.2	288.200	288.078	3.15E-06	1.14E-07
16	16	34662.0	288.462	288.340	9.54E-07	3.44E-08
16	17	34629.8	288.724	288.602	2.62E-07	9.46E-09
16	18	34597.6	288.986	288.864	6.76E-08	2.44E-09
16	19	34565.4	289.248	289.126	1.63E-08	5.89E-10
16	20	34533.2	289.510	289.388	3.75E-09	1.35E-10
17	0	35329.8	283.047	282.935	3.33E-03	1.20E-04
17	1	35302.0	283.270	283.158	1.03E-02	3.63E-04
17	2	35274.2	283.493	283.406	4.86E-03	1.71E-04
17	3	35246.5	283.716	283.616	4.53E-03	1.60E-04
17	4	35218.7	283.939	283.816	3.43E-04	1.21E-05
17	5	35190.9	284.162	284.003	1.11E-03	3.95E-05
17	6	35163.1	284.386	284.177	2.31E-03	8.19E-05
17	7	35135.3	284.609	284.338	1.10E-03	3.91E-05
17	8	35107.5	284.833	284.484	5.50E-05	1.95E-06
17	9	35079.7	285.057	284.617	2.47E-04	8.77E-06
17	10	35051.9	285.281	284.735	6.15E-04	2.18E-05
17	11	35024.1	285.505	284.840	9.99E-04	3.54E-05
17	12	34996.3	285.729	284.931	9.23E-04	3.27E-05
17	13	34968.5	285.953	285.009	6.75E-04	2.39E-05
17	14	34940.7	286.177	285.075	4.21E-04	1.49E-05
17	15	34912.9	286.401	285.129	2.32E-04	8.23E-06
17	16	34885.1	286.625	285.173	1.14E-04	4.04E-06
17	17	34857.3	286.849	285.206	5.42E-05	1.92E-06
17	18	34829.5	287.073	285.230	2.41E-05	8.55E-07
17	19	34801.7	287.297	285.247	1.04E-05	3.68E-07
17	20	34773.9	287.521	285.256	4.27E-06	1.51E-07

V1	V2	WAVENUMBER CM**(-1)	WAVELENGTH (VACUO) NM	WAVELENGTH (AIR) NM	FRANCK-CONDON FACTOR	FRANCK-CONDON DENSITY CM
18	0	35480.5	281.845	281.733	8.87E-03	3.18E-04
18	1	35452.7	282.066	281.954	3.99E-02	1.44E-03
18	2	35425.5	282.283	282.201	1.03E-02	4.06E-04
18	3	35399.3	282.491	282.409	1.62E-02	6.36E-04
18	4	35374.5	282.689	282.607	1.13E-03	4.71E-05
18	5	35351.3	282.875	282.793	1.37E-02	6.12E-04
18	6	35329.7	283.048	282.966	6.54E-03	3.16E-04
18	7	35309.9	283.207	283.135	2.74E-03	1.44E-04
18	8	35291.8	283.352	283.270	3.72E-03	2.16E-04
18	9	35275.4	283.483	283.401	6.83E-03	4.40E-04
18	10	35260.8	283.601	283.519	5.32E-03	3.87E-04
18	11	35247.9	283.705	283.622	2.41E-03	2.00E-04
18	12	35235.7	283.803	283.713	5.25E-04	4.34E-05
18	13	35227.0	283.873	283.791	1.83E-06	2.07E-07
18	14	35219.9	283.938	283.856	1.82E-04	2.47E-05
18	15	35212.2	283.992	283.910	4.85E-04	8.11E-05
18	16	35206.4	284.035	283.953	6.54E-04	1.40E-04
18	17	35202.8	284.064	283.986	6.55E-04	1.47E-04
18	18	35199.9	284.092	284.010	5.44E-04	2.21E-04
18	19	35197.9	284.108	284.026	3.81E-04	2.42E-04
18	20	35196.7	284.118	284.035	2.19E-04	2.51E-04
19	0	35629.7	280.665	280.553	1.05E-02	3.77E-04
19	1	35601.9	280.884	280.772	6.11E-02	2.22E-03
19	2	35574.7	281.099	281.017	3.37E-02	1.26E-03
19	3	35548.5	281.306	281.224	1.71E-02	6.72E-04
19	4	35523.7	281.502	281.420	1.17E-02	4.98E-04
19	5	35500.5	281.684	281.604	2.66E-03	1.19E-04
19	6	35479.9	281.847	281.776	2.95E-03	1.42E-04
19	7	35461.1	281.996	281.933	4.71E-03	2.49E-04
19	8	35444.0	282.132	282.077	1.55E-02	8.99E-04
19	9	35428.6	282.259	282.208	1.72E-02	1.14E-03
19	10	35414.8	282.369	282.324	4.23E-03	3.06E-04
19	11	35402.7	282.466	282.427	1.77E-04	1.43E-05
19	12	35392.1	282.550	282.517	7.43E-04	7.12E-05
19	13	35383.2	282.621	282.594	2.68E-03	3.03E-04
19	14	35376.0	282.678	282.658	3.92E-03	5.37E-04
19	15	35370.4	282.723	282.712	4.04E-03	6.93E-04
19	16	35366.4	282.756	282.744	1.63E-03	3.55E-04
19	17	35363.9	282.776	282.769	2.77E-03	7.55E-04
19	18	35362.8	282.785	282.777	2.77E-03	7.74E-04
19	19	35362.1	282.790	282.784	1.83E-03	7.68E-04
19	20	35361.9	282.792	282.786	6.37E-04	7.56E-04

V1	V2	WAV NUMBER CM**(-1)	WAVELENGTH (VACUO) NM	WAVELENGTH (AIR) NM	FRANCK-CONDON FACTOR	FRANCK-CONDON DENSITY CM
20	0	35777.5	279.505	279.424	4.75E-03	1.71E-04
20	1	35749.7	279.723	279.642	3.52E-02	1.27E-03
20	2	35722.4	279.936	279.855	3.17E-02	1.18E-03
20	3	35696.3	280.141	280.060	4.84E-03	1.90E-04
20	4	35671.5	280.336	280.254	1.68E-02	6.68E-04
20	5	35648.3	280.518	280.437	1.43E-02	6.39E-04
20	6	35626.7	280.688	280.607	1.21E-05	5.43E-07
20	7	35606.9	280.845	280.763	9.44E-03	4.97E-04
20	8	35588.8	280.988	280.906	1.28E-02	7.30E-04
20	9	35572.4	281.117	281.035	5.15E-03	3.33E-04
20	10	35557.8	281.232	281.151	2.39E-04	1.74E-05
20	11	35544.9	281.334	281.253	9.52E-04	7.19E-05
20	12	35533.7	281.423	281.342	3.42E-03	3.28E-04
20	13	35524.0	281.500	281.418	4.76E-03	5.39E-04
20	14	35515.9	281.564	281.482	4.63E-03	6.28E-04
20	15	35509.2	281.617	281.535	3.70E-03	6.19E-04
20	16	35503.9	281.659	281.577	2.62E-03	5.60E-04
20	17	35499.8	281.692	281.610	1.72E-03	4.90E-04
20	18	35496.9	281.715	281.633	1.06E-03	4.31E-04
20	19	35494.8	281.731	281.649	5.10E-04	3.88E-04
20	20	35493.6	281.741	281.659	3.09E-04	3.56E-04

APPENDIX D

STRUCTURAL ANALYSIS OF THE LASER SYSTEM

In this appendix, a structural analysis is given for the laser system described in Section 3.2.2. The linear theory of elasticity (the simplified von Kármán equation) [269] is applied to stress calculations for the end plates (see Fig.D-1) which form the basic supporting structure of the pressurized discharge chamber. In applying the linear theory, we have made the following assumptions:

(a) the deformation of an individual solid plate is small compared to the thickness h, which is itself small (thin plate);

(b) the displacement $w(x,y)$, normal to the plate surface, is independent of the thickness; and

(c) the mid-plane surface remains unchanged before and after the deformation.

Thus, the differential equation to be solved is

$$D \nabla^4 w(x,y) = q(x,y) \quad , \tag{D-1}$$

where the operator $\nabla^4 \equiv \nabla^2(\nabla^2) = (\frac{\partial^2}{\partial x^2} + \frac{\partial^2}{\partial y^2})^2$. The fluxural rigidity of the plate, D, is constant and defined by

$$D = \frac{E h^3}{12(1-\nu^2)} \quad . \tag{D-2}$$

E and ν are the elastic modulus and Poisson's ratio for the material, respectively. The concentrated load q takes into account all forces

Fig. D-1

A load diagram showing the forces acting on an end-plate of the laser supporting structure. The total force Q (gas pressure x internal cross-sectional area of the discharge chamber) is equally shared at eight locations on a pitch circle of radius R, corresponding to the positions of the supporting screws which are used for enclosing an end cap of the discharge chamber. These forces are balanced by reactions at the corners of a square of dimensions 2c x 2c, where the mounting screws for the supporting bars are located. For the purpose of analysis, a rectangular (x,y) coordinate system is set up for an end-plate of dimensions 2a x 2b x h, with origin at the centre of the plate.

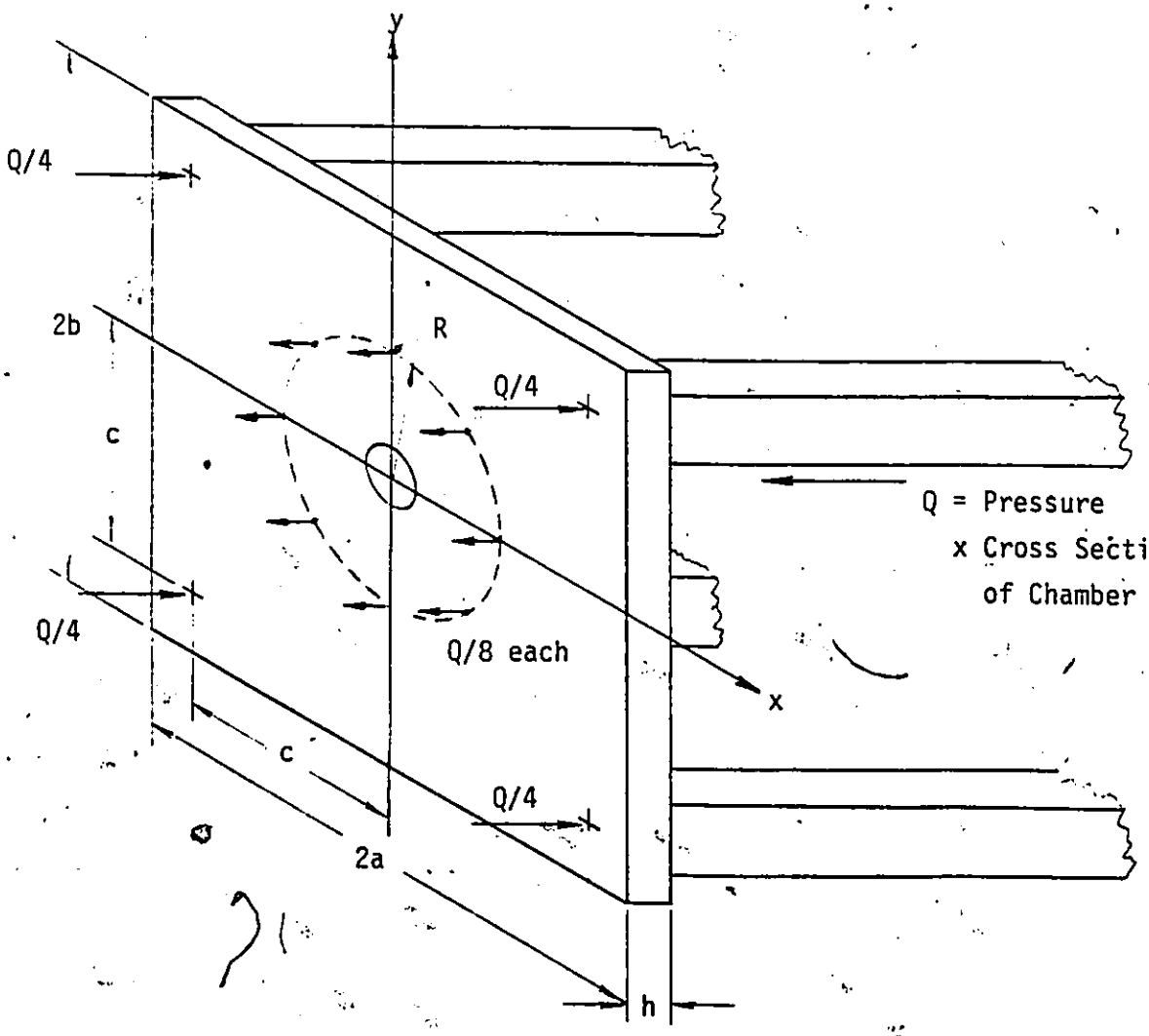
y
Q/4
2b
R
Q/4
c
Q = Pressure
x Cross Section
of Chamber
Q/4
Q/8 each
x
c
Q/4
2a
h

Q_i applied at various locations (x_i, y_i), and is expressed by

$$q(x,y) = \sum_i Q_i \, \delta(x-x_i) \, \delta(y-y_i) \quad . \tag{D-3}$$

For the situation shown in Fig.D-1, the end plate is loaded by a system of eight forces, each of magnitude Q/8, and symmetrically distributed on a central pitch circle of radius R. In our case, these represent the forces exerted on the eight supporting screws due to pressure in the discharge chamber. In the Cartesian coordinate-system used, these are located at $(\pm R, 0)$, $(\pm \frac{R}{\sqrt{2}}, \pm \frac{R}{\sqrt{2}})$ and $(0, \pm R)$. The forces are balanced by the reactions at the four locations $(\pm c, \pm c)$ where the plate is fastened to structural bars. If we expand the delta functions in Eq.(D-3) into the Fourier series

$$\delta(x - x_i) = \frac{1}{2a}\left[1 + 2\sum_{m=1}^{\infty}\left(\cos\frac{m\pi x_i}{a}\cos\frac{m\pi x}{a} + \sin\frac{m\pi x_i}{a}\sin\frac{m\pi x}{a}\right)\right] \tag{D-4a}$$

and

$$\delta(y - y_i) = \frac{1}{2b}\left[1 + 2\sum_{n=1}^{\infty}\left(\cos\frac{n\pi y_i}{b}\cos\frac{n\pi y}{b} + \sin\frac{n\pi y_i}{b}\sin\frac{n\pi y}{b}\right)\right] , \tag{D-4b}$$

then the load, defined by Eq.(D-3), can be represented by

$$q(x,y) = \frac{Q}{8ab}\left[\sum_{m=1}^{\infty}\left(1 + \cos\frac{m\pi R}{a} + 2\cos\frac{m\pi R}{\sqrt{2}a} - 4\cos\frac{m\pi c}{a}\right)\cos\frac{m\pi x}{a}\right.$$

$$+ \sum_{n=1}^{\infty}\left(1 + \cos\frac{n\pi R}{b} + 2\cos\frac{n\pi R}{\sqrt{2}b} - 4\cos\frac{n\pi c}{b}\right)\cos\frac{n\pi y}{b}$$

$$\left. + 2\sum_{m=1}^{\infty}\sum_{n=1}^{\infty}\left(\cos\frac{m\pi R}{a} + \cos\frac{n\pi R}{b} + 2\cos\frac{m\pi R}{\sqrt{2}a}\cos\frac{n\pi R}{\sqrt{2}b}\right.\right.$$

$$- 4 \cos \frac{m\pi c}{a} \cos \frac{n\pi c}{b}) \cos \frac{m\pi x}{a} \cos \frac{n\pi y}{b} \quad , \qquad \text{(D-5)}$$

where the force Q is simply the product of the (gauge) pressure of the gas in the chamber and its cross-sectional area. Equation (D-1) has a solution of the type

$$w(x,y) = \alpha + \sum_{m=1}^{\infty} \beta_m \cos \frac{m\pi x}{a} + \sum_{n=1}^{\infty} \gamma_n \cos \frac{n\pi y}{b}$$

$$+ \sum_{m=1}^{\infty} \sum_{n=1}^{\infty} \delta_{mn} \cos \frac{m\pi x}{a} \cos \frac{n\pi y}{b} \quad , \qquad \text{(D-6)}$$

where the coefficients α, β_m, γ_n and δ_{mn} are constant. By imposing the boundary conditions $w(\pm c, \pm c) = 0$, the solution becomes

$$w(x,y) = \frac{Q}{8abD} \{ \sum_{m=1}^{\infty} (\frac{a}{m\pi})^4 (1 + \cos \frac{m\pi R}{a} + 2 \cos \frac{m\pi R}{\sqrt{2}a} - 4 \cos \frac{m\pi c}{a})$$

$$(\cos \frac{m\pi x}{a} - \cos \frac{m\pi c}{a}) + \sum_{n=1}^{\infty} (\frac{b}{n\pi})^4 (1 + \cos \frac{n\pi R}{b} + 2 \cos \frac{n\pi R}{\sqrt{2}b}$$

$$- 4 \cos \frac{n\pi c}{b})(\cos \frac{n\pi y}{b} - \cos \frac{n\pi c}{b}) + 2 \sum_{m=1}^{\infty} \sum_{n=1}^{\infty} \frac{1}{\pi^4 (\frac{m^2}{a^2} + \frac{n^2}{b^2})^2}$$

$$(\cos \frac{m\pi R}{a} + \cos \frac{n\pi R}{b} + 2 \cos \frac{m\pi R}{\sqrt{2}a} \cos \frac{n\pi R}{\sqrt{2}b} - 4 \cos \frac{m\pi c}{a} \cos \frac{n\pi c}{b})$$

$$x (\cos \frac{m\pi x}{a} \cos \frac{n\pi y}{b} - \cos \frac{m\pi c}{a} \cos \frac{n\pi c}{b})\} \quad . \qquad \text{(D-7)}$$

The bending moments per unit width about the x-axis, the y-axis, and the axis perpendicular to the xy-plane, are calculated from

$$M_x = - D \left[\frac{\partial^2 w}{\partial x^2} + \nu \frac{\partial^2 w}{\partial y^2} \right] , \qquad (D\text{-}8)$$

$$M_y = - D \left[\frac{\partial^2 w}{\partial y^2} + \nu \frac{\partial^2 w}{\partial x^2} \right] , \qquad (D\text{-}9)$$

and $$M_{xy} = (1 - \nu) D \frac{\partial^2 w}{\partial x \partial y} . \qquad (D\text{-}10)$$

Neglecting the presence of the opening at the centre of the end plate, the maximum bending stresses about the two principal axes are

$$\sigma_x^{max} = \frac{3Q}{4abh^2\pi^2} \Bigg| \sum_{m=1}^{\infty} \left(\frac{a}{m}\right)^2 \left(1 + \cos \frac{m\pi R}{a} + \ell \cos \frac{m\pi R}{\sqrt{2}a} - 4 \cos \frac{m\pi c}{a}\right) \cos \frac{m\pi x}{a}$$

$$+ \nu \sum_{n=1}^{\infty} \left(\frac{b}{n}\right)^2 \left(1 + \cos \frac{n\pi R}{b} + 2 \cos \frac{n\pi R}{\sqrt{2}b} - 4 \cos \frac{n\pi c}{b}\right) \cos \frac{n\pi y}{b}$$

$$+ 2 \sum_{m=1}^{\infty} \sum_{n=1}^{\infty} \frac{\frac{m^2}{a^2} + \nu \frac{n^2}{b^2}}{\left(\frac{m^2}{a^2} + \frac{n^2}{b^2}\right)^2} \left(\cos \frac{m\pi R}{a} + \cos \frac{n\pi R}{b} + 2 \cos \frac{m\pi R}{\sqrt{2}a} \cos \frac{n\pi R}{\sqrt{2}b}\right.$$

$$\left. \times \cos \frac{m\pi x}{a} \cos \frac{n\pi y}{b}\right| , \qquad (D\text{-}11)$$

and

$$\sigma_y^{max} = \frac{3Q}{4abh^2\pi^2} \Bigg| \nu \sum_{m=1}^{\infty} \left(\frac{a}{m}\right)^2 \left(1 + \cos \frac{m\pi R}{a} + 2 \cos \frac{m\pi R}{\sqrt{2}a} - 4 \cos \frac{m\pi c}{a}\right) \cos \frac{m\pi x}{a}$$

$$+ \sum_{n=1}^{\infty} \left(\frac{b}{n}\right)^2 \left(1 + \cos\frac{n\pi R}{b} + 2\cos\frac{n\pi R}{\sqrt{2}b} - 4\cos\frac{n\pi c}{a}\right)\cos\frac{n\pi y}{b}$$

$$+ 2\sum_{m=1}^{\infty}\sum_{n=1}^{\infty} \frac{\nu\frac{m^2}{a^2}+\frac{n^2}{b^2}}{\left(\frac{m^2}{a^2}+\frac{n^2}{b^2}\right)^2}\left(\cos\frac{m\pi R}{a} + \cos\frac{n\pi R}{b} + 2\cos\frac{m\pi R}{\sqrt{2}a}\cos\frac{n\pi R}{\sqrt{2}b}\right.$$

$$\left. - 4\cos\frac{m\pi c}{a}\cos\frac{n\pi c}{b}\right)\cos\frac{m\pi x}{a}\cos\frac{n\pi y}{b} \Big| \quad . \qquad \text{(D-12)}$$

These are used to determine the resultant maximum bending stress, according to

$$\sigma^{max} = \sqrt{\left(\sigma_x^{max}\right)^2 + \left(\sigma_y^{max}\right)^2} \quad . \qquad \text{(D-13)}$$

Fig.D-2 shows σ^{max} at various positions on the plate for a chamber pressure of 10 atm acting over an area of $\pi(2.5)^2$ in^2. The aluminum plate has dimensions a = 6.0 in, b = 6.25 in, c = 5.0 in, h = 1.0 in and R = 2.75 in, and Poisson's ratio ν = 0.33. Figure D-2 shows that a maximum value of σ^{max} = 2.9 ksi is induced in the plate at positions near the structural supporting bars. Assuming that the maximum allowable stress for aluminum is 20 ksi, the plate can tolerate a maximum chamber pressure of 68 atm.

Moreover, a bending moment of 510 in-lb about either principal axis is transferred from the end plate to the end of a supporting bar, which has a section modulus of 0.56 in^3. This gives rise to a maximum tensile stress of 1.8 ksi on any one structural bar due to bending. Also taking into account the contribution from the reaction at the

Fig. D-2

Maximum bending stress (σ^{max}) acting on the end-plate shown in Fig.D-1.

The abreviation ksi represents "kilo-pound-force per square inch".

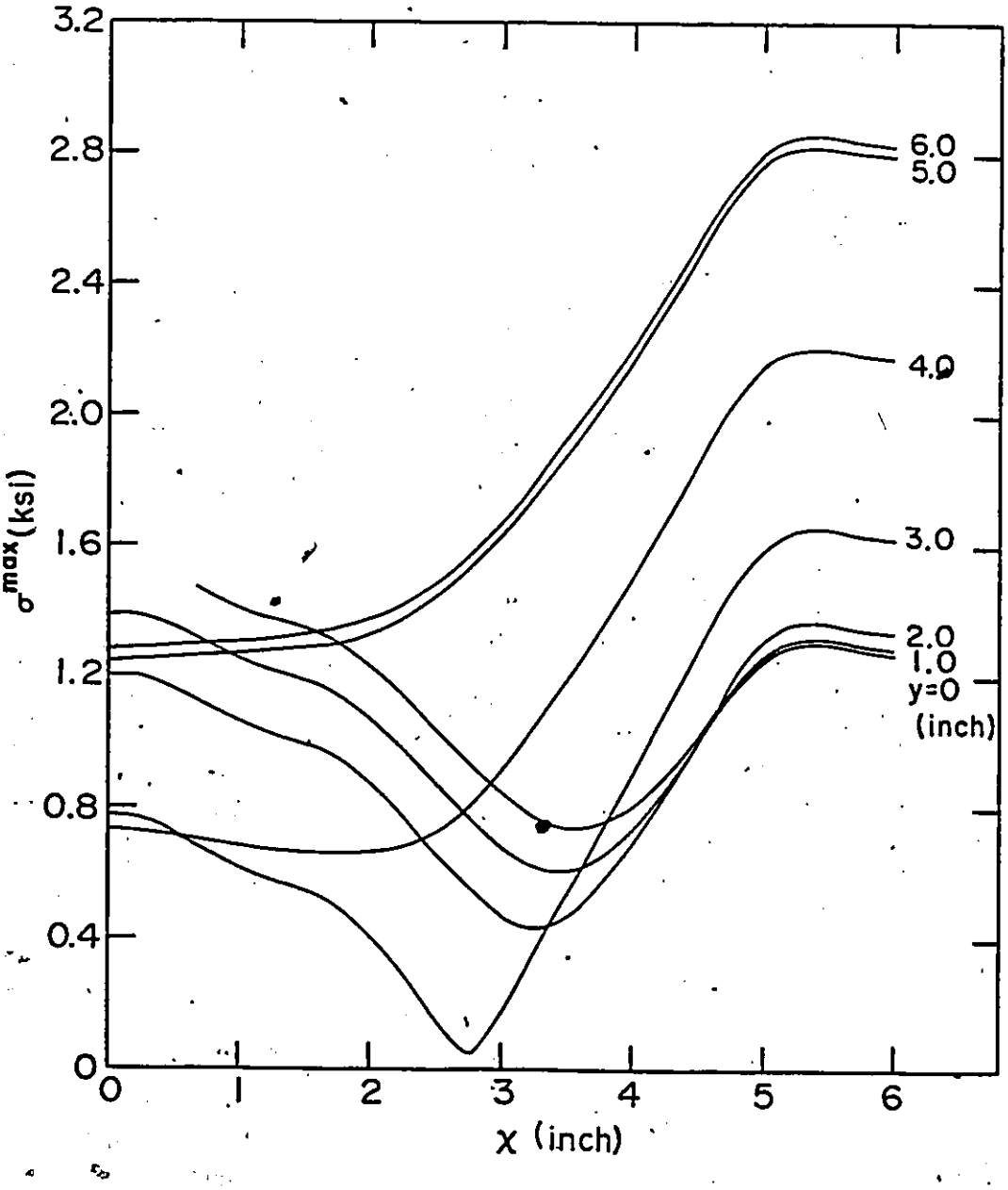
3.2
2.8
2.4
2.0
1.6
1.2
0.8
0.4
0
0
1
2
3
4
5
6
σ^{max}(ksi)
X (inch)
6.0
5.0
4.0
3.0
2.0
1.0
y=0
(inch)

support, the total tensile stress acting upon each bar is ∿2.1 ksi, for 10-atm pressure in the chamber. This stress is smaller than the bending stress induced in the end plate.

If a safety factor of 1.5 is allowed in the design, then the complete supporting structure which includes two end plates and four structural bars is capable of confining a chamber pressure of up to 45 atm. However, it is also necessary to determine if the chamber itself can be safely operated at the same pressure. As described in Section 3.2.2, the discharge chamber of our laser system is primarily an acrylic tube with 5-in ID and 0.5-in wall thickness (i.e., r_1 = 2.75 in and r_2 = 3.0 in in Fig.D-3). Applying the Lamé equations for a thick-walled cylinder given in Ref.[270], namely,

$$\sigma_t = \frac{r_1^2 p}{r_2^2 - r_1^2}\left(1 + \frac{r_2^2}{r^2}\right) \qquad \text{(D-14)}$$

and

$$\sigma_r = \frac{r_1^2 p}{r_2^2 - r_1^2}\left(1 - \frac{r_2^2}{r^2}\right) , \qquad \text{(D-15)}$$

the circumferential (hoop or tangential) stress σ_t and the radial stress σ_r on the inside surface ($r = r_1$) are estimated to be 1.69 ksi and - 0.15 ksi respectively, for a confined pressure p of 10 atm. Therefore, a maximum resultant stress of 1.7 ksi is developed at the wall. Taking a maximum allowable stress of 8 ksi for the tube material (cast acrylic), the chamber can withstand an internal pressure of 47 atm. However, an upper limit of 30-atm pressure is recommended after allowing

Fig. D-3

Representation of the discharge chamber by a thick-walled cylinder. r_1 and r_2 are the inside and outer radii of the cylinder, respectively. A set of two prependicular stresses, a hoop stress σ_t and a radial stress σ_r, are developed in the wall (at $r_1 \leq r \leq r_2$), due to the presence of an internal (differential) pressure p.

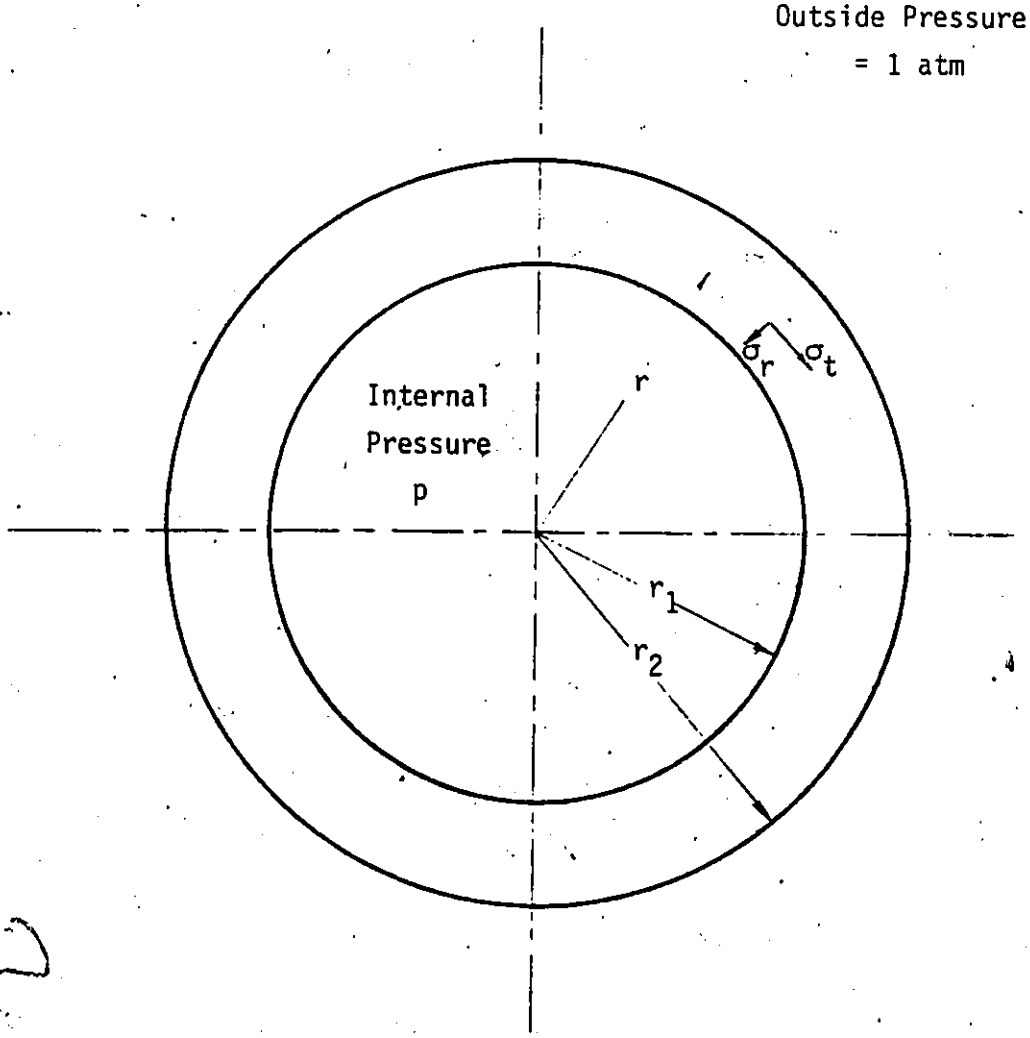
Outside Pressure
= 1 atm
Internal
Pressure
p
r
σ_r
σ_t
r_1
r_2

a safety factor of 1.5 on the design. The research for this thesis was always at operating pressures <10 atm, well below the 30-atm limit.

In conclusion, the mechanical strength of our laser system is only limited by the discharge chamber. If required, it is possible to increase the 30-atm limit to 45 atm by using a thicker chamber wall, or by replacing the Lucite chamber with one made of a stronger material, such as Fiberglass.

APPENDIX E

SOLUTION OF THE BOLTZMANN TRANSPORT EQUATION FOR ELECTRONS

The purpose of this appendix is to illustrate the similarity between the random-walk theory and the exact solution of the generalized Boltzmann equation for electron transport. Although numerous solutions, both exact and approximate, have been given for the transport equation [271], they are usually written in integral form, or expressed as a series, which does not explicitly describe the trajectory of the electrons. In the following, we seek a solution by integrating the equation with respect to time. This solution, in principle, enables us to identify the relative position of an electron to the position at an earlier time. The trajectory of an electron is found to obey the classical laws of motion, as implicitly applied in the random-walk (Monte-Carlo) calculations.

The continuity (Boltzmann) equation which describes the electron distribution function, $f(\vec{r}, \vec{v}, t)$, in phase space (position $\vec{r}$, velocity $\vec{v}$ and time t) is

$$\frac{\partial f}{\partial t} = - \vec{v} \cdot \nabla_r f - \vec{a} \cdot \nabla_v f + \left(\frac{\partial f}{\partial t}\right)_{coll} , \qquad (E\text{-}1)$$

where $\vec{a}$ is the acceleration due to the force $\vec{F}$ acting on an electron of mass m, $\vec{r} \equiv (x, y, z)$ and $\vec{v} \equiv (v_x, v_y, v_z)$. Nonrelativistically,

$$\vec{a} = \frac{\vec{F}}{m} . \qquad (E\text{-}2)$$

When only the electric field is of interest,

$$\vec{F} = q\vec{E} \quad , \tag{E-3}$$

where $q = -e$ is the (electron) charge. Adopting the coordinate system illustrated in Fig. 4-1, the electric field is given by

$$\vec{E} = -E\,\hat{z} \tag{E-4}$$

and $$\vec{a} = \frac{eE}{m}\,\hat{z} \quad . \tag{E-5}$$

After denoting the collision term $(\frac{\partial f}{\partial t})_{coll}$ by $\Gamma(\vec{r}, \vec{v}, t)$, i.e.,

$$\Gamma \equiv (\frac{\partial f}{\partial t})_{coll} \quad , \tag{E-6}$$

and defining an operator

$$\mathcal{L} \equiv \vec{v} \cdot \nabla_r + \vec{a} \cdot \nabla_v \quad , \tag{E-7}$$

Eq.(E-1) can be rewritten as

$$\frac{\partial f}{\partial t} + \mathcal{L} f = \Gamma \quad . \tag{E-8}$$

This equation has the integral solution

$$f(\vec{r},\vec{v},t) = \exp(-\Delta t\,\mathcal{L})\, f(\vec{r},\vec{v},t-\Delta t) + \int_{t-\Delta t}^{t} \exp\{(t-\tau)\,\mathcal{L}\}\, \Gamma(\vec{r},\vec{v},\tau)\, d\tau \quad , \tag{E-9}$$

where Δt is the increment in time.

The operator $\mathcal{L}$, given in Eq.(E-7), can be redefined in terms

of two new operators,

$$A \equiv -\Delta t\, \vec{v} \cdot \nabla_r \qquad \text{(E-10)}$$

and $$B \equiv -\Delta t\, \vec{a} \cdot \nabla_v \quad . \qquad \text{(E-11)}$$

The exponential operator which appears in Eq.(E-9) can now be separated, i.e.,

$$\exp(-\Delta t\, \mathcal{L}) \equiv \exp(A+B) = \exp(B)\, \exp(A)\, \exp([A,B]/2) \quad . \qquad \text{(E-12)}$$

From Eqs.(E-5), (E-10) and (E-11), the commutator of operators A and B is

$$[A,B] \equiv AB - BA = -\frac{eE}{m} (\Delta t)^2 \frac{\partial}{\partial z} \quad . \qquad \text{(E-13)}$$

Then the first term on the RHS of Eq.(E-9) becomes

$$\exp(-\Delta t\, \mathcal{L})\, f(\vec{r},\vec{v},t-\Delta t)$$

$$= \exp\left(-\frac{eE}{m} \Delta t \frac{\partial}{\partial z}\right) \exp(-\Delta t\, \vec{v} \cdot \nabla_r) \exp\left(-\frac{eE}{2m}(\Delta t)^2 \frac{\partial}{\partial z}\right) f(\vec{r},\vec{v},t-\Delta t)$$

$$= f\left(x-v_x\Delta t,\ y-v_z\Delta t,\ z-v_z\Delta t+\frac{eE}{2m}(\Delta t)^2,\ v_x,\ v_y,\ v_z-\frac{eE}{m}\Delta t,\ t-\Delta t\right). \qquad \text{(E-14)}$$

Therefore, the exact solution of Eq.(E-1), represented by Eq.(E-9), is

$$f(\vec{r},\vec{v},t) = f\left(x-v_x\Delta t,\ y-v_y\Delta t,\ z-v_z\Delta t+\frac{eE}{2m}(\Delta t)^2,\ v_x,\ v_y,\ v_z-\frac{eE}{m}\Delta t,\ t-\Delta t\right)$$

$$+ \int_0^{\Delta t} \Gamma\left(x - v_x(\Delta t - \tau),\ y - v_y(\Delta t - \tau),\ z - v_z(\Delta t - \tau) + \frac{eE}{2m}(\Delta t - \tau)^2,\ v_x, v_y,\right.$$

$$\left. v_z - \frac{eE}{m}(\Delta t - \tau),\ \tau + t - \Delta t\right) d\tau \quad . \qquad \text{(E-15)}$$

The first term on the RHS of Eq.(E-15) represents the electron distribution function at a previous time, $t-\Delta t$, when the electron, presently located at (x, y, z) and moving with a velocity (v_x, v_y, v_z), was located at $(x-v_x\Delta t,\ y-v_y\Delta t,\ z-v_z\Delta t+\frac{eE}{2m}(\Delta t)^2)$ and moving with a velocity $(v_x, v_y, v_z-\frac{eE}{m}\Delta t)$. The second term arises from changes in the electrons due to collisions in the time interval between $t-\Delta t$ and t.

APPENDIX F

CALCULATIONS FOR THREE-BODY COLLISION PROCESSES INVOLVING DOUBLE CROSSINGS OF POTENTIAL-ENERGY CURVES

In the discussion of XeCl(B) exciplex formation in Chapter 2, we suggest that two formation channels, in addition to ionic recombination, are important. These channels take advantage of the pseudo-crossings of two Rydberg-state energy curves and an ionic curve. Simple formulae for estimating the three-body rate coefficients for the above formation and associated reverse processes are derived in this appendix. Analysis of a two-body process, involving a single pseudo-crossing of two potential-energy curves, is generally known [272], and therefore is not repeated here.

Consider a typical situation, such as shown in Fig.F-1, where the potential-energy curve of an ionic molecule AB (state 0), correlating to the dissociation limit $A^+ + B^-$ (state 1), is "intersected" at two places, b and c, by the curves for the electronic states, $A^* + B$ (state 2) and $A^{**} + B$ (state 3), respectively. Provided that the properties of the intersecting states permit pseudo-crossing, there is a finite probability, $\mathcal{P}_\ell(m,n)$, of a jump from the initial state m to the final state n, which depends on the angular-momentum quantum-number ℓ. The cross-section for this process is given by

$$\sigma(m \rightarrow n) = \frac{\pi p}{k^2} \sum_\ell (2\ell + 1)\, \mathcal{P}_\ell(m,n) \quad , \qquad \text{(F-1)}$$

Fig. F-1

A schematic diagram illustrating psuedo-crossings of potential-energy curves. The states corresponding to the species are given in parentheses.

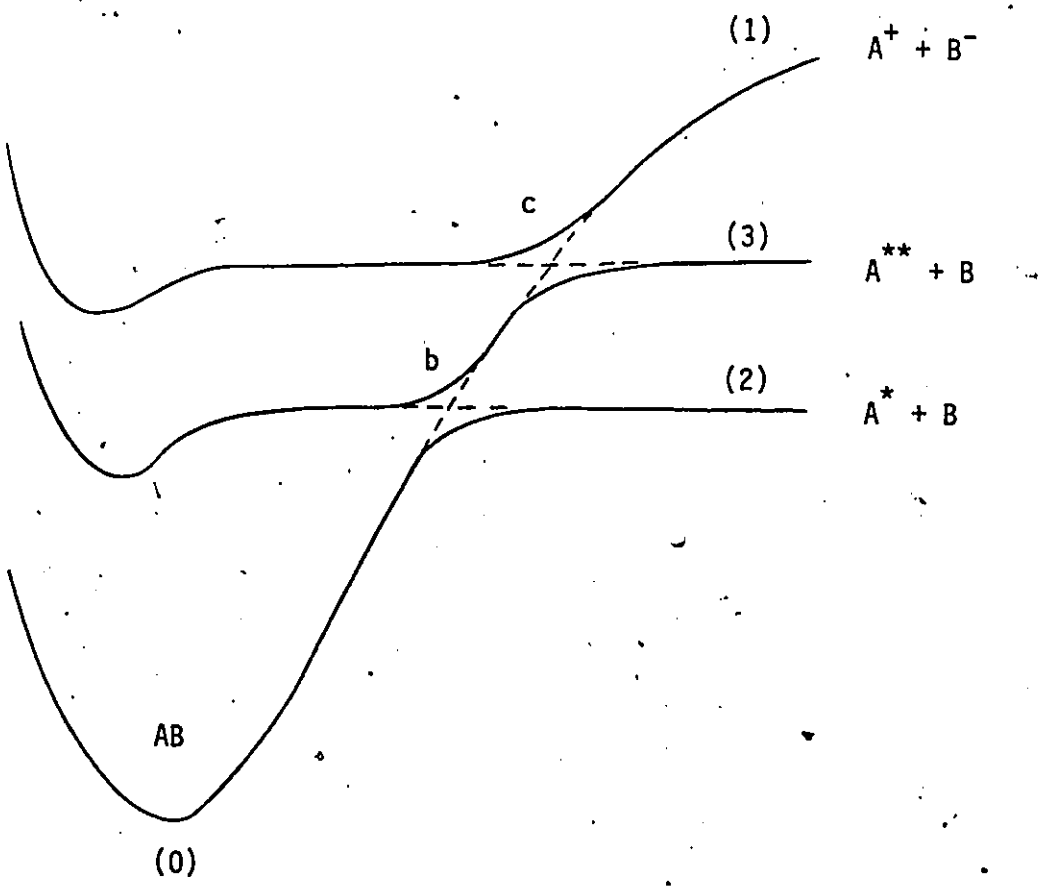
(1)
$A^+ + B^-$
c
(3)
$A^{**} + B$
b
(2)
$A^* + B$
AB
(0)

where $k^2 = \frac{2\mu}{\hbar^2} E$, (F-2)

and where μ is the reduced mass of the initial system, and p is the probability that the separated atoms or ions approach a specified potential with relative kinetic energy E. For the processes considered, p is taken as unity.

Let R_b and R_c represent the internuclear separations at the pseudo-crossing points b and c. The maximum quantum numbers for the various transitions can be determined from

$$\ell_{0b} = R_b \left[k^2 - \frac{2\mu}{\hbar^2} D\right]^{1/2} , \quad \text{(F-3)}$$

$$\ell_{0c} = R_c \left[k^2 - \frac{2\mu}{\hbar^2}(D+\Delta E_{23})\right]^{1/2} , \quad \text{(F-4)}$$

$$\ell_{1b} = R_b \left[k^2 + \frac{2\mu}{\hbar^2}\Delta E_{12}\right]^{1/2} , \quad \text{(F-5)}$$

$$\ell_{1c} = R_c \left[k^2 + \frac{2\mu}{\hbar^2}\Delta E_{13}\right]^{1/2} , \quad \text{(F-6)}$$

$$\ell_{2b} = R_b E^{1/2} , \quad \text{(F-7)}$$

$$\ell_{2c} = R_c \left[k^2 + \frac{2\mu}{\hbar^2}\Delta E_{23}\right]^{1/2} , \quad \text{(F-8)}$$

$$\ell_{3b} = R_b \left[k^2 + \frac{2\mu}{\hbar^2}\Delta E_{23}\right]^{1/2} , \quad \text{(F-9)}$$

and $$\ell_{3c} = R_c\, E^{1/2} \quad , \qquad \text{(F-10)}$$

where ΔE_{mn} is the difference in energy between the states m and n, and D is the depth of the potential-energy well with respect to the energy of state 2. Introducing

$$E_0 = \Delta E_{32}\, R_b^2/(R_c^2 - R_b^2) \qquad \text{(F-11)}$$

and $$E_0' = E_0 + \Delta E_{32} \quad , \qquad \text{(F-12)}$$

the probabilites for transitions between states, involving the processes described in Fig.F-1, can be expressed in terms of the crossing probabilites (P_b and P_c, at b and c, respectively) as follows:

$$\mathcal{P}_\ell(1,0) = P_b\, P_c \quad , \quad \ell<\ell_{1b} \quad ; \qquad \text{(F-13)}$$

$$\mathcal{P}_\ell(0,1) = \begin{cases} P_b\, P_c & , \quad \ell<\ell_{0b} \text{ and } E>D+\Delta E_{12} \\ P_c & , \quad \ell_{0b}<\ell<\ell_{0c} \text{ and } E>D+\Delta E_{12} \end{cases} \quad ; \qquad \text{(F-14)}$$

$$\mathcal{P}_\ell(1,2) = P_b(1-P_b)P_c \quad , \quad \ell<\ell_{1b} \quad ; \qquad \text{(F-15)}$$

$$\mathcal{P}_\ell(2,1) = P_b(1-P_b)P_c \quad , \quad \ell<\ell_{2b} \text{ and } E>\Delta E_{12} \quad ; \qquad \text{(F-16)}$$

$$\mathcal{P}_\ell(1,3) = \begin{cases} (2-2P_b+P_b^2)P_c(1-P_c) & , \quad \ell<\ell_{1b} \\ 2P_c(1-P_c) & , \quad \ell_{1b}<\ell<\ell_{1c} \end{cases} \quad ; \qquad \text{(F-17)}$$

$$\mathcal{P}_\ell(3,1) = \begin{cases} (2-2P_b+P_b^2)P_c(1-P_c) & , \quad \ell<\ell_{3b} \text{ and } E>\Delta E_{13} \\ 2P_c(1-P_c) & , \quad \ell_{3b}<\ell<\ell_{3c} \text{ and } E>\Delta E_{13} \end{cases} \quad ; \qquad \text{(F-18)}$$

$$\mathcal{P}_{\ell}(2,0) = \begin{cases} (1-P_b) & , \quad \ell<\ell_{2b} \text{ and } E>\Delta E_{12} \\ & \quad \text{or } \ell_{2c}<\ell<\ell_{2b} \text{ and } E_0'>E>\Delta E_{32} \\ (1-P_b)/(1-P_b^2P_c^2) & , \quad \ell<\ell_{2b} \text{ and } \Delta E_{12}>E>E_0' \\ & \quad \text{or } \ell<\ell_{2c} \text{ and } E_0'>E>\Delta E_{32} \\ 2(1-P_b)/(2-P_b) & , \quad \ell<\ell_{2b} \text{ and } \Delta E_{32}>E \quad ; \end{cases} \qquad \text{(F-19)}$$

$$\mathcal{P}_{\ell}(0,2) = \begin{cases} (1-P_b) & ; \quad \ell<\ell_{0b} \text{ and } E>D+\Delta E_{12} \\ \dfrac{2(1-P_b)(1-P_c+P_bP_c)}{2-(2-2P_b+P_b^2)P_c} & , \quad \ell<\ell_{0b} \text{ and } D+\Delta E_{12}>E>D+E_0' \\ & \quad \text{or } \ell<\ell_{0c} \text{ and } D+E_0'>E>D+\Delta E_{32} \\ 2(1-P_b)/(2-P_b) & , \quad \ell<\ell_{0b} \text{ and } D+\Delta E_{32}>E>D \quad ; \end{cases} \qquad \text{(F-20)}$$

$$\mathcal{P}_{\ell}(2,3) = \begin{cases} P_b(1-P_b)(1-P_c) & , \quad \ell<\ell_{2b} \text{ and } E>\Delta E_{12} \\ \dfrac{P_b(1-P_b)(1-P_c)}{1-(2-2P_b+P_b^2)P_c^2} & , \quad \ell<\ell_{2b} \text{ and } \Delta E_{12}>E>E_0' \\ & \quad \text{or } \ell<\ell_{2c} \text{ and } E_0'>E>\Delta E_{32} \quad ; \end{cases} \qquad \text{(F-21)}$$

$$\mathcal{P}_{\ell}(3,2) = \begin{cases} P_b(1-P_b)(1-P_c) & , \quad \ell<\ell_{3b} \text{ and } E>\Delta E_{13} \\ \dfrac{P_b(1-P_b)(1-P_c)}{1-(2-2P_b+P_b^2)P_c^2} & , \quad \ell<\ell_{3b} \text{ and } \Delta E_{13}>E>E_0 \\ & \quad \text{or } \ell<\ell_{3c} \text{ and } E_0>E \quad ; \end{cases} \qquad \text{(F-22)}$$

$$\mathcal{P}_{\ell}(3,0) = \begin{cases} P_b(1-P_c) & , \quad \ell<\ell_{3b} \text{ and } E>\Delta E_{13} \\ \dfrac{P_b(1-P_c)}{1-(2-2P_b+P_b^2)P_c^2} & , \quad \ell<\ell_{3b} \text{ and } \Delta E_{13}>E>E_0 \\ & \quad \text{or } \ell<\ell_{3c} \text{ and } E_0>E \quad ; \end{cases} \qquad \text{(F-23)}$$

and $$\mathcal{P}_\ell(0,3) = \begin{cases} P_b(1-P_c) & , \quad \ell<\ell_{0b} \text{ and } E>D+\Delta E_{12} \\ (1-P_c) & , \quad \ell_{0b}<\ell<\ell_{0c} \text{ and } E>D+\Delta E_{12} \\ \dfrac{2P_b(1-P_c)}{2-(2-2P_b+P_b^2)P_c} & , \quad \ell<\ell_{0b} \text{ and } D+\Delta E_{12}>E>D+E_0' \\ & \quad \text{or } \ell<\ell_{0c} \text{ and } D+E_0'>E>D+\Delta E_{12} \\ 2(1-P_c)/(2-P_c) & , \quad \ell_{0b}<\ell<\ell_{0c} \text{ and } D+\Delta E_{12}>E>D+E_0' \end{cases} \quad \text{(F-24)}$$

For a two-body process, the probability of crossing is calculated using the Landau-Zener formula [273,274]. For a three-body collision process, however, it is appropriate to use the Thomson's function [275]

$$w_T(x) = 1 - \frac{1}{2x^2}[1-(1+2x)\exp(-2x)] \quad \text{(F-25)}$$

in determining

$$P_b = w_T(R_b/\lambda_1)+w_T(R_b/\lambda_2)-w_T(R_b/\lambda_1)w_T(R_b/\lambda_2) \quad \text{(F-26)}$$

and $$P_c = w_T(R_c/\lambda_1)+w_T(R_c/\lambda_2)-w_T(R_c/\lambda_1)w_T(R_c/\lambda_2) \quad , \quad \text{(F-27)}$$

where $\lambda_{1,2}$ are the mean-free-paths for collisions of the particles in the initial system.

The rate coefficients for the above processes can now be evaluated by averaging the product of cross-section and relative velocity over a Maxwellian distribution function. This yields

$$\langle v\sigma\rangle = \frac{\hbar^2}{2\mu}\left(\frac{8\pi}{\mu kT}\right)^{1/2} p \int_0^\infty \sum_\ell (2\ell+1)\,\mathcal{P}_\ell e^{-E/kT} d(E/kT) \quad , \quad \text{(F-28)}$$

where k is the Boltzmann constant and T the gas temperature. Table F-1 lists the calculated rate coefficients for three different gas pressures. Note that our calculations yield rate coefficients for the ion-ion recombination which are in good agreement with those obtained using the classical theory [186,187].

Table F-1

Rate coefficients for three-body processes relating to pseudo-crossings of potential-energy curves. These coefficients are calculated for gas pressures of (A) 2957 Torr, (B) 2880 Torr, and (C) 2570 Torr. The rate coefficients in parentheses are calculated using the classical theory [186,187].

Reaction	Rate Coefficients (cm^6/s)			
	A	B	C	
$Xe^+ + Cl^- + He \rightarrow XeCl^* + He$	2.4(3.0)	2.3(3.0)	2.3(2.7)	$\times 10^{-27}$
$\leftarrow$		small		
$Xe^+ + Cl^- + He \rightarrow Xe^* + Cl + He$	1.3	1.3	1.4	$\times 10^{-27}$
$\leftarrow$	5.8	5.8	6.0	$\times 10^{-31}$
$Xe^+ + Cl^- + He \rightarrow Xe^{**} + Cl + He$	7.3	7.7	9.5	$\times 10^{-27}$
$\leftarrow$	3.6	3.8	4.7	$\times 10^{-28}$
$Xe^* + Cl + He \rightarrow XeCl^* + He$	5.7	6.0	6.9	$\times 10^{-28}$
$\leftarrow$		small		
$Xe^* + Cl + He \rightarrow Xe^{**} + Cl + He$	6.7	6.9	7.2	$\times 10^{-30}$
$\leftarrow$	7.6	7.9	8.2	$\times 10^{-28}$
$Xe^{**} + Cl + He \rightarrow XeCl^* + He$	1.4	1.4	1.3	$\times 10^{-27}$
$\leftarrow$		small		

REFERENCES

[1] D.L. Huestis, R.M. Hill, D.J. Eckstrom, M.V. McCusker, D.C. Lorents, H.H. Nakano, B.E. Perry, J.A. Margevicius, and N.E. Schlotter: "New Electronic Transition Laser Systems", SRI Report #MP78-07 (1978).

[2] W.N. Hartley and H. Ramage: R. Dublin Soc. Trans. 7, 339 (1901).

[3] R.W. Wood: Phil. Mag. 18, 240 (1909).

[4] S. Mrozowski: Z. Phys. 76, 38 (1932).

[5] Lord Rayleigh: Proc. R. Soc. (London). A114, 620 (1927).

[6] F.G. Houtermans: Helv. Phys. Acta 33, 933 (1960).

[7] N.G. Basov, V.A. Danilychev, and Yu.M. Popov: Sov. J. Quant. Elect. 1, 18 (1971).

[8] H.A. Koehler, L.J. Ferderber, D.L. Redhead, and P.J. Ebert: Appl. Phys. Lett. 21, 198 (1972).

[9] R.O. Hunter: Presented at the 7th Winter Colloquium on High Power Visible Lasers, Park City, Utah (1977).

[10] M.F. Golde and B.A. Thrush: Chem. Phys. Lett. 29, 486 (1974).

[11] J.E. Velazco and D.W. Setser: Chem. Phys. Lett. 25, 197 (1974).

[12] J.E. Velazco and D.W. Setser: J. Chem. Phys. 62, 1990 (1975).

[13] S.K. Searles and G.A. Hart: Appl. Phys. Lett. 27, 243 (1975).

[14] C.A. Brau and J.J. Ewing: Appl. Phys. Lett. 27, 435 (1975).

[15] E.R. Ault, R.S. Bradford, Jr. and M.L. Bhaumik: Appl. Phys. Lett. 27, 413 (1975).

[16] J.J. Ewing and C.A. Brau: Appl. Phys. Lett. 27, 350 (1975).

[17] J.M. Hoffman, A.K. Hays, and G.C. Tisone: Appl. Phys. Lett. 28, 538 (1976).

[18] J.R. Murray and H.T. Powell: Appl. Phys. Lett. 29, 252 (1976).

[19] R.W. Waynant: Appl. Phys. Lett. 30, 234 (1977).

[20] R. Burnham, N.W. Harris, and N. Djeu: Appl. Phys. Lett. 28, 86 (1976).

[21] R. Burnham and N. Djeu: Appl. Phys. Lett. 29, 707 (1976).

[22] M. Matera and R. Salimbeni: Opt. Comm. 25, 251 (1978).

[23] R.S. Taylor, A.J. Alcock, and K.E. Leopold: Opt. Comm. 31, 197 (1979).

[24] N.G. Basov, V.S. Zuev, L.D. Mikheev, D.B. Stavrovskiĭ, and V.I. Yalovoĭ: Sov. J. Quant. Elect. 7, 1401 (1977).

[25] N.G. Basov, V.S. Zuev, A.V. Kanaev, L.D. Mikheev, and D.B. Stavrovskiĭ: Sov. J. Quant. Elect. 9, 629 (1979).

[26] L.F. Champagne, J.G. Eden, N.W. Harris, N. Djeu, and S.K. Searles: Appl. Phys. Lett. 30, 160 (1977).

[27] Yu.I. Bychkov, N.V. Karlov, I.N. Konovalov, G.A. Mesyats, A.M. Prokhorov, and V.F. Tarasenko: Sov. Tech. Phys. Lett. 3, 427 (1977).

[28] L.F. Champagne and N.W. Harris: Appl. Phys. Lett. 33, 248 (1978).

[29] P. Burlamacchi and R. Salimbeni: Opt. Comm. 26, 233 (1978).

[30] L.F. Champagne: Appl. Phys. Lett. 33, 523 (1978).

[31] D.C. Hogan, R. Bruzzese, A.J. Kearsley, and C.E. Webb: J. Phys. D 14, L157 (1981).

[32] Yu.A. Kudryavtsev and N.P. Kuz'mina: Sov. J. Quant. Elect. 7, 131 (1977).

[33] V.N. Ishchenko, V.N. Lisitsyn, and A.M. Razhev: Opt. Comm. 21, 30 (1977).

[34] Yu.I. Bychkov, M.N. Kostin, V.F. Tarasenko, and A.I. Fedorov: Sov. J. Quant. Elect. 8, 668 (1978).

[35] R. Burnham: Opt. Comm. 24, 161 (1978).

[36] C.A. Brau and J.J. Ewing: J. Chem. Phys. 63, 4640 (1975).

[37] J.J. Ewing and C.A. Brau: Phys. Rev. A12, 129 (1975).

[38] J.H. Kolts, J.E. Velazco, and D.W. Setser: J. Chem. Phys. 71, 1247 (1979).

[39] F.K. Tittel, W.L. Wilson, R.E. Stickel, G. Marowsky, and W.E. Ernst: Appl. Phys. Lett. 36, 405 (1980).

[40] M. Rokni, J.A. Mangano, J.H. Jacob, and J.C. Hsia: IEEE J. Quant. Elect. QE-14, 464 (1978).

[41] A.M. Hawtyluk, J.A. Mangano, and J.H. Jacob: Appl. Phys. Lett. 31, 164 (1977).

[42] M.C. Gower, R. Exberger, P.D. Rowley, and K.W. Billman: Appl. Phys. Lett. 33, 65 (1978).

[43] T.G. Finn, L.J. Palumbo, and L.F. Champagne: Appl. Phys. Lett. 33, 148 (1978).

[44] A. Sur, A.K. Hui, and J. Tellinghuisen: J. Mol. Spectrosc. 74, 465 (1979).

[45] W.W. Rigrod: IEEE J. Quant. Elect. QE-14, 377 (1978).

[46] P.J. Hay and T.H. Dunning, Jr.: J. Chem. Phys. 69, 2209 (1978).

[47] W.J. Stevens and M. Krauss: Paper Tu-A2, presented at IEEE/OSA Topical Meeting on Excimer Lasers, Charleston, South Carolina (1979).

[48] J. Tellinghuisen, J.M. Hoffman, G.C. Tisone, and A.K. Hays: J. Chem. Phys. 64, 2484 (1976).

[49] R.S. Mulliken: J. Chem. Phys. 52, 5170 (1970).

[50] P.C. Tellinghuisen, J. Tellinghuisen, J.A. Coxon, J.E. Velazco, and D.W. Setser: J. Chem. Phys. 68, 5187 (1978).

[51] B. Liu and H.F. Schaefer, III: J. Chem. Phys. 55, 2369 (1971).

[52] D.H. Liskow, H.F. Schaefer, III, P.S. Bagus, and B. Liu: J. Am.

Chem. Soc. 95, 4056 (1973).

[53] S. Huzinaga: Approximate Atomic Functions, Vol. I and II (Univ. of Alberta, Edmonton, Alberta, 1972).

[54] T.H. Dunning, Jr. and P.J. Hay: "Gaussian Basis Sets for Molecular Calculations" in Methods of Electronic Structure Theory, ed. by H.F. Schaefer, III (Plenum Press, New York, 1977).

[55] R.C. Raffenetti: J. Chem. Phys. 58, 4452 (1973).

[56] R.S. Mulliken and W.B. Person: Molecular Complexes (Wiley-Interscience, New York, 1969).

[57] J. Goodman and L.E. Brus: J. Chem. Phys. 65, 3808 (1976).

[58] R. Shuker: Appl. Phys. Lett. 29, 785 (1976).

[59] R.J. Leroy: Specialist Periodic Report on Electron Spectroscopy, ed. by R.F. Burrow, Vol. I, 113 (Chem. Soc., London, 1973).

[60] R. Rydberg: Z. Physik 73, 376 (1931).

[61] O. Klein: Z. Physik 76, 226 (1932).

[62] A.L.G. Rees: Proc. Phys. Soc. (London) 59, 998 (1947).

[63] J.L. Dunham: Phys. Rev. 41, 721 (1932).

[64] P.M. Morse: Phys. Rev. 34, 57 (1929).

[65] E.S. Rittner: J. Chem. Phys. 19, 1030 (1951).

[66] M. Born and J.E. Mayer: Z. Physik 75, 1 (1932).

[67] J.E. Lennard-Jones: Proc. Phys. Soc. (London) 43, 461 (1931).

[68] Y.P. Varnshni: Rev. Mod. Phys. 29, 664 (1957).

[69] R. Mecke: Z. Physik 42, 390 (1927).

[70] G.B.B.M. Sutherland: Proc. Indian Acad. Sci. 8, 341 (1938).

[71] G.B.B.M. Sutherland: J. Chem. Phys. 8, 161 (1940).

[72] M. Alonso and H. Valk: Quantum Mechanics: Principles and Applications (Addison-Wesley, Don Mills, Ontario, 1973).

[73] O.P. Shardin: Opt. Spectrosc. 43, 329 (1977).

[74] C.E. Moore: Atomic Energy Levels (U.S. Nat'l Bur. Stand. Circ 467 Vol. I, 1949; Vol. II, 1952; and Vol. III, 1958).

[75] J. Tellinghuisen and M.R. McKeever: Chem. Phys. Lett. 72, 94 (1980).

[76] D. Kligler, H.H. Nakano, D.L. Huestis, W.K. Bischel, R.M. Hill, and C.K. Rhodes: Appl. Phys. Lett. 33, 39 (1978).

[77] B.S. Ault and L. Andrews: J. Chem. Phys. 65, 4192 (1976).

[78] H. Hotop and W.C. Lineberger: J. Phys. Chem. Ref. Data 4, 539 (1975).

[79] Y.P. Varshni and R.C. Shulka: J. Mol. Spectrosc. 16, 63 (1965).

[80] A.S. Coolidge, H.M. James, and R.D. Present: J. Chem. Phys. 4, 193 (1936).

[81] K. Tamagake, J.H. Kolts, and D.W. Setser: J. Chem. Phys. 71,1264 (1979).

[82] R.W. Nicholls: J. Quant. Spectrosc. Radiat. Transfer 14, 233 (1974).

[83] B. Fontaine and B. Forestier: Appl. Phys. Lett. 36, 185 (1980).

[84] M. Maeda, T. Yamashita, and Y. Miyazoe: Jap. J. Appl. Phys. 17, 969 (1978).

[85] L.A. Levin, S.E. Moody, E.L. Klosterman, R.E. Center, and J.J. Ewing: IEEE J. Quant. Elect. QE-17, 2282 (1981).

[86] P.B. Corkum and R.S. Taylor: IEEE J. Quant. Elect. QE-18, Nov. (1982).

[87] C.A. Brau: "Rare Gas Halogen Excimers" in Excimer Lasers, ed. by C.K. Rhodes (Springer-Verlag, Berlin, 1979).

[88] J.B. Laudenslager: "Ion-Molecule Processes in Lasers" in Kinetics of Ion-Molecule Reactions, ed. by P. Ausloos (Plenum Press, New York, 1978).

[89] D.R. Herschbach: Adv. Chem. Phys. 10, 319 (1966).

[90] R.C. Sze: IEEE J. Quant. Elect. QE-15, 1338 (1979).

[91] E. Wigner and E.E. Witmer: Z. Physik 51, 883 (1928).

[92] S. Watanabe and A. Endoh: Appl. Phys. Lett. 41, 799 (1982).

[93] C.P. Wang, H. Mirels, D.G. Sutton, and S.N. Suchard: Appl. Phys. Lett. 28, 326 (1976).

[94] W.J. Sarjeant, A.J. Alcock, and K.E. Leopold: Appl. Phys. Lett. 30, 635 (1977).

[95] R.C. Sze and P.B. Scott: J. Appl. Phys. 47, 5492 (1976).

[96] A.J. Andrews, A.J. Kearsley, C.E. Webb, and S.C. Haydon: Opt. Comm. 20, 265 (1977).

[97] E.A. Ballik: Private communication (1979).

[98] M.M.T. Loy and P.A. Roland: Rev. Sci. Instrum. 48, 554 (1977).

[99] R.H. Vandre and G.M. Molen: Electronic Design 9, IV-86 (1976).

[100] W.J. Sarjeant, A.J. Alcock, and K.E. Leopold: IEEE J. Quant. Elect. QE-14, 177 (1978).

[101] E.A. Ballik: private communication (1978).

[102] T.G. Finn, R.S.F. Chang, L.J. Palumbo, and L.F. Champagne: Appl. Phys. Lett. 36, 789 (1980).

[103] W.J. Sarjeant and A.J. Alcock: Rev. Sci. Instr. 47, 1283 (1976).

[104] E.A. Ballik: private communication (1981).

[105] T. Holstein: Phys. Rev. 70, 367 (1946).

[106] L.S. Frost and A.V. Phelps: Phys. Rev. 127, 1621 (1962).

[107] L.C. Pitchford, S.V. O'Neil, and J.R. Rumble, Jr.: Phys. Rev. A 23, 294 (1981).

[108] K. Kitamori, H. Tagashira, and Y. Sakai: J. Phys. D 11, 283 (1978).

[109] G.L. Braglia: Beitr. Plasmaphysik 20, 1 (1980).

[110] G.D. Yarnold: Phil. Mag. 36, 185 (1945).

[111] T. Itoh and T. Musha: J. Phys. Soc. (Japan) 15, 1675 (1960).

[112] M.J. Bell and M.D. Kostin: Phys. Rev. 169, 150 (1968).

[113] R.W.L. Thomas and W.R.L. Thomas: J. Phys. B 2, 562 (1969).

[114] M.A. Folkard and S.C. Haydon: Aust. J. Phys. 23, 847 (1970).

[115] G.W. Englert: Z. Naturforsch 26a, 836 (1971).

[116] J. Lucas: Int. J. Electronics 32, 393 (1972).

[117] Y. Sakai, H. Tagashira, and S. Sakamoto: J. Phys. B 5, 1010 (1972).

[118] L.E. Klein and J.G. Siambis: Phys. Rev. A 5, 794 (1972).

[119] H. Skullerud: J. Phys. D 1, 1567 (1968).

[120] A.I. McIntosh: Aust. J. Phys. 27, 59 (1974).

[121] K.G. Müller and W.O. Müller: Z. Naturforsch 30a, 1553 (1975).

[122] G.L. Braglia: Physica 92C, 91 (1977).

[123] I.D. Reid: Aust. J. Phys. 32, 231 (1979).

[124] V.V. Ryzhov and A.G. Yastremskii: Izv. Vyssh. Uchebn. Zaved., Fiz., 11, 140 (1978).

[125] B.E. Cherrington: Gaseous Electronics and Gas Lasers (Pergamon Press, Oxford, 1979).

[126] D. Andrick and A. Bitsch: J. Phys. B 8, 393 (1975).

[127] R.W. Crompton, M.T. Elford, and A.G. Robertson: Aust. J. Phys. 23, 667 (1970).

[128] H.B. Milloy and R.W. Crompton: Phys. Rev. A 15, 1847 (1977).

[129] R.W. LaBahn and J. Callaway: Phys. Rev. 147, 28 (1966).

[130] J. Callaway, R.W. LaBahn, R.T. Pu, and W.M. Duxler: Phys. Rev. 168, 12 (1968).

[131] W.M. Duxler, R.T. Poe, and R.W. LaBahn: Phys. Rev. A 4, 1935 (1971).

[132] T.F. O'Malley: Phys. Rev. 130, 1020 (1963).

[133] T.F. O'Malley, L. Spruch, and L. Rosenberg: J. Math Phys. 2, 491 (1961).

[134] J.J. Lowke, A.V. Phelps, and B.W. Irwin: J. Appl. Phys. 44, 4664 (1973).

[135] G.J. Schulz and R.E. Fox: Phys. Rev. 106, 1179 (1957).

[136] G.J. Schulz: Phys. Rev. 116, 1141 (1959).

[137] G.J. Schulz and J.W. Philbrick: Phys. Rev. Lett. 13, 477 (1964).

[138] J.D. Jobe and R.M. St. John: Phys. Rev. 164, 117 (1967).

[139] R.M. St. John, F.L. Miller, and C.C. Lin: Phys. Rev. 134, A 888 (1964).

[140] F.J. de Heer and R.H.J. Jansen: J. Phys. B 10, 3741 (1977).

[141] K. Jost and R. Möllenkamp: Proc. 10th Int. Conf. on Physics of Electronic and Atomic Collisions, Paris (1977).

[142] D. Rapp and P. Englander-Golden: J. Chem. Phys. 43, 1464 (1965).

[143] P.T. Smith: Phys. Rev. 36, 1293 (1930).

[144] B.L. Schram, F.L. de Heer, M.J. van der Wiel, and J. Kistemaker: Physica 31, 94 (1965).

[145] W.R.L. Thomas: J. Phys. B 2, 551 (1969).

[146] L.S. Frost and A.V. Phelps: Phys. Rev. 136, A 1538 (1964).

[147] F.J. de Heer, R.H.J. Jansen, and W.van der Kaay: J. Phys. B 12, 979 (1979).

[148] M. Schaper and H. Scheibner: Beitr. Plasmaphysik 9, 45 (1969).

[149] A.J. Dixon and A. von Engel: Int. J. Electronics 25, 233 (1968).

[150] B.A. Tozer and J.D. Cragg: J. Electron. Control 8, 103 (1960).

[151] R.K. Asundi and M.V. Kurepa: J. Electron. Control 15, 41 (1963).

[152] K. Rohr and F. Linder: J. Phys. B. 8, L200 (1975).

[153] E. Bürche: Ann. Physik IV 83, 1065 (1927).

[154] K.T. Compton and C.C. Van Voorhis: Phys. Rev. 26, 436 (1925).

[155] K. Rohr and F. Linder: J. Phys. B 9, 2521 (1976).

[156] L.G. Christophorou, R.N. Compton, and F.W. Dickson: J. Chem. Phys. 48, 1949 (1968).

[157] J.P. Ziesel, I. Nenner, and G.J. Schulz: J. Chem Phys. 63, 1943 (1975).

[158] R. Azria, L. Roussier, R. Paineau, and M. Tronc: Rev. Phys. Appl. 9, 469 (1974).

[159] I.S. Buchel'nikova: Sov. Phys.-JETP 35, 783 (1959).

[160] R. Abouaf and D. Teillet-Billy: J. Phys. B 10, 2261 (1977).

[161] R.C. Sze and A.E. Greene: Paper KA-7, presented at the 33rd Annual Gaseous Electronics Conference, Norman, Oklahoma (1980).

[162] L. Dubé and A. Herzenberg: Phys. Rev. Lett. 38, 820 (1977).

[163] R. Azria, Y. Le Coat, D. Simon, and M. Tronc: J. Phys. B 13, 1909 (1980).

[164] M. Mitchner and C.H. Kruger, Jr.: Partially Ionized Gases (John Wiley & Sons, New York, 1973).

[165] I.P. Shkarofsky, T.W. Johnston, and M.P. Bachynski: The Particle Kinetics of Plasmas (Addison-Wiley, Dordrecht, 1966).

[166] B.V. Alekseev and G.V. Nesterov: Sov. Phys. Dokl. 19, 125 (1974).

[167] L.K. Hua and Y. Wang: Scientia Sinica 13, 1009 (1964).

[168] N.M. Korobov: Sov. Math. Dokl. 1, 696 (1960).

[169] A.J. Postma: Physica 43, 229 (1969).

[170] W. Williams, S. Trajmar, and A. Kuppermann: J. Chem. Phys. 62, 3031 (1975).

[171] R. Deloche, P. Monchicourt, M. Cheret, and F. Lambert: Phys. Rev. A 13, 1140 (1976).

[172] D. Ton-That, S.T. Manson, and M.R. Flannery: J. Phys. B 10, 621 (1977).

[173] A.J. Dixon, M.F.A. Harrison, and A.C.H. Smith: J. Phys. B 9, 2617 (1976).

[174] A. Burgess and M.J. Seaton: M.N. Roy. Astr. Soc. 121,471 (1960).

[175] D.R. Bates and S.P. Khare: Proc. Phys. Soc. (London) 85, 231 (1965).

[176] P.V. Feltsan and I.P. Zapesochnyi: Ukr. Fiz. Zh. 13, 205 (1968).

[177] H.A. Hyman: Phys. Rev. A 20, 855 (1979).

[178] H.J. Oskam and V.R. Mittelstadt: Phys. Rev. 132, 1445 (1963).

[179] C. Duzy and J. Boness: IEEE J. Quant. Elect. QE-16, 640 (1980).

[180] M. Allen and S.F. Wong: J. Chem. Phys. 74, 1687 (1981).

[181] H.S.W. Massey and R.A. Smith: Proc. Roy. Soc. (London) A 155, 472 (1936).

[182] K.J. Nygaard, H.L. Brooks, and S.R. Hunter: IEEE J. Qunat. Elect. QE-15, 1216 (1979).

[183] M.V. Kurepa and D.S. Belić: J. Phys. B 11, 3719 (1978).

[184] G.C. Tisone and L.M. Branscomb: Phys. Rev. 170, 169 (1968).

[185] G.J. Schulz and R.K. Asundi: Phys. Rev. 158, 25 (1967).

[186] J.M. Wadehra and J.N. Bradsley: Appl. Phys. Lett. 32, 76 (1978).

[187] M.R. Flannery and T.P. Jang: Appl. Phys. Lett. 32, 327 (1978).

[188] A.J. Palmer: Appl. Phys. Lett. 25, 138 (1974).

[189] F.M. Matsunaga, K. Watanabe, and R.S. Jackson: J. Quant. Spectrosc. Radiative Transfer 5, 329 (1965).

[190] J.A.R. Samson: J. Opt. Soc. Am. 54, 876 (1964).

[191] H.J.J. Seguin, J. Tulip, [illegible]cken: Appl. Phys. Lett. 23, 344 (1973).

[192] H.F. Wellenstein and W.W. Robertson: J. Chem. Phys. 56, 1077 (1972).

[193] W. Lindinger, A.L. Schmeltekopf, and F.C. Fehsenfeld: J. Chem. Phys. 61, 2890 (1974).

[194] W.P. Sholette and E.E. Muschlitz, Jr.: J. Chem. Phys. 36, 3368 (1962).

[195] S. Kubota, C. Davies, and T.A. King: Phys. Rev. A 11, 1200 (1975).

[196] H. Hotop, A. Niehaus, and A.L. Schmeltekopf: Z. Physik 229, 1 (1969).

[197] C.B. Collins and F.W. Lee: J. Chem. Phys. 70, 1275 (1979).

[198] Y.A. Bush, M. McFarland, D.L. Albritton, and A.L. Schmeltekopf: J. Chem. Phys. 58, 4020 (1973).

[199] M.J. Kushner and F.E.C. Culick: J. Appl. Phys. 51, 3020 (1980).

[200] Y. Matsuura and K. Fukuda: Jap. J. Appl. Phys. 17, 977 (1978).

[201] R.S. Hemsworth, R.S. Bolden, M.J. Shaw, and N.D. Twiddy: Chem. Phys. Lett. 5, 237 (1970).

[202] E. Gustafsson and E. Lindholm: Arkiv Für Fysik 18, 219 (1966).

[203] A.K. Chen, R. Johnsen, and M. Biondi: Paper GA-5, presented at the 31st Annual Gaseous Electronics Conference, Buffalo, New York (1978).

[204] R. Johnsen, A. Chen, and M.A. Biondi: J. Chem. Phys. 72, 3085 (1980).

[205] W.B. Maier, II: J. Chem. Phys. 62, 4615 (1975).

[206] C.B. Collins and F.W. Lee: J. Chem. Phys. 68, 1391 (1978).

[207] P.K. Leichner, K.F. Palmer, J.D. Cook and M. Thieneman: Phys. Rev. A 13, 1787 (1976).

[208] W. Wieme: J. Phys. B 7, 850 (1974).

[209] J.K. Rice and A.W. Johnson: J. Chem. Phys. 63, 5235 (1975).

[210] A. Barbet, N. Sadeghi, and J.C. Pebay-Peyroula: J. Phys. B 8, 1776 (1975).

[211] D.C. Lorents and R.E. Olson: Excimer Formation and Decay Processes

in Rare Gases, SRI Semiannual Report #1 (1972).

[212] W. Wieme and P. Mortier: Physica 65, 198 (1973).

[213] J. Sabbagh and N. Sadeghi: J. Quant. Spectrosc. Radiat. Transfer 17, 297 (1977).

[214] D.S. Hacker and H. Bloomberg: J. Chem. Phys. 39, 3263 (1963).

[215] V.P. Vitols and H.J. Oskam: Phys. Rev. A 8, 1860 (1973).

[216] S.G. Lias: Int. J. Mass Spect. and Ion Phys. 20, 123 (1976).

[217] M. Ghelfenstein, R. López-Delgado, and H. Szwarc: Chem. Phys. Lett. 49, 312 (1977).

[218] A.W. Johnson and J.B. Gerardo: J. Chem. Phys. 59, 1738 (1973).

[219] E. Zamir, C.W. Werner, W.P. Lapatovich, and E.V. George: Appl. Phys. Lett. 27, 56 (1975).

[220] C.W. Werner, E.V. George, P.W. Hoff, and C.K. Rhodes: IEEE J. Quant. Elect. QE-13, 769 (1977).

[221] P.F. Ambidge, J.N. Bradley, and D.A. Whytock: J. Chem. Soc. (London) Faraday Trans. I 72, 2143 (1976).

[222] R.G. MacDonald and C.B. Moore: J. Chem. Phys. 73, 1681 (1980).

[223] D. Arnoldi and J. Wolfrum: Ber. Bunsenges, Phys. Chem. 80, 892 (1976).

[224] F.H. Field and F.W. Lampe: J. Am. Chem. Soc. 80, 5583 (1958).

[225] F.C. Fehsenfeld and E.E. Ferguson: J. Chem. Phys. 60, 5132 (1974).

[226] L.W. Bader and E.A. Ogryzlo: Nature 201, 491 (1964).

[227] M.A.A. Clyne and D.H. Stedman: Trans. Faraday Soc. 64, 2698 (1968).

[228] R.T. Watson: J. Phys. Chem. Ref. Data 6, 871 (1977).

[229] A.S.M. Raouf, J.D.C. Jones, D.G. Lister, K.Birkinshaw, and N.D. Twiddy: J. Phys. B 13, 2581 (1980).

[230] C.J. Howard, F.C. Fehsenfeld, and M. McFarland: J. Chem. Phys. 60, 5086 (1974).

[231] P.P. Bemand and M.A.A. Clyne: J. Chem. Soc., Faraday Trans. 73, 394 (1977).

[232] K.G. Anlauf, D.S. Horne, R.G. MacDonald, J.C. Polanyi, and K.B. Woodall: J. Chem. Phys. 57, 1561 (1972).

[233] H.O. Pritchard: J. Phys. Chem. 65, 504 (1961).

[234] J.P. Rink: J. Chem. Phys. 36, 262 (1962).

[235] A. Jones and J.L.J. Rosenfeld: Proc. Roy. Soc. (London) A 333, 419 (1973).

[236] F.C. Fehsenfeld, C.J. Howard, and E.E. Ferguson: J. Chem. Phys. 58, 5841 (1973).

[237] W.B. Maier,II: Phys. Rev. A 5, 1256 (1972).

[238] R.S.F. Chang: J. Chem. Phys. 76, 2943 (1982).

[239] J.E. Velazco, J.H. Kolts, and D.W. Setser: J. Chem. Phys. 65 3468 (1976).

[240] G.P. Glass, F.K. Tittel, W.L. Wilson, M.S. Smayling, and G. Marowsky: Chem. Phys. Lett. 83, 585 (1981).

[241] R.W. Waynant and J.G. Eden: Appl. Phys. Lett. 36, 262 (1980).

[242] K.Y. Tang, D.C. Lorents, and D.L. Huestis: Appl. Phys. Lett. 36, 347 (1980).

[243] F.K. Tittel, W.L. Wilson, and G.P. Glass: Paper CB-4, presented at the 34th Annual Gaseous Electronics Conference, Boston, Mass. (1981).

[244] T.W. Hartquist: J. Phys. B 11, 2101 (1978).

[245] V.L. Facobs: Phys. Rev. A 9, 1938 (1974).

[246] H.H. Michels, R.H. Hobbs, and L.A. Wright: J. Chem. Phys. 71, 5053 (1979).

[247] D.E. Rothe: Phys. Rev. 177, 93 (1969).

[248] D.J. Seery and D. Britton: J. Phys. Chem. 68, 2263 (1964).

[249] L.C. Lee, G.P. Smith, J.T. Moseley, P.C. Cosby, and J.A. Guest: J. Chem. Phys. 70, 3237 (1979).

[250] R.L. Kelly and D.E. Harrison, Jr.: Atomic Data 3, 177 (1971).

[251] K.P. Huber and G. Herzberg: Molecular Spectra and Molecular Structure. IV. Constants of Diatomic Molecules (Van Nostrand Reinhold, New York, 1979).

[252] C.Y. Ng, D.J. Trevor, B.H. Mahan, and Y.T. Lee: J. Chem. Phys. 65, 4327 (1976).

[253] W.A. Chupka and J. Berkowitz: J. Chem. Phys. 55, 2724 (1971).

[254] G. Herzberg: Phys. Rev. Lett. 23, 1081 (1969).

[255] W.J. Stevens and M. Krauss: Appl. Phys. Lett. 41, 301 (1982).

[256] J.C. Ingraham and S.C. Brown: Phys. Rev. 138, A1015 (1965).

[257] R.C. Sze: Paper TuA8-1, presented at IEEE/OSA Topical Meeting on Excimer Lasers, Charleston, South Carolina (1979).

[258] T.D. Dreifing and D.W. Setser: J. Chem. Phys. 75, 4360 (1981).

[259] H.W. Drawin: Report EUR-CEA-FC-453, Décembre 1967.

[260] W.L. Morgan and M.J. Pound: Paper FB-3, presented at the 33rd Annual Gaseous Electronics Conference, Norman, Oklahoma (1980).

[261] A.U. Hazi, T.N. Rescigno, and A.E. Orel: Appl. Phys. Lett. 35, 477 (1979).

[262] R.C. Sze and E. Seegmiller: IEEE J. Quant. Elect. QE-17, 81 (1981).

[263] F.K. Tittel, G. Marowsky, W.L. Wilson, Jr., and M.C. Smayling: IEEE J. Quant. Elect. QE-17, 2268 (1981).

[264] L.F. Champagne, L.J. Palumbo, and T.G. Finn: Appl. Phys. Lett. 34, 315 (1979).

[265] W.W. Rigrod: J. Appl. Phys. 36, 2487 (1965).

[266] G.M. Schindler: IEEE J. Quant. Elect. QE-16, 546 (1980).

[267] D. Eimerl: J. Appl. Phys. 51, 3008 (1980).

[268] M. Abramowitz and I.A. Stegun: Handbook of Mathematical Functions (U.S. Nat'l Bur. Stand. AMS-55, 1970).

[269] J.J. Stoker: Nonlinear Elasticity (Thomas Nelson and Sons, London, 1968).

[270] J.P. Vidoscic: "Mechanics of Materials" in Marks' Standard Handbook for Mechanical Engineers. ed. by T.T. Baumeister and L.S. Marks (McGraw-Hill, New York, 1967).

[271] J.J. Duderstadt and W.R. Martin: Transport Theory (John Wiley & Sons, New York, 1979).

[272] H.S.W. Massey: Electronic and Ionic Impact Phenomena, Vol. III, Ch. 18 (Claredon, Oxford, 1971).

[273] L. Landau: Z. Phys. Sowjet 2, 46 (1932).

[274] C. Zener: Proc. Roy. Soc. A 137, 696 (1932).

[275] J.J. Thomson: Phil. Mag. 47, 337 (1924).